VRIJE UNIVERSITEIT

Orogenesis and Subduction in Analogue Models

Expressions of lateral subduction polarity change below the Alps

ACADEMISCH PROEFSCHRIFT

ter verkrijging van de graad Doctor aan
de Vrije Universiteit Amsterdam,
op gezag van de rector magnificus
prof.dr. L.M. Bouter,
in het openbaar te verdedigen
ten overstaan van de promotiecommissie
van de faculteit der Aard- en Levenswetenschappen
op vrijdag 23 september 2011 om 13.45 uur
in de aula van de universiteit,
De Boelelaan 1105

door

Stefan Wietse Luth

geboren te Amsterdam

promotor:	prof.dr. S.A.P.L. Cloetingh
copromotoren:	dr. E. Willingshofer
	prof.dr. D. Sokoutis

The territory

Up here in the white country

any tree for a totem
any rock for an altar

discover!

this ground is suicidal

annihiliates everything
but the most essential

poet - your kingdom

Kenneth White

The research presented in this thesis was carried out at:

Department of Structural geology and Tectonics
Faculty of Earth and Life Sciences
Vrije Universiteit Amsterdam
De Boelelaan 1085
1081 HV Amsterdam
The Netherlands

Financial support was provided by the Netherlands Organisation for Scientific Research (NWO)

Nederlandse Organisatie voor Wetenschappelijk Onderzoek

Reading committee: prof.dr. C. Faccenna
prof.dr. B. Fügenschuh
prof.dr. T. Gerya
prof.dr. R. Wortel
dr. C. Rosenberg

ISBN/EAN 9789461081902

This is NSG publication Nr. 2011.09.23

Title: Orogenesis and Subduction in Analogue Models. Expressions of lateral subduction polarity change below the Alps.
(PhD thesis, VU University Amsterdam)

Translated title: Gebergtevorming en Subductie in Analoge Experimenten. Kenmerken van laterale subductie polariteitwissel in de Alpen.
(Academisch proefschrift, Vrije Universiteit Amsterdam)

Printed by Gildeprint Drukkerijen, Enschede

Cover: WSW-ward view from Walten on St. Martin (Italy), combined with a top-view image of a lithosphere-scale analogue experiment.

Contents

Acknowledgements

This scientific achievement would have been impossible without the help and support of my nearest and dearest. Javier, what a privilege to have you both as friend and collegue! Many thanks for all the funny and great moments we shared between rocks, puttie, and papers. I will definitely miss the moments we hoisted beautiful models out of the freezer. I should mention the fact that many of the pictures shown in this thesis have that fancy look because of your input. Many thanks also to the Teclab assistants, Inge, Nynke, and Arno, for creating a professional work environment, and of course for all your help and kindness, which allowed me om ook nog eens gezellig Nederlands te kunnen praten tussen al die VU-allochtonen. Arno samen met Jozua en Marten, reuze bedankt voor jullie bijdragen aan de grote hoeveelheid metingen in het Passeier dal. Marten, tevens ben ik je dankbare kamergenoot, niet allerminst omtrent je bruikbare velduitwerkingen en behulpzaamheid, maar ook voor je sociale verdiepingen. Succes nog verder!

Ernst and Dimitrios, my supervisors. I thank you for making all this possible, but also for your never-ending enthusiasm and trust in me. Your doors were always open for a discussion, or just a laugh. I am grateful to everyone from the Earth Science department. In particular, my colleague PhD-students: David, Wart, Maarten, Suzanne, Maud, Nico, Karen, Magdala, Mohammed, Herman, Tarig and Andrea. Thanks to everyone I worked with in the Teclab, such as Melodie, Andrea (runfile), Endre, Ioan, Tadashi, Maria, and Andreas. You all rock! Many thanks to my friends from the Petrology section; Raheleh, Esther, Elco, Sandra, and Josepha. Liviu, I appreciated your daily encouragement a lot. Fred, great that you have introduced me to the CT-scanner. Thanks Sierd, for promoting my work to the scientific community, of which I thank in particular my reading committee for their reviews: Prof.dr. B. Fügenschuh, Prof.dr. R. Wortel, Prof.dr. T. Gerya, Prof.dr. C. Faccenna, and Dr. C. Rosenberg.

Jan, bedankt dat je speciaal voor mij 100 meter van de VU bent gaan wonen. Zo konden we werk/studie toch mooi combineren met onze vriendschap. Je broodjes haring deden het daarbij erg goed. Kees en Willy, bedankt voor jullie interesse, en afleiding tijdens onze traditionele wandelingen en rondom. Irene en Maaike, lievere zussen bestaan niet. Lees dit boekje, als jullie echt alles van me willen weten. Tevens bedankt voor het helpen doorslikken van de stukjes kommer met kwel. En ja Vanja, 5 maanden lang puttie kneden is ook wetenschap. Mama en Peter, bedankt voor de morele steun. Jullie zijn al een tijdje benieuwd naar mijn “What’s next?” Ik ook. Misschien nog een studie? Of gewoon een avondje op de bank bij jullie thuis? We zien wel. Ria, bedankt voor al je stamppotjes gevuld met flink wat gezond verstand. Winneweer is niet ver weg. Mijn liefste Eef, geen bla bla, maar reuze bedankt voor al je liefde en aanmoedigingen!

En verder...

....hoop ik door te bedanken niet teveel af te sluiten. Behalve dit boekje!

Samenvatting

Gebergtevorming is veelal een gevolg van botsingen tussen tektonische platen. De grootschalige opbouw van gebergten kan echter sterk variëren, en wordt bepaald door een samenspel van geodynamische processen. Belangrijke factoren zijn de totale hoeveelheid convergentie, en de relatieve richting en snelheid van de botsende platen. Maar gebergtevorming wordt eveneens beïnvloed door rheologie, ofwel de sterkte van de platen en het gebergte zelf, die grotendeels afhankelijk is van samenstelling, druk, en temperatuur.

Tijdens een botsing reageert een plaat (lithosfeer) door verdikking of door onderschuiving (subductie). Oceanische lithosfeer ondergaat gemakkelijk subductie, terwijl convergerende continentale lithosfeer meestal verdikt. Geofysisch onderzoek naar de diepe ondergrond van gebergteketens heeft aangetoond dat verdikking en subductie echter ook gelijktijdig kunnen voorkomen. Het mantel gedeelte van de lithosfeer ondergaat in een dergelijk situatie subductie, terwijl de korst juist van de mantel wordt afgeschraapt en zich verdikt tot een wig geometrie ("orogenic-wedge"). Door het trage verloop van gebergtevorming en de ontoegankelijkheid van de diepe structuren, is inzicht in de interactie tussen mantel subductie en korstverdikking beperkt. Een beter begrip van continentale botsingzones vereist een multidisciplinaire aanpak, waarin observaties aan het aardoppervlak, geofysische waarnemingen van de diepe ondergrond, en geschaalde modellen worden gecombineerd.

In dit proefschrift wordt de samenhang tussen continentale mantel subductie en gebergtevorming nader onderzocht. Met behulp van analoge modellen worden allereerst de mechanische randvoorwaarden voor mantellithosfeer subductie bepaald. Vervolgens worden de gevolgen van deze randvoorwaarden voor de opbouw van het bovenliggend gebergte nauwkeurig bestudeerd. De nadruk hierin ligt op de grootschalige, geometrische gelijkenissen tussen de modeleerresultaten en gebergteketens wereldwijd.

De Alpen lopen als rode draad door dit proefschrift. De tektonische opbouw van de Alpen is namelijk relatief goed onderzocht, en omvat een rijkdom aan regionale variaties. Op relatief korte afstand variëren de breedte van het gebergte, de tijdsperiode en vergentie van dekblad overschuivingen, en de hoeveelheid opheffing van hooggradig metamorfe gesteenten aanzienlijk. Dieper onder het gebergte heeft recentelijk geofysisch onderzoek een laterale variatie in subductie richting aangetoond. Deze verrassende polariteitwissel in onderschuiving duidt op zuidwaartse subductie van de Europese mantel onder de West- en Centrale Alpen, maar een noordwaartse subductie van de Adriatische mantel onder de Oost-Alpen. In dit proefschrift wordt gezocht naar een mogelijk verband tussen deze "subduction flip" en de genoemde variaties aan het oppervlak. Allereerst wordt bepaald of een laterale polariteitwissel in subductie gevolgen heeft voor de bovenliggende korststructuren. Indien dat zo is, wordt er gekeken of bepaalde structuren in the Alpen inderdaad gerelateerd zijn aan de polariteitwissel in subductie. Een combinatie

van analoge korst- en lithosfeermodellen, en een veldstudie wordt hiervoor ingezet als belangrijkste hulpmiddel.

Inzicht in de regionale verspreiding van afkoelingsdateringen in de Alpen is van grote waarde voor het ontrafelen van de opheffingsgeschiedenis van het gebergte. Hoofdstuk 2 presenteert daarom een compilatie van afkoelingsdateringen in de Oost-Alpen gedurende de laatste (post) fase van de continentale botsing. De dateringen zijn gebaseerd op Rb/Sr en Ar/Ar isotopen verhoudingen, en splijtsporen in zirkoon of apatiet. De resultaten onthullen een overgang van lokale opheffing in het Tauern venster gedurende het vroeg Mioceen, gevolgd door meer regionale opheffing in het midden tot laat Mioceen. Opheffing in het Tauern venster was relatief snel, en werd gedomineerd door verplaatsingen langs de Brenner en Katschberg breuken, maar ook door grootschalige plooiing. Dit duidt op gelijktijdige interactie tussen N-S gerichte verkorting en O-W gerichte extensie.

De eerste serie analoge modellen, gepresenteerd in hoofdstuk 3, verschaft inzicht in de mechanische randvoorwaarden voor subductie van de continentale mantellithosfeer. De geometrie en de rheologie van de plaatgrens spelen hierin een belangrijke rol. Een 45° hellende plaatgrens en de aanwezigheid van zwak, lubricerend materiaal zijn noodzakelijk voor het verkrijgen van subductie. Ook blijkt dat de mantellithosfeer alleen kan subduceren indien de laag ontkoppelt van zijn bovenliggende korst. Deformatie van de korst blijft bij doorgaande subductie gelokaliseerd tot direct boven de plaatgrens. Pas als subductie wordt bemoeilijkt, bijvoorbeeld door de consumptie van lubricerend materiaal, of door een beperkte korst-mantel ontkoppeling, beginnen beide platen intern te deformeren. Ontkoppeling tussen de korst en de mantel gebeurt in analoge modellen langs rheologische contacten. Het gebruik van een relatief zwakke onderkorst bevordert dus ontkoppeling. Uit de experimenten, gepresenteerd in hoofdstuk 4, blijkt echter dat veranderingen in de rheologische stratigrafie van de lithosfeer grote gevolgen heeft voor de opbouw van een gebergte. De aanwezigheid van een ontkoppelniveau in de onderschuivende plaat leidt namelijk tot een verbreding van het gebergte richting het voorland. Beperking van het ontkoppelniveau tot de plaatgrens resulteert juist in een relatief smalle wig. Deze experimenten tonen eveneens het belang van de mate van ontkoppeling voor de totale hoeveelheid subductie van mantellithosfeer, het initiëren van retro-shears, en de topografische ontwikkeling van het gebergte.

In hoofdstuk 5 laat een tweede, meer geavanceerde, serie analoge experimenten zien dat een laterale overgang in subductierichting de geometrie van het gebergte sterk kan beïnvloeden. Deze invloed komt voornamelijk voort uit de laterale interactie tussen de aangrenzende domeinen van tegengestelde subductie. Op manteldiepte resulteert interactie tussen de subductie domeinen in de ontwikkeling van een transitiezone, waarin de hoeveelheid subductie beperkt blijft, en de overschuivende platen juist naar beneden worden getrokken. In deze transitiezone is de grootschalige mantel structuur dus symetrisch. De korst reageert hierop door verdikking van de onderkorst, verbreding van de orogene wig op beide platen, en afname van topografie. De breedte van de transitiezone wordt bepaald door de mate van (ont)koppeling tussen de subductie domeinen. Laterale ontkoppeling verlaagt de interactie, terwijl een sterke koppeling leidt tot een relatief brede transitiezone met een duidelijke oppervlakte expressie.

De resultaten van een uitgebreide veldstudie naar de kinematiek van het Passeier- en Jaufen breuk systeem worden behandeld in hoofdstuk 6. Aan de hand van de veldgegevens wordern deze breuken niet als een enkel breuksysteem geinterpreteerd. De

Jaufen breuk onderging namelijk zowel een ductiele als een brosse deformatie fase, terwijl de Passeier breuk slechts brosse deformatie heeft ondergaan. Tevens onthult een tensor analyse, in combinatie met analoge korstmodellen, dat het ontstaan van de Passeier breuk direct gerelateerd kan zijn aan de Zuid-Alpiene indenter geometrie. Deze uitkomst heeft gevolgen voor de gesuggereerde kinematische verbinding tussen de veel grotere Giudicarie en Brenner breuken, als zijnde de expressie van een laterale subduction flip. Hoewel deze breuken als een uiting van zowel noordwaardse indentatie als subductie kunnen worden beschouwd, wordt een kinematische verbinding van beide in deze context niet ondersteund.

Summary

Orogenesis is often the result of a collision between tectonic plates. The evolution and large-scale geometry of mountain belts vary, and is mainly governed by interplay between several geodynamic conditions and processes. Important parameters during orogenesis are for instance the total amount of plate convergence, and the relative motion as well as the velocity of the colliding plates. In addition, rheological conditions, referring to the strength of the plates and the evolving orogen, play an important role during orogenesis as they are strongly dependent on composition, pressure, and temperature.

The response of a tectonic plate (lithosphere) during collision is by thickening, folding, or subduction. Oceanic lithosphere easily subducts, while continental lithosphere mostly thickens or folds. Geophysical research on the deep subsurface of mountain chains has shown that thickening and subduction can also coincide. In this scenario, the mantle lithosphere undergoes subduction; meanwhile the crust is scraped off and thickens into a wedge geometry (orogenic wedge). Since orogenesis is a very slow process, and the deep sub-surface is inaccessible to direct observations, insights on the interaction between mantle subduction and crustal thickening are so far limited. A better understanding of continental collision zones demands for an integrated approach involving geological and geophysical interpretations as well as a combination of several modelling techniques.

The aim of this thesis is to investigate the mechanical interaction between continental mantle lithosphere subduction and mountain building. With the use of analogue modelling, the favorable mechanical boundary conditions for subduction of the continental mantle lithosphere are first determined. Subsequently, the consequences of these boundary conditions on the development of the overlying orogen are studied in more detail. Emphasis is put on the large-scale geometric similarities between the model results and mountain ranges worldwide.

Throughout this thesis, the evolution of the Alps is an important theme. Therefore the tectonics of the Alps has been investigated in detail, and includes several interesting along-strike variations. On a relative short distance these variations comprise the total width of the orogenic wedge, the timing and vergence of nappe stacking, and the amount of exhumed high-grade metamorphic rocks. At a deeper level, recent geophysical studies have revealed a lateral subduction polarity change, indicating southward subduction of the European mantle lithosphere below the Western- and Central Alps, but northward subduction of the Adriatic mantle lithosphere below the Eastern Alps. This research elaborates on a possible correlation between this “subduction-flip” and the crustal variations observed at shallower depths. First, we investigate if a lateral change in subduction polarity has an imprint on the overlying crustal architecture. Second, if this is the case, we discuss whether certain crustal structures within the Alps can be interpreted in the context of a subduction polarity change at depth. A combination of lithosphere- and crustal-scale analogue modelling together with a detailed field study has been used to address these questions.

Based on the regional distribution of cooling ages throughout the Eastern Alps, insights can be gained on the exhumation history of the orogen. In this context, Chapter 2 presents a compilation of geochronological data, which documents the post-collisional cooling history of the Eastern Alps. The cooling ages were derived from Rb/Sr and Ar/Ar isotope ratios, and zircon or apatite fission tracks. The results portray cooling restricted to the Tauern Window during the early Miocene, followed by regional exhumation during the late to middle Miocene. Exhumation of the Tauern Window occurred relatively fast, and was coincided by normal displacements along both the Brenner- and Katschberg faults, as well as erosion in response to large-scale folding. This indicates a strong interplay between N-S shortening and E-W extension during exhumation of the TW.

The first series of analogue models, presented in Chapter 3, provide insights on the mechanical boundary conditions allowing for subduction of the continental mantle lithosphere. It turns out that the geometry and the rheology of the plate boundary play important roles. A 45° dipping plate boundary and the presence of a weak lubricator are needed to initiate subduction. It also appears that the mantle lithosphere only subducts if it is able to decouple from the overlying crust. With ongoing subduction, deformation of the crust remains localized close to the plate boundary. Only if subduction hampers, for instance by consumption of a lubricator or by limitation of crust-mantle decoupling, both plates begin to deform internally.

In de presented analogue models, decoupling between the crust and the mantle lithosphere occurs along rheological boundaries. Hence, the use of a weak lower crust promotes decoupling. However, the experiments presented in Chapters 4 show that varying the rheological stratigraphy of the lithosphere may also have consequences for the build-up of an orogen. The presence of a decoupling horizon in the lower plate results namely in widening of the orogenic wedge towards the foreland. On the other hand, limiting the decoupling horizon to the plate boundary will produce a relative narrow wedge. In addition, the above experiments emphasize the role of the degree of decoupling on the total amount of subduction of mantle lithosphere, the initiation of retro-shears, and the evolving topography of the orogen.

Within Chapter 5, a second, more advanced, series of analogue experiments shows that a lateral transition of subduction polarity can have a strong influence on the geometry of the orogen. This influence is in particular underlain by a lateral interaction between the adjacent domains of opposing subduction polarity. At mantle depth, interaction between the subduction domains results in the development of a transition zone, in where the amount of subduction is limited, while the upper plates bend down significantly. Hence, within the transition zone, the colliding mantle structure appears symmetric. As a result, the lower crust thickens, the orogenic wedge widens towards both plates, and topography is low. The width of the transition zone is governed by the degree of decoupling between the subduction domains. Lateral decoupling reduces interaction, while strong coupling leads to a relative wide transition zone with a clear surface expression.

The outcome of the field study on the kinematics of the Passeier- and Jaufen fault system is treated in Chapter 6. Field data interpretations indicate that these faults do not form a single fault system. The Jaufen fault underwent a ductile- and a brittle deformation phase, while the Passeier fault solely went through a stage of brittle deformation. Additionally, a tensor analysis in combination with crustal-scale analogue experiments indicates that the formation of the Passeier line can be directly related to the South Alpine indenter

geometry. This interpretation has implications for a suggested connection between the much larger Giudicarie- and Brenner faults. Although these faults may still be considered as expressions of the lateral subduction flip, a kinematic connection between these faults cannot be supported.

Chapter **1**

Introduction

Many convergent orogens are characterized by thickening of buoyant crust and subduction of mantle lithosphere. The thickened crustal unit is commonly referred to as the orogenic wedge and consists of intensively deformed rocks and far displaced thrust sheets indicating a large amount of shortening. The geometry of the wedge differs among orogens, but typically a pro- and retro-side can be recognized (Fig. 1.1). The pro-side overlies the downgoing plate and thus contains mainly crustal material derived from this plate. The retro-side vergence towards the upper plate, and accommodates shortening mainly by exhumation of crustal material along retro-shears. Hence, with the determination of crustal wedge geometries, the direction of mantle lithosphere subduction can be revealed.

Although a typical density structure of the lithosphere allows for subduction of the mantle lithosphere into the asthenosphere, continental crust resists subduction mainly by its buoyancy. For the overall behaviour of the lithosphere this implies decoupling between the crust and the underlying mantle lithosphere. Whether the crust and mantle are strongly- or only weakly decoupled, however, varies among orogens and between orogenic cycles. Variability on the degree of decoupling in turn influences the orogens large scale responses, including the amount of subduction, the architecture of the orogenic wedge as well as the onset and extent of intra plate deformation. It has been shown by previous studies that the degree of crust-mantle decoupling strongly depends on the rheological stratification of the lithosphere (e.g. *Davy and Cobbold* [1991] and *Willingshofer and Soukoutis* [2009]). However, the dynamic aspects of decoupling, as well as its overall effects on the evolving orogen are hitherto only poorly constrained.

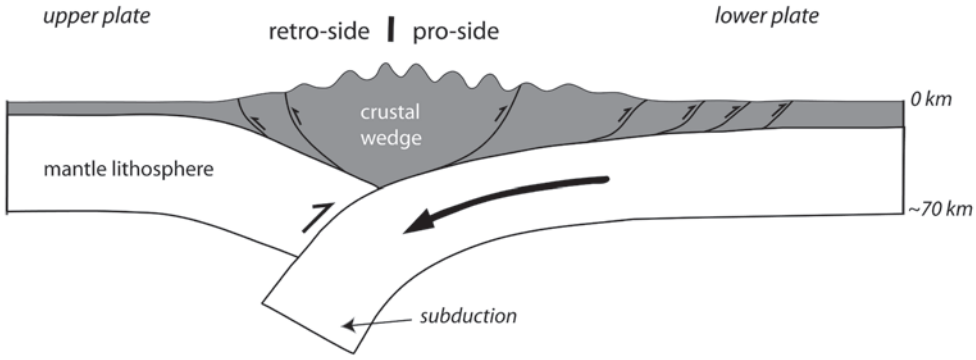

Figure 1.1 Cartoon illustrating the typical build-up of a collisional orogen. Continental crust (dark) responds on collision by the formation of an orogenic wedge, which can be subdivided into a relative narrow retro-side and a wide pro-side. Note that in general the asymmetry of the wedge reveals the subduction direction of the mantle lithosphere (white).

1.1 Subduction polarity change beneath the Alps

Within the Alps, an asymmetric orogenic wedge in the Western- and Central Alps is characterized by a northward facing pro-side, and a narrower southward facing retro-side. This wedge geometry would imply southward subduction of the European mantle lithosphere, which was indeed confirmed by deep seismic transects, such as along the NFP-20-East [e.g. *Pfiffner et al.*, 1997b]. Towards the Eastern Alps the wedge is shaped more symmetrically, and a clear distinction between pro- and retro-sides becomes difficult. As a consequence, determination of the Alpine subduction polarity based on crustal build-up is actually not that straight forward. Nevertheless, the traditional concept in Alpine tectonics that European lithosphere subducted southward underneath the Adriatic plate along the entire Alpine mountain chain was maintained for a long time [e.g. *Pfiffner et al.*, 1997b; *Schmid and Kissling*, 2000; *TRANSALP Working Group*, 2002].

With the application of tele-seismic tomography carried out by *Lippitsch et al.* (2003) the remnants of the subducted slabs could be traced along the entire Alpine chain (Fig. 1.2). Surprisingly, the deep structure revealed a lateral change of the subduction polarity from southeast dipping in the Western- and Central Alps to northeast dipping in the Eastern Alps. This implies subduction of the European mantle lithosphere underneath the Western and Central Alps, whereas the Adriatic/Dinaric mantle lithosphere subducted below the Eastern Alps.

A surface expression of the laterally changing subduction polarity at depth has been discussed by *Schmid et al.,* [2004]. They considered Miocene deformation along the N-S trending Brenner- and Giudicarie lines as well as southward thrusting in the eastern Southern Alp as possible expressions of Adria subducting towards the north-eastward. Whether crustal-scale deformation along the Brenner- and Giudicarie faults indeed reflects the change of subduction polarity at depth remains speculative as does the influence of the polarity change on the structural and topographic evolution of the Eastern and Southern Alps.

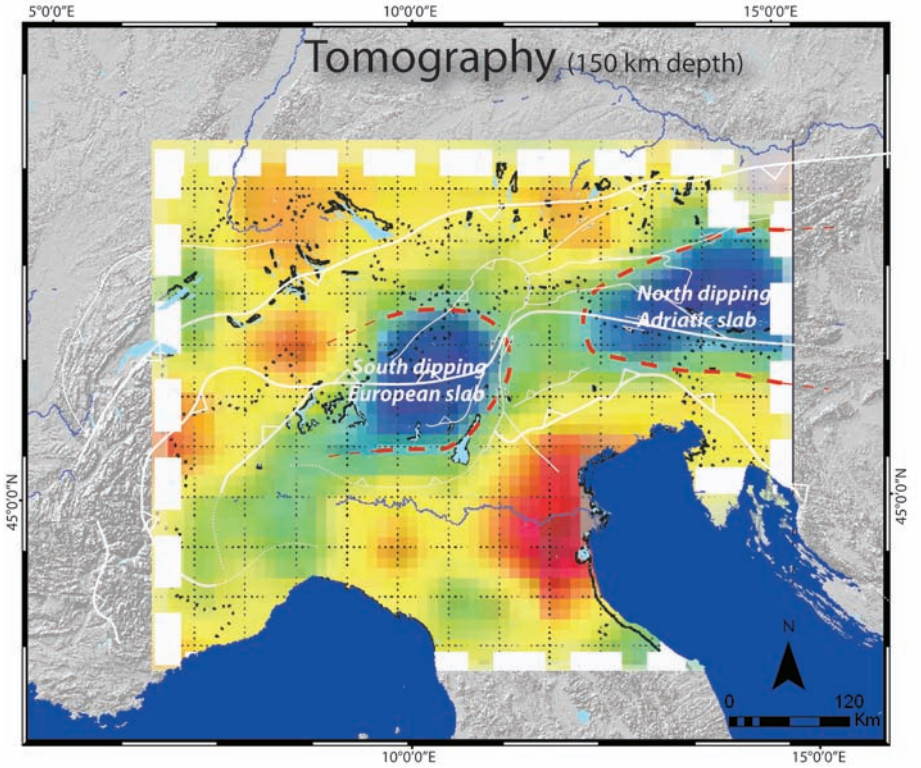

Figure 1.2 High-resolution tele-seismic tomography revealing a subduction polarity change below the Alpine region after *Lippitsch et al.* (2003). Blue regions surrounded by red dashed lines indicate areas of high-P-wave velocity and are interpreted as European and Adriatic mantle lithosphere, which subducted SE and NE, respectively. Interpolated velocities were derived from depths between 135 km and 165 km. White lines indicate major Tertiary faults. Implications for the Alpine orogenesis are further discussed in Chapter 5.

1.2 Scope of the thesis

The aim of this thesis is to provide a better understanding of the first-order crustal and topographic expressions of a lateral polarity change of mantle lithosphere subduction. As such, regional along-strike variations observed within crustal wedges, as for instance in the European Alps but also New Zealand, may be interpreted in the light of a lateral subduction polarity change.

Before investigating complex three-dimensional scenarios, we first need to understand how crust-mantle (de)coupling affects crustal wedge formation within a setting of uni-directed subduction. Therefore, the first part of this thesis focuses on the influence of plate boundary geometry and lower crustal rheology on both mantle lithosphere subduction and mountain building. The second part builds upon those results by elaborating on the lateral interplay between opposing subduction domains and its imprint on crustal deformation and surface topography. The main tools used for investigating these spatial complex relations have been analogue modelling and structural fieldwork.

1.2.1 Analogue modelling

Analogue modelling has already been used in the context of continental collision to study for example; indentation and lateral extrusion tectonics, lithospheric buckling, the mechanics of thrust wedges, and even feedback relations between erosion/ sedimentation and tectonic [e.g. *Weijermars and Schmeling*, 1986; *Davy and Cobbold*, 1991; *Brun et al.*, 1994; *Willingshofer and Sokoutis*, 2009]. The aim of the experiments presented in this thesis is primarily to understand the interrelations between mantle-lithosphere subduction and crustal deformation, and more specifically, how these depend on plate boundary geometry, lithosphere rheology, and subduction polarity.

Our modelled lithosphere comprised three layers representing from bottom to top upper mantle lithosphere, lower crust, and upper crust; all together floating on a low viscosity asthenosphere. Mixtures of silicone polymer putties were used as analogue for the viscous layers whereas feldspar sand represented the brittle deforming upper crust. Additionally to previous analogue modelling studies our density structure allowed for subduction of the mantle lithosphere [see for comparison *Shemenda and Grocholsky*, 1992; *Funiciello et al.*, 2004]. Systematic variation of the degree of plate (de)coupling was induced by the implementation of a relative weak zone and/or a weak lower crust comprised of silicone putty.

1.2.2 Alpine field study and crustal-scale analogue modelling

Correlations between surface features and the subduction polarity change at depth requires a detailed compilation of geochronological- and structural data. For example, the spatial distribution of cooling ages may reveal cooling trends, which in turn can be related to exhumation patterns reflecting the subduction polarity throughout the Miocene. Another more structural expression of the subduction polarity change might be considered the displacement along the Giudicarie- and the Brenner lines. However, a genetic connection between these major N-S trending faults as suggested by some authors [e.g. *Schmid et al.,* 2004] is still poorly constrained. Whether the faults structures are indeed linked requires better kinematic constraints on the complex deformation pattern and the interplay between the Jaufen- and Passeier faults. In addition, considered the close vicinity of the Adriatic indenter, these faults may also contain a kinematic imprint related to crustal indentation. Hence, considering the Passeier and Jaufen faults as connectors between the large Giudicarie- and the Brenner-fault systems, demands to recognize the role played by indentation. With this purpose, a kinematic field study was carried out along the Passeier- and Jaufen lines, of which its result was compared with crustal-scale indentation models.

1.3 Thesis outline

Chapter 2 presents a compilation of geochronological data, which documents the post-collisional cooling history of the Eastern Alps. A series of *cooling maps* were compiled by means of cooling ages derived from different isotope systems covering a temperature window of 550°C to 110°C. Cooling trends appearing from these maps allow for the recognition of along-strike variations in exhumation throughout the Eastern Alps

and its direct surrounding as well as their underlying exhumation mechanisms. In the following chapters these exhumation mechanisms are then further explored by interpreting the various uplift patterns monitored in the analogue experiments.

Chapters 3 to 5 address the mechanical responses of the lithosphere on continental collision by lithosphere-scale analogue models. Special emphasis is put on the rheological layering of the lithosphere affecting decoupling conditions between and within colliding plates.

Chapter 3 focuses on the role of the plate boundary in a convergent setting. Key variables are the degree of plate (de)coupling along the plate interface and along the Moho of the lower plate as well as the geometry of the plate contact. It turns out that these few important parameters largely control the amount of mantle lithosphere subduction, the crustal wedge architecture, and the onset of intra plate deformation.

Chapter 4 aims to further unravel the influence of decoupling conditions on mantle lithosphere subduction and crustal wedge formation by varying the rheological stratification of the lithosphere. These set-ups invoke spatial- and temporal variations in decoupling conditions with major implications for the evolving orogenic wedge. As a result, orogenic wedges are classified according to their mechanical responses in relation to various decoupling conditions. Finally, the obtained modelling results, including the various wedge geometries, are compared with orogens around the world.

Chapter 5 reveals crustal and topographic expressions related to a lateral change in subduction polarity. The lithosphere-scale experiments were designed especially to study the lateral interaction between adjacent subduction domains. It is shown that the degree of coupling between the subduction domains influences subduction and slab geometry as well as the build-up of crustal wedges. Strong lateral plate interaction produces a wide transition zone in where the structural imprint deviated significantly from the overall collisional pattern.

Chapter 6 combines a field study with crustal-scale analogue modelling aiming to improve the kinematic constraints between the Giudicarie- and the Brenner fault zones. Within this region, including the Passeier- and Jaufen faults, Neogene deformation as suggested by *Schmid et al.* [2004] might reflect the lateral change in subduction polarity at depth. In this chapter we investigate, however, if these faults could have resulted from crustal indentation.

Finally, Chapter 7 provides a summary of the main conclusions and discusses the implications of the here presented field- and modelling results on the overall tectonic interpretation of orogens, and in particular the Alps. I will conclude this thesis by briefly suggesting possible directions for further investigations building upon this research.

Chapter **2**

Mapping of the post-collisional cooling history of the Eastern Alps

2.1 Introduction

The European Alps are one of the most intensively investigated orogens on earth. However, many questions remain, particularly in the Eastern Alps, such as the exact timing of deformation, metamorphism and exhumation of rocks and their related feedback loops with deep (mantle) as well as surface processes.

Many conclusions in the context of mountain building have been derived in the past with the help of geobarometry, geothermometry, and geochronology. The latter is useful to constrain the timing of metamorphic and deformation events under certain temperature and pressure conditions within evolving orogens. Geochronological data from the Eastern Alps are abundant and underpins many findings throughout the last decades. For example, the Eastern Alps bear evidence for two independent collisional events in the Cretaceous and the Paleogene, respectively *[e.g. Froitzheim et al., 1994]* or the temporal variations of peak metamorphic conditions [*Inger and Cliff*, 1994; *Hoinkes et al.*, 1999; *Neubauer et al.*, 2000]. The wide spread in recorded ages, both, in time and space, in combination with the complex Alpine history has given rise to different interpretations of their meaning (e.g. crystallization, metamorphism, exhumation). A review of geochronological data in a regional framework can be valuable in deciphering orogen-scale trends, which help to better constrain processes at work and to separate local from regional effects.

This chapter is based on Luth S. W. and Willingshofer E., 2008; Mapping of the post-collisional cooling history of the Eastern Alps. Swiss Journal of Geosciences, 101: 207-223.

Following up on the reviews of e.g. *Frank et al.* [1987], *Thöni* [1999] and *Hoinkes et al.* [1999], we present updated and geo-referenced compilations of isotope data for the Eastern Alps. The presented work aims to map the post-collisional cooling history of the entire Eastern Alps by compiling available cooling ages in one single database. From this database we can extract thematic maps regarding cooling history by using GIS mapping tools. These cooling maps can be used to gain insight into regional cooling trends, cooling rates, and their relation with the tectonics, such as the formation of the Tauern Window (TW), the distribution of north-south shortening due to indentation, or the onset of lateral extrusion. Furthermore, the presented database also highlights regions of poor data coverage and, hence, may be of importance for the planning of future dating projects. The database will be updated regularly and can be accessed via the internet (http://www.geo.vu.nl/~wile/).

2.2 Geological setting

The structure of the Eastern Alps is that of a collisional orogenic belt with the continental Austoalpine (AA) unit as highest tectonic unit overlying the Penninic ("Alpine Tethys") suture and the continental units, including their sedimentary cover of European affinity (i.e. Sub-Penninic sensu Schmid et al., [2004] in lowest structural position (Figs. 2.1a-b). Multiply deformed Austroalpine basement and cover units of Apulian origin are most abundant in the Eastern Alps and their internal structure and last metamorphic overprint is related to Cretaceous stacking of tectonic units following the consumption of the Triassic Meliata ocean further east, e.g. Neubauer et al. [2000] and references therein. The Penninic suture and the Sub-Penninic units are exposed along the central axis of the Eastern Alps within tectonic windows such as the Engadin-, Tauern- and Rechnitz Windows.

They contain from bottom to top, the Zentralgneiss basement unit, (para) autochthonous, highly metamorphosed cover units of the European continental shelf (Lower Schieferhülle), and allochthonous metasediments (Upper Schieferhülle), as well as remnants of the Penninic oceanic crust. The ophiolites belong to the Jurassic, Alpine Tethys (Penninic Ocean) ocean, which separated European from Apulian paleogeographic domains [*Frisch*, 1979; *Oberhauser*, 1995; *Schmid et al.*, 2003]. Subduction of this ocean commenced during the late Cretaceous and lasted until the Eocene [*Frisch*, 1979].

The core of the TW exposes pre-Variscan metamorphic basement and Variscan granitoids, the Zentralgneiss, in a series of domes [*Zimmermann et al.*, 1994; *Oberhänsli and Goffé*, 2004]. The domes form the core of a large anticline with an axis parallel to the window's strike as a result of syn- and post collisional shortening coeval with orogen-parallel extension [*Lammerer and Weger*, 1998].

East of the Bergell intrusion, the Periadriatic Fault separates the AA unit from the Southern Alps, a Miocene, south vergent fold and thrust belt of Apulian origin [*Castellarin et al.*, 1992] (Fig. 2.1). Slip along this fault was right-lateral with a minor (few kilometers) north-side up component during the late Oligocene and Miocene [*Ratschbacher et al.*, 1991; *Mancktelow*, 1995]).

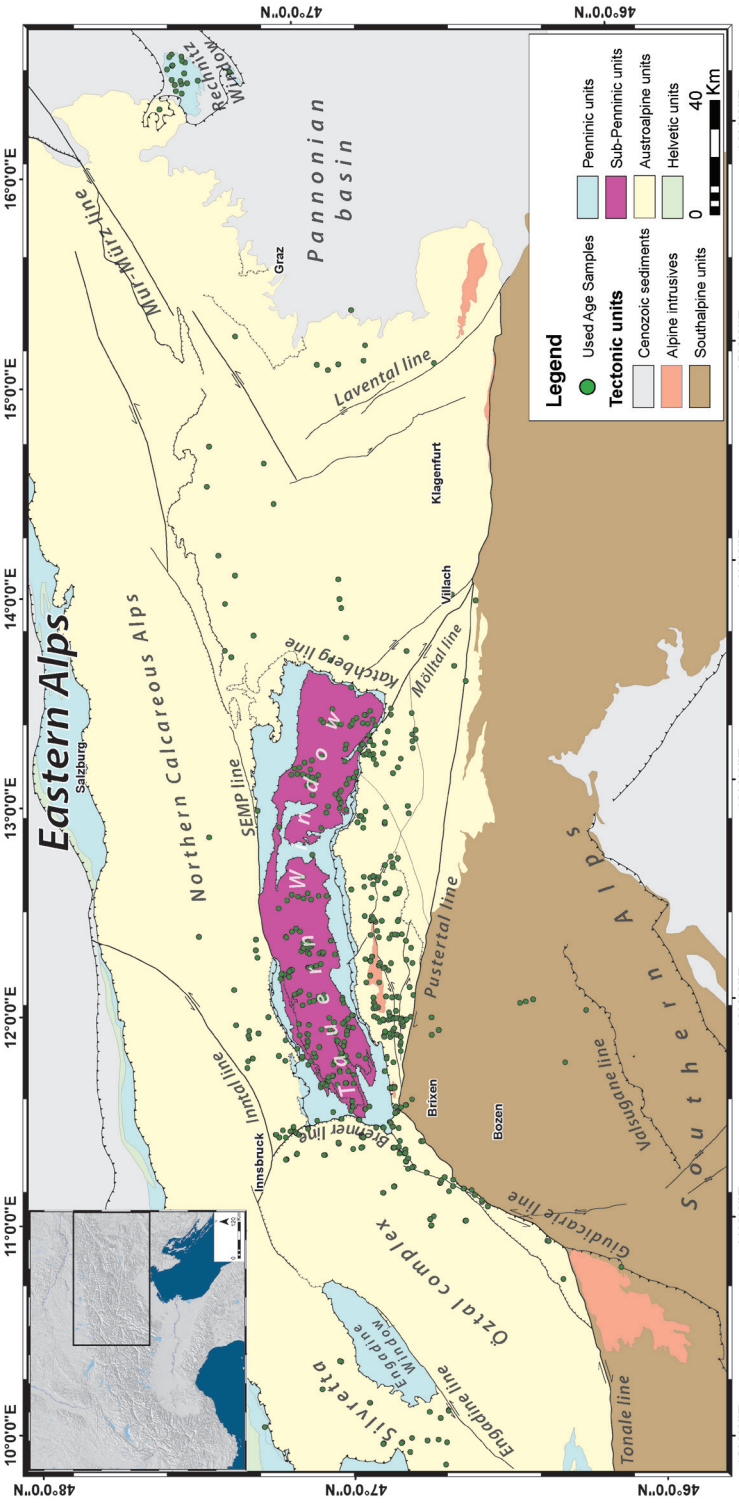

Figure 2.1a Simplified tectonic map of the Eastern Alps based on Bigi et al. [1990-92] and Egger et al. [1999]. The dots represent the age sample locations used in this study. SEMP: Salzach–Ennstal–Mariazell–Puchberg line.

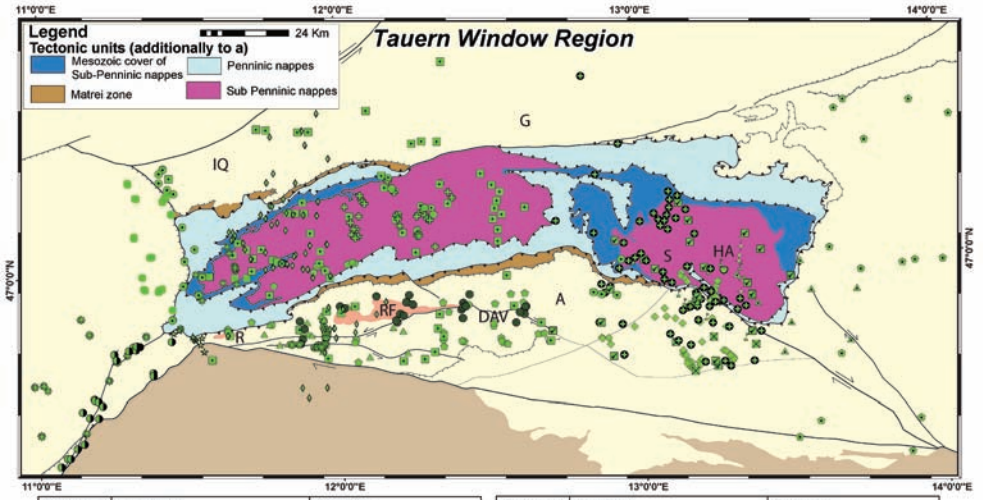

Symbol	Author	System
	Besang et al., 1968	Rb/Sr, K/Ar, biotite
	von Blackenburg et al., 1989	Rb/Sr, K/Ar, biotite
	Borsi et al., 1973	Rb/Sr, biotite
	Borsi, 1977	Rb/Sr, biotite
	Borsi, 1978	Rb/Sr, biotite
	Brewer & Jenkins, 1969	K/Ar, biotite
	Dunkl et al., 2003	ZFT, AFT
	Foeken et al., 2007	AFT
	Fügenschuh et al., 2000	ZFT, AFT
	Fügenschuh et al., 1997	ZFT, AFT
	Grundmann & Morteani, 1985	AFT
	Hawkesworth, 1976	Rb/Sr, biotite
	Hejl, 1997	AFT
	Hoke, 1990	K/Ar, biotite

Symbol	Author	System
	Jäger et al., 1969	Rb/Sr, biotite
	Lambert, 1970	K/Ar, biotite
	Mancktelow et al., 2001	ZFT, AFT
	Most, 2003	K/Ar, biotite, ZFT, AFT
	Oxburgh et al., 1966	K/Ar, biotite
	Raith et al., 1978	K/Ar, biotite
	Satir, 1975	Rb/Sr, K/Ar, biotite
	Satir & Morteani, 1982	Rb/Sr, biotite
	Staufenberg, 1987	AFT
	Steenken et al., 2002	K/Ar, biotite, ZFT, AFT
	Stöckhert et al., 1999	ZFT
	Viola et al., 2001	ZFT, AFT
	Wölfler, 2008	ZFT, AFT
	Zattin et al., 2006	AFT

Figure 2.1b Overview of the distribution of sample locations in the Tauern Window region of which geochronological data have been used in this study. Different symbols refer to previous studies as shown in the table. Abbreviations, R: Rensen pluton, RF: Rieserferner pluton, IQ: Innsbruck Quartzphyllite, G: Greywacke zone, A: Altkristallin.

Several Tertiary plutons are located along or in the vicinity of the Periadriatic line, such as the Rensen and Rieserferner plutons. Rb/Sr and U/Pb dating on these granites revealed Oligocene ages and geochemical analyses demonstrated a source at the base of thickened crust [*Borsi et al.*, 1978b; *Barth et al.*, 1989].

2.3 Metamorphism in the Eastern Alps

2.3.1 Austroalpine Units

The AA units are characterized by widespread Cretaceous (eo-Alpine) metamorphism and a weak post-Cretaceous thermal overprint, which is largely restricted to the vicinity of the TW [e.g. *Hoinkes et al.*, 1999; *Thöni*, 1999; *Schuster et al.*, 2004].

In general, the grade of the eo-Alpine metamorphism increases from north to south from sub-greenschist to ultra-high pressure conditions [*Hoinkes et al.*, 1999; *Oberhänsli and Goffé*, 2004; *Janak et al.*, 2006]. The southern limit of the Alpine greenschist to lower amphibolite metamorphic overprint, as indicated by incomplete resetting of the Rb-Sr

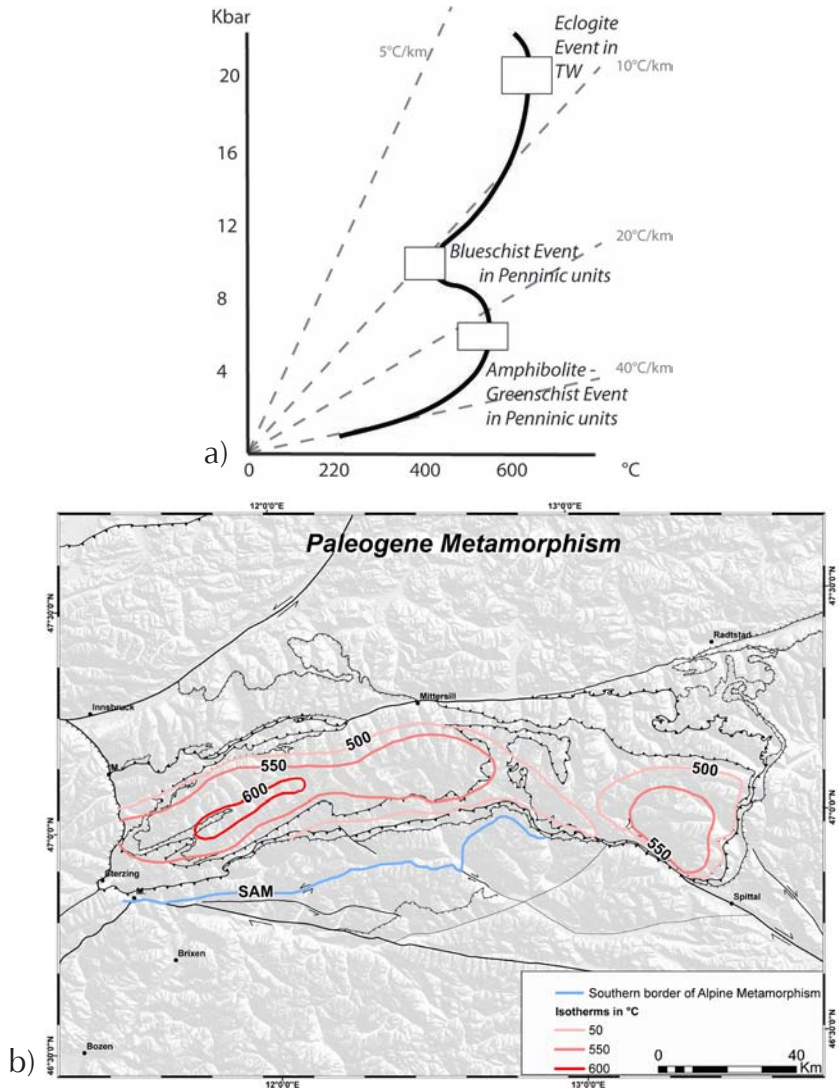

Figure 2.2 a) Generalized pressure-temperature loops of the Penninic units at different locations within the Eastern Alps after Kurz et al. (1998) and Hoinkes et al. (1999). TW: Tauern Window. Dashed lines show different isotherms. b) Map showing Paleogene peak temperatures in the Eastern Alps. After Oberhänsli & Goffé [2004].

white mica system [*Borsi et al.*, 1978b] within AA units, coincides with the Defferegger-Antholz-Vals (DAV) Line (Fig. 2.2b) [*Hoinkes et al.*, 1999 and references therein; *Most*, 2003]. North of the DAV age data within the AA units are only slightly older than those from the TW. In contrast, zircon FT data to the south of the DAV exclusively record pre-Miocene cooling [*Stöckhert et al.*, 1999; *Steenken et al.*, 2002].

The Paleogene thermal overprint within AA units close to the northeastern corner of the TW is related to thrusting within the lowermost AA units [*Liu et al.*, 2001].

2.3.2 Penninic Units

The metamorphic grade within the Penninic units ranges from eclogite- to greenschist facies. In general, PT-loops derived from these units throughout the Eastern Alps show a retrograde path from eclogite facies metamorphic conditions followed by blueschist and amphibolite/greenschist facies metamorphism [*Hoinkes et al.*, 1999].

Eclogite facies metamorphic rocks are restricted to a relatively small strip in the central southern TW (Eclogite Zone) (Fig. 2.2). According to Frank [1987] the eclogites first cooled to blueschist facies conditions followed by reheating again to 500-600 °C and pressures between 5 and 7 kbar. Further cooling to 375-400 °C and 2-4 kbar took place along similar paths for all Penninic units [*Holland*, 1979].

Timing of eclogitization is speculative, but if dating of the subsequent blueschist event is correct, then the eclogites are of pre-Oligocene age. Eclogite formation occurred under peak pressures of 20-25 kbar and temperatures between 580-650 °C [*Holland*, 1979; *Frank*, 1987; *Kurz et al.*, 1998] . These conditions are equivalent to depths of about 60 – 90 km and were characterized by a very low geothermal gradient of 7-9 °C/km typical for subduction zones (Fig. 2.2a).

K/Ar white mica ages from the southern border of the central TW range between 34 and 30 Ma and are interpreted as crystallization ages related to blueschist metamorphism [*Lambert*, 1970; *Cliff et al.*, 1985; *Zimmermann et al.*, 1994]. Data compiled by Frank [1987] suggest that blueschist formation occurred at temperatures between 400 and 500 °C and pressures around 9 kbar in the TW. The blueschist metamorphic event represents a stage of exhumation from ~80 km to ~35 km [e.g. *Kurz et al.*, 1998].

Within the Rechnitz Window remnants of a high-pressure / low-temperature event are found within ophiolitic sequences and yielded metamorphic conditions of 330-370 °C and minimum pressures of 6-8 kbar [*Koller*, 1985]. There is no correlation of the blueschist facies metamorphism throughout the Penninic realm due to a lack of reliable age dating.

Within most of the Penninic units, Oligocene greenschist- to amphibolite facies metamorphism led to penetrative deformation of rocks and the (re)crystallization of mineral assemblages of which white micas from the eastern TW have been dated between 30 and 28 Ma [*Inger and Cliff*, 1994; *Thöni*, 1999]. Peak temperatures of 550 to 600 °C under pressure conditions of 5-7 kbar reflect a geothermal gradient of 20-35 °C/km [*Inger and Cliff*, 1994; *Kurz et al.*, 1998; *Hoinkes et al.*, 1999; *Thöni*, 1999]. The timing of subsequent cooling is not well constrained since Rb/Sr white mica data from the western TW yielded ages as young as 16 Ma [*von Blanckenburg et al.*, 1989]. Whether these young ages reflect crystallization, cooling, or partial isotope resetting due to ongoing deformation, is still debated [*Cliff et al.*, 1985; *von Blanckenburg et al.*, 1989; *Hoinkes et al.*, 1999; *Thöni*, 1999]. However, lower temperature isotope systems reveal a clear westward younging of cooling ages, which possibly existed at higher temperatures as well. Post-metamorphic deformation resulted in folding of the Oligocene isograds along the central axis in the western TW and the Sonnblick and Hochalm domes in the eastern TW as well as the formation of normal faults bounding the TW in the west (Brenner fault) and the east (Katschberg fault). A distinct break in metamorphic grade across both faults affirm their normal fault kinematics [*Behrmann*, 1988; *Selverstone*, 1988; *Genser and Neubauer*, 1989; *Fügenschuh et al.*, 1997].

2.4 Data Compilation

The presented cooling maps are based on *c.* 600 published age measurements derived from Rb/Sr, K/Ar (biotite and muscovite) and fission track (zircon, apatite) dating, portraying a temperature range of 375 – 110 °C (Tab. 2.1). The obtained data were published between 1968 and 2008 and are interpreted as cooling ages. The data covers the entire Eastern Alps from the Silvretta / Engadine region in the west to the Rechnitz Window in the east, but are concentrated in several clusters mainly distributed within the TW region (Fig. 2.1a-b). For a complete reference list for the database, see Figure 2.1b.

Isotope system	Mineral	Used closure temperature (°C)	Closure temperature range (°C)	References
$^{40}Ar/^{39}Ar$ and $^{40}K/^{39}Ar$	Biotite Muscovite	375	300-400 375-430	Grove and Harrision (1997), Villa (1998), Kirschner et al. (1996), Hames and Bowring (1994).
$^{87}Rb/^{86}Sr$	Biotite White mica	375	250-350 or 400 450-550	Jäger et al. (1969), Del Moro et al. (1982), Purdy and Jäger (1976)
Fission track	Zircon	230	180-300	Hurford and Green (1983), Zaun and Wagner (1985)
Fission track	Apatite	110	90-120	Green et al. (1986), Gallagher et al. (1998)

Table 2.1 Closure and partial annealing zone temperatures for the used thermochronometers.

2.5 Construction of the cooling maps

All dating locations have been plotted on a georeferenced tectonic base-map with a Europe Lambert Conformal Conic projection, which is a combination of the "Structural model of Italy" 1:500.000 [*Bigi et al.*, 1990-92] and the "Geologische Übersichtskarte der Republik Österreich", scale 1:1.500.000 [*Egger et al.*, 1999]. Georeferencing and plotting of data has been done with ArcGIS 9® software.

The construction of the cooling maps through time is performed in two steps:

(1) The data were categorized after closure temperature for producing three different age contoured *"isochrone maps"* (Fig. 2.3a-c). The pertinent temperatures to these maps are: 375 °C (K/Ar and Rb/Sr biotite), 230 °C (zircon-FT), and 110 °C (apatite-FT) (Tab. 2.1). Contouring of the ages was carried out after interpolation of separate data clusters by the nearest neighbour technique. The result was compared with and partly adjusted by manual contouring to minimize or remove uncertainties owing to data scarcity and to derive at robust interpretations.

(2) In order to visualize temperature at certain time periods, *"temperature maps"* were constructed (Fig. 2.4a-d). The time periods cover the cooling history between 25 and

10 Ma and are identical to the isochrone age intervals on the time maps. Therefore, temperature contours (isotherms) can be deduced from isochrones as well. For example, the *15 Ma temperature map* contains 110 °C isotherms, which are identical to the 15 Ma isochrones on the *110 °C isochrone map*. The combination of isotherms and the closure temperatures of samples belonging to the same age were used as input for a nearest neighbour interpolation of the temperature. For the 15 and 10 Ma temperature maps, younger ages were also included to allow distinction between samples that had already cooled to 110 °C and those that were still hotter as they show ages younger than 10 Ma. In order to visualize this difference, the younger samples were assigned a few tens of degrees above the high temperature limit of the partial annealing zone for the apatite-FT system on these particular maps.

2.6 Assumptions, uncertainties and simplifications

Since the Rb/Sr, Ar/Ar and K/Ar systems in biotite record lower than peak metamorphic temperatures, which range between 500-650 °C in the Tauern Window, we apply the closure temperature concept and assume that the bulk of the data reflect post-metamorphic cooling. What is considered as closure temperatures are actually averaged temperature ranges. Especially for fission track analysis there is no specific closure temperature but a partial annealing zone defined by a temperature range in which early formed tracks can (partially) anneal and the track lengths can be reduced. Hence, only fission tracks with long track lengths, indicating rapid cooling, are consistent with the closure temperature concept. However, with respect to the rapid exhumation history, observed for instance within the TW, average temperatures seem a reasonable approximation since the variation of ages within the partial annealing zone might be of minor importance (Tab. 2.1). The temperature range of the partial annealing zone for Apatite FT is in the order of 120-60 °C, while that for Zircon FT is 300-180 °C (see Tab. 2.1 for references).

The interpretation of muscovite and phengite ages as cooling ages is still controversial since (re)crystallization of these minerals can occur even below the closure temperature [e.g. *Glasmacher et al.*, 2003]. Some K/Ar muscovite ages in the central TW are younger than nearby K/Ar biotite ages, although the *Tc* of the former is generally regarded as higher [*Raith et al.*, 1978]. Therefore, white mica ages are not shown on a separate time map, but can be used to support interpretations of the *Biotite 375 °C isochrone map* since their closure temperature ranges have some overlap (Tab. 2.1). Additionally, Rb/Sr white mica ages are regarded as crystallization ages and are, therefore, not considered in this compilation.

In this study we filtered apatite fission track data from altitudes higher than 2000m and lower than 1000m in order to avoid topography-induced complexities of the cooling history, which are not representative for the regional cooling of the Eastern Alps (compare Fig. 2.3c-d). The chosen elevation range is based on the large amount of available data within this bracket (see histogram in Fig. 2.3d). Ideally, since positive age vs. altitude relationships are only observed in some sub-regions of the Eastern Alps, corrections for topography should be applied for those sub-areas separately.

Many publications lack accurate coordinates of sample locations. Hence, we applied simple scanning and georeferencing of maps and sketches and adjusted the geographical

projections to our base map. Although some maps have untraceable projections and/or oversimplified sketches have been used, the maximum deviation of the plotted locations does not exceed 100 meters and is therefore a minor source of uncertainty.

2.7 Cooling maps

In the following sections the compiled cooling maps will be described starting with the isochrone maps for different isotope systems followed by the temperature maps, which portray regional cooling through time. Isolines with the same time are referred to as isochrones. References to the underlying data are summarized in Fig. 2-1b and will not be repeated in the context of the description of the cooling maps.

2.7.1 375 °C Isochrone map

Austroalpine units

The majority of the Austroalpine units cooled below 375 °C before Cenozoic times. However, the unit between the TW and the Periadriatic Line behaved differently and can be divided into a southern unit containing pre-Cenozoic ages and a northern unit, which shows a remarkable decrease of ages toward the TW on the 375 °C map (Fig. 2.3a) as well as on the 230 °C map (Fig. 2.3b). Both units are separated by the DAV (for location see Fig. 2.1), which coincides with the 65 and 35 Ma isochrones. In the area between the south-western corner of the TW and the tip of the Southalpine indenter, isochrone-lines trend parallel to the TW and the Brenner fault, respectively. Of particular note is the considerable north-directed age drop from 65 to 20 Ma within ~10 km distance in this zone.

Penninic units

The youngest ages within the TW are found in its south-western corner, ranging between 15 and 12 Ma (Fig. 2.3a). From this location, ages gradually increase towards the northeast. The 20 Ma isochrone surrounds the western TW tracing the Brenner Line in the west and gradually closes along the central axis towards the east. Contouring along the TW's northern boundary is difficult due to lack of data. The higher temperatures there are indirectly deduced, based on relatively old zircon FT ages (Fig. 2.3b). Two trends appear clearly from contouring in the western TW: (1) A younging trend toward the central ENE-WSW trending structural axis of the window, which starts in the Austroalpine units with the DAV as southern limit. (2) A gradual WSW directed younging trend towards the Brenner Line, across which a distinct age break is observed.

Figure 2.3 (*next pages*) Isochrones maps for temperatures of a) 375°C, b) 230°C and c) 110°C, respectively. d) Isochrone map making only use of AFT ages with an altitude range of 1000-2000m (dark range in histogram) in order to reduce topographic effects. Lower right inset shows the frequency of AFT data with respect to altitude. Upper left inset: Engadine Window. Upper right inset: Rechnitz Window. The solid lines represent isochrones and are based on interpolation of the plotted ages. The dashed lines are extended interpretations. Geological boundaries are based on the Structural model of Italy [Bigi et al., 1990-92].

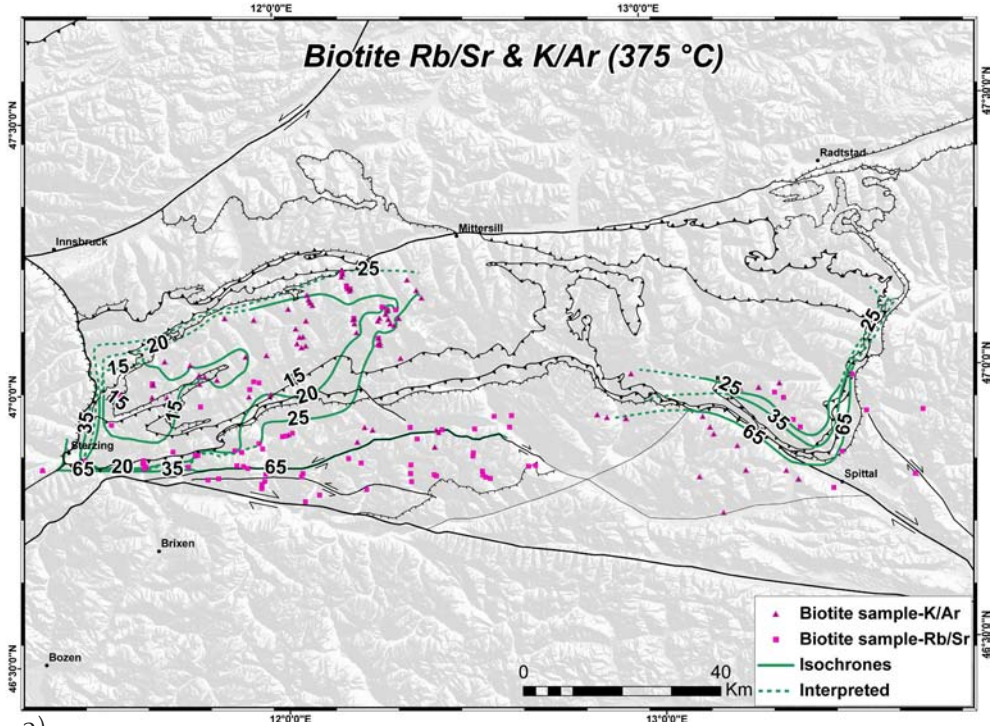
Biotite Rb/Sr & K/Ar (375 °C)
12°0'0"E
13°0'0"E
47°30'0"N
47°0'0"N
46°30'0"N
Innsbruck
Mittersill
Radtstad
Salzburg
Spittal
Brixen
Bozen
Biotite sample-K/Ar
Biotite sample-Rb/Sr
Isochrones
Interpreted
0
40
Km

a)

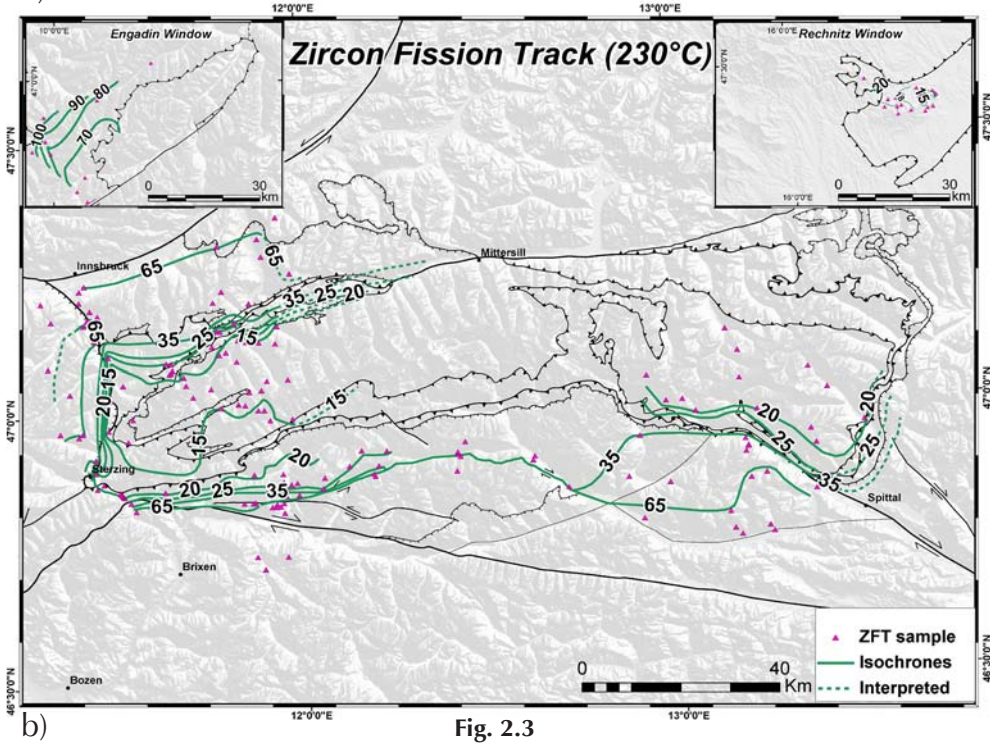
Zircon Fission Track (230°C)
Engadin Window
Rechnitz Window
12°0'0"E
13°0'0"E
47°30'0"N
47°0'0"N
46°30'0"N
Innsbruck
Mittersill
Salzburg
Spittal
Brixen
Bozen
ZFT sample
Isochrones
Interpreted
0
40
Km
30
km

b)

Fig. 2.3

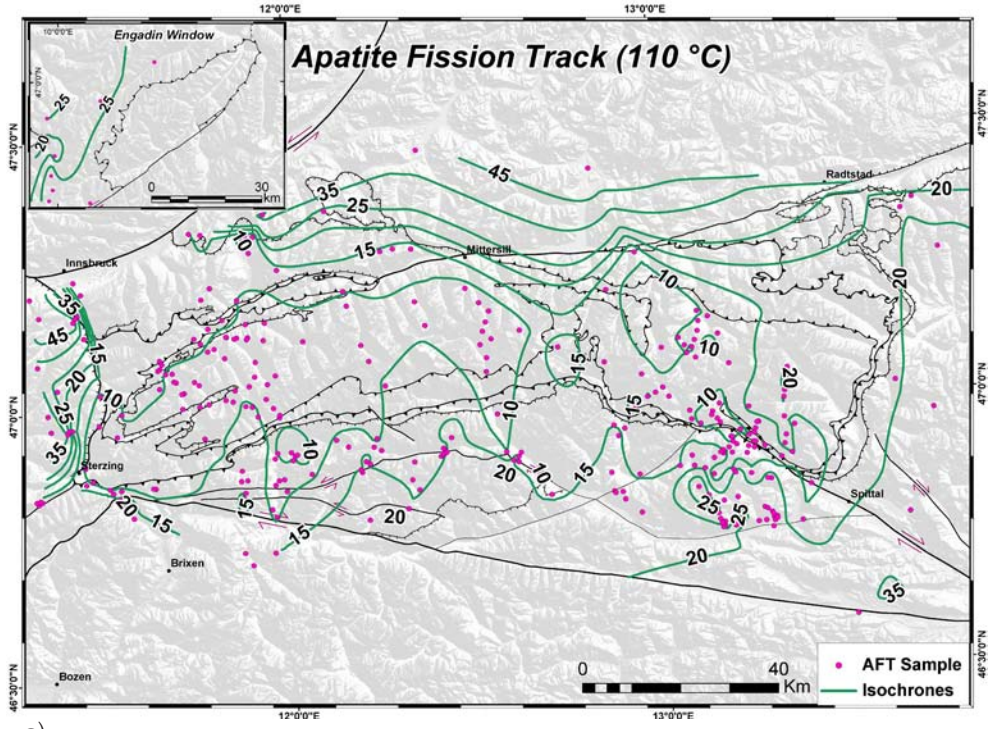

c)

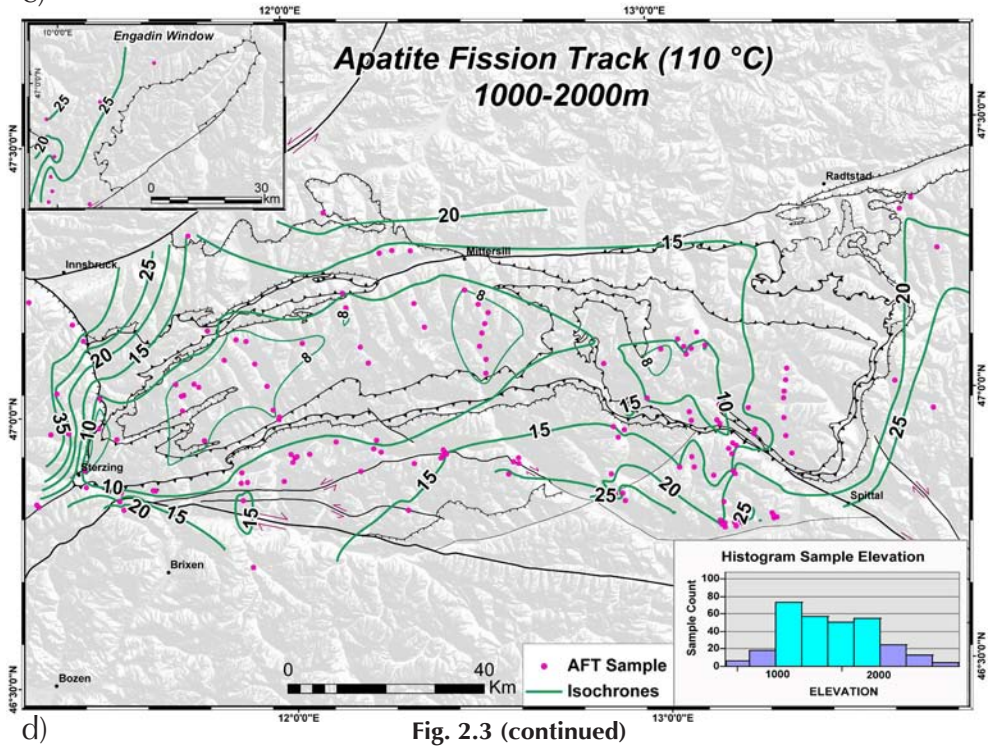

d)

Fig. 2.3 (continued)

The data from the eastern TW, though limited in amount, suggest earlier cooling than in the western TW, which is supported by K/Ar and Ar/Ar muscovite ages ranging between 30 and 20 Ma in the north-eastern TW [*Liu et al.*, 2001], and between 27-18 Ma in the south-eastern TW [*Cliff et al.*, 1985]. Additionally, considering the confinement of Oligocene peak metamorphic conditions within the TW it is expected that the isochrones will largely follow the outline of the TW.

2.7.2 230 °C Isochrone map

Austroalpine units

Parts of the Austroalpine unit between the TW and the Rechnitz Window referred to as "cold spots" by [*Hejl*, 1997], cooled below 230 °C before Cenozoic times. More cold spots have been found in the Ötztal-Stubai basement complex, the north-eastern part of the Innsbruck Quartzphyllite, the Greywacke zone, and AA basement units north of the Periadriatic Line.

Similar to the 375 °C isochrone map, a high gradient of northward younging from 80 Ma just a few kilometers south of the Periadriatic line to 13 Ma adjacent to the TW is observed north of the Southalpine indentor. Further east, the isochrones are parallel to the DAV.

Penninic units

The south-western corner of the TW cooled through 230 °C between 15 and 12 Ma, similar to the 375 °C map indicating high cooling rates (50 °C/Ma).

In contrast, a gradual westward younging within the western TW is not well expressed, which could be due to the lack of data in the central TW. However, along the Brenner fault, isochrones are clearly offset, including a sinistral component in the NW part of the TW. The eastern Tauern Window is characterized by 19-16 Ma zircon FT ages. Owed to the lack of zircon FT ages in the central TW, it is not possible to reconcile whether cooling was progressive from east to west or a separation into domains with different cooling ages. A trend towards younger ages from the window's northern border (20 Ma) towards the central axis (12 Ma) is observed within the western TW. North of the DAV ages drop from 25 to 12 Ma in northerly direction.

Cooling below 230 °C in the Rechnitz Window took place between 19 and 14 Ma. The Rechnitz thermal event also led to rejuvenation of the surrounding AA unit as indicated by a 22 Ma age measurement by *Dunkl and Demeny* [1997].

Southern Alps

Within the Southalpine Basement units zircon fission track ages range between 225 and 213 Ma. Only ages between 81 and 24 Ma from the Permian Brixen pluton close to the Periadriatic Line record Alpine resetting [*Mancktelow et al.*, 2001; *Viola et al.*, 2001].

2.7.3 110 °C Isochrone map

Apatite fission track (AFT) data are displayed in Figure 2.3c utilizing all of the compiled data. In Figure 2.3d, only data within a selected altitude range (1000-2000m) have been used in order to avoid dubious interpretations due to topographic effects. Notice

the exclusion of data also led to smoother contouring in some area's (e.g. NW Tauern Window)

Austroalpine units

Within the Silvretta basement units west of the Engadine Window, AFT-ages vary from 31 Ma in the east and south to 14 Ma towards the southwest.

In the Ötztal-Stubai area AFT-ages get successively younger approaching the Brenner Line in a SE to E direction. The northwestern part of the Innsbruck Quartzphyllite region cooled below 110 °C not before 15 Ma and, therefore, differs from the bulk of the TW's northern surroundings; in the Greywacke zone AFT ages increase northwards to 60 Ma.

Most ages taken from the Austroalpine units between the Periadriatic line and the TW fluctuate between 20 and 10 Ma and increase slightly towards the southeast, similar to the 375 °C and the 230 °C isochrone maps. The irregular curved shape of isochrones resulting in crossing major tectonic boundaries, such as the DAV (compare Fig. 2.3c and Fig. 2.3d), is mainly due to topographic effects. Notice the remarkable difference in timing of cooling at the Brenner- and Katschberg Lines.

Penninic units

Within the TW, cooling below 110 °C started in the east as early as 20 Ma ago and propagated westwards from that time on. No AFT data are available from the north-eastern TW, which has been contoured by extrapolation of ages from farther south. Somewhat younger ages (15-10 Ma) in the south-eastern corner of the TW may be disturbed by high thermal anomalies associated with the Mölltal fault [*Dunkl et al.*, 2003; *Wölfler*, 2008]. Towards the western part of the eastern TW the age variation becomes larger (16-6 Ma) and practically all AFT-ages within the central and western TW fall between 10 and 5 Ma. Here, westward younging is only limited to the Brenner Line region where ages are as young as 9-4 Ma. A younging trend towards the central axis of the TW is not well constrained. The disturbance of the isochrons may partly be due to the age/elevation correlation.

Only two AFT ages have been found in the Rechnitz Window and are dated at 10 and 7 Ma, indicating coeval cooling within the TW and Rechnitz Window below 110 °C at that time.

Southern Alps

A few ages from the Southern Alps can be interpreted only very broadly and isochrones are restricted to the Brixen pluton, which cooled below 110 °C in the Early Miocene, while further south cooling of the Southalpine Basement through 110 °C was not before 15-11 Ma. The general trend, though poorly constrained, is a north-south younging to 10 Ma near the south-vergent Valsugana thrust (Fig. 2.1a).

Figure 2.4 (next pages) Temperature maps at a) 25 Ma, b) 20 Ma, c) 15 Ma and d) 10 Ma, respectively, portraying temperatures based on the interpolation of cooling age data. The plotted ages together with the time-lines from Figure 3 were used as input. Colour scales differ among Figure c and d to optimize visualization of low temperatures.

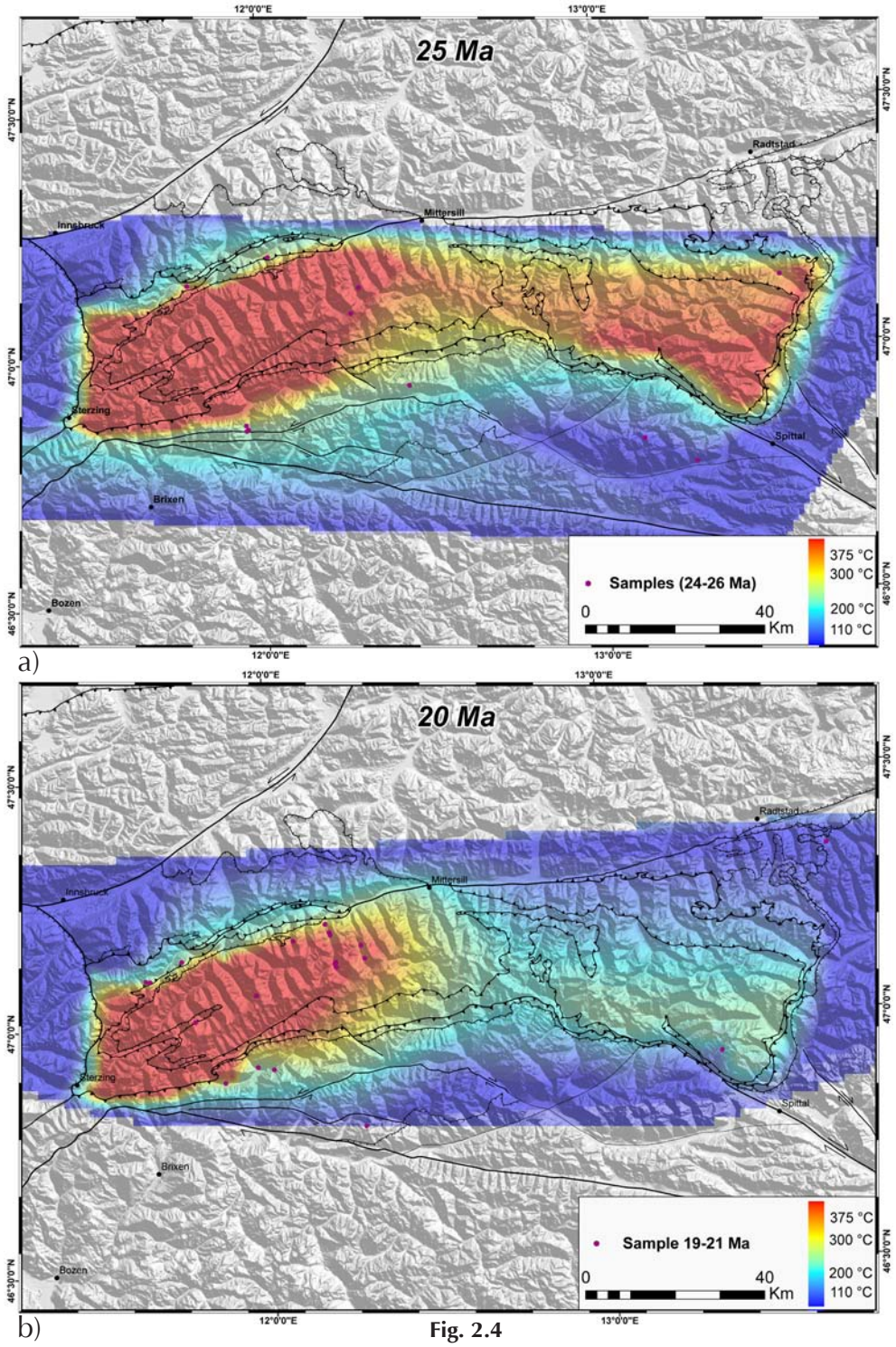
25 Ma
12°0'0"E
13°0'0"E
47°30'0"N
47°0'0"N
46°30'0"N
Innsbruck
Mittersill
Radstadt
Sterzing
Spittal
Brixen
Bozen
Samples (24-26 Ma)
0
40
Km
375 °C
300 °C
200 °C
110 °C
a)
20 Ma
Sample 19-21 Ma
b)

Fig. 2.4

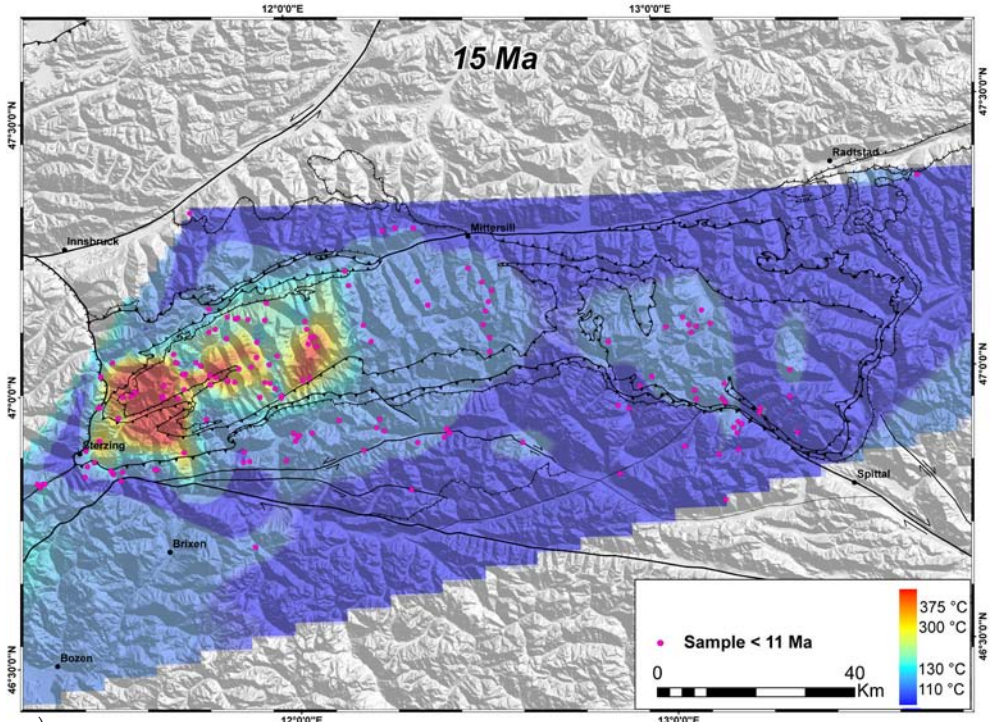

c)

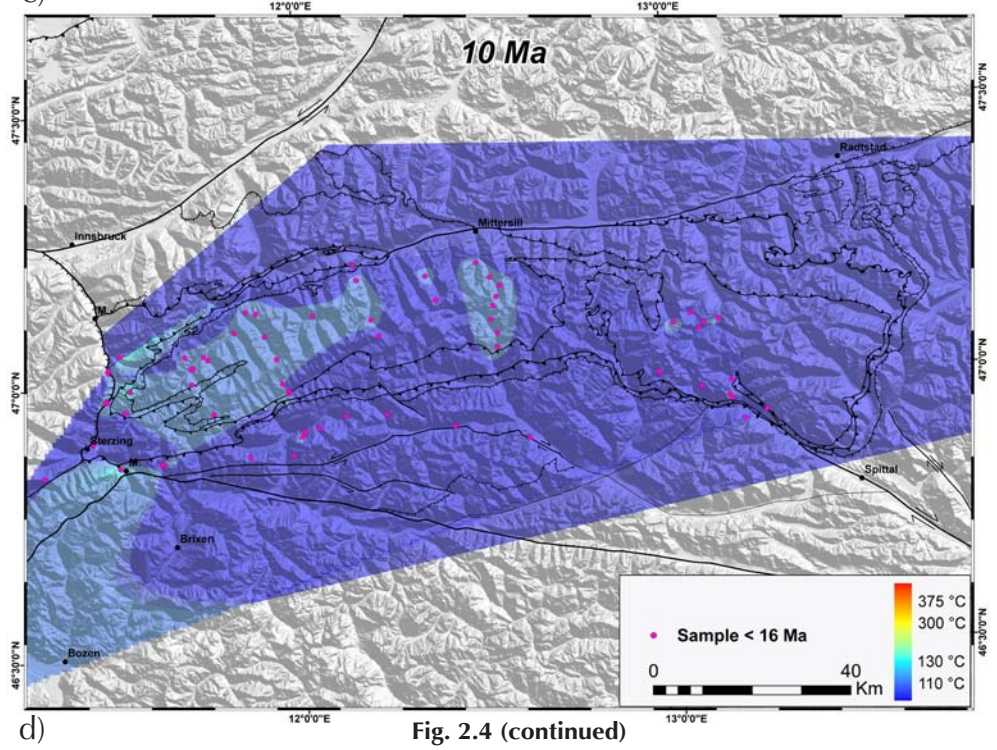

d)

Fig. 2.4 (continued)

2.8 Temperature maps

The four temperature maps (Figs. 2.4a-d) are interpolations derived from the isochron maps and contain the same underlying information, albeit visualizing temperature at a certain time. On a single temperature map, information is combined from all the used dating systems and used as additional control on the internal consistency of the isochron maps. This improved the contouring particularly in areas with scarce data coverage and thus, both map types are complimentary.

In the following section, the temperature maps for the time interval from 25 to 10 Ma will be briefly discussed. At 25 Ma (Fig. 2.4a) temperatures in the entire western and marginal parts of the eastern TW exceeded 375 °C. The "hot cells" of the western and eastern TW, exhibiting the geometry of "elongate thermal domes" are separated by a cooler region in the central TW. The significance of this temperature distribution, however, remains uncertain since few cooling age data are available from the central TW.

At 20 Ma (Fig. 2.4b) the eastern TW had cooled almost entirely below 200 °C with the exception of the Sonnblick and Hochhalm domes (Fig. 2-1b).

Both, the 25 and 20 Ma maps reveal an extension of the thermally defined TW towards the DAV. At 15 Ma (Fig. 2.4c) the AA units and most of the TW had cooled below 110 °C and the highest temperatures are limited to the hinge of the structural antiform of the western TW.

Further cooling through 110 °C at 10 Ma (Fig. 2.4d) is mainly recorded by AFT samples obtained from valleys or along the antiformal hinge of the western TW. During the entire cooling history high temperature gradients are inferred across the Brenner Line whereas temperature seems to have changed more gradually in the vicinity of its eastern counterpart, the Katschberg Line.

2.9 Discussion

2.9.1 General conditions at the onset of post-metamorphic cooling

Tertiary peak temperature conditions, up to ca. 650 °C, related to widespread greenschist and amphibolite facies metamorphism within the Penninic windows of the Eastern Alps, were reached by the end of early Oligocene [*Thöni*, 1999and references therein]. This phase of metamorphism is a consequence of late Eocene to Early Oligocene collision during which parts of the distal European margin, the present-day Penninic units exposed within the Engadin, Tauern and Rechnitz Windows, became part of the orogenic wedge. Since continental basement is only known from the interior of the TW it is assumed that strong lateral gradients (from W to E) in crustal thickness and topography existed by the end of the early Oligocene [*Frisch et al.*, 1998]. Following crustal thickening and thermal relaxation, rapid exhumation of the rocks within the TW occurred under isothermal conditions [*Droop*, 1985; *von Blanckenburg et al.*, 1989; *Fügenschuh et al.*, 1997]. Thermal modelling shows that rapid exhumation of rocks has the capacity to advect heat upward and to produce a transient thermal dome, which leads to softening of the rocks [e.g. *Genser et al.*, 1996]. Hence, further exhumation of Penninic rocks probably occurred within a weak crust, which responded to geodynamic changes on its eastern boundary, i.e. subduction along the Carpathian arc and back-arc opening of the Pannonian basin by

ductile flow within the lower plate Penninc units and by escape of fault-bounded wedges towards the east within the brittle upper plate AA units [*Ratschbacher et al.*, 1991].

2.9.2 The thermal Tauern Window

Within the Eastern Alps the post-collisional cooling path of most of the Austroalpine units differs significantly from that of the Penninic ones. In the former, cooling below 230 °C starting from a thermal maximum around ~90 Ma occurred mostly before Cenozoic times. Within the Penninic Windows, peak temperature conditions of the latest amphibolite to greenschist facies metamorphism were reached only ~30 Ma ago and were followed by rapid cooling from 500 °C to 110 °C, mainly during the Miocene [e.g. *Hoinkes et al.*, 1999 and references therein].

The exceptions to this general observation are the AA units surrounding the TW. The AA units to the north of the DAV show a Oligocene greenschist facies thermal overprint followed by late Oligocene to Miocene cooling, which is similar to that of the Penninic units in the western TW. This means that no major vertical movements have taken place between the TW and the AA units along the southern margin of the window suggesting that the AA units north of the DAV can be considered as a part of the thermally defined TW [*Frisch et al.*, 2000]. The fact that this AA region and the TW share at least part of their tectonic history is also supported by their structural concordant relation with respect to the Oligocene ductile deformation [*Krenn et al.*, 2003]. Regional differences in exhumation along the DAV are expressed by ZFT ages (25-15 Ma) and $^{40}K/^{39}Ar$ biotite ages (27-26 Ma) to the north of the fault, and ZFT ages of 34-28 Ma directly south of the DAV [*Stöckhert et al.*, 1999; *Most*, 2003]. Furthermore, ZFT ages gradually increase eastwards toward Cretaceous ages, indicating that the western part was possibly exhumed from deeper levels, consistent with the deeper intrusion depth of the Rensen with respect to the Rieserferner pluton [*Borsi et al.*, 1978b; *Steenken et al.*, 2002; *Krenn et al.*, 2003]. These lateral differences can be explained by lateral variations in amount of shortening, which is highest at the Southalpine indentor tip [*Borsi et al.*, 1978b; *Frisch et al.*, 1998; *Most*, 2003].

2.9.3 Cooling trends

From the Oligocene onward, the structural boundaries of the TW outline a province of relative younger cooling ages compared to its surrounding Austroalpine units.

Two main cooling trends appear within the TW (Fig. 2.5):

(1) A westward younging towards the Brenner Line, which acts as a major thermal discontinuity, is prevalent in the entire western TW. Termination of the 230 °C isotherms against the Brenner fault reflects fault activity until at least 10 Ma (Fig. 2.4c). An eastward younging towards the Katschberg Line is not that well constrained but is expected as the Katschberg Fault is a first order fault separating two distinct tectono-thermal domains (Fig. 2.4a-b) [*Genser and Neubauer*, 1989].

(2) A north-south cooling trend with the youngest ages (< 10 Ma) along the central axis of the TW is observed in the western TW, but applies also to low temperature isotope systems in the surrounding Austroalpine units with Paleogene and pre-Cenozoic ages.

The E-W cooling trends, which are parallel to flow and escape kinematics, are in

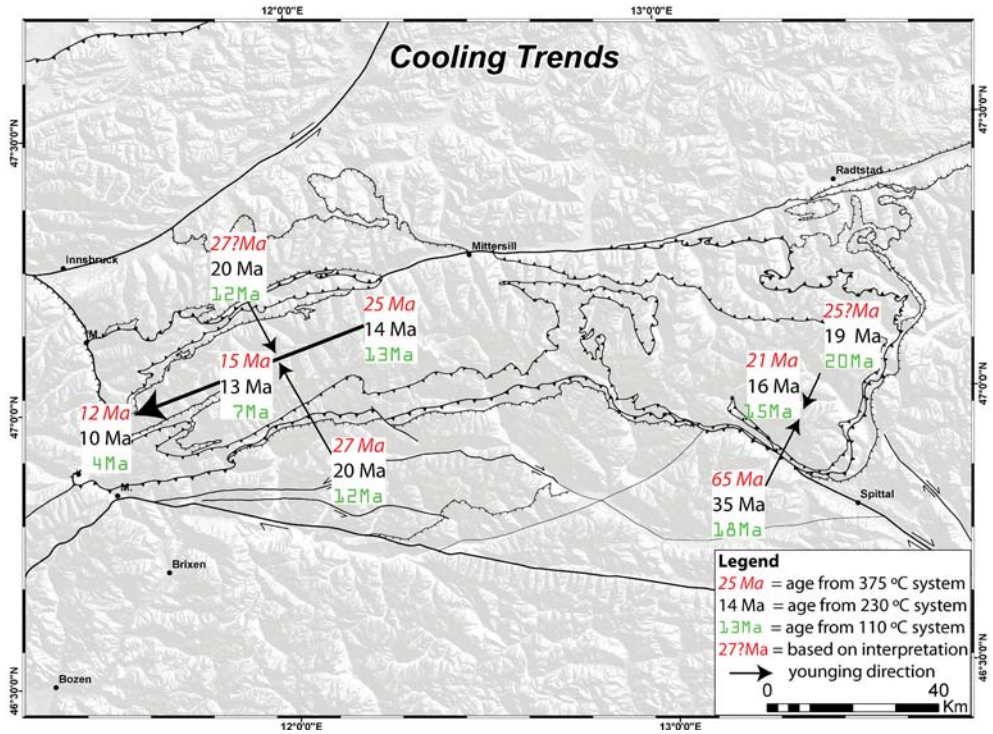

Figure 2.5 Cooling trends deduced from the isochrones and temperature maps (Figs. 2.3 and 2.4). Note that both, the Brenner and the Katschberg Lines are major thermal discontinuities during cooling of the Tauern Window.

agreement with detachment-related gneiss domes as proposed by Yin [2004] and are observed in several core complex-type structures around the world, (e.g. Nevado-Filabride Core Complex, SE Spain, [*Gallagher et al.*, 1998]. In the western Tauern Window, the Brenner normal fault, which became active soon after peak metamorphic conditions at 30 Ma according to *Selverstone* [1988], but somewhat later (Neogene) according to *Fügenschuh et al.,* [1995], seems to exert a strong control on the cooling age distribution [see also *Fügenschuh et al.*, 1997].

The N-S cooling trend, which was already established during the early cooling phase (see Fig. 2.3a), is probably the result of large-scale folding. As to whether the cooling trend already existed prior to folding or if it is the direct consequence of the folding process is difficult to asses. However, structural relationships seem to favour the latter interpretation since they indicate that the folding process must have commenced prior to the intrusion of early Oligocene dykes, which intruded into a sub-vertical foliation representing the axial plane cleavage to outcrop-scale folds at the southernmost TW [*Krenn et al.*, 2003]. According to the age data, which portray the geometry of a thermal dome(s), folding coincided by updoming in the western and central TW most-likely continued during the Miocene. The imprint of both trends within the complete temperature window (375 – 110 °C) is interpreted to reflect ongoing N-S shortening during exhumation along the low-angle Brenner detachment fault.

2.9.4 Temporal variations of post-metamorphic cooling

The temperature maps portray the presence of two thermal domes within the TW and a pronounced diachronous character of cooling (Fig. 2.4a-d).

The distinction into two thermal domes may be partly an artefact due to a scarcity of data from the Central TW, but the diachronous cooling is considered as significant since the age difference between the western and eastern TW (2-8 Ma) is beyond the error pertinent to the different dating techniques. As already noticed by *Frisch et al.* [2000], cooling of the Rechnitz Window and the eastern TW was largely synchronous, whereas cooling in the western TW was delayed by about 4 Ma on average. *Frisch et al.* [2000] account for this difference by introducing a westerly dipping, normal shear zone within the central TW, which led to the separation of the Zentralgneiss-cored domes of the eastern TW from those of the western TW. Hence, in their model, deformation and subsequent cooling propagated from east to west in response to extension in the Pannonian basin. According to our temperature maps (Fig. 2.4b), the rocks of the eastern TW were already in a cool environment with temperatures around 230 °C at 20 Ma when lateral extrusion commenced. *Sachsenhofer* [2001] predicted surface heat flows of up to 200 mWm^{-2} for the eastern TW and easterly adjacent AA units in the main phase of the extrusion process (20-15 Ma) mimicking the geometry of an extrusion corridor (see Fig. 2.5b of *Sachsenhofer* [2001]). Heat flow of that magnitude would imply temperatures of 350 °C at depths of about 5 km and the onset of partial melting at depths of ca. 10 km. Such high temperatures in shallow crustal levels should have reset the zircon fission track system to younger ages and this has yet to be documented with data. This suggests that the predicted high heat flow is rather a local, fault-controlled phenomenon than a regional-scale feature.

Diachronous cooling may have been partly conditioned by the crustal configuration prior to orogen-parallel extension in the Eastern Alps since crustal thickness and topographic gradients must have existed at that time not only in N-S but also in E-W direction (see also *Frisch et al.* [1998]) for a paleo-topography reconstruction). Consequently heat can be efficiently transferred from the thick and hot regions of the eastern TW to the less thick and cool surrounding AA units. Westerly directed heat transfer in the region of the western TW was probably inefficient due to the lack of significant crustal thickness and topographic variations (high mountainous relief from the Ötztal and Silvretta to the Swiss Alps at ca. 29-22 Ma [*Frisch et al.*, 1998].

2.9.5 Cooling rates

Cooling rates in the TW's interior from 375 °C to 230 °C were high (50 °C/Ma) during the Early Miocene, while cooling towards surface conditions slowed down to 25 °C/Ma in the east at around 15-9 Ma and in the west between 12 and 8 Ma.

In the areas close to the major bounding normal faults, near-surface cooling (from 230 °C to 110 °C) was rapid (~ 50 °C/Ma) and happened in the eastern TW between 18 and 14 Ma and in the Brenner pass region between 14 and 10 Ma [*Fügenschuh et al.*, 1997].

Fügenschuh et al. [1997] calculated exhumation rates in the western TW with the use of isotope data and a time-dependant thermal model for erosion. Their results suggest that Oligocene to early Miocene rapid exhumation predates late Early-Middle Miocene rapid cooling. Hence, lateral extrusion in the Eastern Alps coincides with a phase of rapid

cooling. Exhumation related to lateral extrusion, therefore, was not able to maintain the high temperatures of the isothermal exhumation phase suggesting that vertical motions were already slowing down at that stage of TW formation, as also suggested by the geochronologic data of *von Blanckenburg et al.* [1989].

2.9.6 Dome forming mechanisms for the Tauern Window

Different exhumation mechanisms operate at different rates and time-scales and may be diachrounous in space potentially leaving behind different cooling records [*Hames and Bowring*, 1994]. Several mechanisms have been suggested for the exhumation of the Tauern Window with the primary distinction between the models in the relative importance of the N-S shortening tectonics [*Lammerer and Weger*, 1998] with respect to the E-W extensional, extrusion related tectonics [*Selverstone and Spear*, 1985; *Ratschbacher et al.*, 1991; *Frisch et al.*, 1998; *Frisch et al.*, 2000].

Lammerer and Weger [1998] argue, based on strain measurements, that north-south shortening continued during east-west extension and they conclude that shortening was compensated by extension and, therefore, would not have caused substantial uplift of the TW. In their view the Tauern Window is merely a deeply eroded antiformal stack, which experienced crustal-scale folding. A reduction of crustal strength as a consequence of thermal relaxation and early phases of exhumation could have favoured crustal-scale buckling and uplift [e.g. *Genser et al.*, 1996].

On several accounts it has been suggested that the TW is a metamorphic core-complex [e.g. *Frisch et al.*, 1998; *Frisch et al.*, 2000]. With reference to classical metamorphic core complexes as described in the Basin and Range province [*Lister and Davis*, 1989] observations in favour of metamorphic core complex interpretation include: (1) the presence of detachment faults separating brittle upperplate from ductile lower plate rocks; (2) a considerable amount of extension within the Tauern core (E-W), and (3) a lateral decrease of cooling ages towards the main detachment faults (Brenner and Katschberg Lines). However, in Basin and Range-type core complexes the kinematics of the main detachments is uni-directional, which is also documented by uni-directional cooling of the exhumed rocks [e.g. *Foster and John*, 1999]. The early deformation history of both bounding normal faults in the Eastern Alps is still poorly understood and additional research with the focus on the relation between the Brenner Line and the Katschberg Line is needed. Furthermore, Cordilleran-type core complexes are characterised by detachments striking parallel to the mountain range (orthogonal in the Eastern Alps) and their formation post-dates shortening (coeval in the Eastern Alps). Consequently, the TW exhibits a large amount of overprinting relations between extensional and contractional structures.

The elliptical cooling pattern in the TW and close surroundings does not support a Basin and Range-type core-complex origin of the TW but argues for its formation as a syn-orogenic metamorphic dome, which was exhumed by a combination of extension and erosion. Uncertainties remain as to whether the entire TW is a single metamorphic dome or a series of domes.

2.9.7 From regional to orogen-scale exhumation and cooling

Higher temperature isotope systems (Fig. 2.3a), as well as most of the zircon fission track data (Fig. 2.3b), document focused cooling and exhumation confined to the Penninic tectonic windows, whereas the main body of the surrounding AA units already cooled to near surface conditions prior to ca. 20 Ma [*Fügenschuh et al.*, 1997; *Hejl*, 1997; *Fügenschuh et al.*, 2000]. In contrast, cooling through the AFT annealing zone was more synchronic along the Brenner fault [*Fügenschuh et al.*, 1997], the central axes of the TW [*Grundmann and Morteani*, 1985; *Staufenberg*, 1987; *Most*, 2003], the Jaufen, Passeier and Giudicarie faults [*Viola et al.*, 2001], and the Valsugana thrust system [*Zattin et al.*, 2006], arguing for orogen-scale cooling and exhumation since ca. 12 Ma. Late middle Miocene thrusting and uplift within the Southern Alps, also documented by structural and stratigraphic data [*Dunkl and Demeny*, 1997; *Castellarin and Cantelli*, 2000], were coeval with the termination of extrusion tectonics in the Eastern Alps. This mutual relationship indicates that the coupling between the Southern Alps and the internal part of the Alps (the Alps north of the Periadriatic Line) increased, leading to orogen-scale uplift and cooling to near-surface conditions starting at around 12-10 Ma. Large-scale uplift led to an increase in the catchment area and hence to enhanced sediment discharge compared to the main phase of lateral extrusion [*Kuhlemann et al.*, 2001]. Other processes, which possibly contributed to the final widespread uplift stage most likely involve a combination of removal of the lithospheric root either by delamination or convection and surface erosion [*Genser et al.*, 2007].

2.10 Conclusions

The compilation of radiometric data and their presentation in “time” and “temperature” maps allow for interpretation of temporal and spatial variations of post-metamorphic cooling within the Eastern Alps.

Based on available isotope data, we argue that the “thermal” differentiation between the western and eastern TW was well established by the end of the rapid, nearly isothermal exhumation phase during the Oligocene and the early Neogene (ca. 30-20 Ma). This phase of deformation probably led to the separation of the Zentralgneiss cores, now exposed in the western and eastern TW, in response to orogen parallel extension [e.g. *Frisch et al.*, 2000] and is the main reason for diachronous cooling of the TW. As a result, two thermal domes developed within the TW as documented by an increase of cooling ages away from the centre of the domes. Subsequent decay of the thermal domes was synchronous with the main phase of lateral extrusion in the Eastern Alps, which lasted from ca. 20 to 14 Ma. Hence, cooling by heat conduction and possibly also by convecting fluids dominated over exhumation related upward advection of heat, arguing for a decrease of exhumation rates during that period as suggested by *von Blanckenburg et al.* [1989].

While N-S cooling trends possibly reflect folding and updoming within a N-S convergent setting, E-W cooling trends appear to be fault controlled, reflecting top-to-the-W and top-to-the-E normal displacement along the Brenner and Katschberg faults respectively. This cooling pattern is consistent with cooling of detachment-related gneiss domes [e.g. *Yin*, 2004], but differs from uni-directional cooling of Basin and Range-type core complexes.

Orogen-scale uplift involving the Southern Alps post-dates the main phase of lateral extrusion and is documented by late Miocene apatite fission track ages from the Southern Alps, the AA unit and the TW. These data possibly reflect increased coupling between the Eastern and Southern Alps across the Periadriatic Line leading to orogen-scale uplift and erosion in the Alps.

Our synthesis of available isotope data also highlighted that more data are needed from the central and north-eastern TW and across the Katschberg normal fault. In particular, a denser network of (U-Th)/He data is required to be able to link Late Miocene to more recent tectonics [*Willingshofer and Cloetingh*, 2003] of the Eastern Alps. Furthermore, a thorough understanding of the cooling history of the Alps and associated vertical movements should invoke a stronger coupling to the dynamics of the mantle lithosphere.

Chapter **3**

Analogue modelling of continental collision: Influence of plate coupling on mantle lithosphere subduction, crustal deformation and surface topography

3.1 Introduction

Subduction of oceanic lithosphere from its initiation to the accumulation in slab graveyards at the core-mantle boundary is highly investigated over the last decades [e.g. *Cloetingh et al.*, 1982; *Toth and Gurnis*, 1998; *Regenauer-Lieb et al.*, 2001; *Hall et al.*, 2003; *Jarvis and Lowman*, 2005; *Kito et al.*, 2008]. Their clear present day characteristics in terms of surface topography, volcanisms, and earthquakes distribution make oceanic lithosphere subduction accessible for research. On the other hand, less is known about the operating processes in the transition towards continental lithosphere subduction during continental collision.

Ampferer [1906] and *Laubscher* [1977] recognized that restoration of contractional belts leads often to an unbalanced amount of upper crustal shortening relative to the underlying (basement) layers. Therefore, the existence of decollement systems was required in order to form lower crustal "roots" or to create the so called "floating" orogens. More recently, continental lithosphere subduction has been considered as a continuation of oceanic lithosphere subduction except that buoyant continental crust resists subduction and detaches from the underlying mantle lithosphere [*Willett et al.*, 1993; *Ellis*, 1996]. However, evidence that not all of the continental crust is detached and accreted but at least part of it can get subducted to depths beyond 100 km is provided by exhumed ultra high pressure rocks [e.g. *Krabbendam and Dewey*, 1998; *Faure et al.*, 2003].

This chapter is based on Luth S., Willingshofer E., Sokoutis D., and Cloetingh S., 2010; Analogue modelling of continental collision: Influence of plate coupling on mantle lithosphere subduction, crustal deformation and surface topography. Tectonophysics, 484(1-4): 87-102.

3.2 Modelling of subduction and collision: a concise summary

Several numerical studies have attempted to model continental subduction followed by the exhumation of crustal rock [e.g. *Toussaint et al.*, 2004a; *Burov and Yamato*, 2008; *De Franco et al.*, 2008a; *Faccenda et al.*, 2008b]. *Burov and Yamato* [2008] have shown that high plate velocities (> 5-3 cm/yr) and low Moho temperatures (<550 °C) favor subduction of the entire lithosphere, while intermediate Moho temperatures (550 – 650 °C) in combination with a lower crustal strength leads to crust – mantle decoupling. Other parameters affecting the evolution of continental collision zones are convergence rate, lithosphere rheology, buoyancy and inter plate pressure [e.g. *Sobouti and Arkani-Hamed*, 2002; *Toussaint et al.*, 2004b]. In addition, De Franco et al. (2008) pointed out that the most relevant parameter during the initial stage of continental collision is the geometry and (de)coupling along the plate contact. In that sense the plate contact is in an early stage decisive whether the lithosphere will entirely subduct, delaminate, or will not subduct at all [*De Franco et al.*, 2008a]. To obtain subduction *Tagawa et al.* (2007) suggested that weakening of the plate boundary is even more important than the rheology of the lithosphere.

The amount of plate coupling depends on the geometry of the plate contact, the amount of water-rich sediments, the presence of a slab pull force caused by still attached oceanic lithosphere, or shear heating; and hence on the plate velocity [e.g. *Toussaint et al.*, 2004a; *Faccenda et al.*, 2009]. Plate coupling is spatially and temporally variable and can increase after the consumption of water-rich sediments, by slowing down of convergence, arrival of buoyant material, or a change in plate contact geometry. An increase in coupling changes the style of lithosphere deformation by the transmission of far field stresses, which can result in buckling and regional uplift of both plates and the orogenic wedge [*Ziegler et al.*, 2002; *Willingshofer and Sokoutis*, 2009].

The role of the plate boundary and its development during continental collision has been studied in both numerical and physical modelling studies [*De Franco et al.*, 2008b; *Willingshofer and Sokoutis*, 2009]. In most models the plate contact was represented by a predefined weak zone dipping 45° with respect to direction of shortening [*Hassani and Jongmans*, 1997; *Chemenda et al.*, 2001; *Regard et al.*, 2003; *Willingshofer et al.*, 2005; *Tagawa et al.*, 2007; *De Franco et al.*, 2008a].

In this study we investigated the influence of (a) plate- and (b) lower plate crust-mantle coupling on the mode of deformation of the different rheological layers. Special emphasis has been put on monitoring surface topography development in order to be able to link deep to shallow processes.

3.3 Experimental design

3.3.1 Analogue materials and model set-up

The presented models consisted of three different layers overlying a viscous fluid mixture of polytungstate and glycerol representing the asthenosphere. From bottom to top these layers were composed of: strong silicon putty, weak silicon putty, and feldspar sand; they are used as analogues for the ductile mantle lithosphere, the ductile lower crust, and the brittle upper crust, respectively (Fig. 3.1). The viscous layers were mixtures of polydimethyl-siloxane polymer (PDMS) with barium sulphate showing slightly

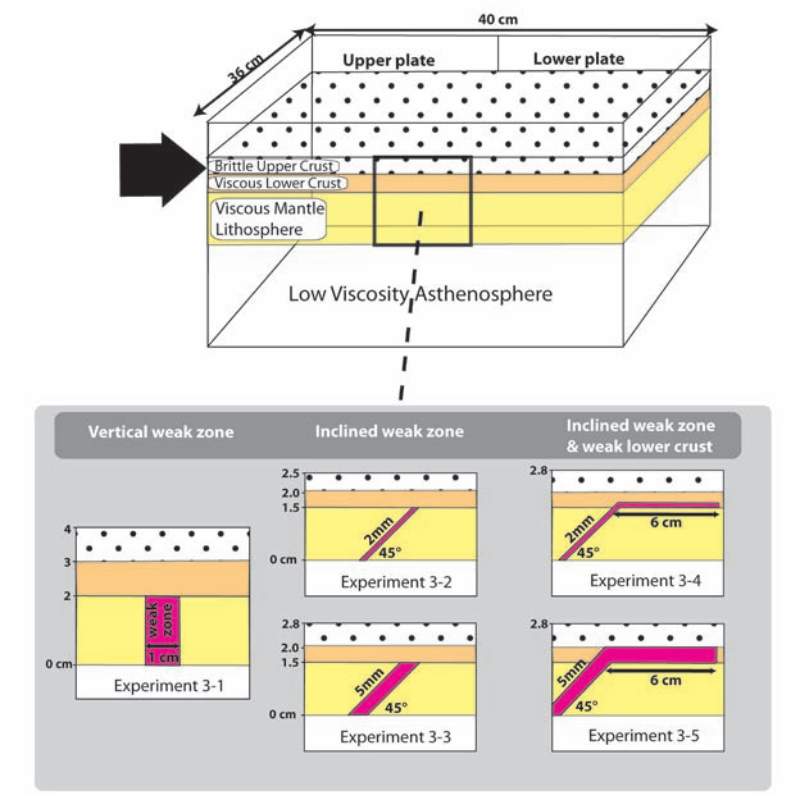

Figure 3.1 Experimental set-up showing the plexi-glass tank containing a three-layer lithosphere floating on a low-viscosity, high-density asthenosphere. The different set ups with respect to the geometry, thickness and extent of the weak zone in the lower crust refer to the models central zone. Black arrow indicates the direction of shortening.

non-Newtonian behavior (Tab. 3.1). With the low shortening rate used (0.5 cm/h) the silicon mixtures deformed in a ductile manner, while dry feldspar sand a Mohr-Coulomb-type material. The density structure of the model allows for subduction, as the mantle lithosphere (1.5 g/cm^3) was denser than the asthenosphere (1.46 g/cm^3).

The models were performed in a transparent tank with one moving wall, which induces convergence of the plates (Fig. 3.1). The horizontal dimensions for all models were 40 x 36 cm^2, and the thickness of the layers varied between the models (Tab. 3.2). However, thickness variations between the experiments was not the main parameter to investigate, but was a result of different length scales. In order to simulate subduction of the lithosphere we implemented a weak zone of Rhodorsil-type silicone, which separated the mantle lithosphere of the converging plates. This weak zone represents a weak plate interface or subduction channel (Fig. 3.1). Additionally, in experiments 3-4 and 3-5 the weak zone continued along the Moho of the lower plate for 6 cm to allow full crust-mantle decoupling. During the experiments top and side view pictured were taken every 30 minutes. The development of the topography was accurately monitored by a 3-D laser with DEM outputs.

3.3.2 Scaling

The physical parameters in the models need to be accurately balanced with respect to nature in order to derive meaningful interpretations [e.g. *Weijermars and Schmeling*, 1986; *Davy and Cobbold*, 1991; *Brun*, 2002]. Dynamic and geometric scaling between model and nature can be achieved when respecting the stress-scale factor:

$$\sigma^* = \rho^* g^* L^* \quad (1)$$

Where σ refers to stress, ρ to density, g to gravitational acceleration and L the length scale. The asterisk refers to the ratio between model and nature. Since in our study g^* equals 1 and the densities of the used silicon putties (~1500 kg/m^3) and rocks in nature (2300 – 3000 kg/m^3) are in the same order of magnitude equation 1 can be simplified to: $\sigma^* = L^*$. Considering the physical properties of the used materials and assumed values for their equivalents in nature (Tab. 3.2) we obtain a stress ratio of 3.3×10^{-7}, which implies a geometric scaling of 1 cm in the model to 30 km in nature.

To fulfill dynamical similarities of the ductile layers the viscous forces depending mainly on viscosity and strain rate need to be balanced between nature and the model. This balancing of the involved parameters can be done by calculating the Ramberg number (R_m) [*Weijermars and Schmeling*, 1986], which represents the ratio of gravitational to viscous forces:

$$R_m = \frac{\rho g h^2}{\eta V} \quad (2)$$

Where h, η, and V are the ductile layer thickness, the viscosity, and the compression rate, respectively. By adopting natural strain rates, viscosities, and thicknesses, we calculated according to R_m the model viscosities and obtain a shortening rate of 0.5 cm/h (Tab. 3.2).

3.3.3 Modelling assumptions and simplifications

The existence of a thermal gradient determining largely the strength of the lithosphere is not incorporated within the models and hence the rheological behavior of our layers is solely influenced by material composition and strain rate. For this reason the strength of the viscous layers remains constant at varying depths, while in nature the strength of the ductile layers decreases exponentially [*Ranalli*, 1995; 1997]. Consequently, temperature driven time-space variability of rheology during shortening cannot be accounted for, and we assume an initial homogenous plate rheology which did not suffer pre-extensional thinning or earlier thickening effecting the bulk strength of the lithosphere. As such, only the mantle lithosphere with a significant amount of strength is considered, which is slightly thinner compared to its natural equivalent [e.g. *Willingshofer et al.*, 2005].

The models are deformed by a constant shortening rate, which does not respond to stress variations related to e.g. mountain build-up, thickening of the viscous layers, or the presence/absence of a slab-pull force. In this study stresses are transmitted horizontally stemming from the advancing wall and convection related drag at the base of the lithosphere is neglected.

Layer	Analogue material	Density ρ (kg/m^3)	Coefficient of friction μ	Viscosity η (Pa · s)	Power n
Upper crust	feldspar sand	1300	0.7 35 Pa (Cohesion)		
Lower crust	silicon mix 1 (PDMS)	1390		$4.8 \cdot 10^4$	1.9
Mantle lithosphere	silicon mix 2 (PDMS)	1500		$1.2 \cdot 10^5$	1.7
Asthenosphere	sodium polytungstate solution	1450		1.2	
Weak zone	silicon mix 3 (Rhodorsil gum)	1100		$1.7 \cdot 10^4$	1.1

Table 3.1 Physical properties relevant for scaling of the experimental materials.

Layer	Density ρ (kg/m^3)	Viscosity η (Pa · s)	Layer thickness h (m)	Velocity v (m/s)	R_m
Upper crust model	1300	-	$1 \cdot 10^{-2}$ (Exp. 3-1) $5 \cdot 10^{-3}$ (Exp. 3-2) $8 \cdot 10^{-3}$ (Exp. 3-3 to 3-5)	$1.4 \cdot 10^{-6}$	-
Upper crust nature	2750	-	$2.4 \cdot 10^4$ (Exp. 3-3 to 3-5)	$9.8 \cdot 10^{-10}$	-
Lower crust model	1390	$4.8 \cdot 10^4$	$1 \cdot 10^{-2}$ (Exp. 3-1) $5 \cdot 10^{-3}$ (Exp. 3-2 to 3-5)	$1.4 \cdot 10^{-6}$	8.8
Lower crust nature	2950	10^{21}	$1.5 \cdot 10^4$ (Exp. 3-2 to 3-5)	$9.8 \cdot 10^{-10}$	6.6
Mantle lithosphere model	1500	$1.2 \cdot 10^5$	$2 \cdot 10^{-2}$ (Exp. 3-1) $1.5 \cdot 10^{-2}$ (Exp. 3-2 to 3-5)	$1.4 \cdot 10^{-6}$	11.3
Mantle lithosphere nature	3300	$4 \cdot 10^{21}$	$4.5 \cdot 10^4$ (Exp. 3-2 to 3-5)	$9.8 \cdot 10^{-10}$	16.7

Table 3.2 Comparison between experimental materials and nature. Together with the scaled shortening velocities these values are used to balance the Ramberg number (R_m) between the model and the natural analogue.

We assume that the use of one moving wall instead of two has no significant effect on the deformation pattern, and whether the upper plate or the lower plate borders the moving wall should not influence the stress and strain patterns.

Furthermore, natural recovery processes such as erosion and sedimentation are not taken into account.

3.4 Plate contacts in nature and models

To restore the initial plate boundary within an orogen is a difficult task requiring detailed geological mapping and high resolution teleseismic profiling. From a global perspective we can robustly distinguish between orogenic cycles following oceanic lithosphere subduction, and orogenic episodes without oceanic lithosphere involved. As an example, the formation of the Alps and also the Himalaya was preceded by subduction of the Tethys Ocean, while the Pyrenees and the Caucasus are mostly interpreted as inverted continental basins [*Roure*, 2008 and references therein]. Both scenarios imply that the plate boundary is already formed during an earlier extensional phase, and that these locations of weakness are subsequently undergoing reactivation. During convergence the plate boundary can become further weakened by multiple processes, such as shear heating, water release and partial melting due to dehydration and/or metamorphism, and heat contribution by radiogenic sediments [e.g. *Pawley*, 1994; *Tagawa et al.*, 2007; *Faccenda et al.*, 2008b]. In addition, the shear zone is maintained by far field stresses generated by the attachment of an earlier subducted oceanic slab [e.g. *Toussaint et al.*, 2004a].

Far field stresses within the model generated by the moving wall are mostly accommodated within the much thicker ductile layers. Therefore, we limited our weak pre-defined weak plate interface to the mantle lithosphere and to keep the influence on the evolving crustal architecture as low as possible. The implementation of a weak lower crust close to the plate boundary within the lower plate in experiment 3-4 and 3-5 (Fig. 3.1) simulates the effect of strong crust-mantle decoupling. Such conditions can be explained by a relative high thermal gradient (>25 °C/km) resulting in Moho temperatures in the order of 750 °C and hence deformation by flow of the lower crust [*Bird*, 1979; *Toussaint et al.*, 2004b]. Lateral variations in the thermal gradient might be related to earlier phases of rifting (Pyrenean case) or mountain building like in the Alps where Late Cretaceous stacking of Austroalpine units resulted in regional metamorphism and resetting of its thermal tectonic age. Since we aimed for one-sided continental lithosphere subduction, [sensu *Gerya et al.*, 2008], we limited the existence of a weak lower crust to the subducting plate.

The thickness of the weak plate contact is another important variable, which has been addressed by different authors [e.g. *Gerya and Stockhert*, 2002; *De Franco et al.*, 2008b]. Numerical models by De Franco et al. (2008) distinguish between "fault-type" and "channel-type" plate contacts with thicknesses up to 6 km. Low velocity layers appearing on seismic sections at the plate interfaces support channel thicknesses of a few kilometers [e.g. *Tsuru et al.*, 2002; *Abers*, 2005]. Also the presence of ultra high pressure rocks in several plate bounding regions is in favor of a channel along which crustal blocks can

Figure 3.2 (facing page) Final top view and cross-sections of experiment 3-1 after 12% of bulk shortening (a, b). Interpreted faults are chronologically numbered. Arrows refer to shortening direction and dash line to profile location. Within the cross-sections white material corresponds to mantle lithosphere, beige to lower crust, brown to the weak zone, and sand to upper crust. Dark line represents Moho. A DEM overlies the cross sections showing the initial elevation in green, areas of subsidence in blue and elevated regions in yellow and red. c) Topographic evolution profiles taken from the center of the model parallel to shortening direction (arrow) after different amounts of bulk shortening. Numbers along the axis indicate only a relative space dimension. The vertical exaggeration is by a factor 3.

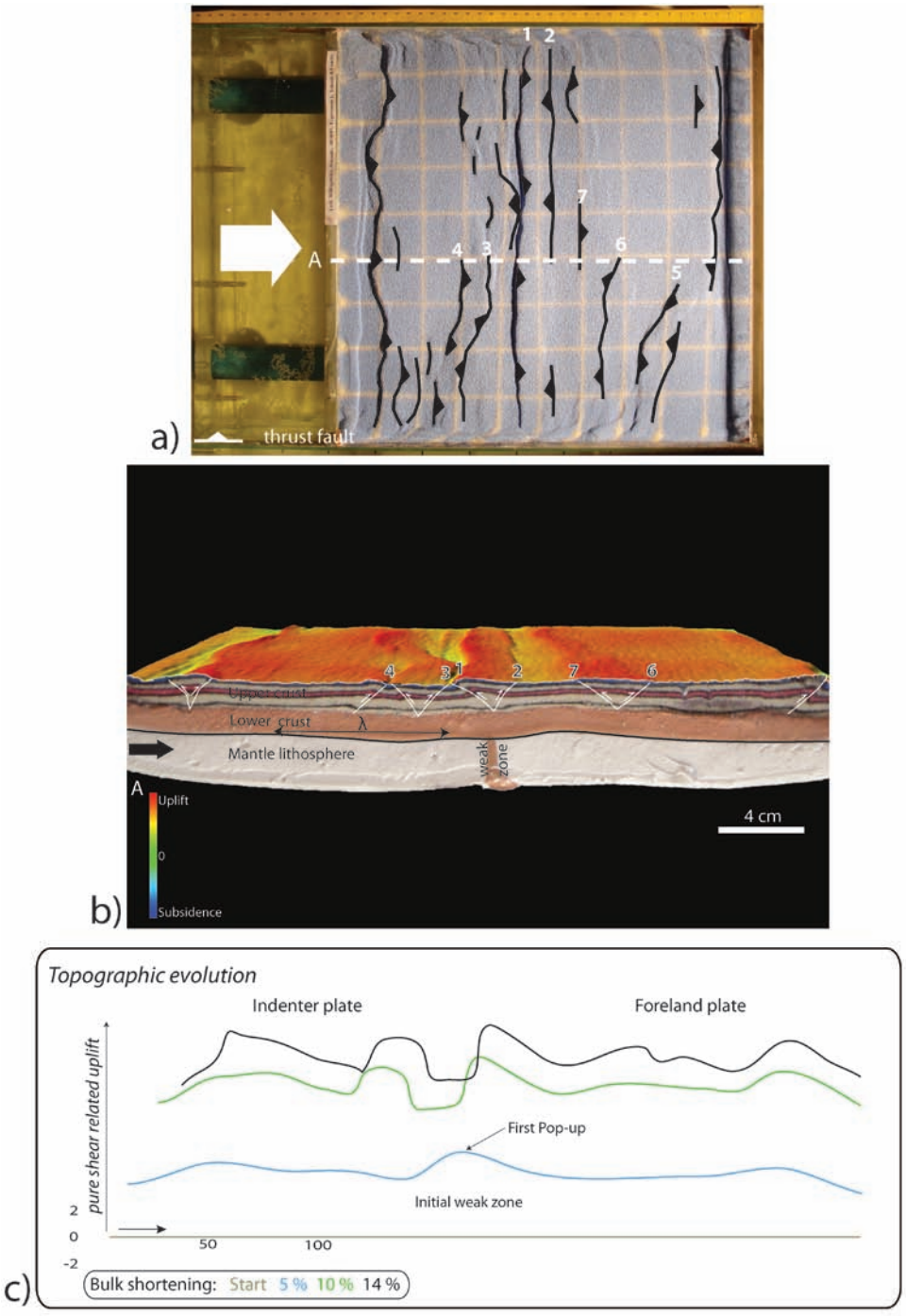
a)
thrust fault
A
1
2
3
4
5
6
7
b)
Upper crust
Lower crust
Mantle lithosphere
weak zone
Uplift
0
Subsidence
4 cm
c)
Topographic evolution
Indenter plate
Foreland plate
pure shear related uplift
First Pop-up
Initial weak zone
2
0
-2
50
100
Bulk shortening: Start 5 % 10 % 14 %

Figure 3.2

be exhumed after subduction. However, depending on the availability of lubricants and with the assumption that sediments play an important role, the plate contact zone can be very narrow, along which stress can built up as indicated by interplate seismicity in the upper crust (0-50 km) [*Tichelaar and Ruff*, 1993]. In numerical models, specific values of friction coefficients can be assigned to the predefined weak plate contact [e.g. *Hassani and Jongmans*, 1997; *Tagawa et al.*, 2007], which we consider in our study as the equivalent of a certain thickness and viscosity of the weak zone (Tab. 3.1). The thickness of the weak zone (~ 0.5 cm in Exp. 3-3 and 3-5) is exaggerated with respect to nature (~15 km) to compensate for the fact that no weak material is added to the system, e.g. by incoming sediment. However, continental subduction will cease at a certain moment in nature as well. This can be caused by a shortage of lubricants, a slowing down of plate convergence resulting in less shear heating, the arrival of strong coupled buoyant crust, or by removing the slab-pull force by slab break-off [e.g. *von Blanckenburg and Davies*, 1995; *Ranalli*, 2000; *Burov and Yamato*, 2008; *Faccenda et al.*, 2008b].

3.5 Modelling results

Within this section the results of the experiments will be briefly discussed and the reader is referred to Figures 2 to 6 showing the final top-view, a cross section and the topographic evolution of each experiment. The following subsections are categorized according to the main changing parameters: the orientation and the extent of the predefined weak zone. Thickness variations are integrated within the subsections, and a comparison between all the experiments will be given at the end of this section. Finally, interpretations of the results together with an integration of previously published work are presented in the discussion.

3.5.1 Experiment with a vertical plate boundary

Experiment 3-1

The first pop-up structure appeared in the upper crust above the weak zone at 4% bulk shortening (% BS) and remained active until the end of deformation, i.e. 12% BS (Fig. 3.2). Progressively several laterally discontinuous pop-up structures developed on both plates propagating mainly away from the weak zone. As it appears from the cross sections very gentle folding of the competent upper mantle at wavelength of 8 cm (*~240 km in nature*) occurred. Synclines of the mantle folds coincide often with pop-up structures in the upper crust. Folding was accompanied by vertical thickening of up to 30% of the viscous layers. In contrast to the other experiments no displacement occurred along the vertical weak zone boundary. The surface scans show the development of local topography related to the upper crustal pop-up's together with a continuous mean surface uplift with ongoing shortening as response to crustal thickening (Fig. 3.2c).

3.5.2 Experiments with an inclined plate boundary

Experiment 3-2

A large fore thrust (1) developed after 2% BS above the weak plate interface, which remained active during the entire experiment (Fig. 3.3a). With ongoing shortening little displacement occurred along small fore- and back thrusts on the lower plate directly in front of the plate contact. Contemporarily, small and curved structures forming a

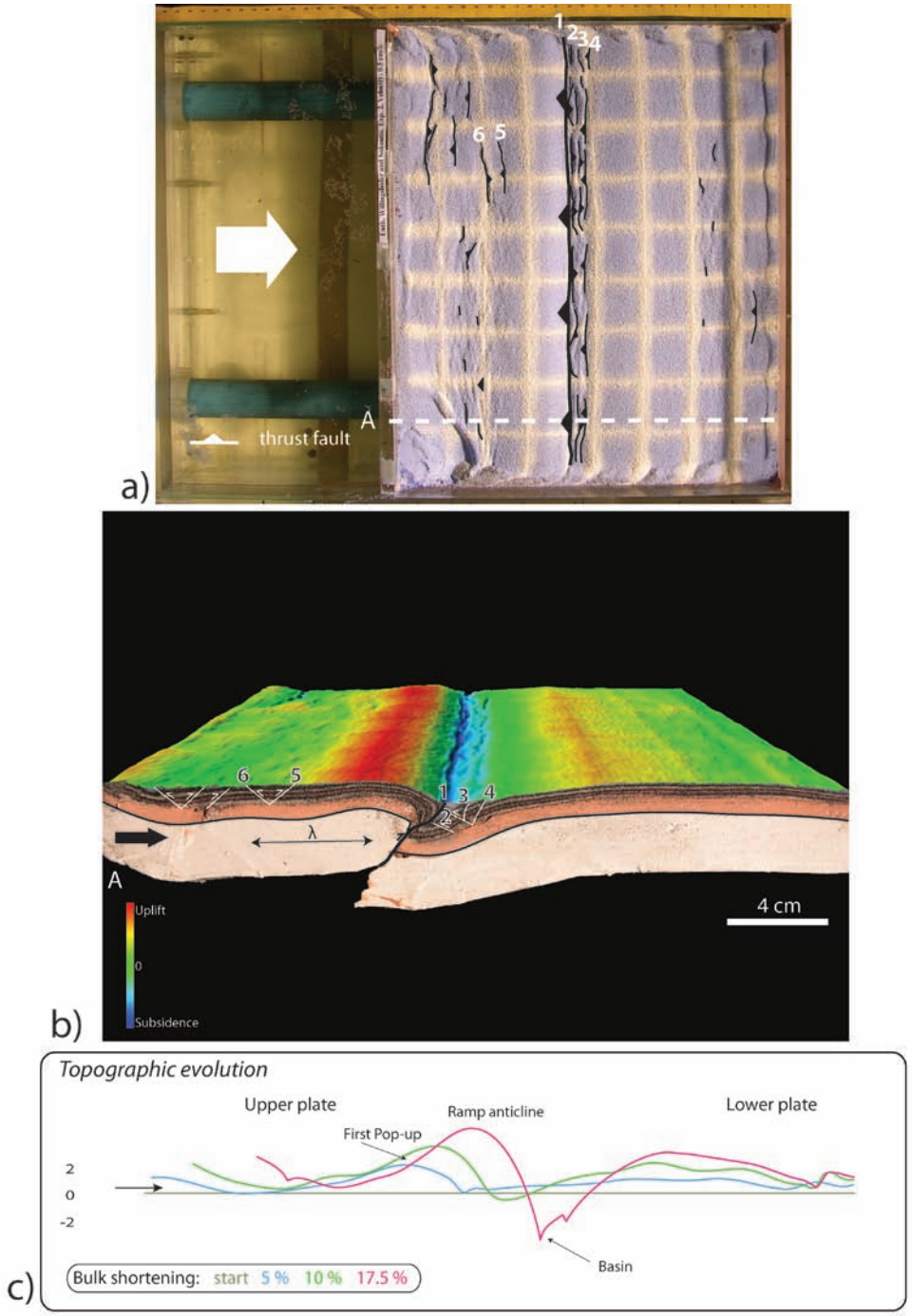

Figure 3.3 Final top view and cross-sections of experiment 3-2 after 19% of bulk shortening (a, b). Layer colors see caption of Fig. 3.2. c) Topographic evolution profiles taken from the center of the model parallel to shortening direction (arrow) after different amounts of bulk shortening. The vertical exaggeration is by a factor 3.

discontinuous pop-up structure evolved on the interior of the upper plate. After 13% BS continuous migration of the major thrust zone caused the underthrusting of some small thrusts on the lower plate, and new thrusts were formed in front of the plate contact. Other compressive structures started to deform the interior of the foreland plate, but remained small until the end of the experiment (19% BS) (Fig. 3.3a).

Although no initial vertical decoupling zone existed between the lower crusts of both plates, a significant amount of vertical displacement occurred along thrust 1 resulting in an 1.3 cm (*~40 km in nature*) offset of the Moho between the plates (Fig. 3.3b). As a consequence of strong horizontal coupling between the crustal layers the upper crust of the lower plate was partly overridden by the upper pate. The mantle of the upper plate was folded on a wavelength of ~4.4 cm (*~130 km in nature*) and a high amplitude ramp anticline formed above the plate boundary. Additionally, the viscous layers were thickened in the range of 20-30% albeit with some lateral variations. On the upper plate thrusts 5 and 6 are probably related to a synformal deflection of the Moho. The laser scans monitor topography related to the early-stage deformation in the overriding plate and the formation of a ramp anticline near the suture zone (Fig. 3.3c). Throughout the models run this structure remained the highest topographic domain with a steep gradient towards the partly overridden adjacent foreland basin. Progressively deepening of the basin resulted in the formation of a slightly elevated flexural fore-bulge on the foreland plate (Fig. 3.3c). During the final stage of shortening the interior of both plates was uplifted with the formation of upper crustal thrusts and the accentuation of fold amplitudes.

Experiment 3-3

Localized deformation commenced after 2.5% BS along thrust 1, which developed above the weak zone interface perpendicular to the direction of shortening (Fig. 3.4a). Ongoing shortening resulted in a steep topographic gradient between the upper and lower plates, and after 5% BS deformation occurred along a back-thrust (2) located on the upper plate as well. From this moment on mainly small scale structures started to develop within the interior of the upper plate, of which some finally merged to form an anastomosing pop-up structure (thrusts 3 and 4). At the same time, short-lived, foreland propagating, upper crustal structures formed before finally getting rotated and/or overridden by the overriding plate (e.g. thrusts 5 and 6).

Within the cross sections, and similar to experiment 3-2, thrust 1 can be extrapolated throughout the entire lithosphere defining the plate boundary with a Moho offset of at least 2 cm (*~60 km in nature*) (Fig. 3.4b). The upper- and lower crust remained coupled within the lower plate and was overridden by upper plate derived mantle in the suture zone. The development of thrust 3 to 6 was strongly governed by folding of the underlying ductile layers. The pop-up (thrust 3 and 4) on the upper plate is rooted into a synform of the upper mantle, which was folded at a wavelength of 8 cm (*~240 km in nature*). Thrusts 5 and 6 originated from the inflection points of the fold and belong to a set of small-scale accommodation structures.

The digital elevation models document the initiation of topography directly along the plate contact with positive relief on the overriding plate and a topographic low on the lower plate. Ongoing shortening resulted in topography on the plate interiors with a fault governed relief with steep gradients overlying a plateau on the upper plate, but

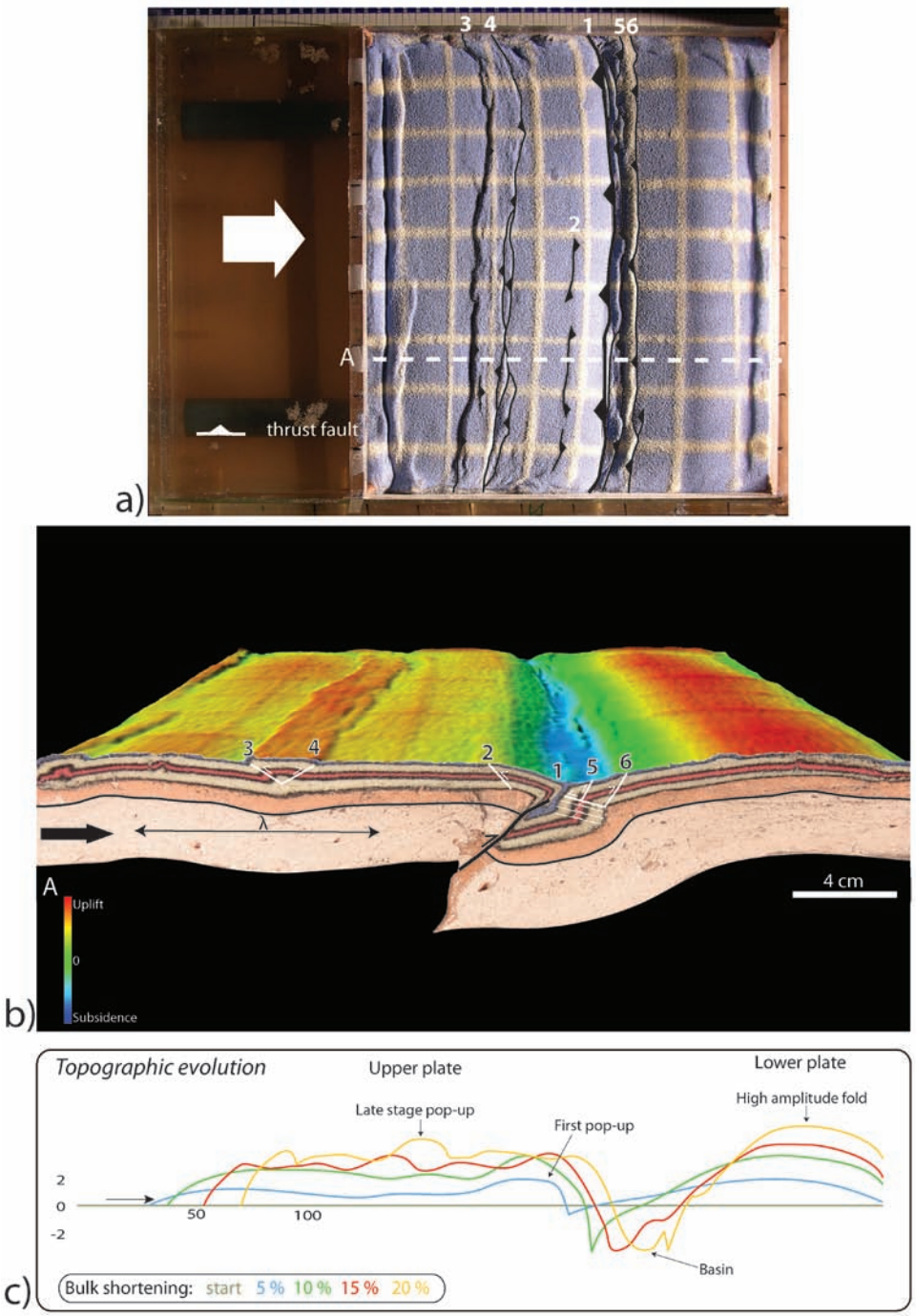

Figure 3.4 Final top view and cross-sections of experiment 3-3 after 19% of bulk shortening (a, b). Legends as in Figure 3.2. c) Topographic evolution profiles taken from the center of the model parallel to shortening direction (arrow) after different amounts of bulk shortening. The vertical exaggeration is by a factor 3.

the models highest point is located along the hinge of the folded foreland plate (Fig. 3.4c). Moreover, it can be observed from the topographic profiles that deepening of the foreland basin and growth of the ramp anticline diminished already after 10% BS (Fig. 3.4c) and topographic growth was essentially confined to the lower plate until the end of the experiment.

3.5.3 Experiments with an inclined plate boundary and a weak lower crust

Experiment 3-4

A direct response to shortening was the formation of a pop-up structure above the weak suture zone. With further shortening the pop-up became part of the upper plate and accommodated most deformation along its fore thrust (1) (Fig. 3.5a-b). After 5% BS a second pop-up structure evolved above the weak zone / lower crust transition on the lower plate. Subsequently, three generations of fore thrusts related to the second pop-up were active throughout the model run. Finally, after 19% BS the interior of the lower plate started to deform by local brittle deformation together with long-wavelength folding of the viscous layers.

The cross-sections reveal that the first crustal pop-up is located on the upper plate and no coherent lithospheric fault, such as in the previous experiments, can be identified (Fig. 3.5b). As a result of horizontal decoupling the forelands upper crust remained at relatively shallow depths avoiding a direct contact with the mantle. On the lower plate the lower crust together with the weak zone material has thickened up to 30 % meanwhile the mantle lithosphere delaminated from the crust. The second upper crustal pop-up borders this zone of lower crustal thickening and developed further onto the lower plate as a series of fore-thrusts (4-6) (Fig. 3.5). Both pop-up structures are cored by up thrusted lower crustal material leading to local wedging and crustal thickening. Remarkably, lower crustal thickening above the predefined suture zone is only minor suggesting that stresses were transferred into the lower plate and localized deformation along the weak- to strong lower crust transition. Displacement along the plate contact was 2.5 cm (*~75 km in nature*) measured from the subducted slab, and evolved in the smearing out of the weak zone material.

From the analysis of topographic data it can be observed that a narrow basin developed on the foreland side of the first pop-up, but with the formation of the second pop-up on the lower plate this basin became incorporated into the orogen (Fig. 3.5c). After ~10% BS the second pop-up was elevated, meanwhile the frontal part of the upper plate and the first pop-up subsided. From this moment onward high topography remained restricted to the second pop-up and to a large scale fold hinge on the upper plate. After 15% BS a narrow foreland basin developed in front of the second pop-up, together with modest topography on the interior of the lower plate.

Experiment 3-5

As in experiment 3-4, the first response to shortening was the formation of a pop-up structure above the weak suture zone, and was followed after 5% BS by the development of second pop-up structure on the lower plate (Fig. 3.6a). Both pop-ups remained

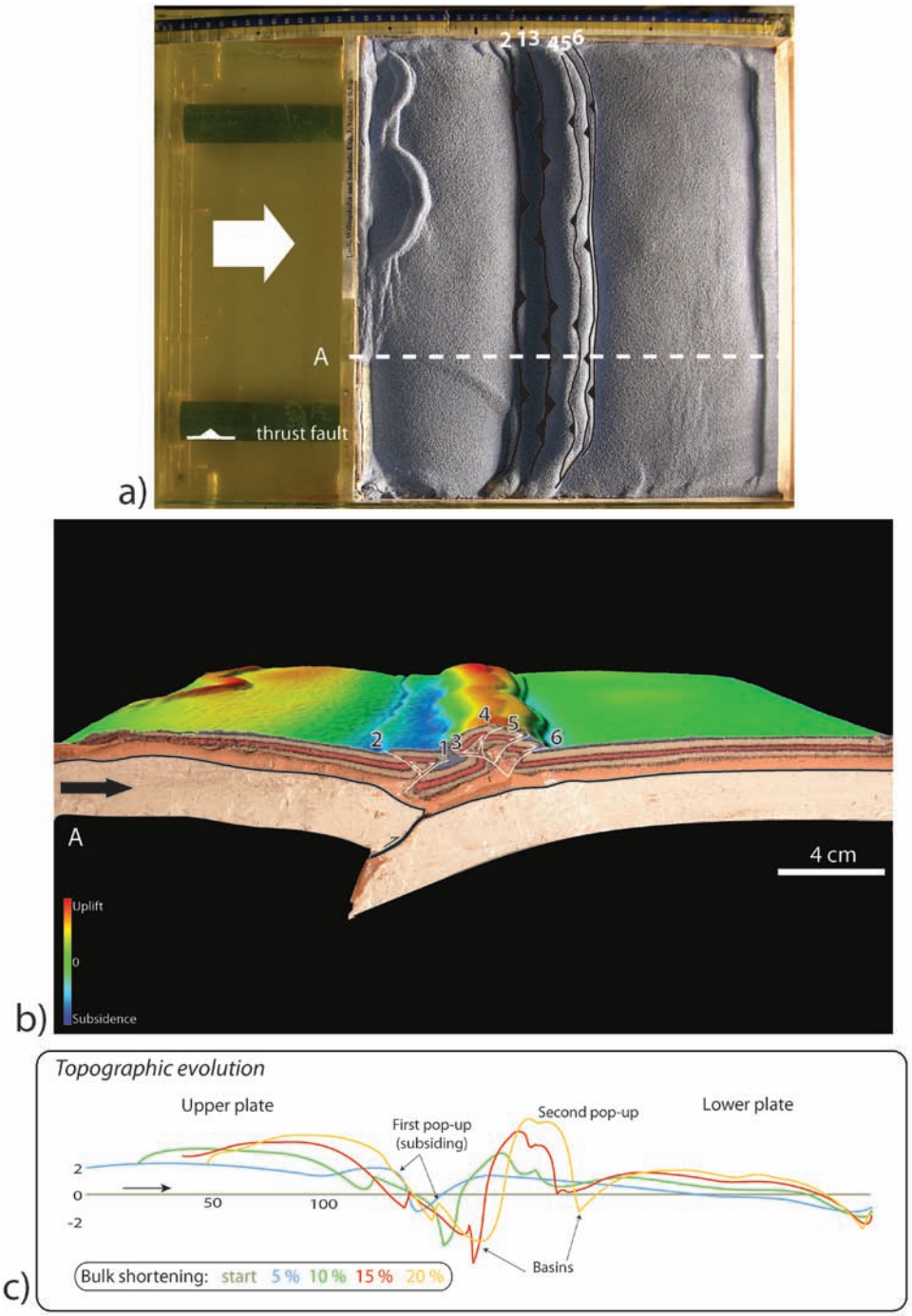

Figure 3.5 Final top view and cross-sections of experiment 3-4 after 19% of bulk shortening (a, b). Legends as in Figure 3.2. c) Topographic evolution profiles taken from the center of the model parallel to shortening direction (arrow) after different amounts of bulk shortening. The vertical exaggeration is by a factor 3.

active throughout duration of the model. From the cross sections it can be observed that ongoing deformation led to the coalescence of both pop-ups into a single symmetrical pop-up structure, which was rooted and cored by thickened lower plate derived weak-zone material (Fig. 3.6b). In addition, shortening was largely accommodated by lower plate crustal deformation at the suture zone and subduction of mantle lithosphere and some weak lower crust. Subduction of the mantle occurred where the upper crust was initially underlain by a weak lower crust, whereas in a subsequent stage the subduction of stronger lower crust resulted in the burial of highly coupled upper crust down to 55 km. The final subducted slab length was 7.5 cm, which is 75% of the total amount of shortening and corresponds to 225 km in nature.

The topographic profile (Fig. 3.6c) shows that between 5% and 10 % BS a symmetric basin formed between two pop-ups, which gets subsequently narrowed and uplifted together with both pop-ups. At the same time adjacent asymmetrical foreland basins deepened on both plates. After 15% BS the orogen underwent a phase of rapid topographic growth, coinciding with deepening of the foreland-type basin and folding of the interior of the lower plate. Finally, between 20% and 25% BS the entire orogen subsided and shifted towards the subducting plate The foreland and retro-foreland-type basins narrowed and deepened, respectively. Besides lithosphere-scale folding resulting in uplift of the plate interiors no intra plate crustal deformation occurred.

3.6 Interpretation and comparison between the experimental results

In this section the most important similarities and differences between the experiments will be briefly discussed. This comparison is primarily qualitative because small variations in crustal thicknesses (Tab. 3.2) and the amount of shortening make a quantitative comparison difficult.

In general, all experiments with the exception of experiment 1 illustrate two distinctive phases: 1) localized deformation and topography development limited to the plate contact, 2) regional deformation affecting the entire model space leading to uplift of the plate interiors and the accentuation or impediment of preexisting fold and basin geometries. Analyzing the results, it became clear that the transition between both phases is strongly influenced by temporal changes in the degree of plate coupling and the presence of a weak lower crust in the lower plate.

3.6.1 Plate boundary deformation and orogenic wedge formation

In all experiments deformation initiates along the plate contact by the formation of a pop-up structure in the upper crust. For the experiments with an inclined plate boundary this upper crustal pop-up can be compared to an orogenic wedge rooted in a singularity point located at the brittle-ductile transition [*Willett et al.*, 1993; *Beaumont et al.*, 1996]. With ongoing deformation all models start to behave differently. Flow of the weak lower crust in experiment 3-4 and 3-5 widens the orogen by the formation of second pop-ups initiating at the transition towards stronger lower crust [e.g. *Beaumont et al.*, 2000]. The large amount of shortening and lower crustal flow in experiment 3-5 favors

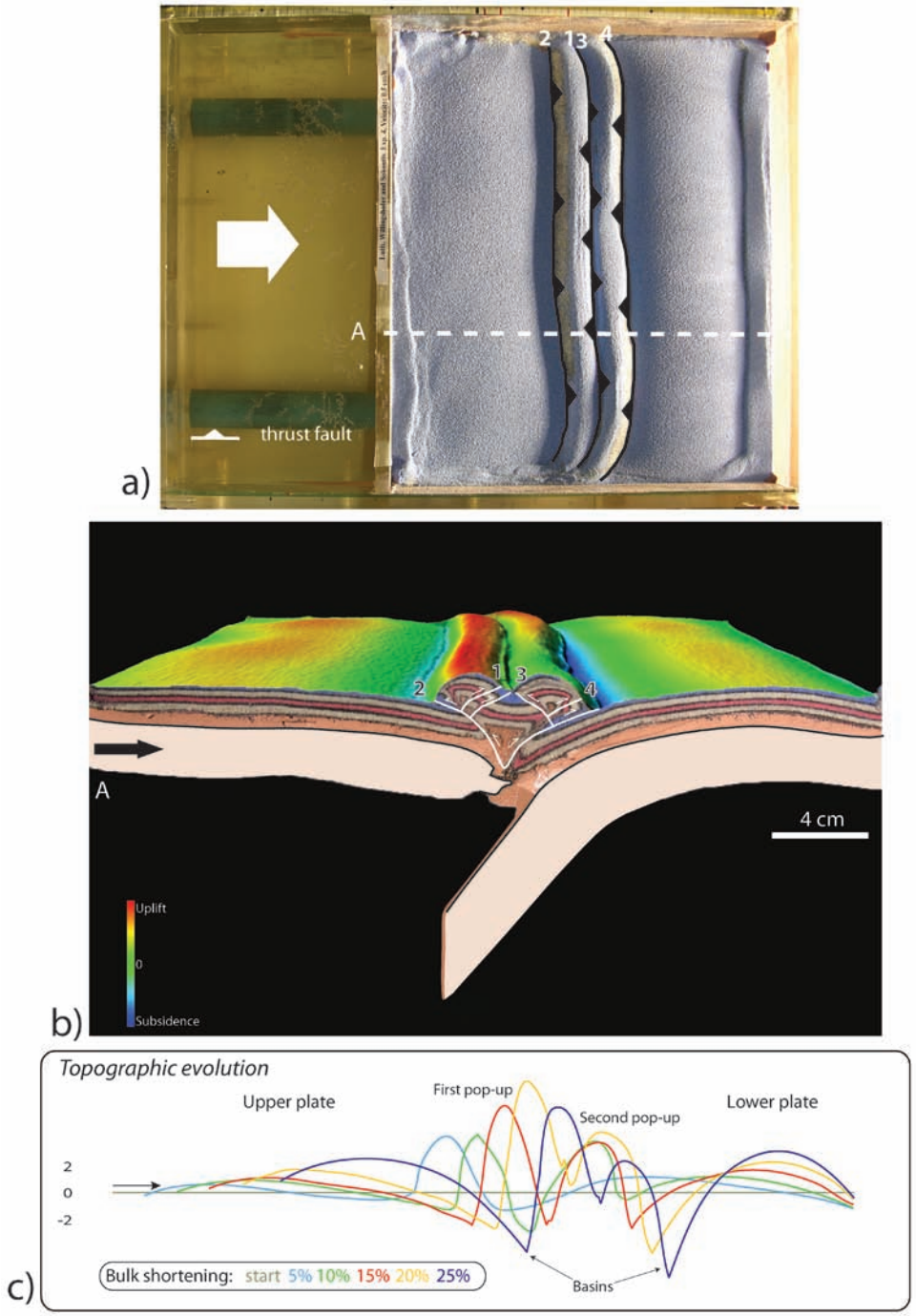

Figure 3.6 Final top view and cross-sections of experiment 3-5 after 24% of bulk shortening (a, b). Legends as in Figure 3.2. c) Topographic evolution profiles taken from the center of the model parallel to shortening direction (arrow) after different amounts of bulk shortening. The vertical exaggeration is by a factor 3.

the coalescence of both pop-ups into a single, symmetrical structure, which can be compared to a bivergent orogenic wedge on the scale of the crust, while the structure of the mantle lithosphere is strongly asymmetric due to subduction of the lower plate [*Willett et al.*, 1993]. In the absence of a very weak lower crust (experiment 3-2 and 3-3) no second pop-up developed on the lower plate. Instead, subsidence of the lower plate occurred, probably due to the weight of the overriding plate and the first pop-up.

3.6.2 Deformation of the plate interior: Influence of plate boundary on crust-mantle decoupling

The topographic profiles of the intra plate regions reveal significant differences among the experiments (Figs. 3.2c, 3.3c, 3.4c, 3.5c & 3.6c), which can be interpreted as reflecting variations in plate- and crust-mantle coupling. A thicker weak zone (experiment 3-3) and hence a higher degree of decoupling results in uplift of the entire overriding plate and less intra plate deformation in an early stage. In experiment 3-2 (Fig. 3.3c) a relative thin weak zone, which is analogue for a relative high friction plate boundary, leads to more pronounced folding of the upper plate and higher topography of the antiform above the plate boundary. However, since deformation in the beginning is strongly localized along the plate interface the weak zone material is displaced rapidly (especially in the low friction plate boundary experiment 3-3). This reduces the efficiency of decoupling and hence locking of the fault zone occurs. The increasing coupling along the plate boundary through time is portrayed by a gradual switch from localized deformation along the plate boundary to more distributed deformation affecting also the upper and lower plate through folding.

The results of the above described experiments differ notably form those where crust-mantle decoupling was incorporated for parts of the lower plate (experiments 3-4 and 3-5). In experiment 3-4 both the plate interface and the lower crust were represented by a thin weak zone (see Fig. 3.5). This time no ramp anticline forms on the upper plate, but subsidence led to the formation of a retro foreland-type basin (Fig. 3.5c). Subsidence continued until 15% BS, and from that point onwards the basin underwent uplift indicating an increased coupling

The combination of a thick weak plate interface and a thick weak lower crustal zone in experiment 3-5 resulted in a high degree of decoupling and finally subduction of the mantle lithosphere. As a result, intra plate deformation was only minor during most of the models run (Fig. 3.6c). However, after 20% BS both plates started to fold causing rapid uplift of the hinge zones and deepening of the basins, probably indicating an increase in resistive forces like buoyancy or plate coupling. Additionally, in contrast with experiment 3-4 the weak zone material was consumed entirely leading to a high degree of stress transfer through the orogen towards the interior of the subducting plate.

Notably, late stage intra plate deformation observed in experiments 3-2 and 3-3 disclose different deformation styles between upper and lower plates. The upper plate is characterized by crustal pop-ups rooted in low amplitude, long wavelength synclines comparable to experiment 3-1 and previous studies [*Davy and Cobbold*, 1991; *Sokoutis et al.*, 2005], while the foreland plate is folded into a single high amplitude anticline structure (Figs. 3.3 and 3.4). Additionally, accurate observations on the timing of onset

folding in experiment 3-5 reveals that lower plate folding started slightly before folding of the upper plate's interior (Fig. 3.6c). Therefore, lower plate folding might be interpreted as being related to flexure of the lithosphere during mantle lithosphere subduction. With ongoing shortening the plates coupling increases and deformation spreads throughout the entire model accentuating this preexisting flexural fore-bulge.

3.6.3 Basin formation

The timing of basin subsidence, widening, and subsequent uplift is of importance for identifying the transition from a decoupled towards a coupled system (Figs. 3.2c, 3.3c, 3.4c, 3.5c and 3.6c). Together with the monitored adjacent topography constraints can be made on the timing of the deeper processes, such as crust-mantle decoupling.

A distinction can be made according to the amount of basins present in the different experiments. In experiments with a strong lower crust (exp. 3-2 and 3-3) a single basin develops on the lower plate in front of the plate contact (Fig. 3.3c and 3.4c). The basins have asymmetric foreland-type geometries with the deepest point located near the plate contact and shallow gradually towards the foreland. Remarkably, the timing of basin deepening and widening differs between experiment 3-2 and 3-3. In experiment 3-2 both deepening and widening of the basin was gradually lasting until the end of shortening (Fig. 3.3c). On the contrary, deepening was rapid in experiment 3-3 and the lowest topographic point was reached already at 10% BS (Fig. 3.4c). With ongoing shortening the basin widened, but subsequent narrowing commenced after 15% BS. In order to interpret this difference we need to underpin the processes underlying basin formation. Although the basin geometry is similar to a foreland basin it remains uncertain whether the operating mechanisms are the same. A foreland basin typically forms by flexure due to loading forces applied by adjacent topography or subsurface loads [*Karner and Watts*, 1983; *Ziegler et al.*, 2002; *Naylor and Sinclair*, 2008]. However, since the plate contact developed into a thrust cutting the lithosphere subsidence might partly also be related to dragging along the plate contact as suggested by the geometry of the lower plate at the plate boundary. For this reason we argue that basin evolution and the degree of plate (de)coupling are intimately related. Consequently, the gradual subsidence and widening of the basin in experiment 3-2 indicates a slow but constant movement along the plate boundary whereas early high subsidence rates in experiment 3-3 support a high degree of plate decoupling preceding the moment of increased coupling resulting in stagnation of basin subsidence and the onset of narrowing.

Including a weak lower crustal zone (exp. 3-4 and 3-5) gives rise to foreland type basins on both sides of the orogen. In the early phase of experiment 3-4 a basin evolved on the foreland side of the first pop-up, but eventually became a retro-foreland basin with ongoing shortening (Fig. 3.5). A similar basin overlying the upper plate can be observed in experiment 3-5 (Fig. 3.6). This basin is probably not only the result of a topographic load, but also to a sub-surface load, namely a slab pull force, which became important as the slab length increased. We therefore, suggest that relative subsidence of the basins and the model orogen during the last increment of shortening is due to slab pull force (compare topographic sections of 20% and 25% BS in Figure 3.6c). On the other hand, the retro foreland basin in experiment 3-4 is uplifted after 15% BS due to increased plate coupling and the lack of a significant vertical slab pull force. During this

final stage another foreland basin started to develop on the lower plate in front of the second pop-up.

Within experiment 3-5 even a third, intramontane-type basin developed between both pop-ups, which showed early deepening and narrowing, and by the time both pop-ups started to behave as a single pop-up the basin was uplifted as well.

3.7 Discussion

3.7.1 The role of plate interface rheology on continental collision

The implementation of a weak interface separating the upper and lower plate with varying thickness, length and angle resulted in different styles of continental collision in terms of orogenic structure and topography.

Although vertical rheological boundaries in all our experiments were locations for deformation, a vertical weak zone has only minor influence on the deformation pattern, and the lithosphere responds by buckling without any displacement along the plate boundary. This result is consistent with the analogue modelling studies of *Martinod and Davy* [1994], *Sokoutis et al.* [2005] and *Willingshofer et al.* [2005]. In contrast, experiments with an inclined plate interface (exp. 3-2 to 3-5) favor simple shear deformation and hence subduction of the lower plate. However, the presence of a weak plate interface, which is restricted to the mantle lithosphere, does not evolve in incipient continental subduction (exp. 3-2 and 3-3). Instead, this results in the development of a lithosphere cutting fault of which the lower part is localized along the pre-defined plate contact, while its upper equivalent separates the crustal segments. The strong coupling between the mantle lithosphere and the buoyant crust of the lower plate resulted in lithosphere-scale underthrusting rather than subduction of the continental mantle lithosphere.

To obtain subduction of the mantle lithosphere and formation of a collisional mountain belt a combination of a weak plate interface with sufficient thickness and weak lower crust in the lower plate is needed. Only in such a scenario the required decoupling between the buoyant crust and denser upper mantle can occur. The demand for a weak plate interface to obtain subduction has also been inferred from numerical [e.g. *De Franco et al.*, 2008a; *Gerya et al.*, 2008; *Faccenda et al.*, 2009] as well as analogue modelling studies [e.g. *Chemenda et al.*, 1996, 2001].

3.7.2 Temporal changes of plate coupling

Thinning of the weak zone plate boundary and the absence of softening mechanisms or addition of new weak material result in strengthening of the plate contact. Together with the increasing length of the brittle segment of the plate contact where high stresses can accumulate [*Hassani and Jongmans*, 1997; *Lamb*, 2006], the degree of coupling among the plates can increase through time.

Displacement along the plate interface results in thinning and/or consumption of the weak zone material and increased plate coupling facilitating stress transmission. For example, in experiment 3-4, high friction along the plate contact caused the upper plate to be dragged down together with the lower plate. This can be interpreted as an early

phase on the initiation of double sided subduction as proposed by *Gerya et al.* [2008]. However, when both plates became too strongly coupled with ongoing shortening subduction ceased, and regional uplift including the basin began. This result is consistent with the findings of *Willingshofer and Sokoutis [2009]* who argue that strong coupling between an orogenic wedge and its foreland can lead to uplift of the latter. Deducing vertical motions as a function of the degree of plate coupling is limited to cases where no significant slab pull force is present. Experiment 3-5 (Fig. 3.6) shows that the effect of the slab pull force may dominate over those related to the changes in plate coupling leading to net subsidence of the foreland basins. Additionally, in experiments (3-1 to 3-4) plate coupling results in uni-formal thickening of the ductile layers and uplift of the mean surface, while contemporaneous folding redistributes local topography.

Other processes which can influence plate coupling at depth are erosion and sedimentation [e.g. *Burov and Toussaint*, 2007]. Transportation of material from the upper plate towards the subducting plate will flex down the foreland plate and, hence favors subduction. However, in our experiments continental subduction involves only the mantle lithosphere, and flexure due to surface loading plays probably a minor role relative to mantle delamination.

3.7.3 The effect of lower crustal rheology on crust-mantle (de)coupling

The importance of the lower crustal physical properties in terms of density and strength on the deformation pattern of the entire lithosphere has long been recognized [e.g. *Ranalli and Murphy*, 1987; *Burov and Watts*, 2006]. It is especially this part of the lithosphere, which is subjected to strength variation depending on composition, crustal thickness, and geothermal gradient [e.g. *Windley and Tarney*, 1986].

In orogenic systems the role of the lower crust can be divers depending on among others the thermal history of the accreted blocks. Considering its style of deformation there are geological examples where lower crustal material is incorporated into the orogenic wedge and subsequently brought to the earth's surface by nappes or by the updoming of gneiss domes in the internal parts [e.g. *Laubscher*, 1988b; *Yin*, 2004]. Alternatively, the upper and lower crust are detached leading to the formation of a lower crustal root or even subduction [e.g. *Laubscher*, 1977]. In this case no lower crustal material crops out at the surface. However, the behavior of the lower crust is often debated and the intermediate case might be a better interpretation in which the crust is brought to depth and metamorphosed into eclogites of which detached slivers are returned to shallower levels, while the bulk of the lower crust is subducted [e.g. *Schmid and Kissling*, 2000].

An important parameter determining the fate of the lower crust in an orogenic setting is the presence of a weak middle crust promoting delamination at the Conrad discontinuity. Numerical models reveal that this will especially occur when Moho temperatures are low (< 550 °C), resulting in subduction of both the lower crust and the mantle lithosphere [*Regard et al.*, 2003; *Toussaint et al.*, 2004a; *Burov and Yamato*, 2008]. On the other hand, higher Moho temperatures (550-650 °C) will support crustal separation from the mantle lithosphere, and hence subduction of only the mantle lithosphere.

In experiments presented here the lithosphere consists of three layers with a decisive role for the lower crustal rheology in terms of crust-mantle decoupling.

Only in experiments with a weak lower crust (exp 3-4 and 3-5, Figs. 3.5 and 3.6)

crust-mantle decoupling occurred. Experiment 3-4 shows that a thin weak zone at the base of the lower crust is sufficient to achieve crust-mantle decoupling. As the mantle lithosphere detaches thickening of the lower crust occurs inducing uplift and deformation (2nd pop-up) of the brittle crust above (Fig. 3.5b and Fig. 3.7b).

If we compare the difference in the premature slab geometry of the mantle lithosphere between experiment 3-3 and 3-4 we notice a concave and convex shape, respectively. This difference can be ascribed to the combination of a buoyant crust and the degree of coupling along the Moho, which prevent mantle delamination in experiment 3-3 and due to the weight of the overriding plate can only deform in a concave down bending of the entire lithosphere. While a slight decoupling zone along the Moho is sufficient to bend the lower plate in a convex shape.

In experiment 3-5 the weak zone along the Moho comprises the entire lower crust and strongly deforms by ductile flow and thickening. As a result the upper crust is uplifted and is maximal shortened above this region leading finally to the coalescence of the two pop-ups (Fig. 3.7d).

3.8 Comparison between experiments and natural analogues

3.8.1 Pyrenees

The Pyrenees are a suitable candidate for a comparison with the obtained modelling results because the orogen is highly investigated, the amount of shortening is within the same range (100-160 km), no accretion or exhumation of additional crustal pieces occurred; and collision was without strong obliquity. The onset of contraction in the early Paleocene between the European plate in the north and the Iberian plate in the south resulted in a typical asymmetrical bivergent crustal wedge with a relative long southern flank (Fig. 3.7a,c). At deeper crustal levels the ECORS seismic transect monitored a fan shaped crustal geometry partly within a thickened southward overthrusted Iberian crust [*Choukroune*, 1989; *Roure et al.*, 1989]. Also the progressive down flexing of the Iberian Moho towards the internal zone followed by a ~15 km vertical Moho offset along the north dipping plate contact below the Pyrenees internal parts underline its asymmetrical character. For a more detailed review on the lithospheric structure and deformation history of the Pyrenees the reader is referred to e.g. [*Choukroune*, 1989; *Roure et al.*, 1989; *Muñoz*, 1992; *Souriau et al.*, 2008].

Experiments 3-4 and 3-5 show the development of a crustal orogenic wedge albeit with more symmetry of the latter. This difference in crustal structure between the models is mainly due to a larger amount of lower crustal decoupling and bulk shortening in experiment 3-5, causing two pop ups to agglomerate into a symmetrical wedge with progressive mantle lithosphere subduction. While in experiment 3-4 crustal deformation initiated also along rheological boundaries, but due to a thinner weak zone resulted in a modest amount of mantle lithosphere subduction, and thus in preservation of crustal asymmetry. Interpretations of the ECORS seismic transect emphasize the asymmetry at lower crustal levels, which is also evident in both experiments (Fig. 3.7c-d). The amount of vertical Moho offset along the plate contact is only modest in experiment 3-4, and wedging of the lower plate's mantle lithosphere caused lower crustal thickening below the orogen, as also interpreted by Roure et al. [1989] (Fig. 3.7a-b). On the other hand,

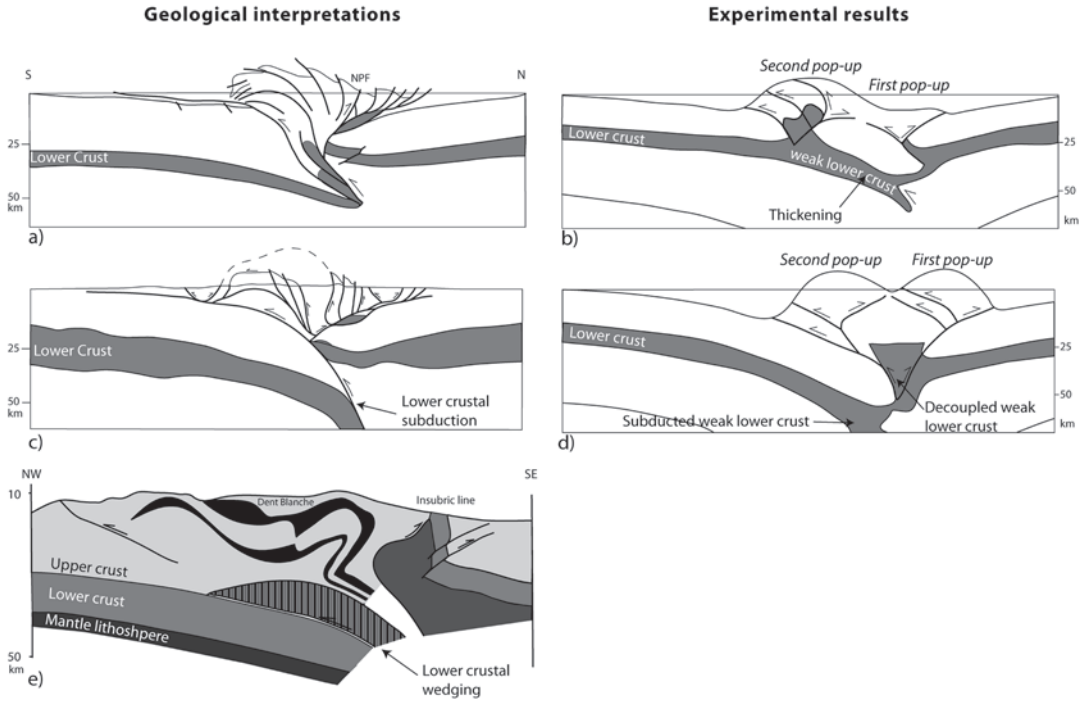

Figure 3.7 a) Interpretation of the ECORS seismic transect through the Pyrenees modified after Roure et al. [1989], showing asymmetrical upper crustal fanning and stacking of the lower crust. b) Crustal simplification of experiment 3-4 highlighting lower crustal thickening between both crustal pop-ups related to crust-mantle detachment. Notice the formation of the second pop-up above the weak to strong lower crust transition. c) Interpretation of the ECORS transect by Muñoz [1992] showing lower crustal subduction instead of stacking. d) Sketch of experiment 3-5 for comparison with interpretation by Muñoz of the Pyrenees. A wide predefined weak plate interface together with a weak lower crust and a high amount of shortening result in lower crustal subduction beneath a symmetrical orogen cored by upthrusted weak lower crust. e) Interpretation of NFP-20 after Schmid and Kissling [2000] shown as a natural analogue for lower crustal wedging on the lower plate observed in experiment 3-4 (see b). The formation and shortening along the crustal fore thrust might be linked with the evolving lower crustal wedge (vertical lines). Black region refers to Penninic units.

in experiment 3-5 the lower crust partly subducted together with the lower mantle lithosphere similar to the lithosphere-scale interpretation of Muñoz [1992] (Fig. 3.7c) However, recent teleseismic tomography through the Pyrenees is incapable to trace the remnants of subducted lower crust [*Souriau et al.*, 2008].

Balancing of the ECORS profiles indicates a pre-collisional asymmetry and a thicker Iberian crust with respect to Europe prior to contraction [*Roure et al.*, 1989]. Numerical modelling of the orogenic phase by Beaumont et al. [2000] advocate the importance of this inherited asymmetry on the final structure of the Pyrenees. Of special importance is

the crustal extension during Cretaceous times resulting in mantle uplift and strengthening of the European plate boundary with respect to Iberia. In addition, north dipping listric faults formed during the Hercynian orogeny flattening out at lower crustal levels favors crustal decoupling at the onset of contraction, while steep south dipping reactivated normal faults on the European side enhance an asymmetric development of the orogeny [*Beaumont et al.*, 2000]. Therefore, implementing a weak lower crustal zone simulating a horizontal decoupling in our experiments seems a realistic assumption. Moreover, our models suggest that the condition of decoupling at the lower crust is sufficient to explain the large-scale asymmetry in the Pyrenees and no call on a multitude of inherited complexities is needed. The transition from localized deformation along and in the vicinity of the plate boundary to an intra plate deformation as observed in the experiments (switch from decoupled to coupled mode), is in agreement with the recorded shift from mountain building in the Pyrenees towards lithospheric folding of Iberia in the Neogene [*Cloetingh et al.*, 2002].

3.8.2 Examples from the Caucasus, Colombian Cordillera, Sierra Pampeanas, and the Alps

Other inverted rift basins to which the results of this study are relevant include the Colombian Cordillera and the Caucasus [*Philip et al.*, 1989; *Dengo and Covey*, 1993; *Saintot and Angelier*, 2002; *Roure*, 2008]. As in the Pyrenees no oceanic lithosphere was involved in mountain building since no high grade metamorphic terrains, nor ophiolites or volcanic arcs make part of the recent orogenic structure and the amount of shortening is comparable to experiments 3-2 to 3-4. Also the amount of different accreted blocks is limited and there are no deep earthquakes due to the lack of a Benioff zone.

During the Caucasus orogeny Cenozoic inversion of an Early to Mid-Jurassic rift occurred resulting in the formation of the Transcaucasus in the south and the somewhat younger and higher Greater Caucasus to the north [e.g. *Philip et al.*, 1989; *Saintot and Angelier*, 2002] (Fig. 3.8). A well-developed fold- and thrust belt has formed on the northern side of the Greater Caucasus with Dagestan in an apparent "back-arc" setting. The relative timing of deformation within the different regions of experiment 3-2 is comparable with the eastern part of the Caucasus. Namely, the first pop-up structures appearing on the lower plate are progressively subsided by the load of the overriding plate and can be seen as part of the Transcaucasus, which are now partially overlain by the Kura basin (Fig. 3.8b). The highest topography is formed on the overriding plate comparable to the Betcha anticline of the Greater Caucasus, which show high Neogene uplift rates and is thrusted onto the foredeep. The even more recently uplifted Dagestan region is located on the upper plate and has been interpreted as an inverted Jurassic basin [*Roure*, 2008]. This inversion accommodated most of the intraplate stresses during what can be considered as the coupled phase. A similar expression of intraplate deformation can be seen in experiment 3-2 albeit farther away from the plate boundary as is the case in Caucasus and relates most likely to lithospheric buckling, since pre-existing crustal faults were not included (Fig. 3.8c).

Even more dramatic examples of mountain belts interpreted as being related to far field stresses are the Eastern Cordillera of Colombia and the Sierras Pampeanas in Argentina.

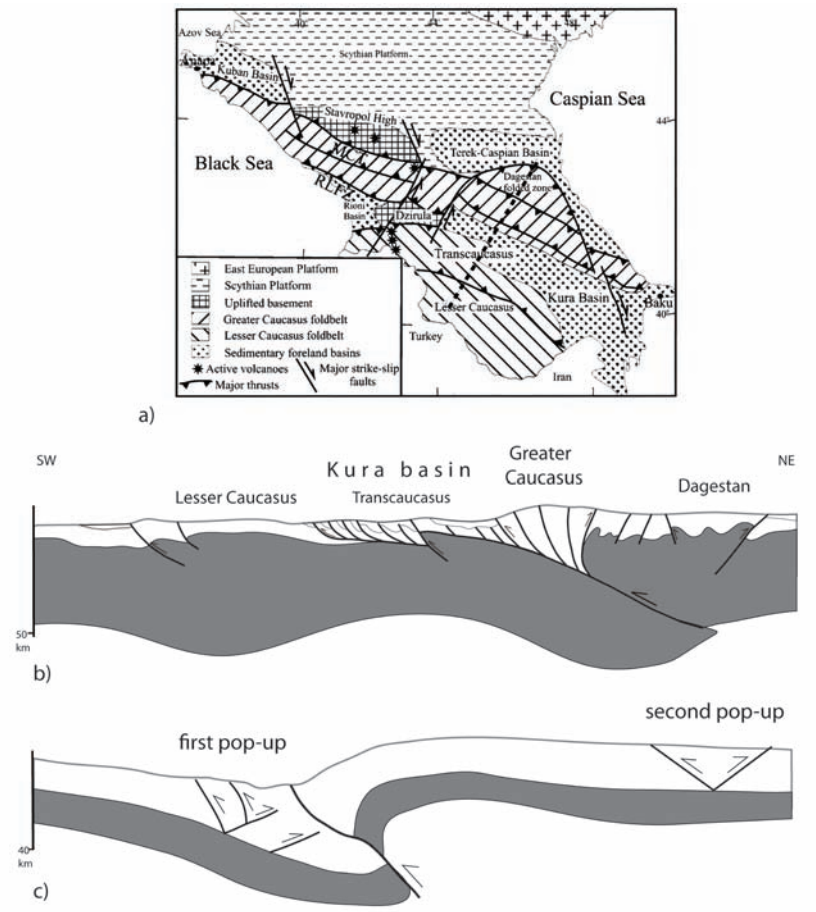

Figure 3.8 a) Tectonic map of the Caucasus from Ruppel and McNutt [1990]. The dashed line indicates the location of the crustal section. b) Interpreted crustal section from Philip et al. [1989]. Dark grey refers to lower crust, which is hardly subducted but mainly under thrusted resulting in an asymmetric orogen. c) Simple drawing of a cross section from experiment 3-2 in which the timing and geometry of the structures are comparable with the eastern Caucasus. Notice the large distant of the "Dagestan" pop-up from the suture zone relative to the geological section. See text for more discussion.

In both orogens crustal shortening was induced by the ongoing oceanic subduction below the Andes much farther towards the west [e.g. *Dengo and Covey*, 1993; *Costa et al.*, 2001]. The Eastern Cordillera is interpreted as a Late Jurassic – Early Cretaceous inverted rift basin, which is according to Dengo and Covey (1993) connected by a mid crustal detachment zone to the Andean subduction zone in the west and allows for the transmission of shortening from the convergent plate margin. The Sierras Pampeanas is even more than 600 km located away from the Chilean trench, but is due to the fact of the flat lying orientation of the subducted Nazca plate linked to the plate convergence within this latitude [e.g. *Stauder*, 1973]. The orogen comprises uplifted basement blocks

thrusted on Pleistocene sediments along faults which produce ongoing seismic activity [*Costa et al.*, 2001]. However, looking back at the results of experiment 3-2 and 3-3, where intra plate deformation of the upper crust evolves during the coupling stage, an alternative explanation for both orogens can be an increase of plate coupling. Therefore, neither pre-existing crustal structures, nor changes in subduction angle are directly needed to develop mountain belts away from the zone of convergence.

Lower crustal wedges, as imaged in reflection seismic profiles, are prominent features in the Western and central Alps [e.g. *Schmid and Kissling*, 2000], but are missing in the Eastern Alps [*TRANSALP Working Group*, 2002] (Fig. 3.7e). The processes by which these wedges form are still unclear. The results of experiment 3-4 suggest that one possible mechanism for producing lower crustal wedges invokes flow of lower crust (Fig. 3.7b). This thickening of the lower crust also enhances uplift of the overlying orogenic wedge with a younging trend towards external regions. The formation of the more external second pop-up in experiment 3-4 is conditioned at the end of the weak lower crust (Fig. 3.7b). In natural systems, the transition from a weaker lower crust in internal parts of orogens, where temperatures are higher to a less weak lower crust in the external regions presumably occurs gradually. Inspired by our modelling results, we infer that wedging of the European lower crust in the Western Alps can be explained by shortening of a ductile lower crust, which deforms and thickens dominantly by flow processes. The aerial extent of lower crustal thickening is governed by the lateral strength variation within the lower crust, which might be the underlying cause for deformation and uplift of the external massifs. This view is supported by Ar/Ar biotite cooling ages from the Western Alps documenting uplift of a relative wide area with slightly younging towards the north, the direction of lower crustal wedging [*Schlunegger and Willett*, 1999; *Schmid and Kissling*, 2000].

3.9 Conclusions

Our modelling study emphasizes the importance of the plate boundary on the structural and topographic evolution of collision zones. The geometry of the plate contact together with the abundance and distribution of lubricants along the plate contact control the initial response of surface deformation and the amount of mantle lithosphere subduction. A vertical plate contact with respect to the shortening direction will result in buckling of the lithosphere and the formation of fold related pop-ups in the upper crust. An inclined boundary leads to underthrusting of the lower plate, but does not necessarily result in mantle lithosphere subduction. Favourable conditions for subduction of the continental mantle lithosphere and continental collision include strong crust – mantle decoupling and the presence of a weak plate interface. Consequently, the distribution and amount of weak lower crust influences orogenic wedge architecture by delamination of the mantle lithosphere, but also affects wedge geometry and topography by lower crustal thickening. Whether lower crust subducts beneath the orogen depends mainly on the thickness of the weak plate interface and the amount of weak lower crust.

The transition from a decoupled to a coupled collisional stage, by thinning or consumption of the weak zone, is recorded by a change from localized to distributed deformation. The coupled stage comprises concomitant folding and thickening of both the upper and

lower plate, and therefore late-stage uplift or subsidence of orogens, foreland basins, and flexural fore-bulges.

A change from decoupling to coupling during the collisional stage as occurs in our experiments matches well with observations from orogens around the world, like for instance the Pyrenees, Caucasus, Colombian Cordillera, and the Sierra de Pampeanas in Argentina. In addition, wedge-shaped geometries of the lower crust as inferred for the Western Alps may be produced even when the lower crust deforms by viscous processes.

Chapter **4**

Plate decoupling and wedge formation

4.1 Introduction

Within the previous chapter it was concluded that the degree of (de)coupling along the plate interface strongly governs continental subduction and wedge build-up. Plate decoupling and subduction of mantle lithosphere were maintained by weak lower crust. Moreover, limiting decoupling by introducing "strong" lower crust in the lower plate not only hampered further subduction, but also (re)shaped the overlying crustal wedge in terms of width, uplift pattern, and internal structure. This chapter elaborates further on the role of decoupling on mantle subduction and in particular crustal wedge formation. Analogue models were constructed which hypothetically led to continental subduction, but different crustal responses. In Chapter 3, plate interface rheology and geometry were varied, whereas the focus of this chapter is on how rheological stratification of the plate itself affects plate decoupling and wedge development. Different plate (de)coupling conditions were induced by: 1) *very* weak lower crust restricted to the plate interface and direct surroundings, 2) weak lower crust throughout the entire lower plate, and 3) weak mantle lithosphere within the lower plate or both plates. These set-up's intended to invoke spatial- and temporal variations in decoupling conditions within and between colliding plates. By means of these variations the importance of lithosphere (de)coupling as a fundamental condition for continental mantle lithosphere subduction and crustal wedge build-up was investigated. Finally, after classifying the model results according to their different mechanical responses, a comparison with continental collision zones such as the Alps is discussed.

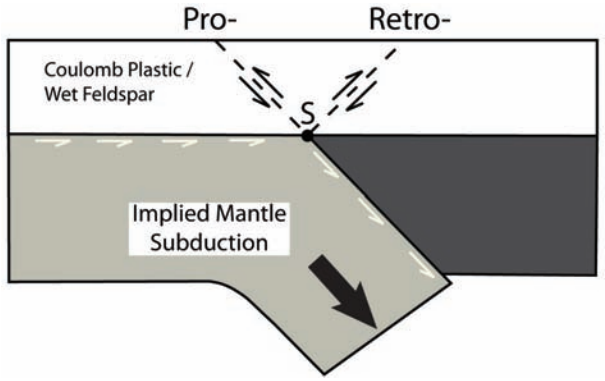

Figure. 4.1 Configuration of the Alpine-style model configuration after Beaumont (1996). The model is deformed by the application of basal velocity boundary conditions (white arrows) and a load (large arrow). The crust responds by the formation of a pro- and retro-shear rooting in a singularity point (S-point). Note that ductile properties within the crust play no significant role and the upper crust remains strongly coupled to its base. Illustration redrawn from Beaumont et al. [1996].

4.2 Modelling of orogenic wedges

Based on previous comparisons between modelling- and field studies on continental convergence, large-scale deformation styles within orogens have been recognized. As discussed in *Willet et al.* [1993] and presented in the numerical studies of *Beaumont et al.* [1994; 1996], a typical crustal response on subduction of the continental mantle lithosphere is the formation of an doubly vergent wedge. Initially, this symmetric wedge consists of a pro-shear (facing towards the lower plate) and a retro-shear (facing towards the upper plate), which both root at a predefined singularity point (S-point) (Fig. 4.1). With ongoing shortening the style of wedge geometry strongly differs depending on various input parameters, such as the strength of crust-mantle coupling or the presence of a predefined mid-crustal detachment. For instance, a weak layer at the base of the crust resulted in a wider spread of crustal deformation. They also showed that an increase of denudation or buoyancy of the subducted lithosphere leads to a significant amount of retro-shearing [*Beaumont et al.*, 1994; *Beaumont et al.*, 1996]. Note that within these models, retro-shearing strongly regulated the material flux by transporting material from the pro- to the retro-side. More recently, *Yamato et al.* [2007], pointed out, by a combination of petrological data and numerical models, the interrelation between exhumation paths and plate (de)coupling conditions. In addition, the above models are considered very successful in explaining the asymmetric wedge shape and exhumation pattern of the Central Alps as recorded along the NFP-20 east transect [*Schmid et al.*, 1996] (Fig 4.11).

Although these simple models significantly broadened our view on mountain building in a convergent setting, they are strongly driven by fixed boundary conditions, and therefore have some important shortcomings. The predefined and static S-point does not allow for dynamic interactions between the ductile layers of both plates, and the

fixed upper plate behaves as a rigid undeformable unit. Also the crustal response in terms of shear localization and influx of crustal material from the subducting plate is largely governed by the S-point. Furthermore, the applied amount of shortening within these models was limited, and dynamic variations appearing with ongoing shortening, such as increasing buoyancy owed to a reduced slap-pull force, were introduced by the modelers themselves.

From this point onwards, we aim for lithosphere-scale modelling focusing on wedge development in a more dynamic setting of plate convergence, including deformation of the viscous lithosphere. We also want to determine the effect of increasing plate coupling with ongoing shortening on mantle lithosphere subduction and its implications for wedge build-up. In addition, varying the rheology of the lower crust and mantle lithosphere probably affects the degree of plate coupling, and therefore the shape and dimension of the crustal wedge.

4.3 Model design and scaling

The experimental set-up and the properties of the used material are shown in Figure 4.2 and Table 4.1. The physical parameters are balanced to nature by respecting the scaling principles presented by *Weijermars and Schmeling* [1986].

In experiment 4-1, a *very* weak silicone putty mixture was used along the plate interface and to a limited extent within the lower plate representing very weak lower crust (Fig. 4.2). The viscosity of this silicone putty was even lower than the weak putty used in experiments 4-2 to 4-4 (see Tab. 4.1). The "strong" lower crust and mantle lithosphere were made of similar putties described in Chapter 3. In experiment 4-2, the entire lower plate contained a weak lower crust. This might be an overestimate for "cold" orogens such as the Alps where lower crust was only weakened along narrow horizons, but not for "hot" orogens like for instance the Mozambique Belt where horizontal flow affected a vast area of exposed granulites [e.g. *Fritz et al.*, 2009]. However, in both scenarios a (partial) reduction of lower crustal strength could already caused decoupling between lower crust and relative cool upper crust. In experiment 4-3, the thickness of the overlying upper crust was slightly increased (12 mm) in order to investigate the role of a high vertical load on plate decoupling and wedge formation (Fig. 4.2). Furthermore, the influence of weak mantle lithosphere on slab deformation, continental subduction and plate (de) coupling has been examined in experiment 4-4. This experiment consisted of two set-up domains. The 4a domain comprised a weak mantle lithosphere in both the upper- and lower plates, whereas the 4b domain only contained weak mantle lithosphere in the lower plate. Both domains had a weak lower crust within their lower plate.

Figure 4.2a (next page) Experimental set-up. A three layer continental lithosphere overlays a low viscosity asthenosphere within a plexi-glass tank. The inclined weak zone (red) within the mantle lithosphere localizes and lubricates subduction of the mantle lithosphere (see also Chapter 3). The upper plate is pushed by the moving wall (arrow). Coloured top layer consists of feldspar sand and represents upper crust. Note that experiment 4-4 is laterally divided into a 4a and 4b domain.

Exp. 4-1: *Very weak limited lower crust*

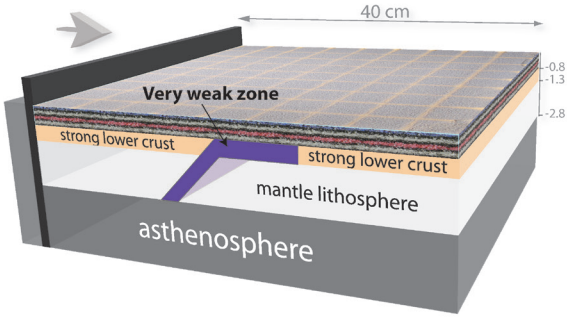

Exp. 4-4: *Weak mantle lithosphere*

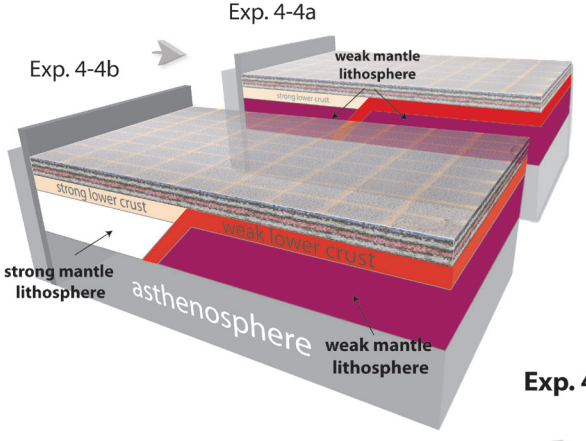

Exp. 4-2: *Entire weak lower crust*

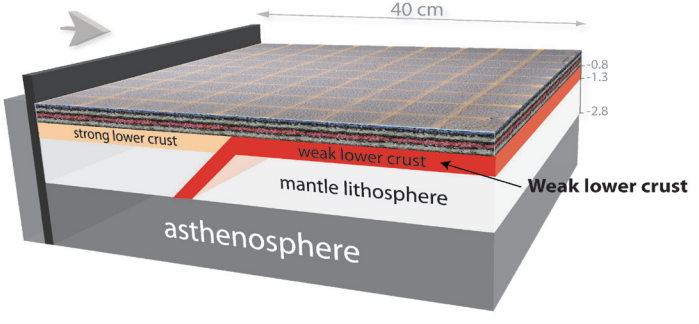

Exp. 4-3: *Thicker upper crust*

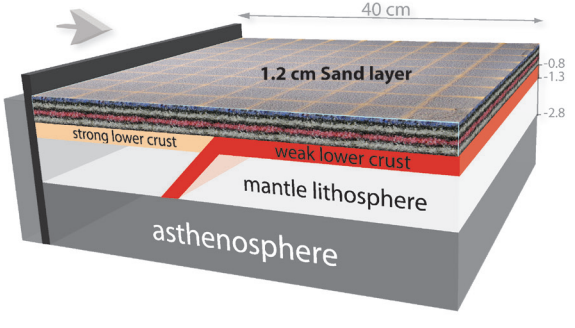

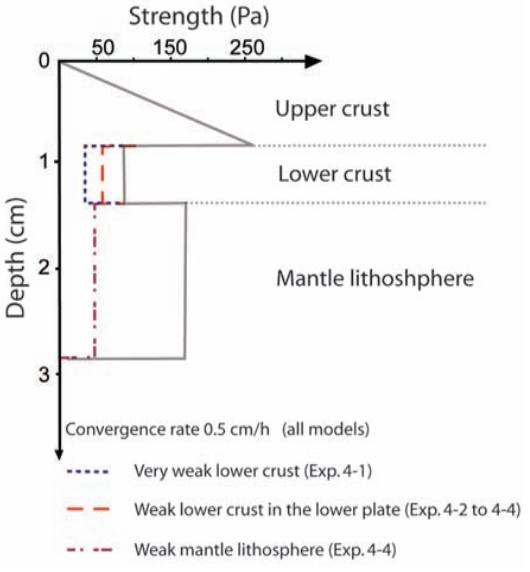

Figure 4.2 (continued) b) Calculated strength profiles for the different set-ups.

Layer	Analogue material	Density ρ (kg/m³)	Coefficient of friction μ	Viscosity η (Pa s)	Power n
Upper crust	Feldspar sand	1300	0.7 35 Pa (Cohesion)		
Lower crust	Silicon mix 1 (PDMS)	1400		$4.8 \cdot 10^4$	1.9
Weak plate interface + weak lower crust	Silicon mix 3 (Rhodorsil gum)	1400		$1.8 \cdot 10^4$	1.3
Very weak lower crust	Silicon mix 4 (Rhodorsil gum)	1480		$9.7 \cdot 10^3$	1.3
Mantle lithosphere	Silicon mix 2 (PDMS)	1500		$1.2 \cdot 10^5$	1.7
Weak mantle lithosphere	Silicon mix 5 (PDMS)	1500		$1.6 \cdot 10^4$	1.3
Asthenosphere	Sodium polytungstate solution	1450		1.2	

Table 4.1 Physical properties relevant for scaling of the experimental materials.

4.4 Modelling results

Short summaries of each experiment based on the analysis of top view images, surface scans, and cross sections, are presented. The experiments are classified according to the investigated variables: *very* weak limited lower crust, entire weak lower crust within the lower plate (incl. thick sand model), and weak mantle lithosphere. A comparison between experiments and their interpretations in terms of (de)coupling conditions will be discussed in section 4.5.

4.4.1 Experiment with "very weak" limited lower crust

Experiment 4-1

Crustal deformation initiated by the development of a symmetrical pop-up structure above the predefined plate boundary (Fig. 4.3). After 6% Bulk Shortening (BS) a second, asymmetric pop-up formed above the transition between very weak lower crust and strong lower crust within the lower plate. This second pop-up subsequently evolved into a foreland directed thrust accommodating and localizing most of the residual crustal shortening. From the surface scans it can be seen that both the elevation of the first pop-up and the width of the entire orogen remained roughly constant throughout the model run (Fig. 4.3c). From 10% to 15% BS the topography of the second pop-up increased, but in turn decreased between 15-25% BS. During this final episode, the lower plate underwent lowering and widening of the adjacent "foreland-type" basin; meanwhile its interior was slightly uplifted. Note that the interior of the upper plate remained at a constant level. The cross-section reveals a large amount of subduction (Fig. 4.3b). The upper crust, which initially overlaid the very weak lower crust, detached completely from the subducting weak lower crust and mantle lithosphere. Hence, this accretionary-like wedge was solely composed of upper crustal material derived from the lower plate. The wedge remained decoupled from the subducting lower plate by a thin film of weak silicone at the base of the major fore-thrust (nr. 3). At deeper levels, lithosphere made of strong lower crust subducted coherently into the asthenosphere. Furthermore, the upper plate suffered gentle bending and updoming, which suggestively result from an increased coupling after the consumption of very weak lower crust.

Figure 4.3 (facing page) Final top view and cross-section of experiment 4-1 after 25% of bulk shortening. Arrows refer to shortening direction and dashed line to profile location. Interpreted thrust faults are chronologically numbered. Within the cross sections, white colour corresponds to mantle lithosphere, beige to lower crust, dark purple to the weak zone material, and different colours of sand to the upper crust. Dark line represents the Moho discontinuity. A DEM overlies the cross-sections showing the final elevation (see scale bar). The lower images show elevation graphs revealing the topographic evolution along the profile after different amounts of bulk shortening. Numbers along the axis are in millimetres.

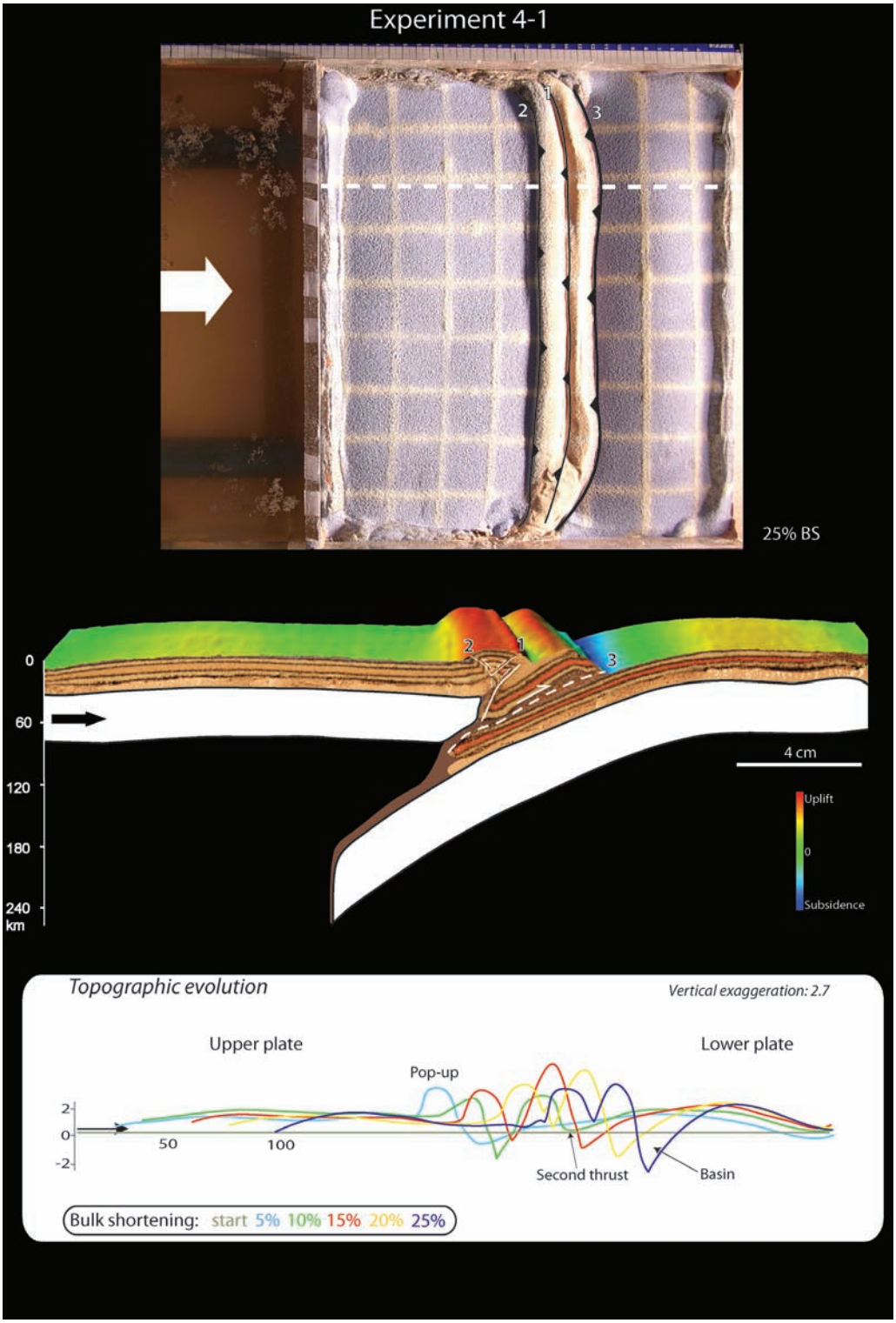
Experiment 4-1
1
2
3
25% BS
0
60
120
180
240
km
4 cm
Uplift
0
Subsidence
Topographic evolution
Vertical exaggeration: 2.7
Upper plate
Lower plate
Pop-up
2
0
-2
50
100
Second thrust
Basin
Bulk shortening: start 5% 10% 15% 20% 25%

4.4.2 Experiments with an entire weak lower crust of the lower plate

Experiment 4-2

Crustal deformation along a first pop-up above the plate interface was directly followed by the propagation of several fore-thrusts onto the lower plate (Fig. 4.4a). With ongoing shortening, some of these early structures were overridden by the advancing upper plate. Until the end of shortening, newly formed thrusts on the lower plate continued widening the orogen.

The surface scans point out an early-stage of wedge widening and thrust-related uplift. While from 15% BS onwards topography increased more rapidly (Fig. 4.4c). We can distinguish between regions along the orogens strike where this rapid uplift affected mainly the lower plate-directed thrust sheets (e.g. profile 1), and regions where uplift was more restricted to the first pop-up (e.g. profile 2). In both profiles, the interior of the lower plate was only modestly uplifted. In contrast, the interior of the upper plate remained at a constant elevation, while close to the orogen the plate was gradually uplifted. Furthermore, a foreland-type basin formed early, but became finally incorporated into the developing wedge. No significant basins were formed during a later stage.

Cross-sections display a large amount of mantle lithosphere subduction overlain by an asymmetric crustal wedge located on the lower plate (Fig. 4.4b). The plate interface remained lubricated by weak lower crust, and the downgoing mantle lithosphere decoupled along the Moho, while the upper plate mantle lithosphere slightly thickened. Note that most of the weak lower crust remained at crustal levels. Within the wedge, lower crustal material fulfilled the role of lubricator along thrust sheets (profile 1), or was thickened and extruded vertically (profile 2). Hence, the ductile lower crust showed significant thickness variations, which caused upper crustal deformation to differ along strike as well. Profile 1 is namely characterized by a high amount of individual thrust sheets extending far onto the lower plate. In profile 2 pop-ups are symmetric (box-type), undergoing less horizontal shortening in the foreland region, but more retro-shearing occurred. Deformation of, the mantle lithosphere of the upper plate is restricted to the collision zone where it is slightly thickened.

Experiment 4-3 (12 mm thick sand layer)

Crustal deformation above the plate interface initiated along a major fore thrust, and was coeval with the development of small, lateral discontinuous back thrusts (Fig. 4.5a). At ~6% BS deformation shifted to the lower plate by the formation of a pop-up. With ongoing shortening several fore-thrusts propagated towards the foreland, and the upper plate started to override older structures. After 10% BS, topographic scans recorded the initiation of upper plate subsidence near the plate boundary including the first pop-up, meanwhile the interiors of both the upper- and lower plates were strongly up domed

Figure 4.4 (facing page) Final top view and cross-section of experiment 4-2 after 25% of bulk shortening. Top view colours refer to initial lower plate (blue) and upper plate (beige). Within the cross sections, white colour corresponds to mantle lithosphere, beige to lower crust, red to weak lower crustal material, and different colours of sand to the upper crust. The lower images show elevation graphs revealing the topographic evolution along the profiles after different amounts of bulk shortening.

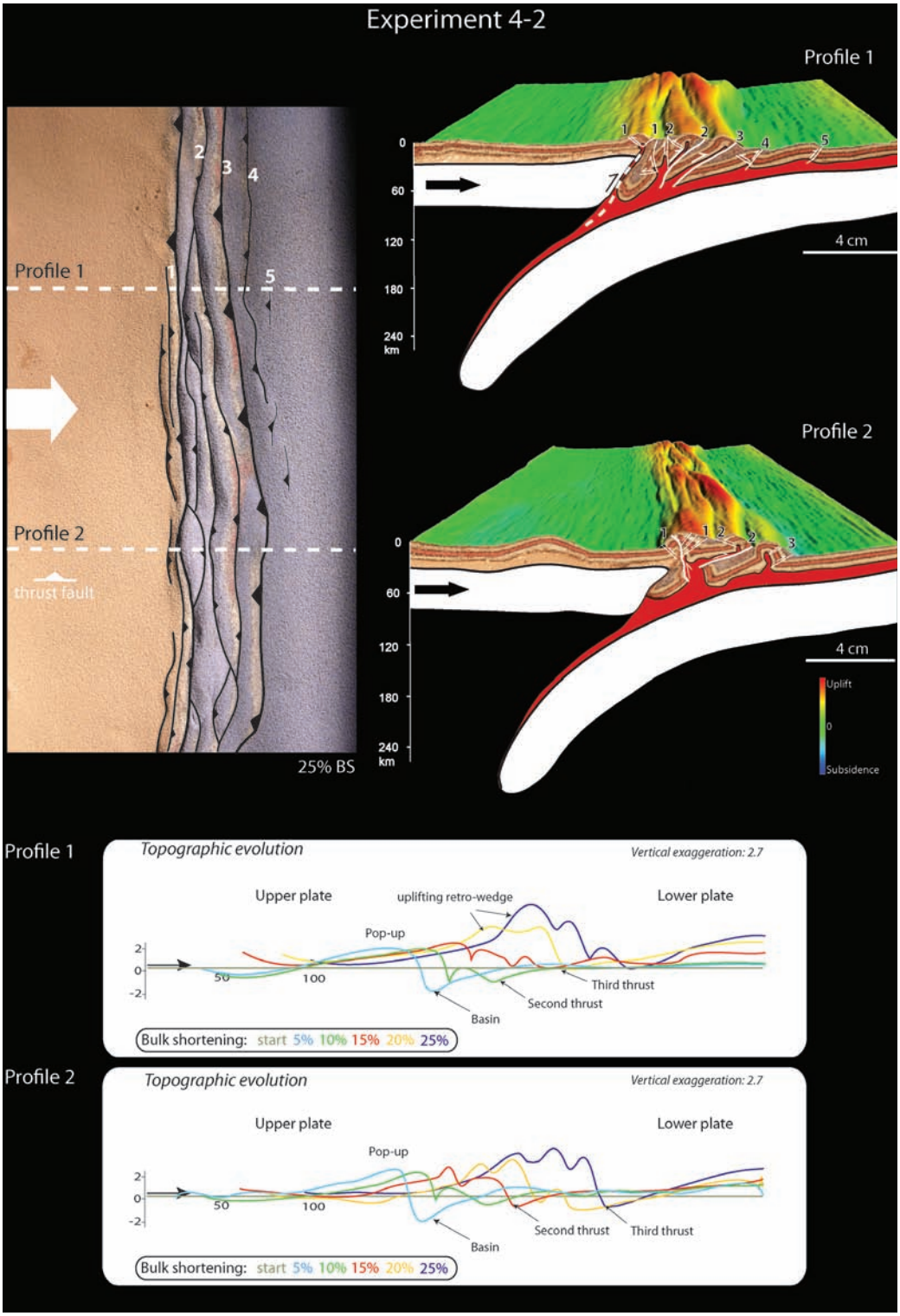
Experiment 4-2
Profile 1
Profile 2
thrust fault
25% BS
0
60
120
180
240
km
4 cm
Uplift
0
Subsidence
Profile 1
Topographic evolution
Vertical exaggeration: 2.7
Upper plate
uplifting retro-wedge
Lower plate
Pop-up
Third thrust
Second thrust
Basin
Bulk shortening: start 5% 10% 15% 20% 25%
Profile 2
Topographic evolution
Vertical exaggeration: 2.7
Upper plate
Lower plate
Pop-up
Second thrust
Third thrust
Basin
Bulk shortening: start 5% 10% 15% 20% 25%

(Fig. 4.5c). Cross-sections portray that subduction was only modest compared to the previous experiments (Fig. 4.5b). Near the plate interface the upper plate curved down as it remained partly attached to the subducting slab separated by only a thin layer of weak lower crustal material. Despite the weak lower crust thickened below the orogenic wedge, no significant crust-mantle decoupling is observed. Note that the lateral termination of lower crustal thickening coincided with the frontal thrust at upper crustal levels. Besides lower plate vergent thrusts, the crustal wedge comprised a pop-down structure near the plate interface. This crustal fragment acted as a strong coherent unit as it forced separation between strong lower crust and mantle lithosphere in the upper plate (see profile 2). It might be plausible to assume that the crustal pop-down caused locking of the subduction zone by reshaping the plate interface and forced down bending of the upper plate. Hampering of subduction is also expressed by updoming of both plate interiors and subsidence near the plate boundary.

4.4.3 Experiments with weak mantle lithosphere

Within experiment 4-4 the induced lateral variation between weak- and regular mantle lithosphere in the upper plates resulted in different deformation patterns. We therefore describe the domains separately (4a, 4b), and subsequently zoom in on the transition zone dividing the domains.

Experiment 4- 4a. Weak mantle lithosphere in both upper- and lower plates

Crustal deformation as recorded by top-view images is roughly similar to experiment 2: A pop-up formed above the plate boundary followed by foreland-directed thrusting mainly onto the lower plate (Fig. 4.6a). In addition, from 15% BS onward small thrusts appeared within the interior of the upper plate as well.

Topographic profiles show uplift correlated with thrusting inside a foreland-type basin at 10% BS (Fig. 4.6c). As foreland-directed thrusting progressed, the orogen underwent uplift and widening, meanwhile the basins slightly narrowed. From 15% BS onward, topography became distributed asymmetrically with a relative high elevated first pop-up (retro-side). This uplift was contemporaneous with updoming of the lower plate, while upper plate topography remained only minor.

The cross-sections disclose less subduction with respect to the other experiments (Fig. 4.6b). A significant amount of lower crust remained attached to the thickened slab. Consequently, less lower-crustal material was incorporated into the orogenic wedge, compared for instance to experiment 4-2. Also the upper crustal response differs from experiment 4-2 in a way that thrust spacing and displacements were relatively low. This resulted in a narrower and lower orogenic wedge. Despite modest displacement, a well developed retro-shear accommodated from 20% BS onward uplift and shearing onto the

Figure 4.5 (facing page) Final top view and cross-section of experiment 4-3 after 25% of bulk shortening. Note the thick sand layer compared to the other experiments. Within the cross sections, white colour corresponds to mantle lithosphere, beige to lower crust, red to weak lower crustal material, and different colours of sand to the upper crust. The lower images show elevation graphs revealing the topographic evolution along the profiles after different amounts of bulk shortening.

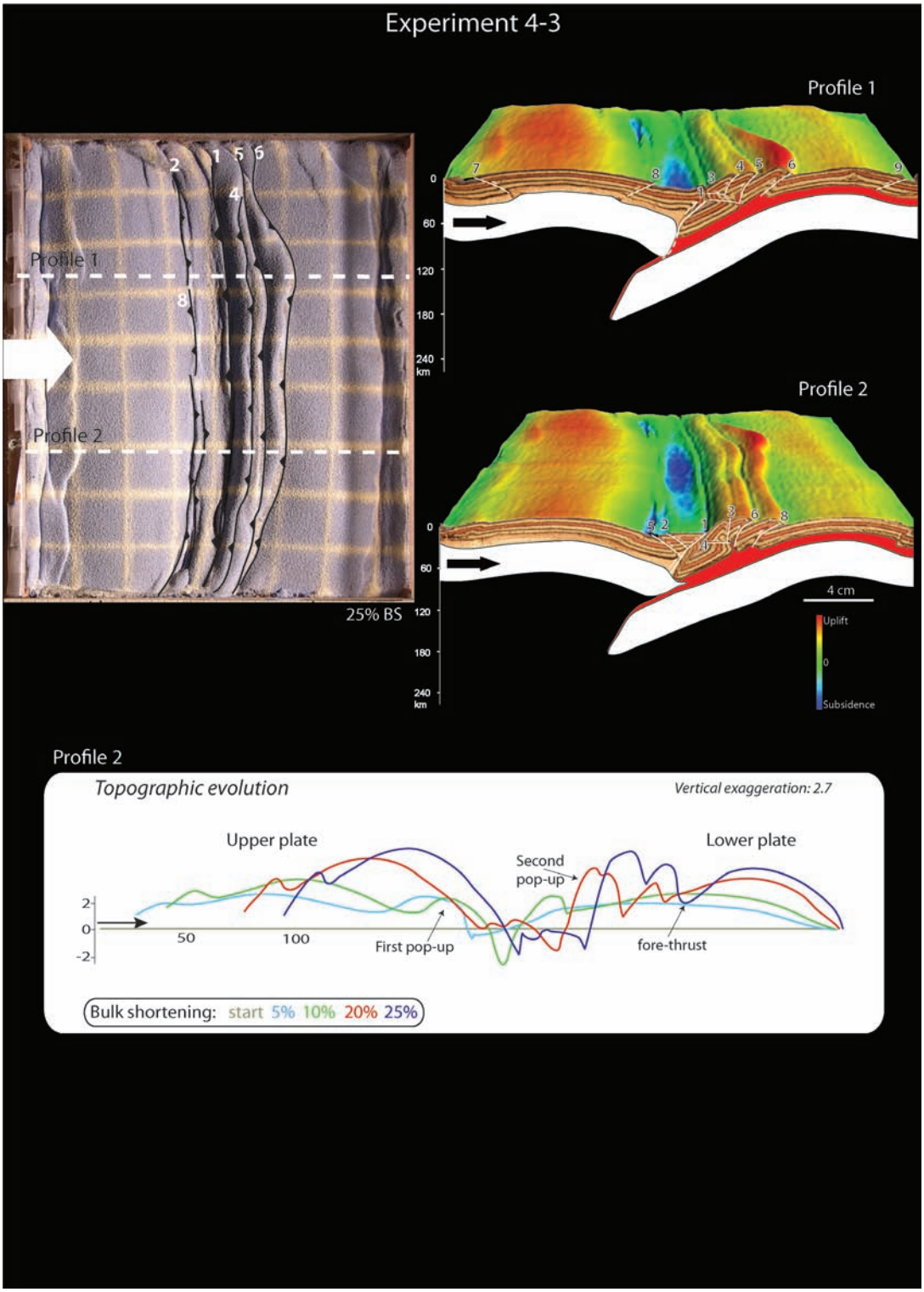
Experiment 4-3
Profile 1
Profile 2
25% BS
0
60
120
180
240
km
4 cm
Uplift
0
Subsidence
Profile 2
Topographic evolution
Vertical exaggeration: 2.7
Upper plate
Lower plate
Second pop-up
First pop-up
fore-thrust
2
0
-2
50
100
Bulk shortening: start 5% 10% 20% 25%

upper plate. Hence, some wedge material became "re-uplifted" along the retro-shear after transient subsidence, whereas the remaining crustal material subducted to mantle depths.

Experiment 4-4b. Weak mantle lithosphere in lower plate only

Top-view images show initial deformation along the plate boundary by the formation of a major fore-thrust overriding the lower plate (nr. 1, Fig. 4.6a). With ongoing shortening pop-ups and fore-thrusts formed in sequence onto the lower plate. Early structures formed on the lower plate were eventually overridden by the major fore thrust (nr. 1).

The topographic profiles display several evolving pop-ups roughly all measuring similar elevations, which underwent only minor subsidence during further widening and shortening of the wedge (Fig. 4.6c). No late-stage (>15% BS) uplift occurred within the wedge as observed in experiment 4a. In addition, the foreland basins became narrower and uplifted; meanwhile doming elevated the lower plate.

The cross-sections reveal a larger amount of subduction compared to experiment 4-4a. As far as the lower crust is concerned, roughly half of its initial thickness remained attached to the subducting slab, while the other half was scraped of and thickened below the orogenic wedge. The upper crust deformed similarly by the formation of closely spaced pop-ups and fore-thrusts involving little lower crust material. However, retro-shears and upper plate deformation were absent.

Experiment 4-4: the transition zone

The transition zone between the domains is marked by a small offset of the first pop-up. The offset can be partly explained by a lateral difference in the amount of slip along the plate interface. As such, internal deformation observed only within the "weak" upper plate (Exp. 4a) reduced plate motion near the plate boundary. In addition, the lateral offset expresses the difference between a well defined back-thrust (or retro-shear) in the weak domain (4a), and its absence in the strong domain (4b). Note however that the "retro-side" or first-pop-up crosses the transition zone. This indicates interaction between the adjacent domains, and is probably caused by a certain degree of lateral coupling between the domains and subducting slabs. We will elaborate further on the effects of lateral coupling between subduction domains in Chapter 5.

Figure 4.6 (facing page) Final top view and cross-section of experiment 4-4 after 25% of bulk shortening. Colours in top view image relate to subduction domains: blue for upper plate, pink for upper plate, beige for weak upper plate. Within the cross sections, white colour corresponds to mantle lithosphere, purple to weak mantle lithosphere, beige to lower crust, red to weak lower crustal material, and different colours of sand to the upper crust. The lower images show elevation graphs revealing the topographic evolution along the profiles after different amounts of bulk shortening.

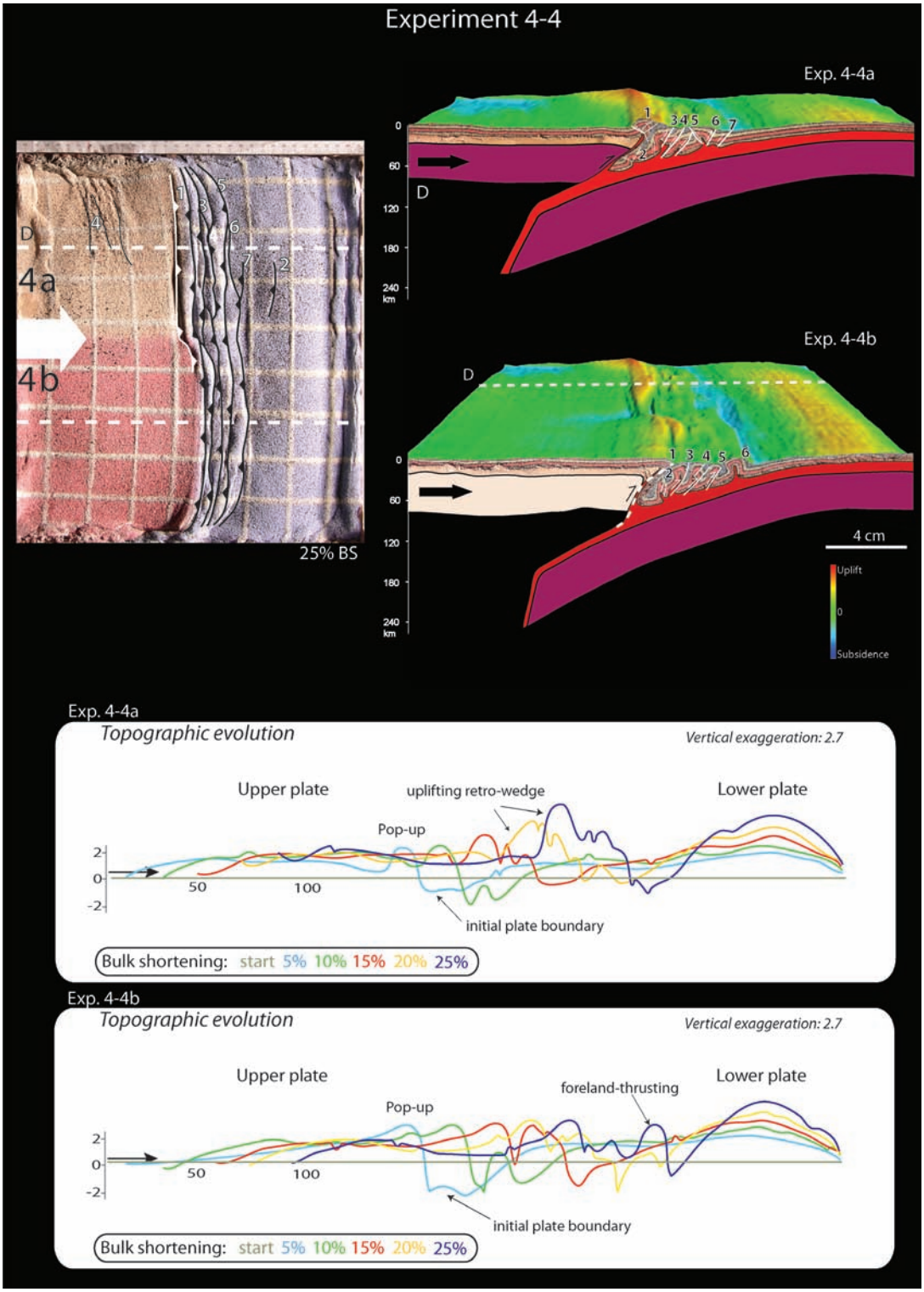
Experiment 4-4
Exp. 4-4a
Exp. 4-4b
4a
4b
D
25% BS
0
60
120
180
240
km
4 cm
Uplift
0
Subsidence
Exp. 4-4a
Topographic evolution
Vertical exaggeration: 2.7
Upper plate
uplifting retro-wedge
Lower plate
Pop-up
initial plate boundary
Bulk shortening: start 5% 10% 15% 20% 25%
Exp. 4-4b
Topographic evolution
Vertical exaggeration: 2.7
Upper plate
foreland-thrusting
Lower plate
Pop-up
initial plate boundary
Bulk shortening: start 5% 10% 15% 20% 25%

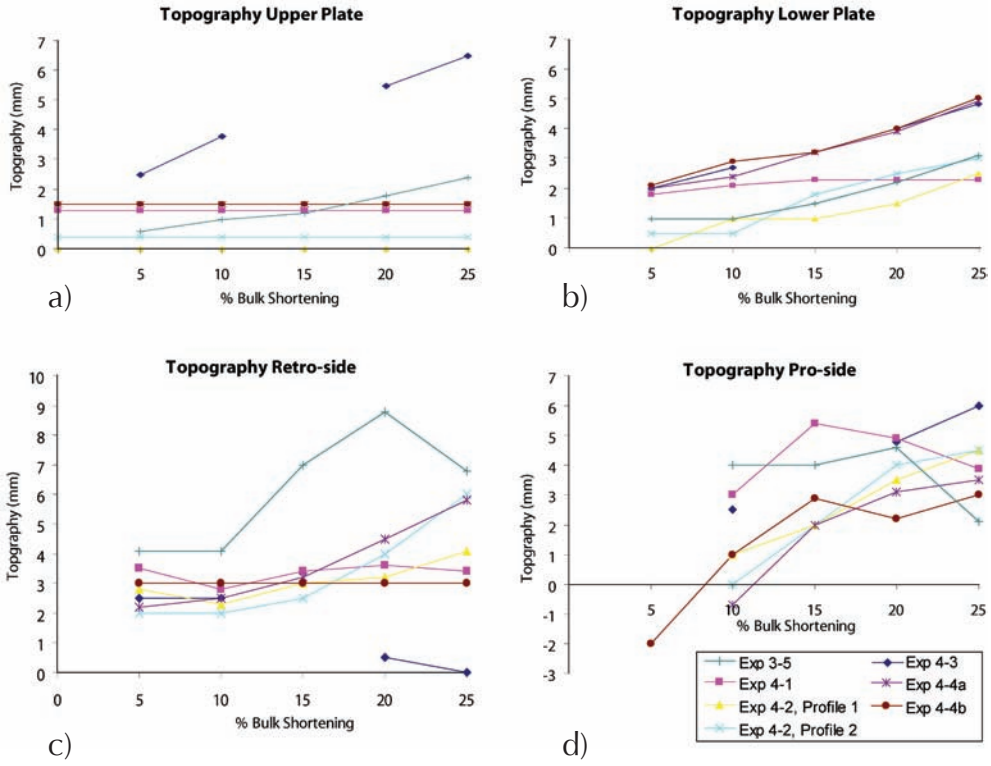

Figure 4.7a Topographic evolution of experiments presented in this chapter including experiment 3-5 (see text for details).

4.5 Comparison and interpretation of experimental results

4.5.1 Topography development

The evolving topography of the various experiments is displayed and summarized in Figures 4.7a-b. These graphs show topography in relation to the amount of bulk shortening for four different locations in each experiment. Topography within graphs A and B refers to the highest points of the two plate interiors, whereas C and D refer to the highest elevations from the first pop-up domain (retro-side) and from the wedge domain overlying the lower plate (pro-side), respectively.

Graph A displays uplift of the upper plate interiors for experiments with a limited weak lower crust and experiments with a relative thick upper crust (exp. 3-5 and 4-3). Within the other experiments the upper plate remained flat. In contrast, the lower plate topography, plotted in graph B, exponentially increased with progressive shortening. Only in the experiment with a very weak limited lower crust (exp. 4-1) uplift of the lower plate stagnated around 15% BS (exp. 4-1).

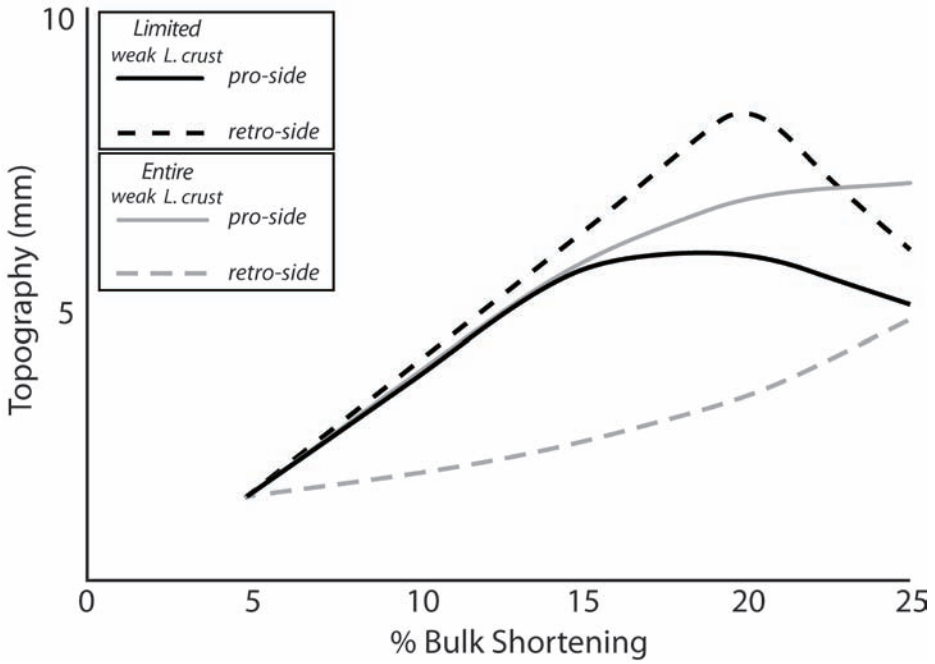

Figure 4.7b Generalized topographic trends derived from Figure 4.7b.

Within the wedge domain, graph C discloses trends of constant, increasing, and decreasing uplift within the retro-side. In experiments without retro-shears (exp. 4-1 and 4-4a) topography of the first pop-up remained constant. Experiments with clearly developed retro-shears typically show increased uplift rates between 10% and 15% BS (graph C). Final subsidence (>20% bs) of the first-pop was monitored in experiments with a limited weak lower crust or a relative thick upper crust (exp. 3-5 and 4-3). The pro-side surface topography, shown in graph D, was uplifted in each experiment between 5% and 15% BS. However, from 15-20 % BS onwards experiments with a limited lower crust (exp 4-1 and 3-5), recorded subsidence of the pro-side. Also where the lower plate consisted of weak mantle lithosphere wedge topography slightly lowered during final shortening (exp 4-4b). On the contrary, extending the weak lower crust throughout the lower plate resulted in ongoing wedge uplift, albeit with a reduced uplift rate from 20% BS onward.

The uplift trends observed in the wedge domain are summarized in Fig. 4.7b and categorized according to the investigated parameters. In general, in experiments with a limited weak lower crust, rapid uplift of both the pro- and retro-sides was followed by final subsidence of first the pro- (>15% BS) and then the retro-side (>20% BS). In contrast, in experiments with an entire weak lower crust in the lower plates, the pro-side was rapidly uplifted but the retro-side was hardly uplifted. Nevertheless, with progressive shortening uplift rates in the pro-side finally decreased, meanwhile uplift rates in the retro-side increased (Fig. 4.7b).

4.5.2 Wedge classification

The experiments reveal a variety of orogenic wedge build-up (Fig. 4.8). With a brief comparison between the experiments, including experiment 3-5 from the previous chapter, we intent to classify the different wedge geometries according to: a) size, b) symmetry, and c) pro-vergent versus doubly vergent. How these wedge characteristics relate to the degree of plate coupling and crust-mantle coupling will then be discussed in the next section.

The effect of a weak layer on the shape of the wedge becomes evident by comparing experiments with a *limited-* or an *entire*-weak lower crust (Fig. 4.8). A limited amount of weak lower crust (exp. 4-1 and exp. 3-5), results in a narrow wedge localized at the plate boundary. Outward growth is restricted to the extent of weak lower crust, which acts as decollement layer separating upper crust from the underlying mantle lithosphere. Only in the scenario of an entire weak lower crust, the wedge can widen by the formation of several fore-thrusts onto the lower plate (exp. 4-2 and 4-4). Hence, we can distinguish between *narrow wedges* and *wide wedges*.

The internal structure of *narrow wedges* strongly differs according to the strength of the lower crust (Fig. 4.8). Very weak silicone along the plate interface results in localization of deformation along a major fore thrust. The wedge remains *asymmetric,* consists of lower plate material and mainly overlies the lower plate (Fig. 4.8). By slightly increasing the silicone putty strength from “very weak” to “weak”, (Fig. 4.10), crustal deformation propagates further onto the lower plate by the formation of a second pop-up (exp. 3-5) (Fig. 4.9a stage 2). Remember that crustal deformation remains restricted to the extent of weak lower crust. Finally, with ongoing mantle lithosphere subduction the wedge becomes *symmetric* and crustal deformation localizes along a pro- and retro-shear (Fig. 4.9a, stage 3). Activation of retro shearing initiates around 10-15% BS as can be deduced from uplift of the first pop up (Fig. 4.7c). *Wide wedges* can be subdivided according to their internal structure in terms of the presence of a pro- and retro-side. In Figure 4.9b the evolution of a wide wedge is sketched based on our model results. After the formation of a first pop-up above the plate interface, deformation propagated onto the lower plate by foreland-directed thrusting (stage 2). During this stage the first pop-up is inactive as indicated by the stable topography (Fig. 4.7c). Note that experiment 4-4b remains within stage 2 for the entire run. Experiment 4-2 and 4-4a, however, underwent at about ±15% BS uplift of the first pop-up, presumably underlain by the initiation of retro-shearing (stage 3), meanwhile pro-shearing onto the lower plate continued. Hence, we can distinguish between experiments generating *doubly wedges*, and experiments with only *pro-wedges* (Fig. 4.8). Furthermore, by comparing the wedges of experiments 4-2 and 4-4a-b two types of pro-shearing can be recognized (Fig. 4.8). In experiment 4-2, thrust sheets are displaced far onto the lower plate and generate high topography. While in experiment 4-4, shortening resulted in symmetric, narrowly spaced, box-type pop-ups with only modest elevation (Fig. 4.7d). Based on cross-sections, the behavior of the underlying lower crust seems to underlie these distinctive wedge responses, as lower crust subducts or only thickens below the wedge in exp. 4-4, but is incorporated within the upper-crustal-wedge in experiment 4-2. In order to explain these wedge distinctions we need to place wedge formation in a larger context, and discuss the behavior of both viscous layers in the following section.

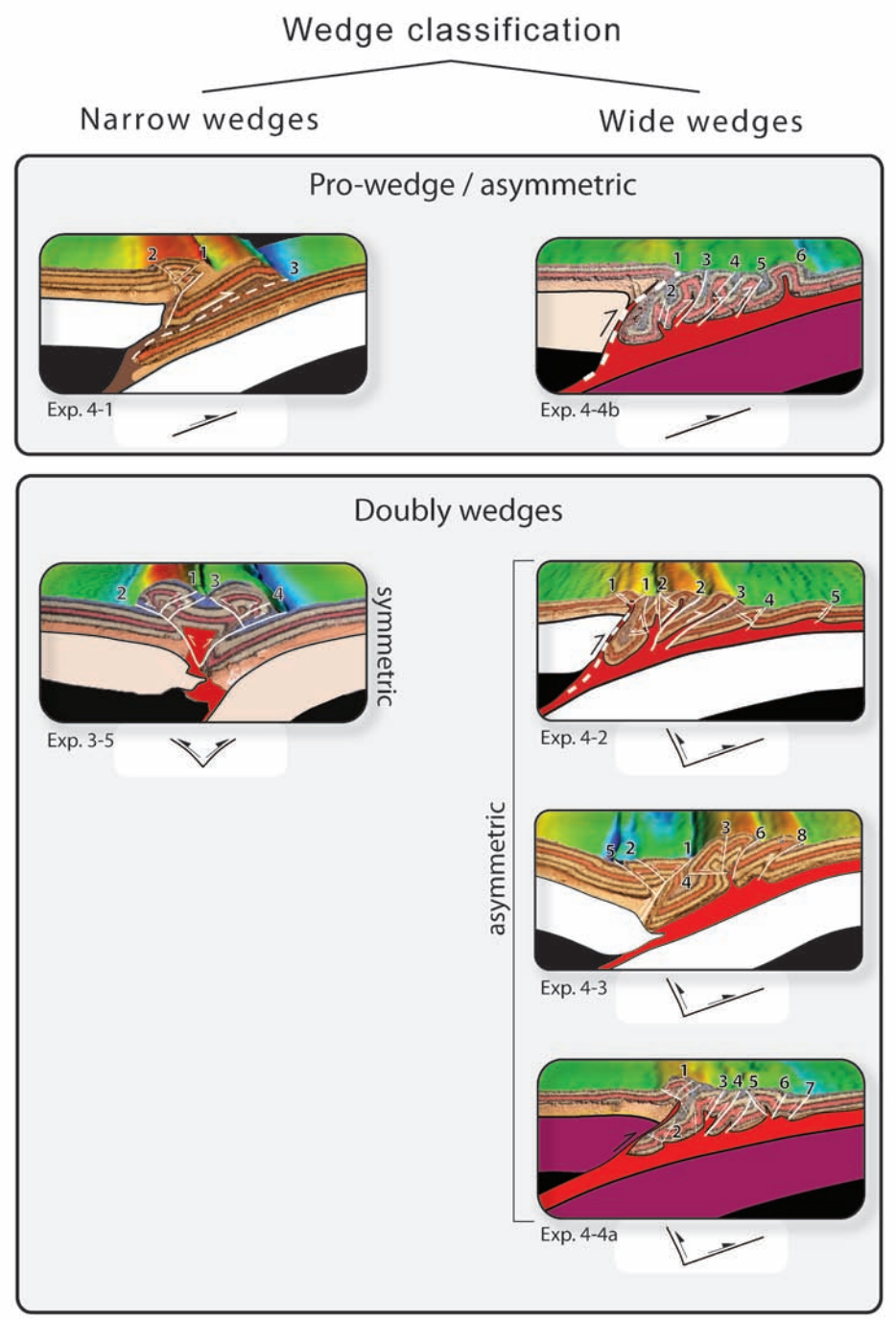

Figure 4.8 Zoom-in on the experimental cross-sections highlighting the variety of modelled wedge geometries. The bottom sketches indicate whether displacement occurred along pro- and/or retro shears.

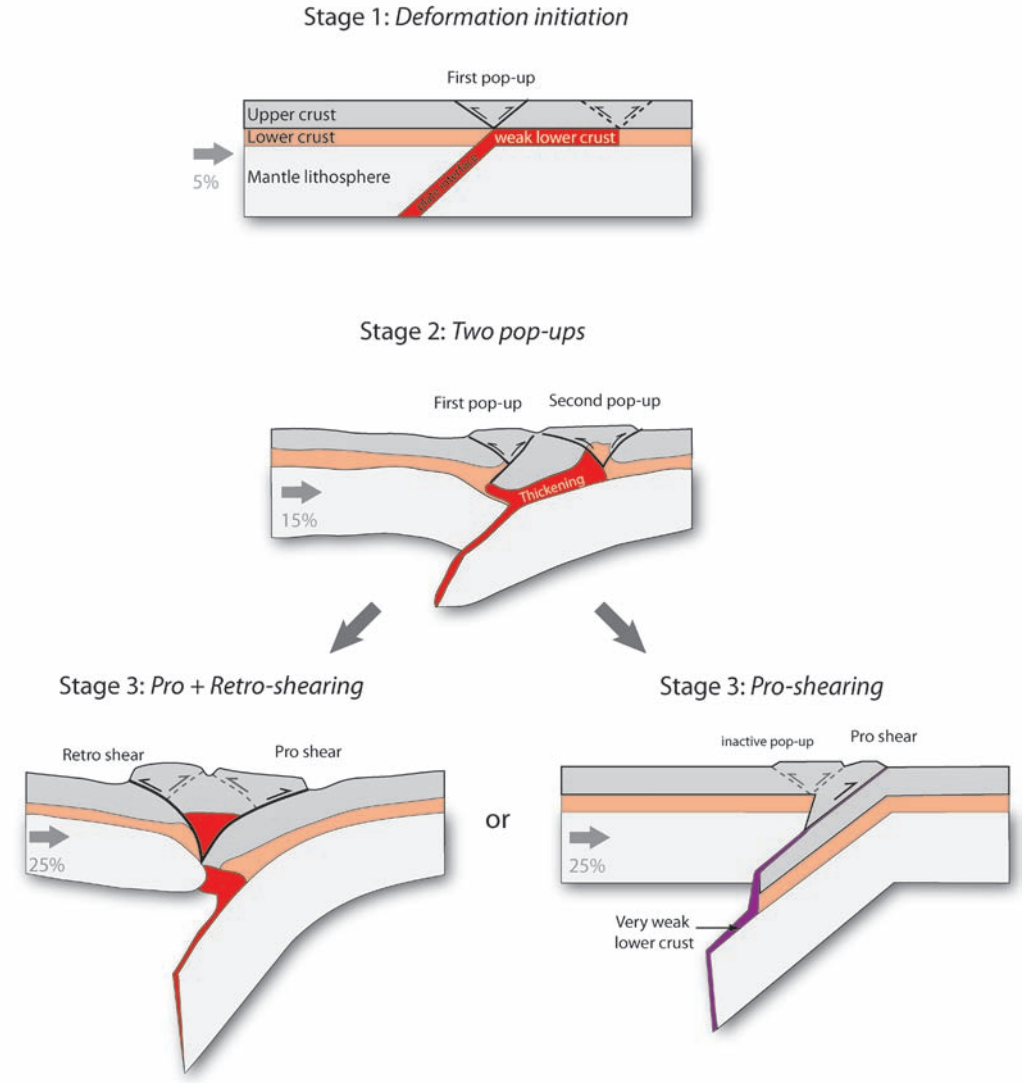

Figure 4.9a Sketched deformation stages of experiments with narrow wedges based on top view, surface scans, and final cross sections. The left and right panels are based on experiment 3-5 and experiment 4-1, respectively. Note that the inner structure of stage 1b is only a rough estimate.

4.5.3 Expressions of plate (de)coupling

To investigate the role of plate (de)coupling on the style of plate collision the expression of these dynamic conditions within the experiments need to be reconciled. From the previous chapter we learned that plate coupling can be inferred from features such as intra-plate deformation, down drag of both plates near the plate boundary, and cessation of subduction. In this section we follow this line of plate (de)coupling determination based on intra plate deformation, but subsequently discuss how an orogenic wedge relates to these (de)coupling conditions in terms of geometry and surface topography.

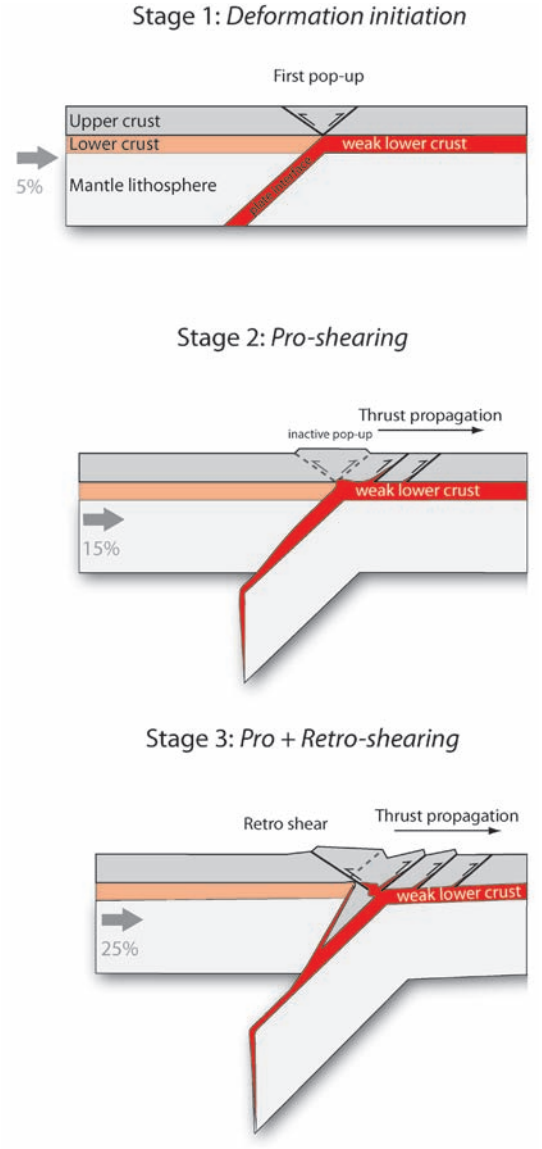

Figure 4.9b Sketched deformation stages of experiments with wide wedges based on top view, surface scans, and final cross sections. Note the reactivation in terms of back thrusting and uplift affecting the first pop-up at stage 3.

As such, the above monitored wedge responses might directly reveal plate (de)coupling conditions.

4.5.4 Degree of plate coupling and intra-plate deformation

Intra-plate deformation indicating plate coupling is present in experiments 3-5, 4-3 and 4-4a. The degree of plate coupling, however, seems to differ among these experiments. The gradual uplift trends observed in experiment 4-3 (Fig. 4.7a-b) suggests constant high

plate coupling conditions from the beginning onward. Whereas in experiment 4-4, an increasing uplift rates from 15% BS onward can be interpret as a gradual rise of plate coupling with ongoing shortening (Fig.4.7a-b). In experiment 4-4a, increased plate coupling conditions, which finally led to hampered subduction, could be indirectly inferred from thickening of the subducting slab, and thrusts appearing within the upper plate interior (Fig. 4.6).

4.5.5 Plate decoupling and wedge formation

Within experiments, of which intra-plate deformation suggests plate coupling, subsidence of the crustal wedge was most likely caused by down drag of the viscous layers along the plate contact. As a result of this subsidence, no retro-shearing seem to have affected the wedge during coupled conditions. On the lower plate, however, outward propagation and uplift could still continue, depending on the lateral extent of a weak lower crust. Analyzing the crustal wedges of the remaining experiments allows for recognizing additional kinematic and topographic responses on plate (de)coupling. For instance, in experiment 4-1, gentle folding of the plate interiors indicates plate coupling, which probably arose from the consumption of the very weak lower crust (Fig. 4.3). Coeval subsidence of the orogenic wedge during the final phase of shortening may be related to this increased plate coupling. Similarly, we can attempt to interpret the presence or absence of retro-shears in terms of plate (de)coupling conditions. It was already pointed out that the orogenic wedges observed in experiments 4-2, 4-4a, and 3-5 are characterized by retro-shearing which led to uplift and displacement of the first pop-up onto the upper plate. In this perspective, retro shearing occurred between 10-15% BS, long after the initiation of pro shearing. Moreover, as vertical uplift within the lower wedge domain slowed down at around 20% BS, uplift rates along the retro-shear increased. To explain this type of crustal deformation we propose two possible mechanisms. 1) The increase of retro shearing is an expression of increased plate coupling, or 2) Retro-shearing is a response on thickening of the wedge itself. In experiment 4-2, subduction of mantle lithosphere is ongoing and seemed not hampered as it smoothly delaminates from the crust. As such, the observed transition between active pro-shearing towards more intense retro-shearing should not be considered an expression of increased plate coupling. On the other hand, in experiment 4-4a, plate coupling has been inferred from thickening of the subducting slab. Here, hampering of subduction and the buoyancy of subducted lower crust may indeed be the cause of profound retro-shearing. From these two examples we infer that retro-shearing can occur in settings where the colliding plates are decoupled at mantle depths with mantle lithosphere subduction still ongoing. In this scenario, retro-shearing is more likely a result of crustal thickening due to accretion of crustal material and concomitant indentation at the level of the lower crust or upper mantle. In other words, retro shearing is not necessarily a result of increased plate coupling. Furthermore, retro shearing occurred also in experiment 3-5 around 10-15%, BS when subduction of mantle lithosphere was still ongoing. Here, the relative large amount of retro shearing with respect to lower plate thrusting is likely due to the limited amount of weak lower crust, which restricted fore-thrusts propagation onto the lower plate. After consumption of this weak lower crust (>15% BS), plate coupling increased, causing accelerated uplift in the plate interior and subsidence of the entire symmetric orogenic wedge, but no retro-shearing.

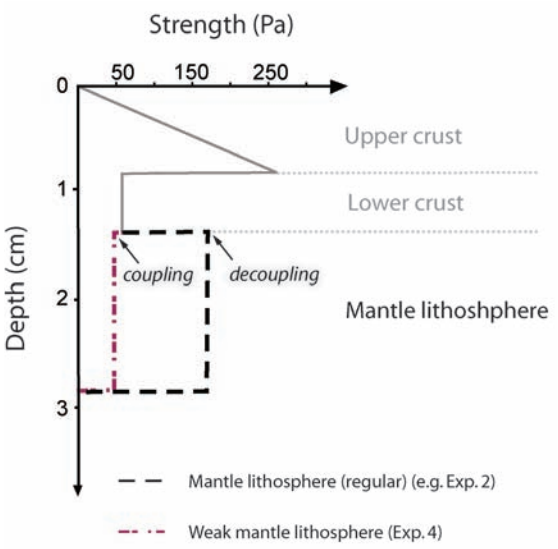

Figure 4.10 Vertical strength profile of the modelled lithospheres. A weak mantle lithosphere with close to similar strength as the overlying lower crust leads to strong coupling along the Moho (e.g. Exp. 4-4), whereas a high strength contrast along the Moho results in decoupling (e.g. Exp. 4-2).

4.5.6 The role of the mantle lithosphere rheology on plate (de)coupling and wedge formation

In this experimental work, the degree of decoupling between the mantle lithosphere and its overlying crust is primarily governed by rheology contrast. As such, the bulk of the lower crust remains attached to the subducting mantle lithosphere, or detaches from the the downgoing mantle, and thus thickens at crustal levels (compare exp.4-2 and 4-4b). These different responses strongly influence wedge build-up and surface topography. For instance, if most of the lower crust detaches from the downgoing mantle lithosphere it can thicken below the wedge or even lubricates thrust sheets and contributes to surface uplift. On the other hand, if lower crust subducts together with the mantle lithosphere, thrust displacement and surface uplift is less. In order to explain lower crustal subduction versus thickening and thrusting, we assign an important role to the mantle rheology, which is two-fold:

First: Relative mantle strength. If the lower crust and mantle lithosphere transition is marked by a high strength contrast both layers separate easily, such as seen in experiment 4-2. On the other hand, only a minor strength contrast between the viscous layers results in stronger coupling (Fig. 4.10), such as in experiment 4-4a-b. In this scenario, the lower crust responds stronger on the downgoing mantle and is less involved in orogenic wedge formation. If almost no strength and density contrast exists between the layers, the lower crust subducts together with the mantle lithosphere as it entirely delaminates from the upper crust along the brittle ductile transition (Exp. 4-4a). The relative mantle strength between the plates is also important for plate decoupling. A relative strong mantle in the upper plate facilitates decoupling of the lower crust from the subducting slab by wedging into the lower plate at Moho levels (exp. 4-2 and 4-4b). This mantle wedging becomes insufficient if the upper plate is relatively weak (exp 4-4a). For example, in experiment

4-4a, the relative strength ratio between the weak lower crust and the weak mantle lithosphere in both plates is too low to induce decoupling by wedging. Hence, the vertical strength contrast within the plate as well as the strength contrast between the colliding plates strongly influences the degree of crust-mantle decoupling, and thus the behavior of the lower crust during wedge formation.

Second: Absolute mantle strength. A weak mantle lithosphere easily deforms internally and is incapable of transferring stress to neighboring regions. Consequently, a weak upper plate is a less effective indenter. Moreover, internal deformation by thickening of weak mantle lithosphere along the plate boundary can even produce high plate coupling conditions. For instance, owed to a relative strong plate coupling, subduction is hampered in experiment 4-4a (Fig. 4.6). As a result, the weak mantle slab thickens and the weak plate interface becomes strongly deformed enhancing hampering of subduction even more.

In summary, a relative weak mantle lithosphere influences wedge build-up as it typically leads to plate coupling conditions by reducing the strength contrast along the plate interface as well as within the plate (Fig. 4.10). On the other hand, reducing the strength of only the lower plate increases the indentation effect of the upper plate, resulting in a larger amount of subduction.

4.6 Orogenic wedges in models and nature

The performed experiments provide an overview of wedge geometries and subduction-styles related to continental collision. Considered the roughness of the model set-ups and the applied parameters, our models were not prescribed for any particular orogen, and their outcomes have to be treated as general lithospheric scale expressions of plate convergence. However, it is remarkable that by changing only a few rheological parameters a strong variety of output geometries could be obtained. This result can be explained by the interplay between plate rheology, plate (de)coupling conditions, subduction-style and wedge build.

These findings are consistent with many analogue and numerical modelling studies, which emphasize coeval continental mantle lithosphere subduction and crustal wedge formation [e.g. *Willett et al.*, 1993; *Beaumont et al.*, 1996]. In this context, already several authors argued for the need of a weak plate interface in combination with (partly) weak lower crust to delaminate the subducting mantle lithosphere [e.g. *Ellis*, 1996; *Ranalli*, 2000; *Toussaint et al.*, 2004b; *De Franco et al.*, 2007; *Tagawa et al.*, 2007; *Burov and Yamato*, 2008; *Faccenda et al.*, 2008b; *Willingshofer and Sokoutis*, 2009]. In many of these studies crustal wedge formation was, however, strongly restricted by boundary conditions. For instance, in Beaumont-type models outward growth of the wedge was limited by the pre-defined S-point. In our experiments no such S-point existed, resulting in more distribution of strain and crust-mantle interaction. Also the flux of crustal material from the subducting plate towards the retro-wedge was in many studies governed by the S-point, whereas in our experiments this material flux was significantly reduced by widening of the pro-wedge. In addition, the role of a weak lower crust was not solely restricted to crust-mantle decoupling horizon, but contributed to wedge formation and surface topography by both thickening and lubricating thrust sheets. As a result and in contrast to many numerical models, wedge geometry and faulting were not pre-constrained [e.g. *Beaumont et al.*, 1996; *Hassani and Jongmans*, 1997; *Tagawa et al.*, 2007].

Many studies modeled fold- and thrust-belts as brittle-ductile systems [e.g. *Lu and Malavieille*, 1994; *Smit et al.*, 2010]. These often two-layer set-ups provided good insights in wedge-build up, but could not account for the dynamic behavior of a convergent plate boundary at lithosphere-scale. However, the role of different plate coupling conditions on wedge response have been treated in several analogue and numerical studies [e.g. *Beaumont et al.*, 1996; *Faccenda et al.*, 2008b; *Willingshofer and Sokoutis*, 2009]. Dynamic changes of plate (de)coupling conditions were often induced from boundary condition, such as introducing buoyant fragments or reducing the slab pull force [e.g. *Beaumont et al.*, 1996], but less from solely shortening. Although Willingshofer and Sokoutis (2009) modeled wedge response and intra-plate deformation in relation to plate coupling, (de)coupling conditions did not vary much within a single experiment. In our models, variations in plate coupling conditions were not only obtained by lateral changes in rheology, but also by deformation of a lateral homogenous lithosphere.

Furthermore, varying (de)coupling conditions revealed that retro-shearing is not necessarily an expression of increased plate coupling conditions, but can also be a result of solely crustal thickening. The retro-wedge can even become mechanically isolated from the shearing of the subducting plate, as indicated from experiments performed by *Faccenda et al.,* [2008a], but also by our model results. Retro-shearing should therefore be considered variable, since its initiation does not necessarily coincide with the onset of continental collision as proposed by i.e. *Beaumont et al.* (1996a) and *Schmid et al.* (1996). Bases on our results, we reject the simple idea that plate decoupling results in one-sided orogens, and coupled plates results in two-sided orogens [*Faccenda et al.*, 2008b; *Willingshofer and Sokoutis*, 2009].

Hence, although our models lacked input from temperature variations, erosion, pre-collisional inherited structures, they provide important general insights on the dependence of a wedge formation and subduction on lithosphere rheology.

4.7 Natural Analogues

The model outcomes show likelihood with several orogens around the world i.e. Pyrenees, Carpathians, and Alps. In the context of this thesis the here presented results can especially contribute to the discussion on the lateral variations in wedge build-up observed within the Alps. We therefore briefly summarize Alpine wedge formation based on studies by *Schmid et al.* [2004] and *Rosenberg and Berger* [2009], and discuss the underlying tectonic mechanisms in the light of our modelling results.

4.7.1 The Central Alps

A short review on the Cenozoic tectonic evolution

The Central Alpine geometry of several stages of orogeny is represented in the NRP-20-east transect (Fig. 4.11 and 4.12a-c). The retro-deformation of the present-day geometry of the transect compiled by Schmid et al. [1996; 2004] provide insights in the mechanisms of orogeny through time (Fig. 4.12). We consider the period of continental collision starting during Eocene times as being most relevant to our modeled time interval. Folding and exhumation of the Penninic units to crustal levels took place by stacking during oceanic subduction mainly before the Oligocene. However, the bulk of the Penninic

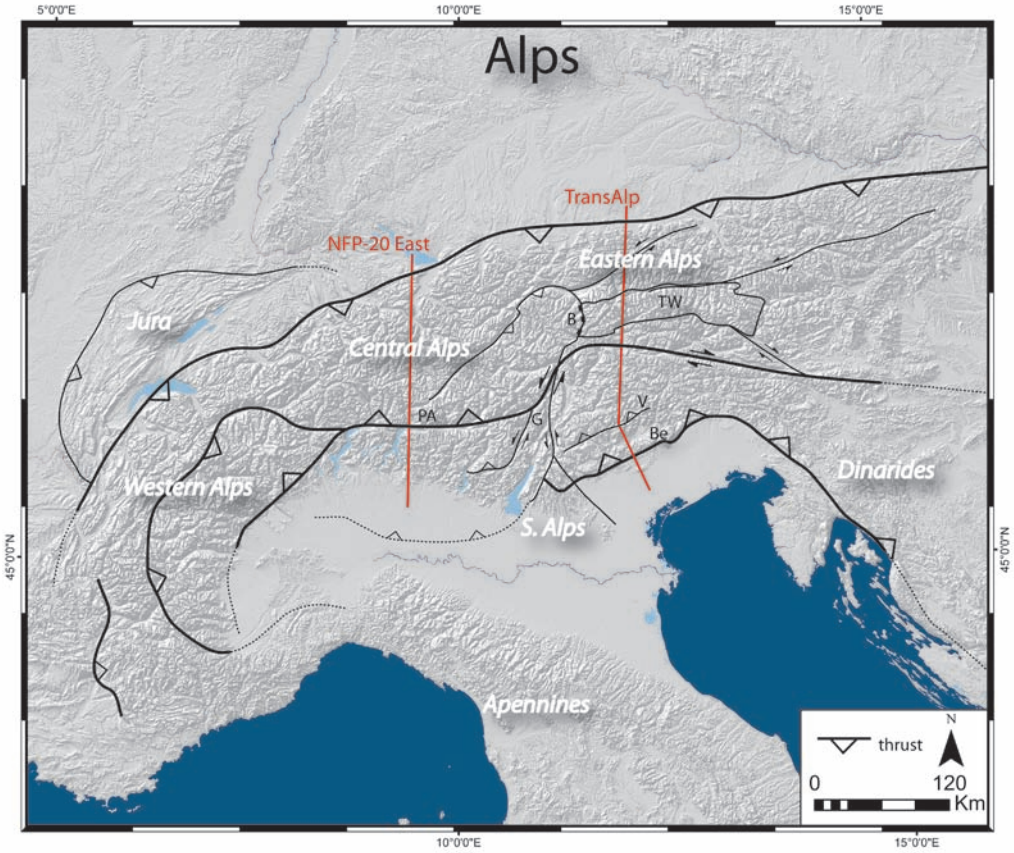

Figure 4.11 Tectonic map displaying the main Alpine faults and the location of the NFP-20 East and TRANSALP transects.

units together with a large amount of the European distal margin was subducted [*Schmid et al.*, 1996].

The following period (~32 Ma) was marked by two important events (Fig. 4.12a). At deep levels opposing buoyancy forces between relatively dense subducted lithosphere and lighter continental lithosphere resulted in slab break-off [*von Blanckenburg and Davies*, 1995]. As a consequence, upwelling of asthenosphere and melting of the overriding lithosphere led to the formation of the Periadriatic plutons, such as the large Bergell or the Adamello. Contemporaneously, at crustal levels, retro shearing initiated along the Insubric line and was coeval with progressively north-directed transport in the northern foreland [*Schmid et al.*, 1996]. Vertical displacements along the Insubric line *(18-20 km)* led to back-folding and rapid exhumation of detached upper crustal slices, and lasted until ~20 Ma, as constrained by cooling ages [*Rosenberg et al.*, 1995] (Fig. 4.12b). During this episode, at crustal levels, 33 km out of total 58 km of shortening took place in the northern foreland. Slab break-off, the formation of a retro- shear, and thickening of the wedge, are interpreted as a reaction on the arrival of European continental

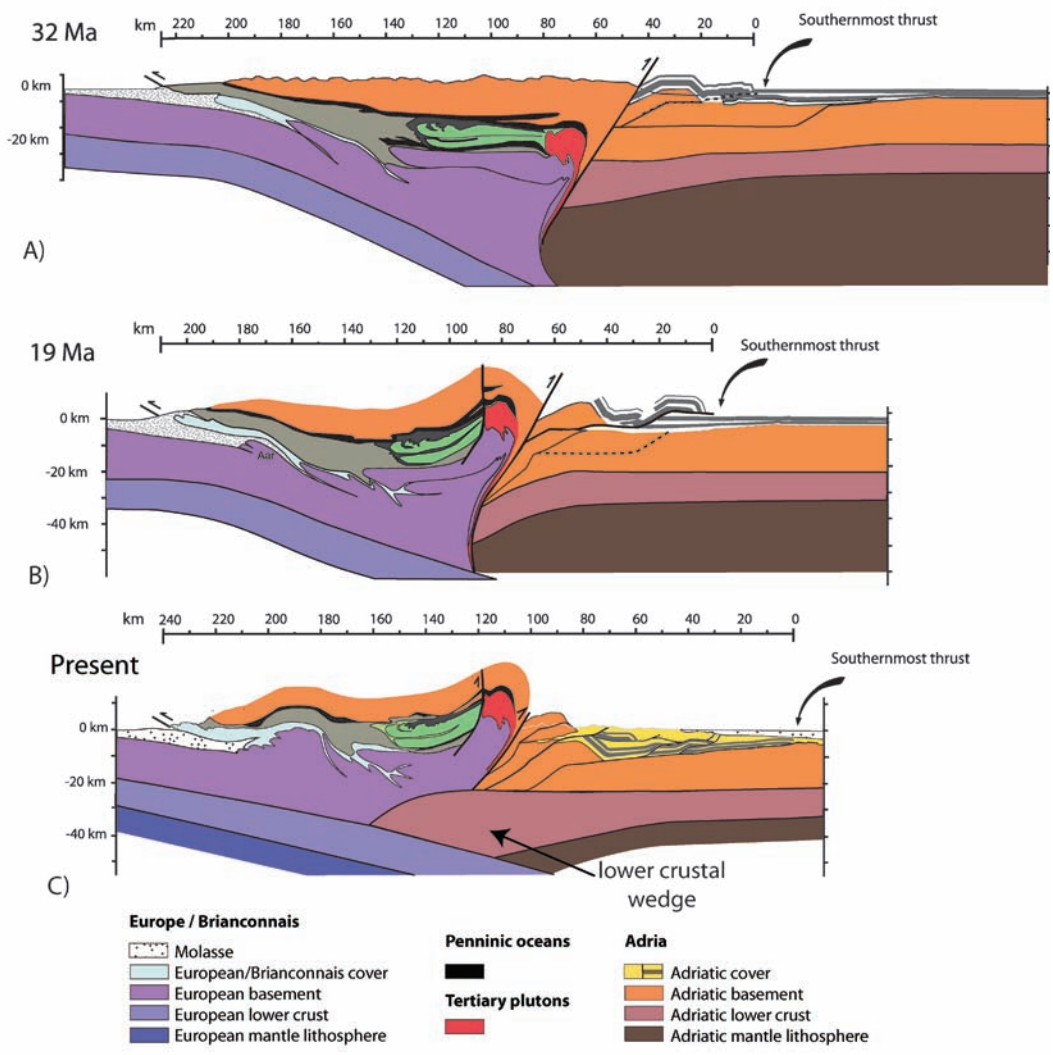

Figure 4.12 Cross-sections showing the Central Alpine Tertiary evolution from Rosenberg et al. (2009). Horizontal scale indicates the width of the orogen during the late Oligocene, middle Miocene and present. The northern part is redrawn after Schmid et al., (1996) and the southern part is redrawn after Schönborn (1992). Large events characterize different periods starting with slab break off during the Oligocene followed by coeval back thrusting along the Insubric line and foreland-directed thrusting during the Early Miocene. Around 18 Ma the onset of lower crustal wedging into the European middle-crust modified the orogen into its present shape.

lithosphere into the subduction zone [*Schmid et al.*, 1996]. These features record but also contribute to a decrease of the effectiveness of the subduction system. *Schmid et al.* [1996; 2004] and *Pfiffner et al.* [1997b], however, argue for a continuation of subduction of both European mantle lithosphere and lower crust. Note that the interpretation of subducting lower crust is highly uncertain and cannot be resolved by teleseismic tomography yet [*Kissling et al.*, 2006].

The most recent episode of post-collisional shortening (<20 Ma) is marked by wedging of the Adriatic lower crust into the European middle crust [e.g. *Valasek and Mueller*, 1997] (Fig. 4.12c). As a result, the central part of the Alps north of the Insubric line was uplifted, meanwhile the Southern Alps underwent upper-crustal shortening [*Pfiffner et al.*, 2000]. The resulting asymmetric uplift pattern on the scale of the entire wedge is well expressed by the distribution of cooling ages [*Rosenberg and Berger*, 2009]. It has been argued that recent deformation affecting the Molasse basin and even the Jura Mountains are driven by this lower crustal wedging as well [*Rosenberg and Berger*, 2009]. Slightly towards the west, recent cooling age studies in the Gotthard massif document accelerated exhumation rates (~0.7 km/Ma) between 16-14 Ma, and are also interpreted as resulting from Adriatic wedging [*Glotzbach et al.*, 2010]. Since then, geochronological data indicates nearly steady, moderate exhumation rates (~0.5 km/Ma) [*Glotzbach et al.*, 2010]. Elaboration on the cooling pattern follows in Chapter 6.

Within the Central Alps, simultaneous activity of pro- and retro-shears throughout the Neogene is consistent with the Beaumont-type models [*Beaumont et al.*, 1996; *Schmid et al.*, 1996]. In this context, there exists consensus on the driving force of wedge formation by underthrusting of the European mantle lithosphere [*Beaumont et al.*, 1994]. Our experiments of subduction of mantle lithosphere in combination with crustal stacking on the incoming plate fit are also comparable with this Central Alpine setting (Fig. 4.13). Dominantly foreland directed stacking was largely coeval with retro-shearing onto the upper plate (exp. 4-2 and 4-4a). The main difference between those two experiments however is the behavior of the lower crust: only partly subducting in experiment 4-2, but almost entirely subducting in experiment 4-4a. Hence, the deep structure of experiment 4-4a shows most similarity with the interpretation of the NRP-20 east transect by *Schmid et al.* [1997]. Especially, the reconstruction profile from the Early Miocene is very much alike (Fig. 4.13). In this scenario, the lower crust and mantle lithosphere below the Alps were strongly coupled. During the Early Miocene Adriatic, lower crustal wedging did not yet modify the "European" wedge, and shortening in the Southern Alps was minor. In addition, we argue that the interpreted uplift in the Central Alps fit well with the late-stage asymmetric uplift patterns observed in experiments 4-2 and 4-4a. Therefore, the uplift pattern of the Central Alps can be explained by a combination of pro- and retro shearing during a "mature" stage of collision and ongoing mantle lithosphere subduction without the need to call upon lower crustal wedging.

4.7.2 The Eastern Alps

From the Central Alps towards the Eastern Alps the style of collision changes in several ways (Fig. 4.11). First, Miocene- to recent thrusting affected largely the Southern Alps. Second, besides some recent uplift affecting the Southern Alps, the bulk of Miocene uplift and exhumation was localized in the Tauern window, as documented by pressure-temperature time paths [e.g. *Cliff et al.*, 1985; *Fügenschuh et al.*, 1997]. Third, convergence was partitioned into a component of north-south shortening and a component of eastward extrusion [*Ratschbacher et al.*, 1991]. Fourth, interpretations on the deep structure document a change of subduction polarity where the mantle lithospheric slab dips towards the northeast [*Lippitsch et al.*, 2003]. Note that the location of the TransAlp transect is considered as a lateral transition zone of changing subduction polarity, a

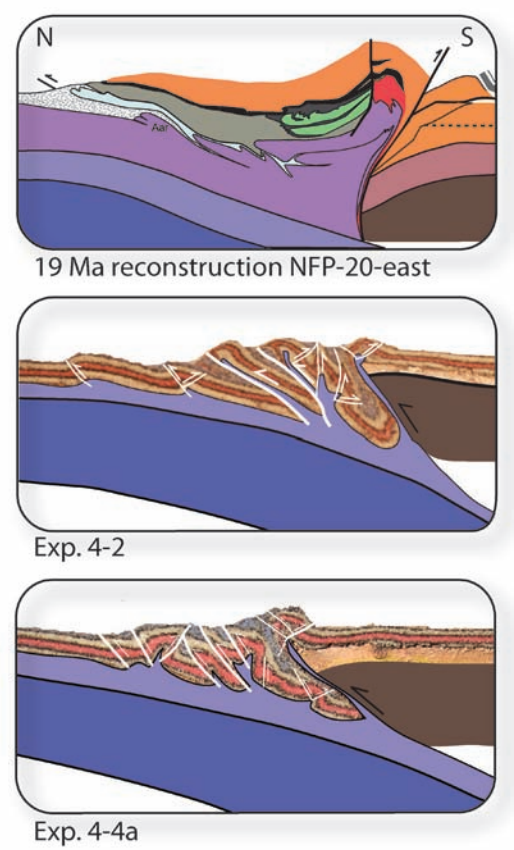

Figure 4.13 Comparison between the NFP-20 East reconstruction at 19 Ma, and cross sections of experiments 4-2 and 4-4a, respectively.

region where no clear subduction polarity is determined [e.g. *Kissling et al.*, 2006]. Considered all these lateral variations throughout the Eastern Alps, which all in some way may contribute in shaping the orogenic wedge, a direct correlation with our model results is difficult. Nevertheless, we should emphasize that our experiments suggest possibilities to reproduce a symmetric orogen overlying both plates equally, which shows similarities with both interpretations of the TransAlp transect by *TransAlp Working Group* (2002) and *Schmid et al.,* (2004). A symmetric wedge was reproduced in experiment 3-5. This symmetry was caused by a combination of limited thrust propagation towards the foreland, and profound retro-shearing (Fig. 4.14 b). In this scenario, retro-shearing around 10-15% BS can be compared to the early Miocene activity along the Periadriatic line *(4 km)* and rapid exhumation in the Tauern Window [*Mancktelow et al.*, 2001]. However, we should realize that the present-day symmetry along the TransAlp transect actually results from two subsequent events. As such, northward thrusting prevailed between 30 and 20 Ma, while southward thrusting dominatied only from 20 Ma onwards. In this way, the present-day wedge geometry can be treated very roughly as the combination of

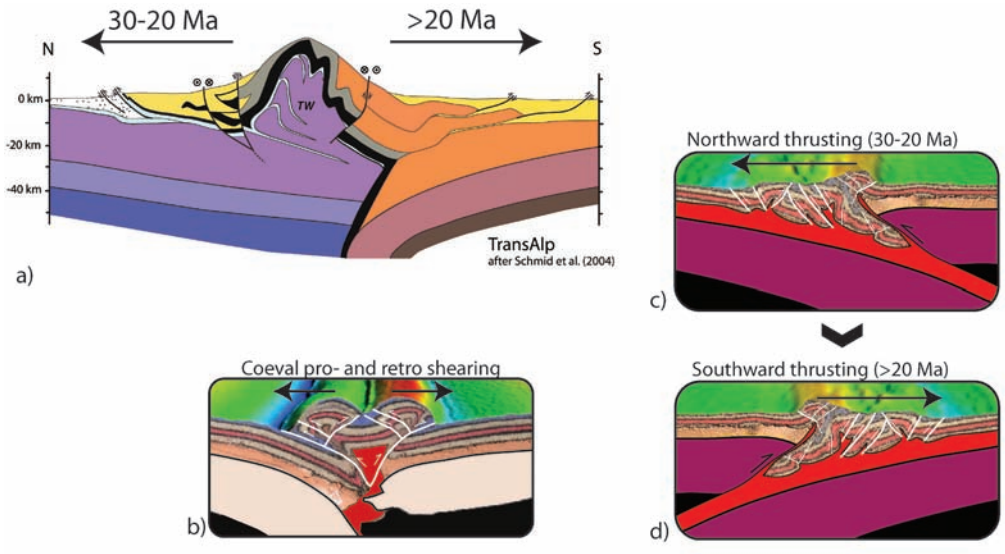

Figure 4.14 a) Interpreted TransAlp traverse by Schmid et al. (2004) and related experiments. Uncertainties on the subduction polarity and a possible flip around 20 Ma allows for different interpretations explaining the observed symmetry of the crustal wedge. b) No call for a subduction polarity change is needed to obtain a symmetrical wedge as shown by experiment 3-5. However, in contrast to this experiment, pro- and retro shearing was probably not coeval in the Eastern Alps. c-d) Relative late southward-directed thrusting in the eastern Southern Alps can be underlain by northward subduction of the Adriatic lithosphere since Miocene times.

two wedges, formed by opposing vergence of mantle lithosphere subduction (Fig. 4.14 c-d). The response of wedge geometry on such a change in subduction polarity is further discussed in the next chapter.

Finally, regional and mechanical modelling studies emphasize that the Alpine orogen evolved from a decoupled to a coupled system throughout the Late Miocene [e.g. *Ziegler et al.*, 2002; *Genser et al.*, 2007; *Willingshofer and Sokoutis*, 2009]. This would explain the transition from dominant localized vertical motions towards more regional, but reduced uplift rates as recorded by the distribution of cooling ages [e.g. *Luth and Willingshofer*, 2008; *Glotzbach et al.*, 2010]. *Willingshofer and Sokoutis* (2009) documented from their analogue experiments the transition towards enhanced coupling by decreasing uplift rates affecting both the orogenic wedge and the plate interiors. On the other hand, in the experiments presented in this chapter the coupled stage is characterized by regional subsidence of the orogenic wedge and adjacent basins (e.g. Fig. 4.7b). In nature, there are no indications for a late phase of regional subsidence. However, within the experiments subsidence was maybe caused by the absence of erosion and in combination with a strong slab-pull force. Therefore, we can still consider the regional uplift and subsidence trends observed in these two studies as comparable since both monitor a transition from rapid localized uplift towards more regional, but reduced vertical motion.

4.8 Conclusions

The performed lithosphere-scale analogue models allow to relate first-order wedge geometries and subduction of the mantle lithosphere to the rheology of the lithosphere and the plate interface.

Varying the degree of plate coupling, by changing the rheology of viscous layers, influences orogenic wedge formation. As such, the extent of a weak lower crust largely determines the width of the wedge, while restriction of weak lower crust to the plate boundary region results in a narrow wedge, which in the scenario of a very weak lubricant remains asymmetric. Ongoing subduction by crust-mantle decoupling could only be obtained by weak lower crust throughout the lower plate. This weak horizon also allows for widening of the wedge onto the lower plate. Reducing the strength contrast between the lower crust and mantle lithosphere invokes lower crustal subduction, and thus decreases the volume of crustal material accumulated within the orogenic wedge. As a result, the topography of the orogenic wedge is relatively low, and the displacement along individual thrusts is less. A relative weak upper plate in terms of mantle lithosphere promotes thickening of the mantle lithosphere near the plate interface and causes a reduction in the amount of mantle subduction. Interpretation on plate (de)coupling conditions at mantle depth by means of retro-shearing is uncertain, since retro-shearing can occur in settings where the colliding plates are both decoupled or coupled at mantle depth. The geometrical consistency between our modelling results and the diverse lithospheric structures observed below the Central- and Eastern Alps imposes an important role for plate (de)coupling conditions, in particular on crustal wedge formation.

Chapter 5

Surface expressions of the subduction polarity change in the Alps: Inferences from analogue modelling

5.1 Introduction

Many orogens comprise along-strike variations affecting the entire lithosphere. Commonly observed features are for instance lateral variations in wedge geometry, amount of shortening and surface uplift patterns. Hence, the build-up of a collision zone should be considered as a three-dimensional process.

The Alpine orogen is a good example of several well studied along strike-variations. Some recognized lateral changes are expressed by cooling ages (exhumation patterns) [e.g. *Grundmann and Morteani*, 1985; *Hejl*, 1997; *Rosenberg and Berger*, 2009] (Fig. 5.1), variation in (paleo-) topography [e.g. *Frisch et al.*, 1998; *Dunkl et al.*, 2005; *Willett et al.*, 2006; *Kuhlemann*, 2007], and termination of the Austroalpine unit in the eastern Central Alps. Additionally the structural style varies along-strike, such as huge amounts of back-thrusting appear in the Central Alps versus very little back-thrusting, but prominent strike-slip faulting in the Eastern Alps [e.g. *Ratschbacher et al.*, 1991; *Mancktelow et al.*, 2001; *Handy et al.*, 2005]. On a larger scale, the Western- and Central Alps are characterized by relative large pro-wedges overlying the downgoing European plate and relative narrow retro-wedges. In the Eastern Alps, crustal deformation is more symmetrically distributed above the colliding plates, and the orogen widens reaching maximum values along the TRANSALP profile (Fig. 5.1). At lower crustal levels, wedging of Adriatic lower crust has been interpret below the Central Alps, whereas in different interpretations of the TRANSALP transect lower crustal wedging diminishes or even vanishes below the Eastern Alps [*Schmid et al.*, 1996; *TRANSALP Working Group*, 2002; *Schmid et al.*, 2004].

Figure 5.1 (next page) a) Tectonic outline of the Alps displaying regions, major fault lines, and topography. b) Major along strike-variations throughout the Alps occurring since Neogene times.

Figure 5.1

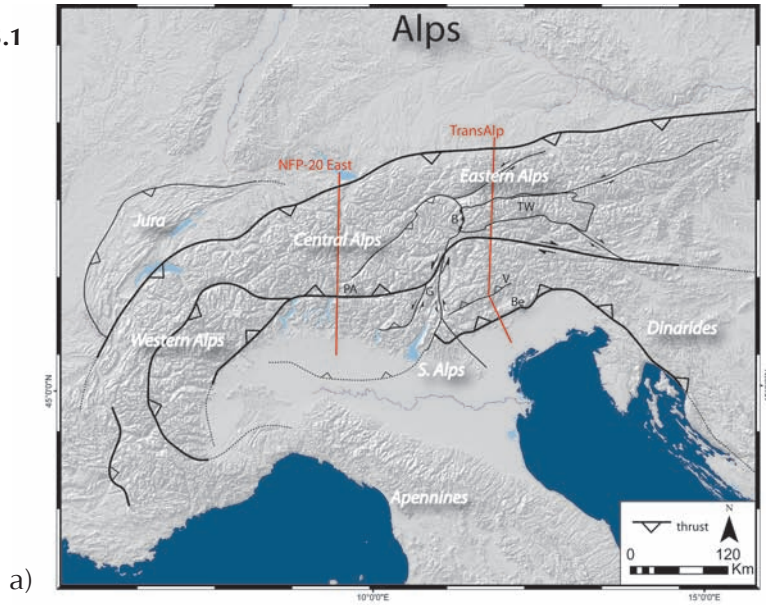

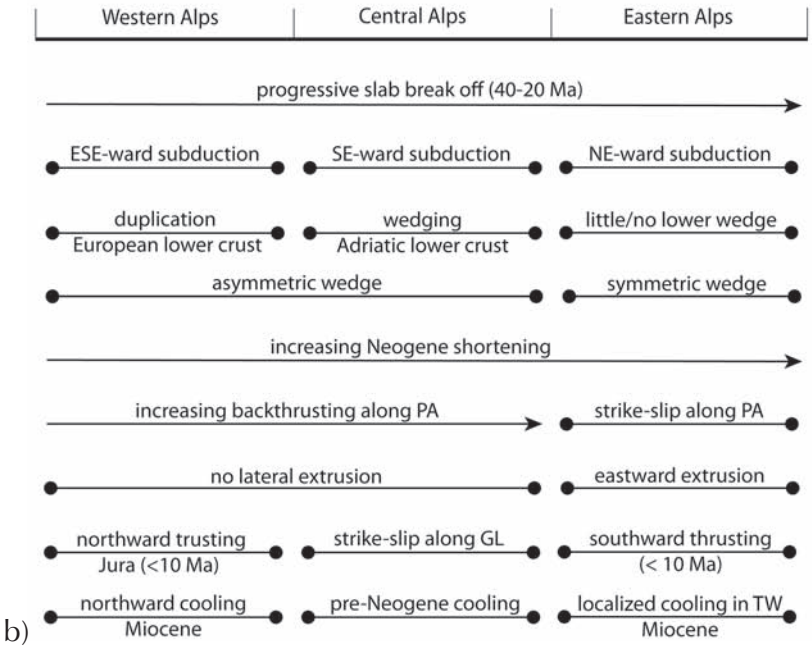

Figure 5.2 (facing page) High resolution tele-seismic tomography revealing along-strike variations in continental subduction polarity. a) Interpolated P-wave velocity distribution between 135 km and 165 km depth from Lippitsch et al. (2003). Red dashed lines indicate areas of high-velocity European and Adriatic mantle lithosphere, which is subducted SE and NE, respectively. Thin black lines mark locations of lower lithosphere transects. White lines indicate major faults. b) Lower lithosphere transect through western Central Alps imaging SE-dip of subducted European lower lithosphere. Bold dashed line indicates lithosphere-asthenosphere boundary. c) Lower lithosphere transect through Eastern Alps imaging NE-dip of subducted Adriatic lower lithosphere. Both transects were compiled by Lippitsch et al. (2003) and Kissling et al. (2006).

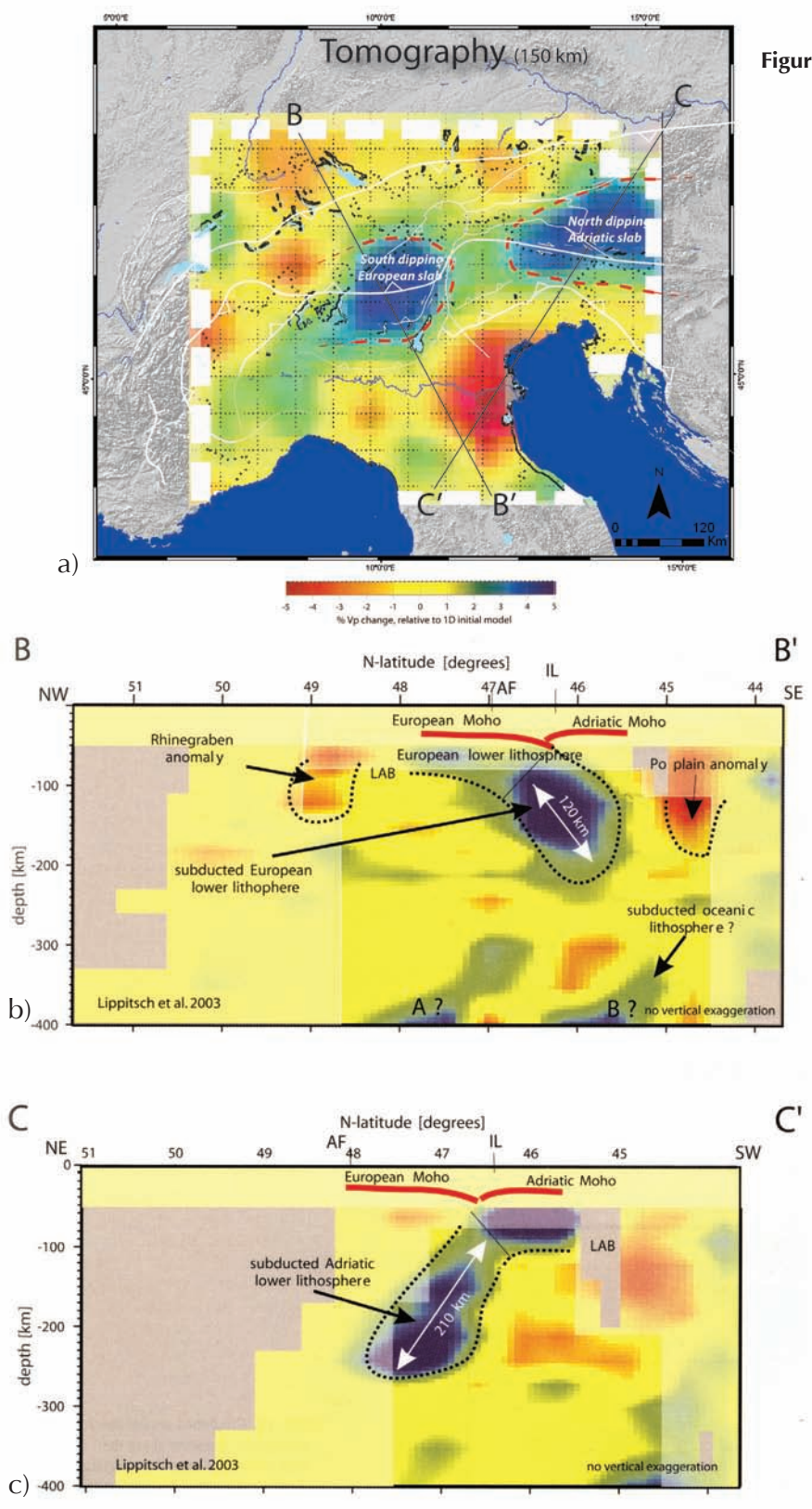
Tomography (150 km)
B
C
North dipping Adriatic slab
South dipping European slab
C′
B′
N
0
120
Km
a)
% Vp change, relative to 1D initial model
B
B'
N-latitude [degrees]
NW
SE
AF
IL
European Moho
Adriatic Moho
Rhinegraben anomaly
European lower lithosphere
LAB
Po plain anomaly
120 km
subducted European lower lithophere
subducted oceanic lithosphere ?
depth [km]
Lippitsch et al. 2003
A ?
B ?
no vertical exaggeration
b)
C
C'
NE
SW
European Moho
Adriatic Moho
LAB
subducted Adriatic lower lithosphere
210 km
depth [km]
Lippitsch et al. 2003
no vertical exaggeration
c)

Figure 5.2

At the level of the lithospheric mantle, a remarkable along strike-variation is interpreted from high resolution tele-seimic tomography [*Lippitsch et al.*, 2003] (Fig. 5.2). These tomographic images reveal southeast-directed subduction of the European mantle lithosphere below the Central Alps, but surprisingly a north-east dipping subduction of the Adriatic mantle lithosphere underneath the Eastern Alps [*Lippitsch et al.*, 2003; *Kissling et al.*, 2006](Fig. 5.2). Although this observation of opposing dipping slabs was primarily not derived from extensive studies of the surface geology, a correlation between this lateral subduction "flip" and along-strike variations at crustal levels might exist. Reversely, the lateral variations of crustal architecture (symmetry of mountain belts) may be considered indicative for changes in the subduction polarity of the mantle lithosphere.

Lithosphere-scale analogue modelling, as presented in the previous chapters, convincingly proved to be a convenient tool investigating complex 3-D geometries arising from plate convergence. Hence, to examine the surface/crustal expression of a lateral change in subduction polarity we are challenged by increasing model complexity by implementing a pre-defined lateral flip in subduction polarity at mantle lithosphere level. Special emphasis has been given on along strike-variations in terms of wedge build-up and topography, and how these possibly depend on lateral interaction between the adjacent subduction domains. The main parameters investigated are (a) the degree of lateral coupling between the domains of opposing subduction polarity, (b) the width of the zone separating the domains, and (c) different obliquity between the opposing subduction domains with respect to de direction of shortening. The assigned values to parameters (b) and (c) are based on the subducting slab configuration below the Alps. In addition, the role of vertical decoupling on crust-mantle interaction has been studied by implementing a weak lower crust in both plates. By this, crustal deformation within the collision zone is hypothetically less influenced by the underlying mantle lithosphere, and thus subduction polarity. Finally, we conclude by comparing the model results with observations from the Alps in order to infer diagnostic features for lateral subduction polarity change.

5.2 Experimental design

A lateral subduction polarity change was implemented by juxtaposition of two domains with pre-defined opposing subduction directions (Fig. 5.3). Construction of these "subduction domains" was similar to the experiments presented in Chapter 3 and 4, where subduction was triggered by a 45° inclined weak zone in the mantle lithosphere. In experiment 5-1, the subduction domains were separated at mantle-lithosphere and lower-crustal levels by a 5 mm wide horizon consisting of weak silicon putty (Fig. 5.3). Such a layer was absent in the other experiments, resulting in strong coupling between

Figure 5.3 (facing page) Experimental set-up. All layers were confined by plexi-glass and a moving wall (arrow). Lithosphere exhibits two viscous layers of different silicone mixtures overlain by a layer of feldspar sand. Red colour represents relative weak viscous material allowing for mantle lithosphere subduction (see Chapter 3). Opposing dips of weak zones define two subduction domains to invoke a lateral change in subduction polarity. In exp. 5-1 a 5 millimeter wide zone of weak viscous material separating the subduction domain is indicated by *. Obliquity and lower crustal rheology are investigated parameters in exp. 5-3 and exp. 5-4, respectively. A wide transition consisting of "regular" lithosphere domain has been included in exp. 5-5.

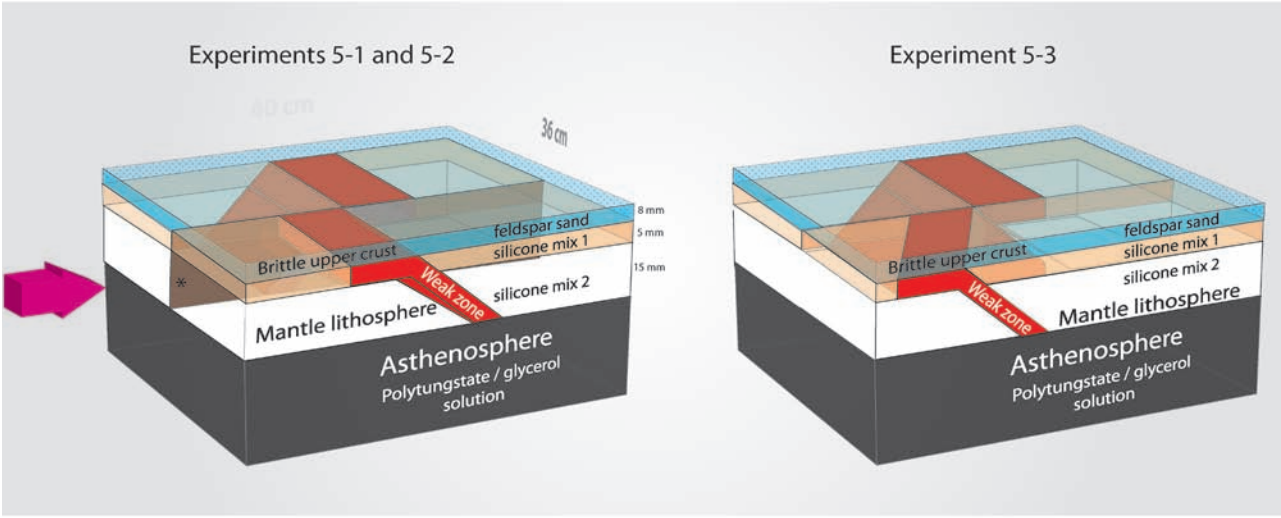
Experiments 5-1 and 5-2
36 cm
8 mm
5 mm
15 mm
feldspar sand
silicone mix 1
Brittle upper crust
Weak zone
silicone mix 2
Mantle lithosphere
Asthenosphere
Polytungstate / glycerol solution
Experiment 5-3
feldspar sand
silicone mix 1
silicone mix 2
Brittle upper crust
Weak zone
Mantle lithosphere
Asthenosphere
Polytungstate / glycerol solution

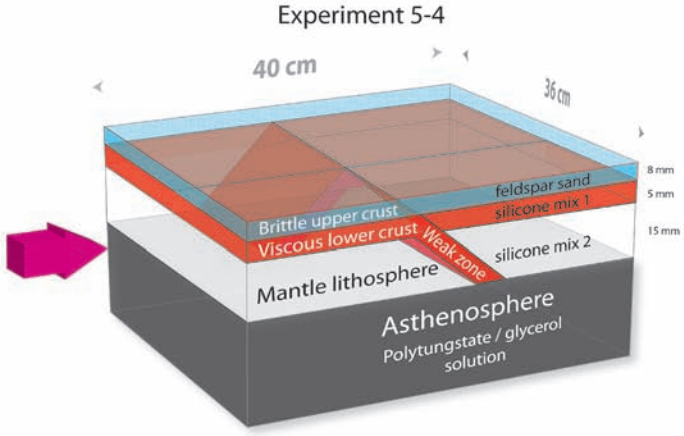
Experiment 5-4
40 cm
36 cm
8 mm
5 mm
15 mm
feldspar sand
silicone mix 1
Brittle upper crust
Viscous lower crust
Weak zone
silicone mix 2
Mantle lithosphere
Asthenosphere
Polytungstate / glycerol solution

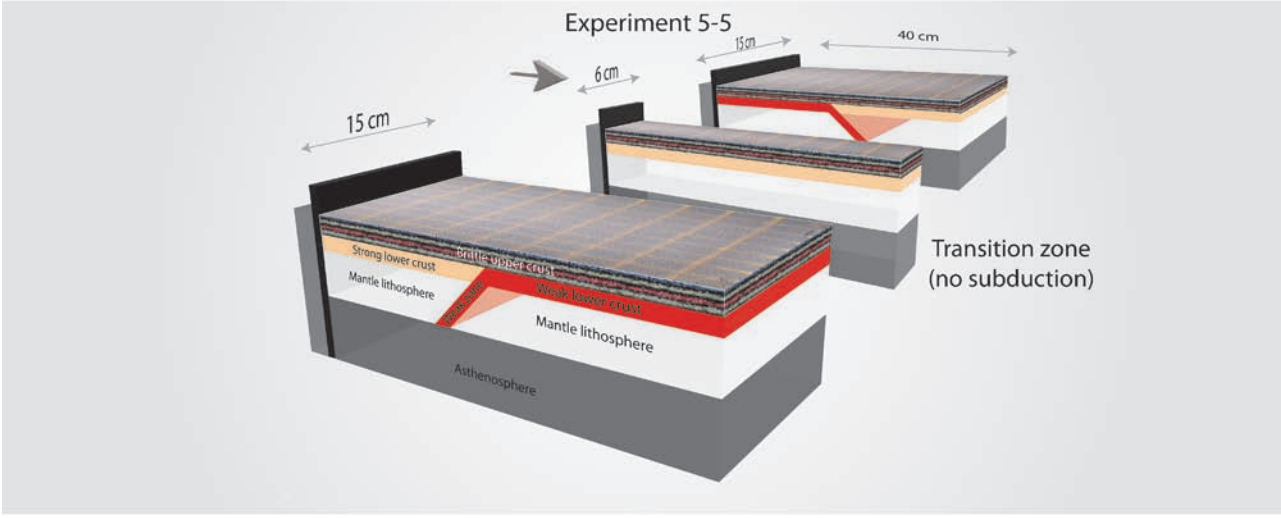
Experiment 5-5
15 cm
6 cm
15 cm
40 cm
Strong lower crust
Brittle upper crust
Mantle lithosphere
Weak zone
Weak lower crust
Mantle lithosphere
Asthenosphere
Transition zone
(no subduction)

the subduction domains (e.g. exp. 5-2). In experiment 5-3, the role of obliquity on lateral interaction and surface deformation was investigated to mimic oblique subduction of Adria below the Dinarides (Fig. 5.1). As such, one of the subduction domains was orientated 60°oblique with respect to the shortening direction. Experiment 5-4 aimed for unravelling the effect of weak lower crust in combination with a lateral change in subduction polarity on crustal deformation. Low viscosity lower crust was implemented in both upper- and lower plates. In experiment 5-5, the subduction domains, with solely weak lower crust in the lower plates, were intervened by a 6 cm broad transition zone where no weak plate interface was predefined. In this way, lateral strain patterns within a continental subduction zone adjacent to a "regular" (non-subducting) lithosphere could be studied.

5.3 Modelling results

5.3.1 Decoupled subduction domains

Experiment 5-1

Initial deformation produced a symmetric pop-up above the entire length of the plate interface, regardless of the predefined subduction polarity (Fig. 5.4a). However, fore-thrusts (nr. 1), verging towards the lower plates formed slightly earlier than back thrusts. Around 5% BS, a second pop-up formed on the lower plates, which terminated laterally in the transition zone between the opposing subduction domains. From this moment onward a surface expression of the imposed subduction polarity at depth existed. Further shortening localized along second pop-up fore-thrusts, meanwhile back-thrusting was restricted to the first pop-up. Hence, shortening was accommodated along the wedge margins with only little shortening between the pop-ups. From 15% BS onwards, formation of new structures was limited to the domain boundary (transition zone) region. Here, small thrusts sprouted laterally from the lower plate and then crossed the transition zone towards the upper plates. With ongoing shortening these thrusts continued to propagate further onto the upper plates.

In the early phase topography is restricted to the collision zone (Fig. 5.4a). From 10% BS onwards topographic gradients along-strike can be recognized. Peak elevations border the transition zone and are probably the result of back–thrusting (retro-shearing). Between these highs, the transition zone is characterized by a topographic low. From 15% BS onwards uplift affected mainly the second pop-up. On the other hand, along strike propagation of the second pop-up onto the overriding plates resulted in only minor relief. Hence, topography of the transition zone is marked by a lateral termination of "pro-side" topography. During the final stage (19% BS) wedge topography only slightly increased, and the interiors of the pushed plates (adjacent to the moving wall) began to uplift.

Between the cross-sections the geometry of the collision zone varies (Fig. 5.4b). In profile 2 the amount of lithosphere subduction was high with respect to profiles from the interior region. At crustal level asymmetric pop-ups coalesced into a symmetric wedge, which was thrusted equally onto both plates and was underlain by weak lower crust. This wedge geometry is comparable to the "narrow-symmetric" wedges observed in experiment 4-5, (Chapter 3). Further towards the transition zone the amount of mantle

lithosphere subduction becomes less (compare profiles 2 and 3). In addition, the upper plate now dips at a low angle towards the plate boundary along which the mantle lithospheres from both plates slightly thickened. The overall symmetric crustal wedge is widened by two small thrusts located onto the upper plate. Note that these small thrusts root within strong lower crust. Profile 4 crosses through the pre-defined transition zone and thus discloses weak silicone putty. Although no subduction vergence was initially pre-determined within the transition zone, a small slab dipped towards the moving wall. Crustal deformation resulted in a wide and symmetric collision zone comprising three pop-ups divided equally on both plates. Subduction polarity reversed in profile 5 showing a "mirrored" pattern of profile 3: a symmetric crustal wedge overlying weak lower crust and modest crustal deformation within the upper plate. With increasing distance from the transition zone the amount of mantle lithosphere subduction increased and crustal shortening became in turn more localized (Profile 6). Note that the crustal wedge was not symmetric and the bulk of crustal shortening was accommodated along a major fore-thrust.

5.3.2 Coupled subduction domains

Experiment 5-2

Similar to experiment 5-1, a symmetric pop-up formed within the first 5% BS above the weak plate interface regardless of the predefined subduction polarity (Fig. 5.5a). However, lower plate vergent fore-thrusts forming slightly before the back-thrusts express the lateral change of subduction polarity at depth. The fore-thrusts were in general short-lived, while both back thrusts remained active. With ongoing shortening deformation jumped to a second pop-up on the lower plate. These structures propagated and widened until the transition zone. Between 15-20% bulk shortening both pop-ups coalesced into a single orogenic wedge, and subsequent displacements localized along their margins. In addition, splays of short-lived thrusts extended the second pop-ups laterally by crossing the transition zone onto the adjacent upper plates. Note that this deformation pattern is comparable to experiment 5-1. However, final upper plate thrusting is more intense within this model. Another larger scale surface expression is a gradual increase in obliquity between the strike of the collision zone and the shortening direction from 10% BS onwards.

The evolving topography strongly relates to thrusting and is in the early phase comparable to experiment 5-1 (Fig. 5.5a). From 15% BS onwards, however, uplift of the first pop-up stagnated and topographic growth became restricted to the second pop-up. Moreover, the first pop-up now subsided, and in particular along the transition zone. In addition, during the final episode the wedge became bordered by narrow basins, meanwhile the plate interiors were uplifted. Similar to experiment 5-1, lateral propagation of thrusts onto the upper plate did not result in high elevations. Hence, the along-strike topographic gradient between the second pop-up and the upper plate along the transition zone was maintained.

Cross-sections shown in Figure 5.5b reveal along strike geometric variations of the evolved collision zone. Profile 2 shows a symmetric crustal wedge comprised of two asymmetric pop-ups cored by weak lower crust above the suture zone. Most crustal shortening has been accommodated along the outer fore- and back-thrusts, which

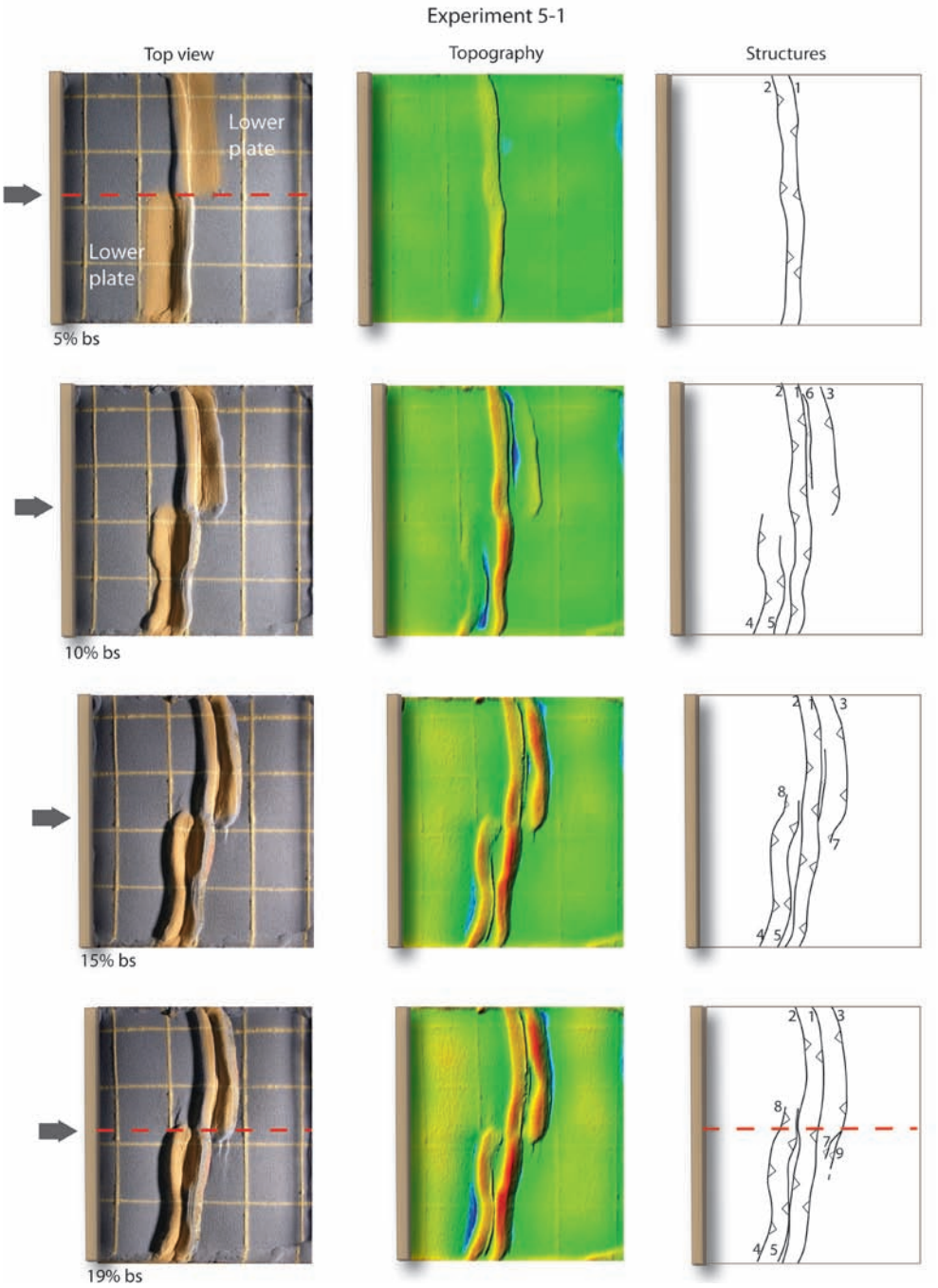

Figure 5.4a Experiment 5-1. Top views shown at intervals of 5% bulk shortening (bs). Pictures are shown in left column. Arrows refer to shortening direction. Red dashed line marks weak zone dividing subduction domains with opposing subduction polarity. Yellow sand marks the region of underlying weak lower crust. Middle column: topographic surface scans in where green is initial elevation while red and blue colors mark regions of uplift and subsidence, respectively. Right column: interpret faults chronically numbered.

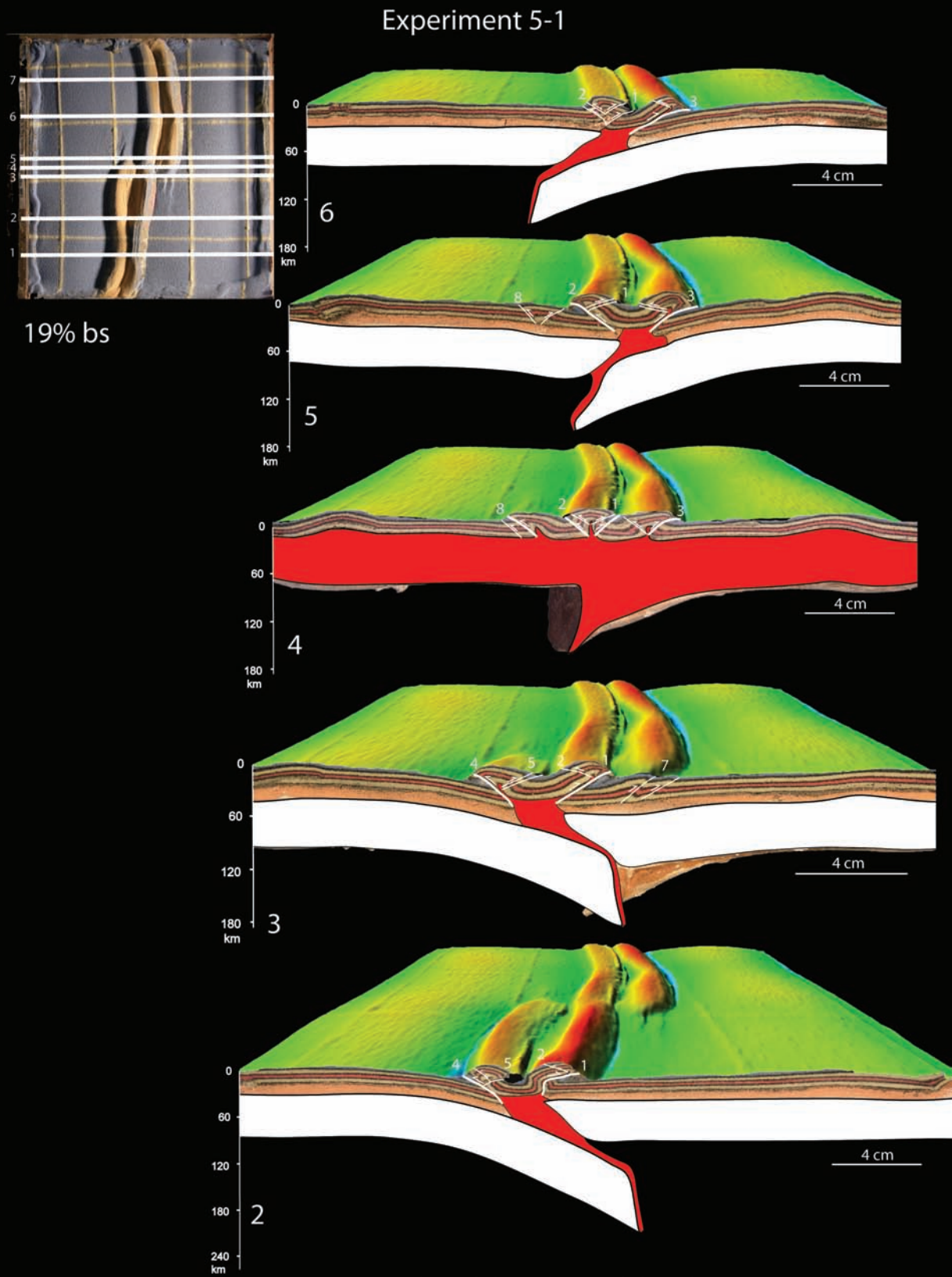

Figure 5.4b Experiment 5-1. Cross-sections located along white profile lines shown in top view inset. Within the cross-sections white material corresponds to mantle lithosphere, beige to strong lower crust, red to weak zone, and colored sand to upper crust. Black line represents Moho. White lines are interpreted faults, which are chronically numbered. A DEM overlies the cross sections (see Fig. 5.4a).

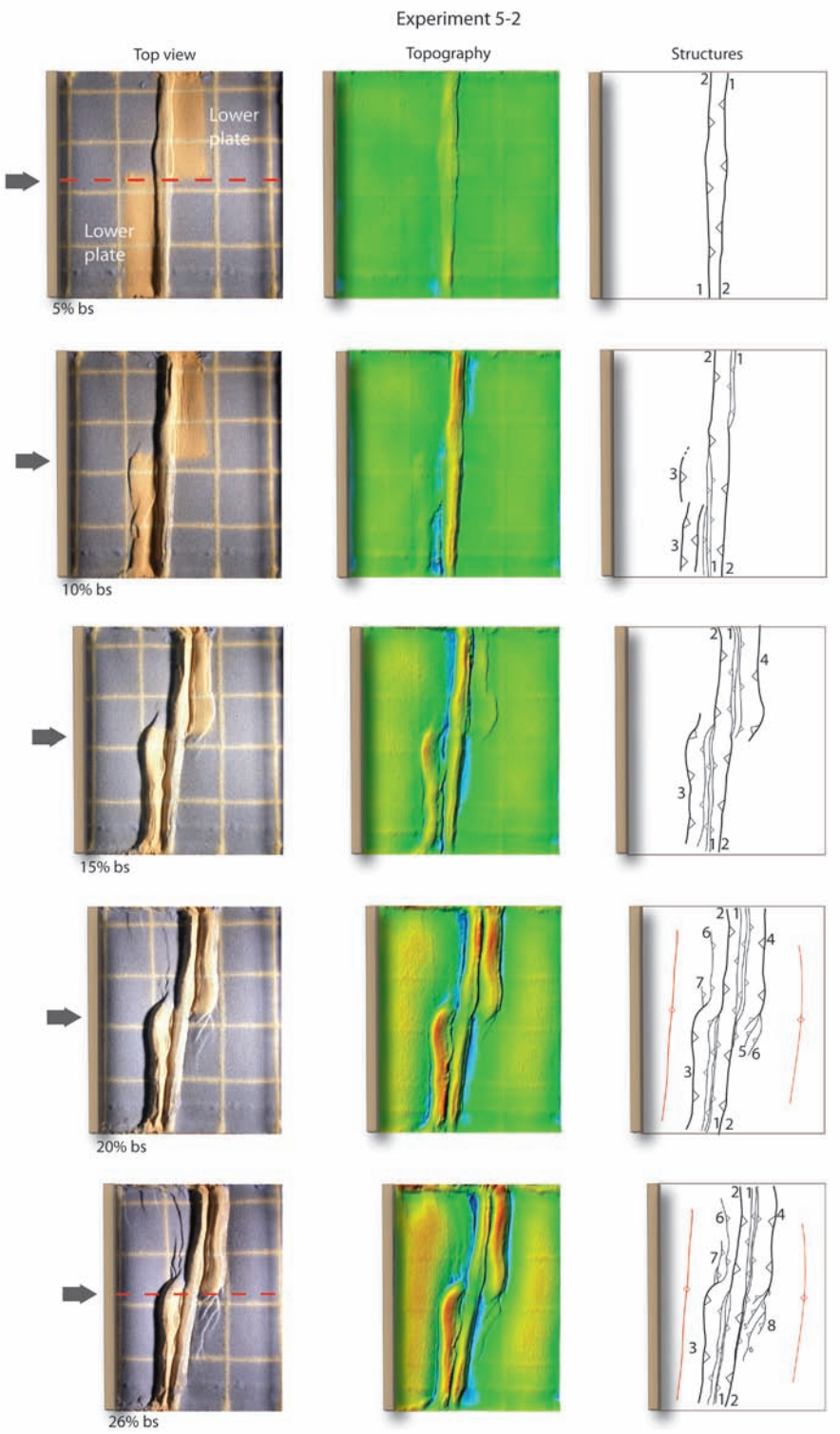

Figure 5.5a Experment 5-2. Top view images at 5% BS interval. See caption of Fig. 5.4a

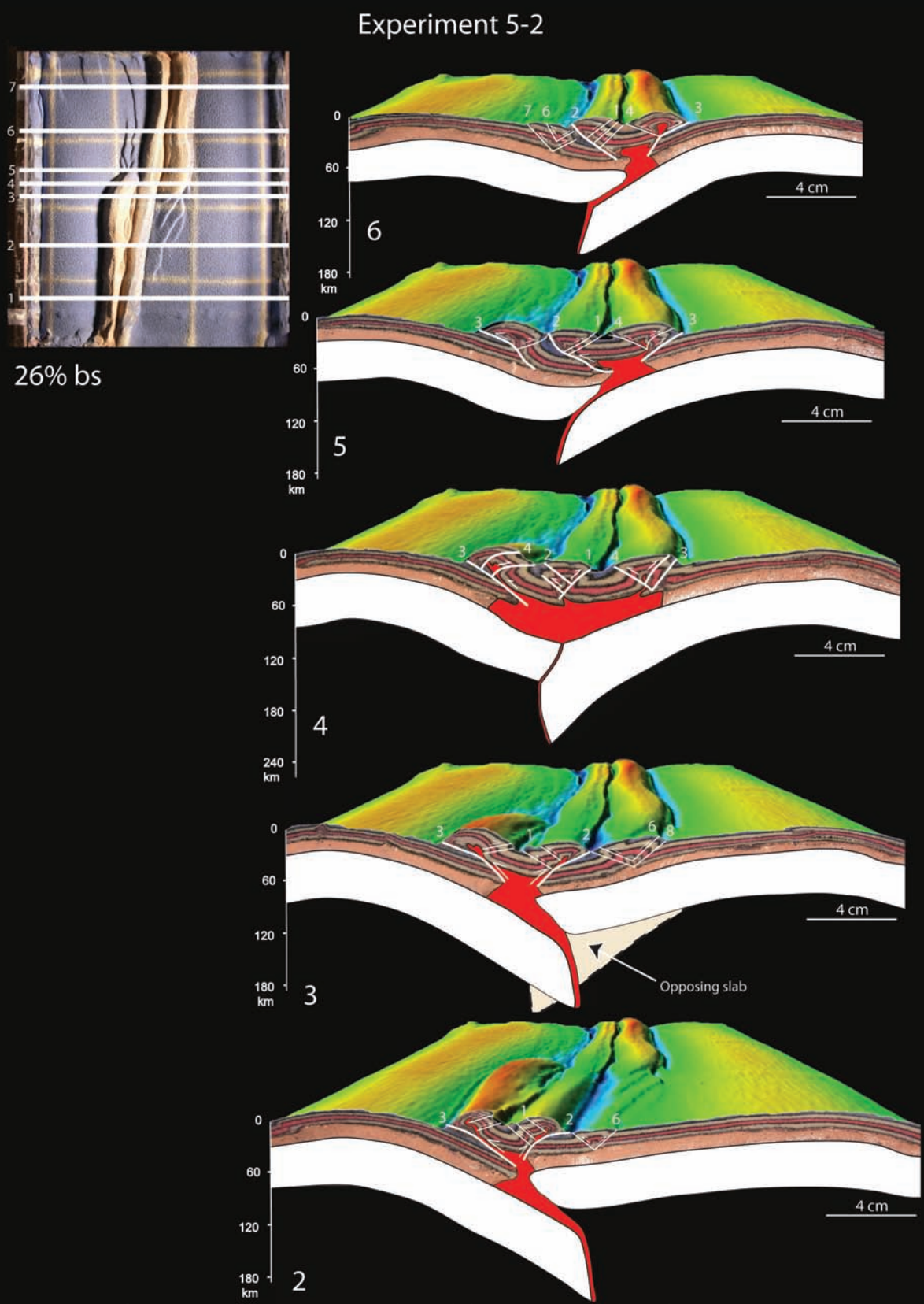

Figure 5.5b Experiment 5-2. Cross-sections located along white profile lines shown in top view inset. Within the cross-sections white material corresponds to mantle lithosphere, beige to strong lower crust, red to weak zone, and colored sand to upper crust. Black line represents Moho. White lines are interpreted faults, which are chronically numbered. A DEM overlies the cross sections (see Fig. 5.5a).

displaced several short-lived faults. The upper plate was slightly tilted towards the suture zone and hosted a small pop-up. Towards the transition zone (profile 3) the amount of subduction was less, and the tilt of the upper plate increased. Within the transition zone, upper plate down bending is highest and seemed to counteract subduction of a steep dipping slab (profile 4). Crustal deformation led to an overall symmetry of equally sized pop-ups overlying an area of thickened weak lower crust. Within profile 5 the subduction polarity is reversed and the intensity of upper plate down bending decreased. Note that some large thrust affected the overriding plate and thus were rooted into strong lower crust (thrust nr. 6-7). Further away from the transition zone (profile 6) the upper plate recovered from down bending and the width of the crustal collision zone is reduced. As in the other profiles, a large amount of back thrusting occurred.

5.3.3 Oblique subduction

Experiment 5.3

Thrusting initiated in the "straight" domain and propagated along-strike towards the "oblique" domain (Fig. 5.6a). Lower plate directed fore-thrusts (nr. 2) formed relatively late in the oblique domain and propagated gradually towards the transition zone. Between 5% and 10% BS a second pop-up formed on the lower plates propagating also from the sidewalls towards the transition zone. From 15% BS onwards these second pop-ups crossed the transition zone. As such, thrusts originating from the oblique domain curved to parallel the wedge of the straight domain. Note that during the last 10% BS oblique domain pop-ups were slightly rotated clockwise.

The topographic evolution is not significantly different compared to experiment 5-1 and 5-2 (Fig. 5-6a). Until 10 % BS uplift is equally distributed along the first pop-up. Only from 15 % BS onwards more local topographic gradients evolved along strike. The first pop-up underwent strong uplift near the transition zone, while the second pop-up shows higher elevations at larger distance from the transition zone (Fig. 5.5a). A narrow zone of relative low topography marks the transition zone itself.

Also the cross sections show strong similarities with experiment 5-1 and 5-2 (Fig. 5-6b). The amount of mantle lithosphere subduction decreases towards the transition zone, meanwhile upper plate tilting increased. However, within the transition zone (profile 4) the extreme interfering of the opposing slabs led to the steeping of the slabs. Owed to this steeping, the slab reached finally deeper levels in profile 4 (TZ) compared to for instance profile 7. Wedge geometries corresponded to changes of the underlying subduction-style with local lower plate vergent thrusting at distance of the transition zone, (profile 1 and 7), and an increased amount of back-thrusting onto the upper plate near the transition zone. As such, the orogen shown in profiles 4 and 5 is wide and doubly vergent with thrusts rooting in strong lower crust as well (nr. 3 in Fig. 5.6b).

5.3.4 Weak lower crust in upper- and lower plates

Experiment 5.4

Low viscosity lower crust was implemented in both upper- and lower plates, in combination with a lateral change in subduction polarity. Before crustal deformation localized along the plate boundary the first 7% of shortening was accommodated directly in front of the moving wall (Fig. 5.7a). Around 15% BS thrusting shifted from a symmetric pop-up located above the plate boundary towards the lower plates. Thrusts propagated laterally from the side walls to the model's centre. In the centre, a transition zone was characterized by subsidence bounded by inward verging thrusts (nr. 3 and 5). Between 20%-25% BS crustal deformation extended further onto the plate interiors, meanwhile deformation within the transition zone remained localized. Note that in contrast to the previous experiments several thrusts formed during the final phase, which verge towards the collision zone (e.g. thrusts 5 and 6). As in experiment 5-2, the angle between the strike of the collision zone and the shortening direction gradually increases reaching a final maximum of 18°. This large-scale rotation is probably partly expression of the polarity change and not a boundary affect.

The evolving topography reveals subsidence on the lower plates along the plate boundary even before the first pop-up was formed (Fig. 5.7a). Subsidence continued until ~15% BS adjacent to a fast rising pop-up. At 20% BS a second pop-up formed on the lower plates, meanwhile the first pop-up slightly subsided in particular within the transition zone. Ongoing shortening induced further topographic asymmetry between the subduction domains.

Cross sections portray the lateral change of subduction polarity (Fig. 5.7b). Compared to the previous experiments crustal deformation included more pop-downs and thrusts verging towards the plate boundary. However, the most remarkable difference is the localization of crustal deformation on the upper plates, while crustal deformation hardly affected the lower plates. In addition, most localization of crustal deformation occurred within the transition zone (profile 3), in contrasts to other experiments where the transition zone was marked by a relative wide deformation zone. The amount of mantle lithosphere subduction is not as strongly reduced within the transition zone as observed in the other experiments. Moreover, no strong gradients on the amount of subduction occurred within the subduction domains. However, a difference in the amount of subduction exist between the domains. As such, a relative large amount of mantle lithosphere subducted beneath the domain where the upper plate was pushed (profiles 4 and 5). Here, the development of a small gap along the suture zone suggests that slab rollback occurred.

5.3.5 Weak lower crust in lower plates

Experiment 5.5

The lower plates comprised weak lower crust and the opposing subduction domains were intervened by "regular" (non-subducting) lithosphere as transition domain. Thrusting in the subduction domains initiated around 2% BS (Fig. 5.8a). Instead of symmetric pop-ups, thrusting was strongly asymmetric and advanced further onto the lower plates. Lateral fault propagation onto the transition domain occurred around 5% BS. Ongoing shortening was accommodated within the subduction domains by major

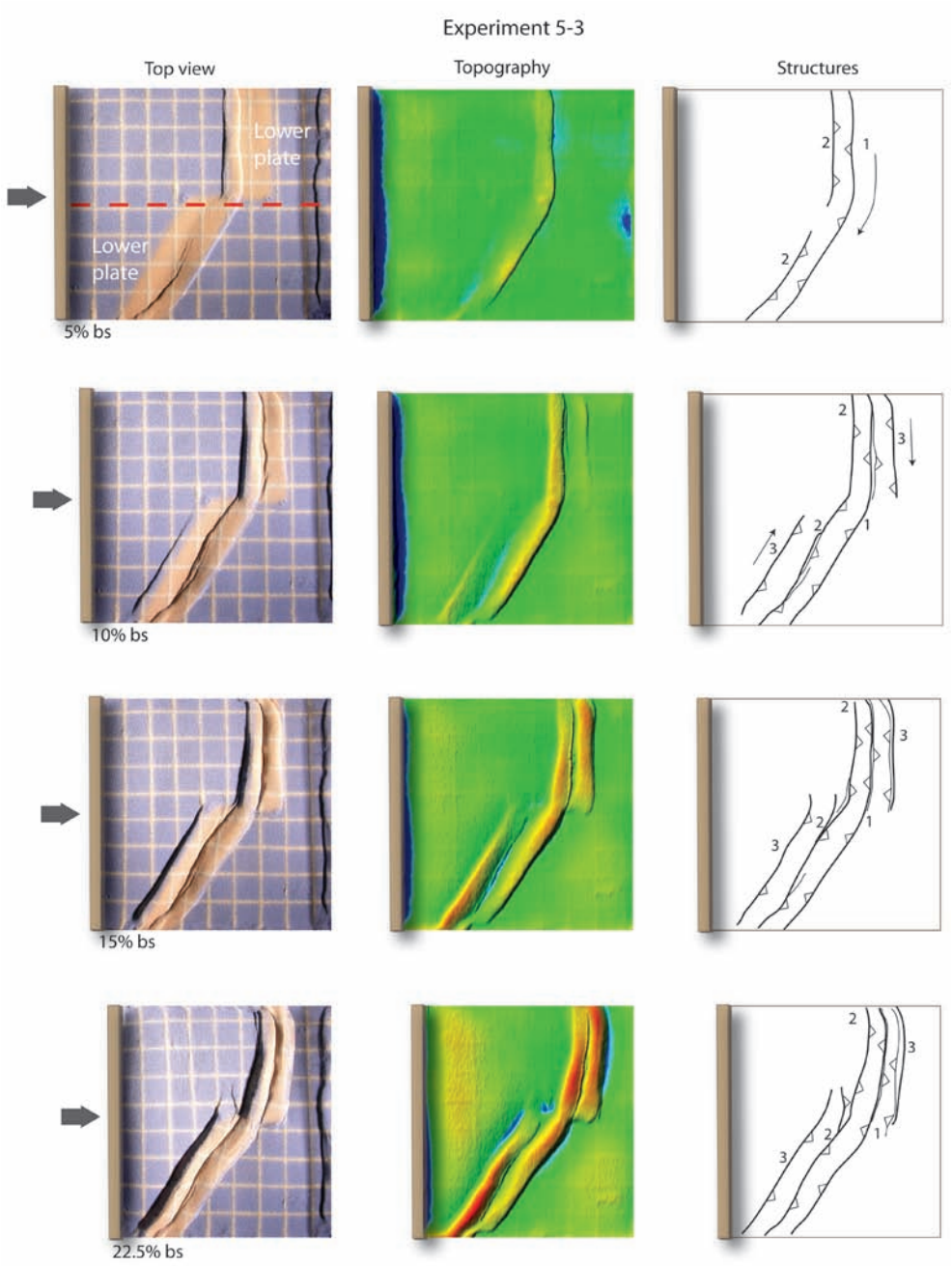

Figure 5.6a Experiment 5-3. Top views shown at intervals of 5% bulk shortening (bs). Pictures are shown in left column. Arrows refer to shortening direction. Red dashed line marks border between subduction domains with opposing subduction polarity. Yellow sand marks the region of underlying weak lower crust. Middle column: topographic surface scans in where green is initial elevation while red and blue colors mark regions of uplift and subsidence, respectively. Right column: interpret faults chronically numbered. Black arrows indicate direction of lateral fault propagation.

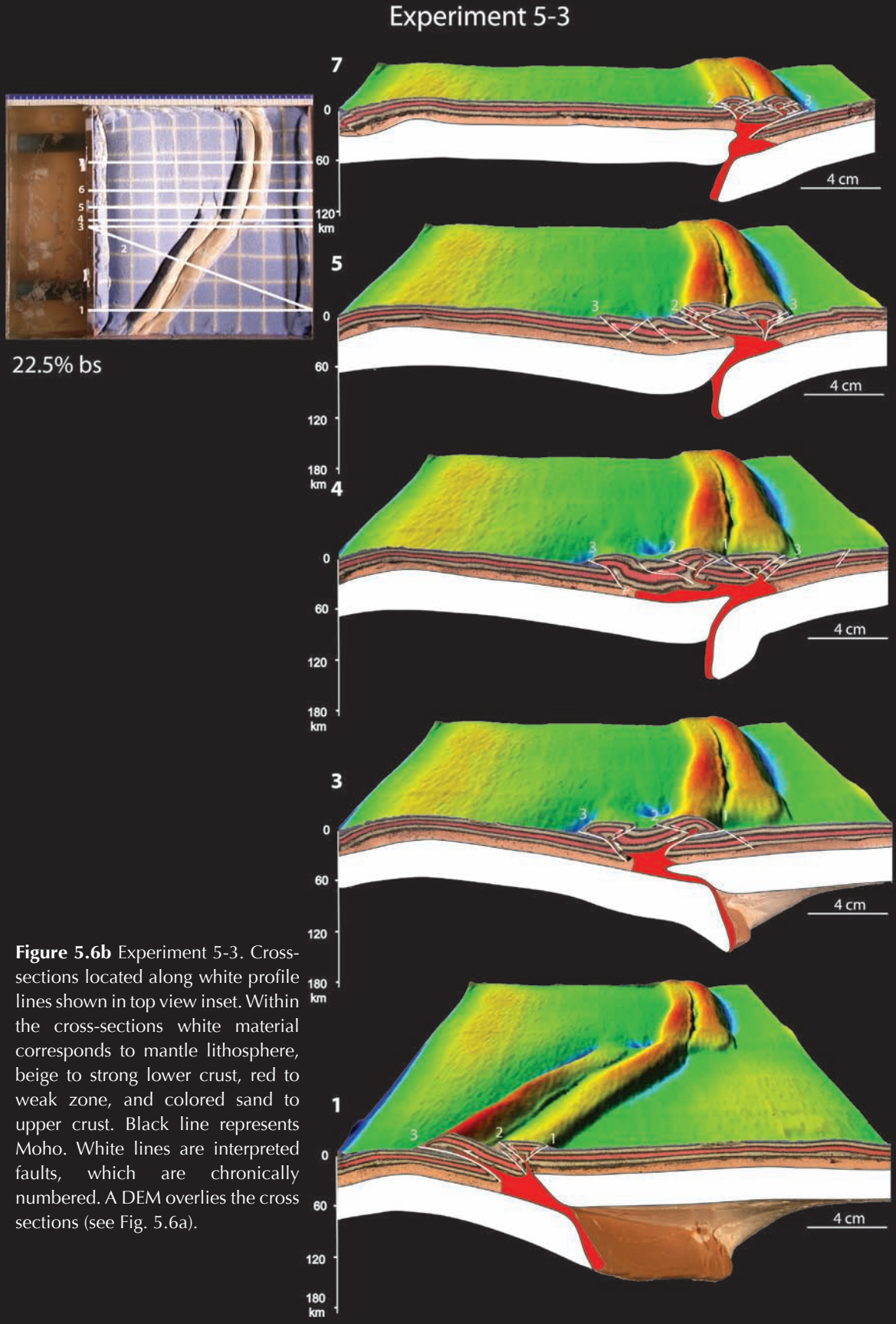

Figure 5.6b Experiment 5-3. Cross-sections located along white profile lines shown in top view inset. Within the cross-sections white material corresponds to mantle lithosphere, beige to strong lower crust, red to weak zone, and colored sand to upper crust. Black line represents Moho. White lines are interpreted faults, which are chronically numbered. A DEM overlies the cross sections (see Fig. 5.6a).

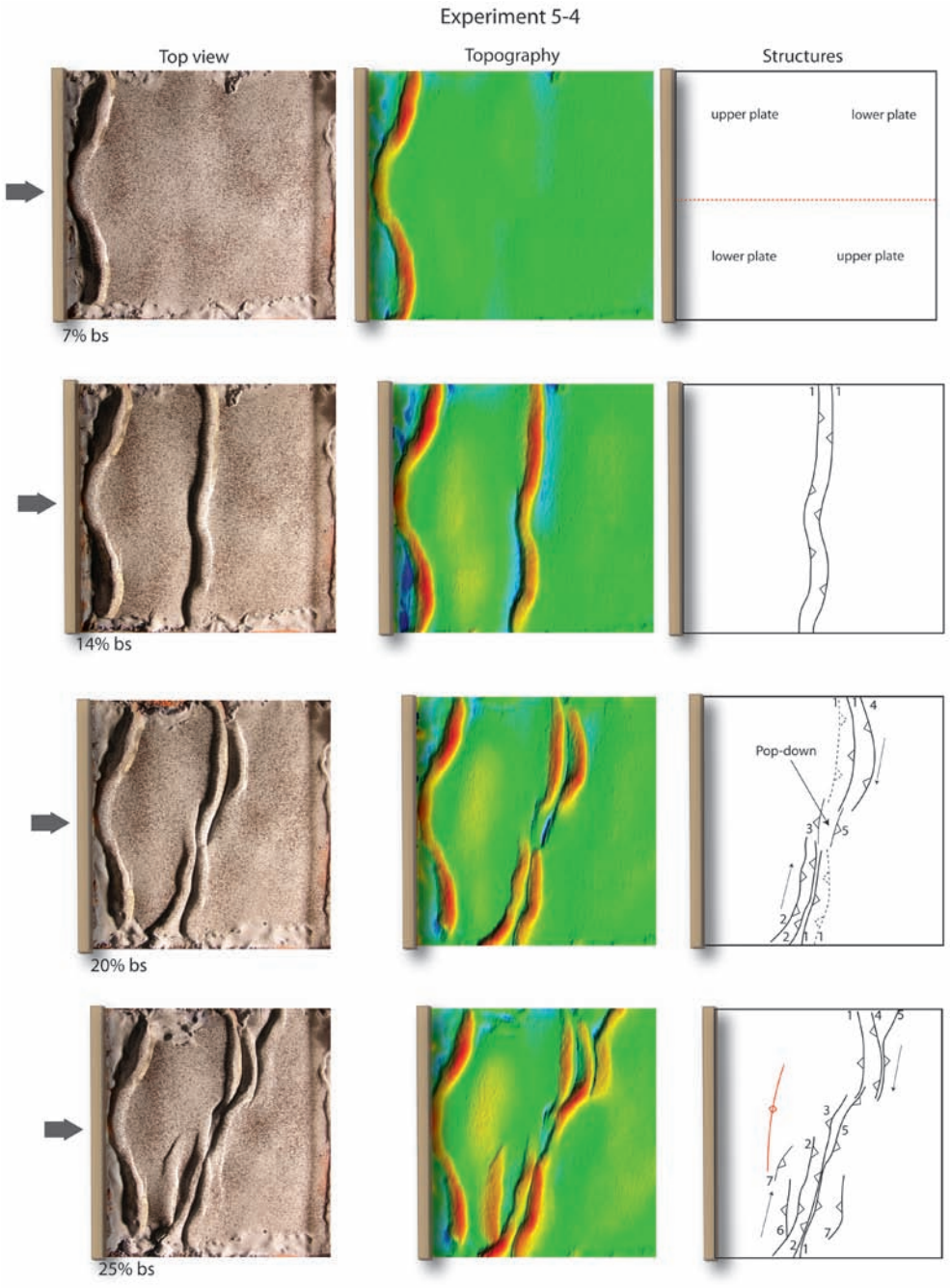

Figure 5.7a Experiment 5-4. Top views shown at intervals of 5% bulk shortening (bs). Pictures are shown in left column. Arrows refer to shortening direction. Red dashed line marks border between subduction domains with opposing subduction polarity. Middle column: topographic surface scans in where green is initial elevation while red and blue colors mark regions of uplift and subsidence, respectively. Right column: interpret faults chronically numbered. Black arrows indicate direction of lateral fault propagation and red line marks intra-plate fold axis.

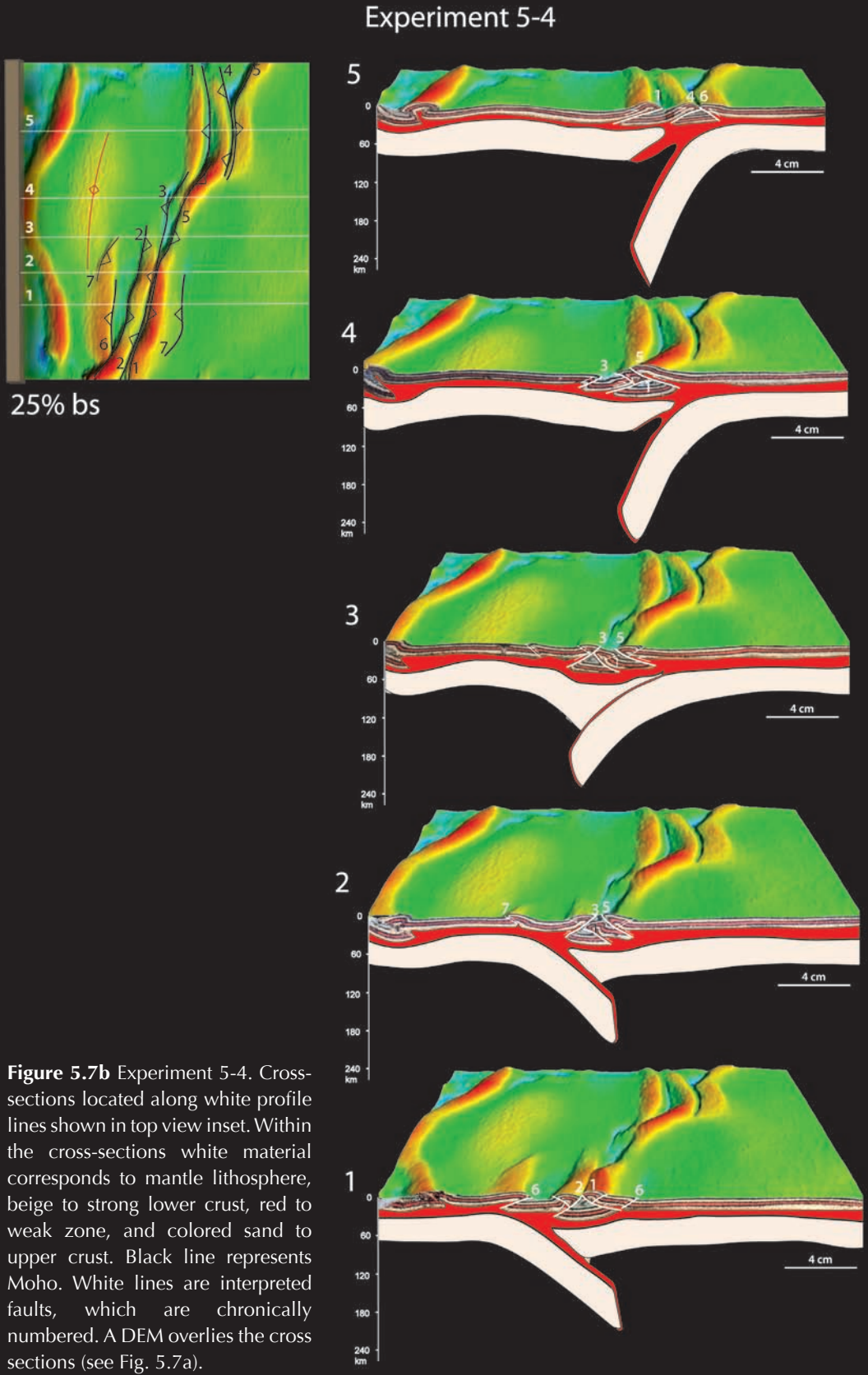

Figure 5.7b Experiment 5-4. Cross-sections located along white profile lines shown in top view inset. Within the cross-sections white material corresponds to mantle lithosphere, beige to strong lower crust, red to weak zone, and colored sand to upper crust. Black line represents Moho. White lines are interpreted faults, which are chronically numbered. A DEM overlies the cross sections (see Fig. 5.7a).

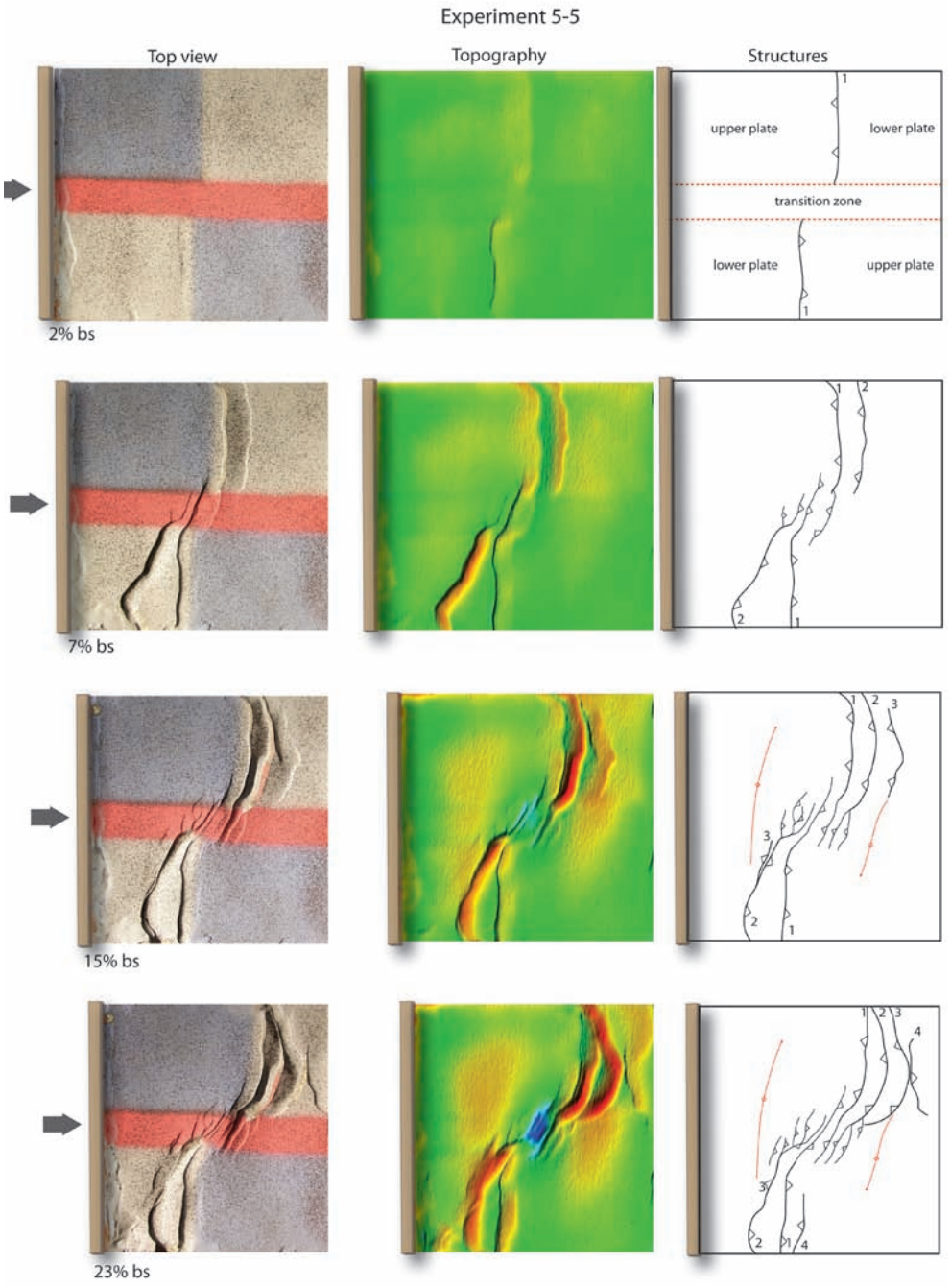

Figure 5.8a Experiment 5-5. Top views shown at intervals of 5% bulk shortening (bs). Pictures are shown in left column. Arrows refer to shortening direction. Red zone marks lithosphere domain without pre-defined subduction. Middle column: topographic surface scans in where green is initial elevation while red and blue colors mark regions of uplift and subsidence, respectively. Right column: interpret faults chronically numbered. Red line marks intra-plate fold axis.

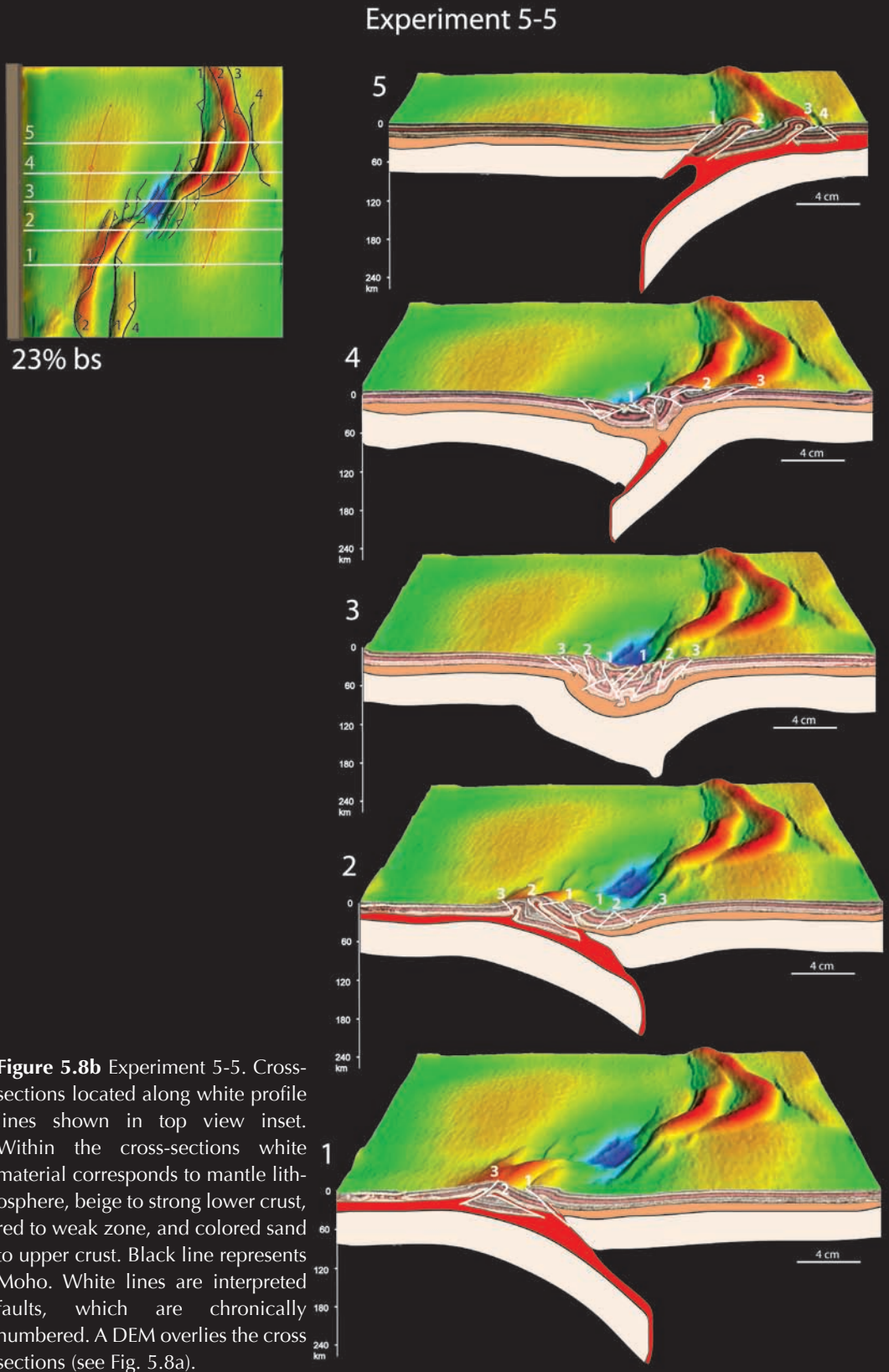

Figure 5.8b Experiment 5-5. Cross-sections located along white profile lines shown in top view inset. Within the cross-sections white material corresponds to mantle lithosphere, beige to strong lower crust, red to weak zone, and colored sand to upper crust. Black line represents Moho. White lines are interpreted faults, which are chronically numbered. A DEM overlies the cross sections (see Fig. 5.8a).

fore-trusts located onto lower plates, while within the transition zone a number of in sequence small thrusts propagated on both plates. The topographic portrays initial thrust induced uplift (Fig. 5.8a). Already in an early stage the highest elevations are found not along the plate contact, but on the lower plates. Laterally, topography lowered rapidly towards the transition zone, in which subsidence was bounded by minor thrust-related topography. Between 15% and 23% BS the plate interiors were uplifted. Cross sections show at mantle levels a combination of a reduction in the amount of subdcution and an increase of upper plate down bending towards the transition zone (Fig. 5.8b). Crustal deformation was largely restricted to the lower plates and resulted in lower crustal thickening and large thrust displacements. The dominant thrust direction is towards the lower plate, but also a few late-formed thrusts were orogen directed (e.g. thrust nr. 4 in profile 5). Near the transition zone, down bending of the upper plates resulted in minor pop-ups overlying strong lower crust as observed in profiles 2 and 4. The transition zone deformed as a large syncline (profile 3). Within this lithosphere fold, shortening was accommodated by many small thrusts within the brittle crust and by thickening of the ductile layers.

5.4 Short summary and comparison of modelling results

All experiments showcased strain pattern variability's in three-dimensions. Especially within the transition zone, subduction-style and wedge-geometry varied at relative short distances. Lateral widening of the transition zone was a general response on progressive shortening. Hence, an initial sharp boundary between the subduction domains grew out laterally into a wide region in where the amount of subduction was reduced, upper plates bended down, lower crust was thickened, crustal wedges were widened, and topography was lowered.

The final width of the transition zone as well as the expressions of related features were strongly influenced by the degree of coupling between the adjacent domains.

If the subduction domains were only weakly coupled (exp 5-1) widening of the transition zone was modest. As such, subduction below the transition zone seemed hardly hampered, and upper plate down bending and thrusting was only minor. Within the relative narrow transition zone the crustal wedge widened and symmetrically overlaid both plates. Directly adjacent to the transition zone, retro-shearing was more pronounced and shaped the wedge, resulting in high surface topography. This lateral structural difference resulted in a gradient of topographic lowering towards the transition zone.

If the subduction domains were strongly coupled, widening of the transition zone was more intense, as indicated by significant upper plate down bending, upper plate thrusting, and a broad area of only little uplift (exp. 5-2 and 5-3). Adjacent to the transition zone, retro-shearing affected the first pop-up, but owed to strong down bending of the upper plates, it did not produce a high relief. Subsidence of the entire wedge in combination with the onset of intra plate deformation during final shortening (20-26% BS) suggests increased plate coupling. Therefore, caution is needed in considering final subsidence and thrusting only the result of lateral interaction between subduction domains. A subsiding wedge and upper plate thrusting are namely also diagnostic for increased plate coupling (see Chapters 3 and 4).

Ongoing plate decoupling was assured for in experiments with an entire weak lower

crust (exp. 5-4 and 5-5). Moreover, crust-mantle decoupling affecting both plates (exp. 5-4) resulted in unconventional wedge structures including crustal pop-downs onto the upper plates. Consequently, lower lithosphere behaviour including subduction polarity could not be inferred from the crustal deformation pattern. The transition zone remained identifiable by subsidence as well as a lateral termination of faults. Where weak lower crust was limited to the lower plate, a relative wide pro-wedge formed on the subducting plates, allowing for determination of subduction polarity from surface structures. Near the transition, crustal faulting occurred on down bended upper plates.

5.5 Interferences between deforming layers

Deformation of the brittle crust strongly depends on the behaviour of the underlying viscous layers. In most of the presented experiments, crustal thrusting coincided with the presence of underlying weak lower crust. Here, deformation by shearing or thickening of the weak lower crust seemed to be the prime control on thrust initiation, localization of pop-ups, and therefore contributed significantly to surface topography as well. On the other hand, we have also seen that some thrusts root into strong lower crust (e.g. upper plate). In this scenario, less pronounced lower crustal shearing and thickening limited displacement and topography related to these faults. Based on their coexistence, upper plate thrusting was most likely triggered by down bending of the upper plates. This implies that the lateral extent of upper plate thrusting was underlain by lateral variations in the amount of down bending of primarily the mantle lithosphere. Therefore, to further interpret crustal deformation in relation to lateral change of subduction polarity we need to discuss the behaviour of the viscous layers along the transition zone in more detail.

Interferences in the transition zone

The mantle lithosphere responds on a lateral change of subduction polarity mainly by a reduction of subduction and increased down bending of the upper plate. Suggestively, both are the result from the interplay between lateral (along-strike) and orthogonal plate boundary forces. As such, the upper plates hamper subduction of the lower plates on the other side of the transition zone. The lower plates in turn drag down the adjacent upper plates (Fig. 5-9). The result is that the transition zone between the subduction domains is characterised by a mixed mode of deformation entailing subduction and folding. In addition, subduction within the transition zone was not only hampered by along-strike plate interaction, but also by increased plate coupling between colliding plates as a result from upper plate bending. Hence, lateral interplay existed at the junction between all four adjacent plates (Fig. 5.9).

The degree and lateral extent of this plate interaction is determined by: the degree of lateral decoupling, the initial width of the transition zone, the amount of bulk shortening, the angle between the subduction domains, and the strength of the mantle lithosphere(s). Lateral interaction is drastically reduced if the domains are decoupled by a “weak” horizon. A natural analogue of such a weakness can be for instance a STEP-fault [*Govers and Wortel*, 2005]. The initial width of the transition zone is also important on the extent of developing surface features. A relative wide transition zone, as implemented in exp. 5-5, accommodates most lateral induced strain and thus buffers the lateral forces

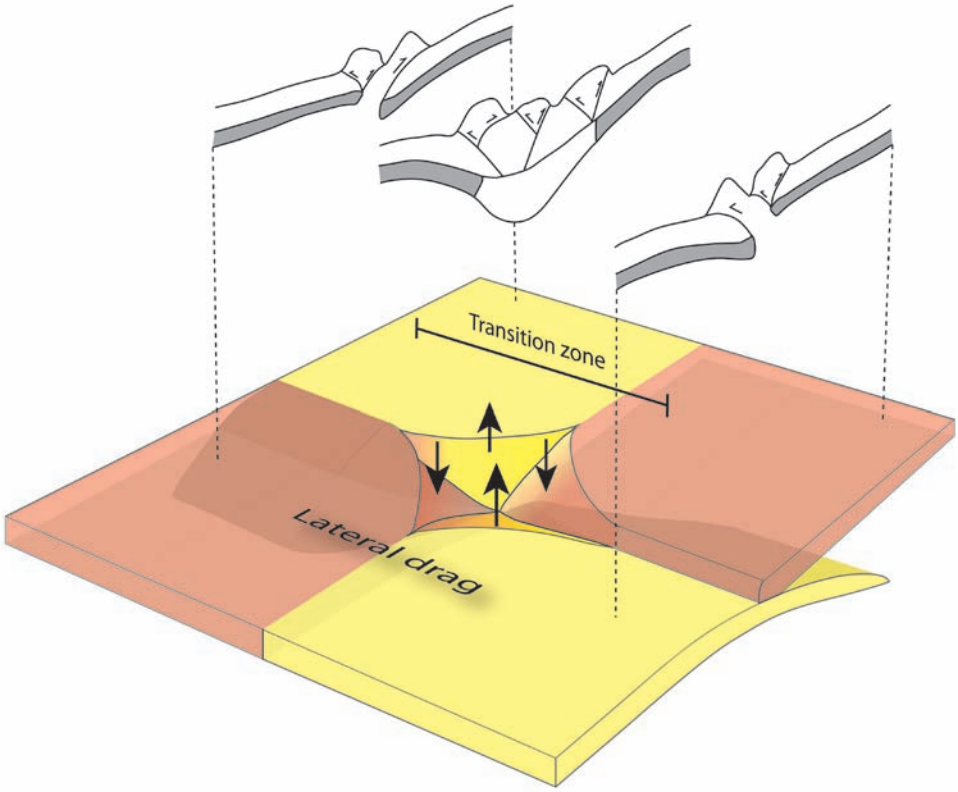

Figure 5.9 Sketch highlighting the development of a transition zone resulting from interplay between adjacent mantle lithospheres with opposing subduction polarity. Within the transition zone subduction of lower plates is hampered (up-pointed arrows) while upper plates are dragged down (down-pointed arrow). Simplified crustal sections at the top indicate lateral changes, such as wedge widening and lower crustal thickening, and are largely considered a response on the deforming mantle lithosphere. See text for more detail.

induced by the subduction domains. Increasing the amount of shortening increases lateral interaction by widening of the transition zone. In a very early stage of shortening (<3% BS), no significant interaction can be determined from surface features as the first pop-up crosses the domain boundary undisturbed. The angle between the domains with respect to the direction of shortening is important since it can create a space problem at depth. In experiment 5-3 for instance, oblique subduction transposed the slab below the "straight" domain and hence caused collision between subducting slabs at depth. The surface response of the adjacent upper plates on oblique subduction is difficult to reconcile. However, the relative narrow transition zone with respect to experiment 5-2, suggests interaction between the domains at crustal levels was less. In this series of experiment mantle lithosphere rheology has been kept constant, and therefore it is hard to pronounce upon its influence on strain patterns resulting from a lateral changing subduction polarity. Nevertheless, we presume that a weak mantle lithosphere easily "absorbs" lateral induced stresses resulting in a relative narrow transition zone.

5.6 Comparison with natural analogues

The presented modelling results indicate interplay between ductile and brittle deforming layers. Additionally it is shown that a lateral change in subduction polarity produces a region of reduced subduction, down bended upper plates, and thickened lower crust. A typical crustal response on these deep rearrangements is considered widening of the crustal wedge, and lowering of topography.

Implications of the modelling results concerning the interpretation of natural analogues, such as the Alps, are discussed below. First, a brief descriptive summary on the structural outline of the Alps from the deep structure towards the surface, highlighting the lateral variations observed at different depth levels, is presented. Second, alterations of wedge geometry during the Alpine Neogene evolution are compared with our modelling results.

5.6.1 Deep Alpine structure

The Alpine mantle lithosphere

Oppositely dipping European and Adriatic slabs have been inferred from high velocity zones observed on tomographic images [*Lippitsch et al.*, 2003] (Fig. 5.2 and 5.10). Below the Central Alps, the subducted European slab dips towards the southeast and reaches a depth of 240 km. The inferred 164 km of subducted material is consistent with the estimate on post-collisional crustal shortening from *Schmid et al.* (1996). In contrast to the Western Alps, the slab is still connected to the European lower lithosphere. Below the Eastern Alps, the slab represents 210 km of subducted Adriatic lower lithosphere and reaches a maximum depth of 230 km (Fig. 5.2). The amount of subduction is higher than below the Central Alps, but consistent with the estimated 210 km post-collisional shortening over the last 20 Ma [*Schmid et al.*, 2004]. Further east, the slab does not continue beyond 15° E (longitude of Zagreb), but despite this discontinuous slab, the Adriatic lithosphere can be traced continuously from the Eastern Alps into the Dinarides [*Ustaszewski et al.*, 2008]. The lateral transition between the opposing slabs measures about 80 km, and occurs roughly between the Tauern Window and the Giudicarie line (Fig. 5.10). Its subsurface is characterized by a sub-vertically dipping slab, which extends to 220 km depth into the surrounding asthenosphere (Fig. 5.10). Note, however, that the fuzzy outline does neither allow for defining its polarity nor for an accurate estimate on the amount of subduction [*Kissling et al.*, 2006].

Speculations on the underlying mechanisms producing the observed subduction polarity change are beyond the scope of this thesis. However, it should be noted that some authors proposed that the subduction of the Adriatic slab below the Eastern Alps is only an apparent one. In this view, the NE-dipping slab may represent a remnant of the Eocene orogeny in the Dinarides where Adria subducted towards the northeast [*Schmid et al.*, 1997; *Kissling et al.*, 2006]. The effect of displacement of the slab below the Alps is then prescribed by counter clockwise rotation of Adria [*Ustaszewski et al.*, 2008]. Note that emplacement of this “Dinaridic“ slab would have only been possible if the European slab gave way by slab break off around 30 Ma followed by slab retreat [*Ustaszewski et al.*, 2008].

Figure 5.10

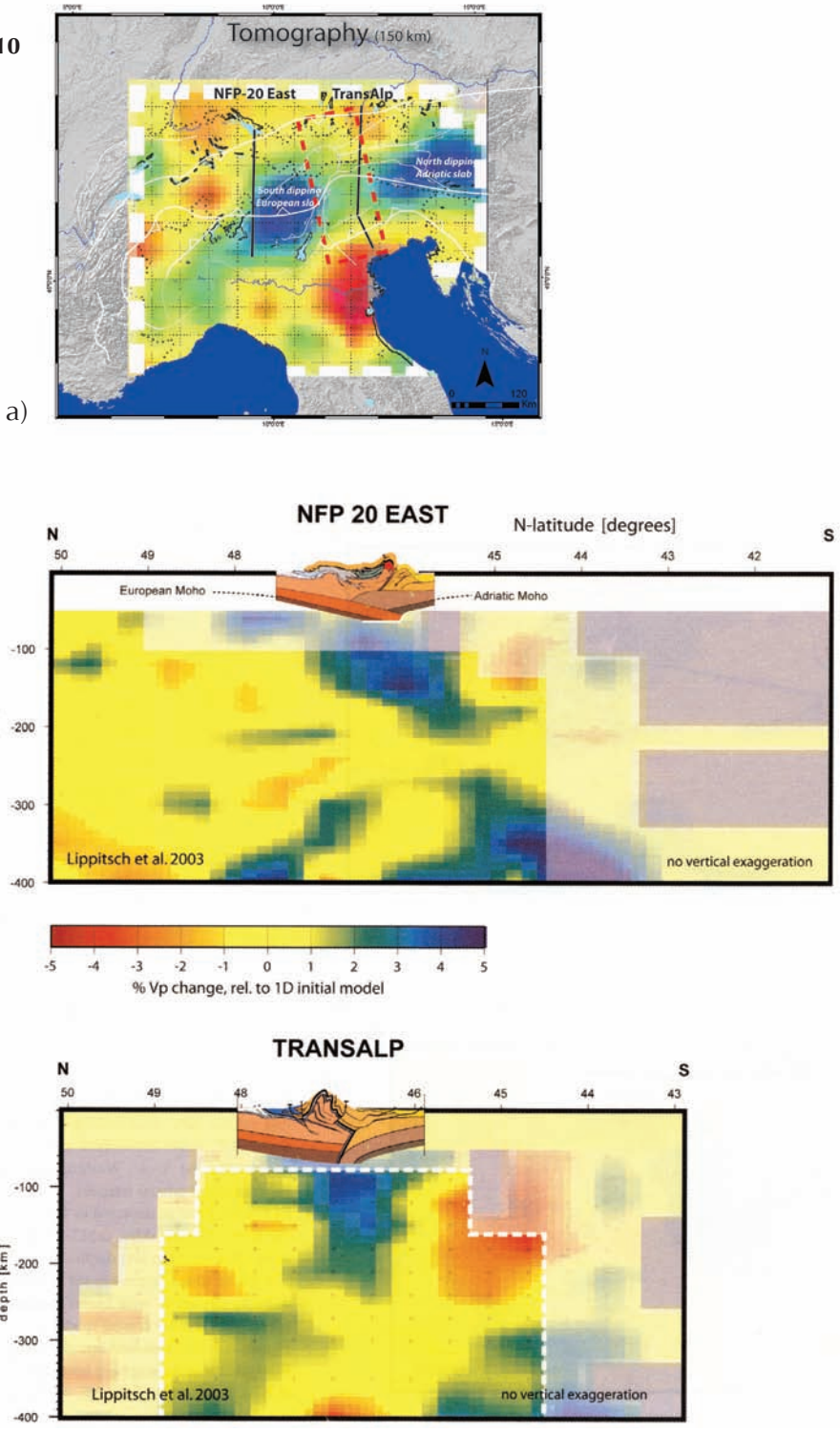
a)
Tomography (150 km)
NFP-20 East
TransAlp
North dipping Adriatic slab
South dipping European slab
N
0
120
km
b)
NFP 20 EAST
N-latitude [degrees]
N
S
50
49
48
45
44
43
42
European Moho
Adriatic Moho
-100
-200
-300
-400
depth [km]
Lippitsch et al. 2003
no vertical exaggeration
-5
-4
-3
-2
-1
0
1
2
3
4
5
% Vp change, rel. to 1D initial model
c)
TRANSALP
N
S
50
49
48
46
45
44
43
-100
-200
-300
-400
depth [km]
Lippitsch et al. 2003
no vertical exaggeration

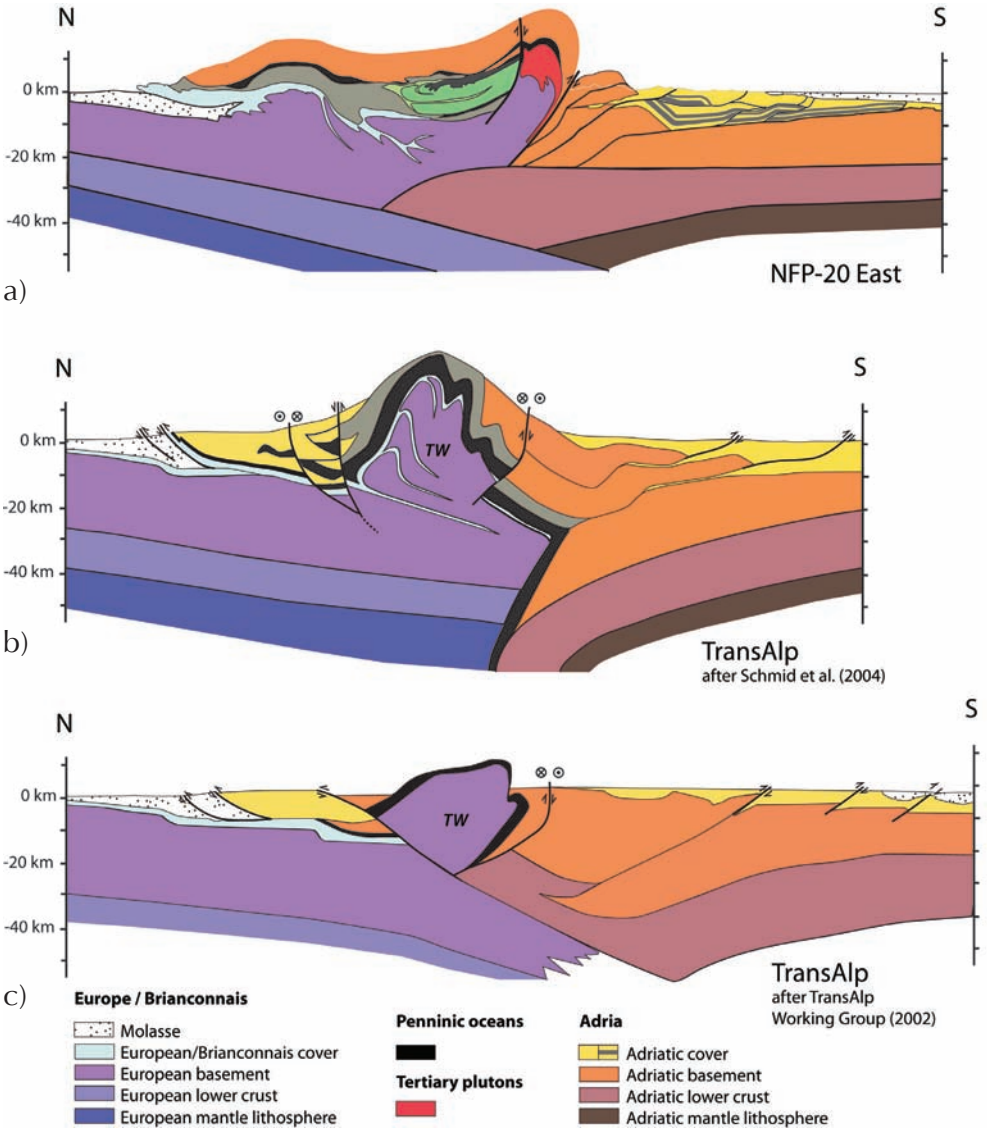

Figure 5.11 Lithosphere-scale cross-sections of the Alps. a) NFP-20 east modified after Schmid et al. (2004), and Schönborn (1999). b) TransAlp profile modified after Schmid et al. (2004). c) TransAlp profile modified after TransAlp Working Group (2002).

Figure 5.10 (facing page) Lower lithosphere transects, with superimposed crustal transects. a) Tomography of P-wave velocities conform Fig. 5.2a and locations of transects shown below. Red dashed square marks the transition zone region between the subducted slabs (see text for explanation). b) NFP-20 East. c) TransAlp. After Kissling et al. (2006).

The Alpine Moho geometry

The Alpine Moho topography reflects the large-scale Alpine structure resulting from the latest stage of continental collision [*Schmid and Kissling*, 2000]. Provided their relative positions are clearly defined, the sense of subduction can be inferred. The European and Adriatic Moho is contoured by *Dèzes and Ziegler* [2005] and displayed in Figure 5.12. Southward deflection of in particular the European Moho led to large scale asymmetry below the Western- and Central Alps. Deepest levels of the European Moho are reached directly north of the Periadriatic line (PA). The recorded Moho offset between Europe and Adria corresponds well with a subducting European plate. South of the PA the Adriatic Moho dips northward albeit less deep than its European counterpart. The very shallow Moho levels observed in the southwest are related to the Ivrea body and the Po plain. From here, the Adriatic Moho deepens eastward and curves together with the plate boundary northward below the Giudicarie region. Finally, the Moho pattern becomes more symmetric and deflections of both plates widen in the Eastern Alps. Here, the European and Adriatic Moho reach similar depths approximating 50 km near the PA just south of the Tauern Window. As a result of this symmetry, no clear subduction polarity can be deduced from the Moho topography below this region. Lateral contrasting Moho patterns below the Central- and Eastern Alps is also inferred by comparing the NFP 20-east and TransAlp transects, respectively (Fig. 5.11). Further east the European Moho shallows to 28 km at the transition to the Pannonian Basin [*Brückl et al.*, 2010]. The eastward extent of the Adriatic plate boundary into the Dinarides remains speculative [e.g. *Ustaszewski et al.*, 2008; *Brückl et al.*, 2010] To summarize the above, a lower plate position of Europe below the Western- and Central Alps is in line with the deeper slab geometry as derived from seismic tomography, whereas below the Eastern Alps northward subduction of Adria could not be inferred from the Moho topography, but solely from the underlying slab geometry.

The Alpine lower crust

The geometry of Alpine lower crustal units differs along strike, such that in the Western Alps wedging has doubled European lower crust resulting from collision with the relative strong Ivrea body [*Schmid et al.*, 1996]. On the other hand, below the Central Alps, Adriatic lower crust indents into European lower crust since mid- to late Miocene times [*Schmid et al.*, 1996]. This interpretation implies a relative strong Adriatic lower crust, as well as decoupling along the Moho and the brittle-ductile transition. In addition, lower crustal wedging was used to explain the northward exhumation trend seen in the Central Alps. [*Rosenberg and Berger*, 2009] (Fig. 5.13). The eastward continuation of this lower crustal wedge is however uncertain. Different interpretations of the TransAlp seismic transect involve various lower crustal geometries. The TransAlp Working Group (2002) suggests that wedging of Adriatic lower crust is continuous below the Eastern Alps (Fig 5.11), while interpretations from *Schmid et al.* (2004) include no lower crustal wedging. In either case a significant amount of European lower crust thickened below the Tauern Window, while the bulk of lower crust must have been subducted in order to balance the amount of total post-collisional shortening.

5.6.2 Alpine Neogene Evolution: Central Alps versus Eastern Alps

In order to relate uplift and topography formation in the model to exhumation and cooling in nature, the Neogene tectonic evolution of the Alps is briefly summarized. Emphasis is given on the Neogene evolution since this is the period of slab retreat leading to subduction polarity change [*Lippitsch et al.*, 2003; *Kissling et al.*, 2006; *Ustaszewski et al.*, 2008]. A distinct evolution throughout the Neogene between the Central- and Eastern Alps has been previously summarized by *Rosenberg and Berger* (2009). In this section their most relevant conclusions are highlighted as a run-up to a comparison with our model results.

Cooling patterns

The first phase of post-collisional shortening affecting the Western- and Central Alps was characterized by back thrusting and nappe folding in the axial zone located directly north of the Periadriatic line [*Escher et al.*, 1988; *Rosenberg and Berger*, 2009]. The coinciding uplift resulted in the exhumation of the internal massifs, such as the Lepontine dome, which cooled below 110 °C between 23 Ma and 15 Ma [e.g. *Hurford*, 1986]. The distribution of ZFT and AFT ages reveals that rapid cooling shifted northward from the area bounding the retro-wedge (PA) to the area bounding the pro-wedge (Aar Massif) (Fig. 5.13). The second phase of post-collisional shortening is defined by uplift of the external massifs, such as the Aar massif occurring between 15 Ma and 2 Ma. [*Reinecker et al.*, 2008; *Rosenberg and Berger*, 2009]. The external crystalline massifs are expressions of exhumation of the lower plate (Europe) in an external position [*Fügenschuh and Schmid*, 2003]. The shift of exhumation front from the Leopontine to the northern margin of the external massifs led to a relative wide zone of exposure of Tertiary metamorphic rocks. This metamorphic zone is much wider compared to the metamorphic Tauern Window of the Eastern Alps [*Bousquet et al.*, 2008]. In the Eastern Alps, fission track ages indicate focussed exhumation within the TW throughout the Miocene [for compilation see *Luth and Willingshofer*, 2008, or Chapter 2] (Fig. 5.13). The dome-like cooling pattern distinguishes the Tauern Window from the metamorphic massifs in the Western- and Central Alps (Fig. 5.13b). In addition, the vast amount of Austroalpine units observed in the Eastern Alps cooled already before Neogene times [e.g. *Hejl*, 1997].

Wedge geometry from Miocene to present

Widening of the wedge varied both in time and geometry between the Central- and Eastern Alps. In general, the width of the active orogen, defined as the distance between the most external active thrusts, did increase from Oligocene to early Miocene times as concluded on the basis of sedimentological findings (Fig. 5-14) [*Schumacher et al.*, 1996]. From the early Miocene onward lateral differences between the Western/Central- and the Eastern Alps initiated both in the northern external zones as well as in the Southern Alps.

The northern frontal zone of the Western Alps is characterized by an increase of width when deformation jumped more than 80 km into the foreland forming the Jura Mountains during late Miocene-Pliocene times. Besides the presence of weak anhydrite layers being the cause of this transfer into thin skinned tectonics, Pliocene overprinting

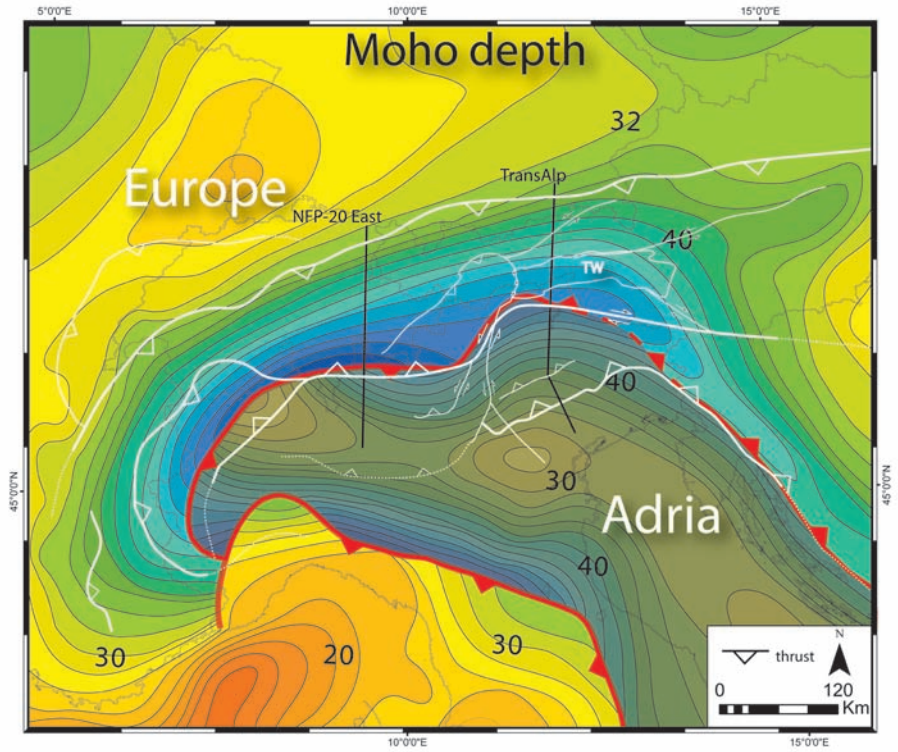

Figure 5.12 Contoured Moho depth map of the European and Adriatic plate (brownish) modified after Dèzes and Ziegler [2005]. Suture zone and subduction polarity are marked in red. Numbers are in kilometers.

relationships and seismicity indicate more recent thick-skinned tectonics [*Giamboni et al.*, 2004; *Madritsch et al.*, 2008; 2009]. This northward shift of recent deformation was restricted to the northwestern corner of the Alpine arc. In contrast, despite some reactivation of thrusts in the North Alpine Molasse Basin until 5 Ma, northward thrusting of Austroalpine units already ended at 17 Ma in the Eastern Alps [*Linzer et al.*, 2002]. Since then the internal Eastern Alps were deformed by the process of eastward lateral extrusion [*Ratschbacher et al.*, 1991]. Extrusion initiated probably not before 23 Ma and major strike-slip motions lasted until 13 Ma [*Frisch et al.*, 1998]. However, cessation of extrusion is debated since recent dating of damaged speleothems indicates ongoing extrusion along the SEMP fault [*Plan et al.*, 2010]. Throughout the Miocene, the northern Eastern Alps were characterized by a lateral topographic gradient [*Frisch et al.*, 1998]. In here, the western Eastern Alps were already mountainous in the Early Miocene, whereas

Figure 5.13 (facing page) a) Along-strike variations in AFT- and ZFT-cooling trends transposed on the outlined (dashed line) subducting slabs at 150 km. Northward distributed Neogene cooling is the overall pattern in the (western) Central Alps, while in the Eastern Alps a dome-like cooling pattern is restricted to the Tauern window. b) Temperatures in the Tauern Window around 20 Ma (See Chapter 2) indicating diachronous cooling between the western and eastern TW. Note the abrupt temperature drop along the western border (Brenner line).

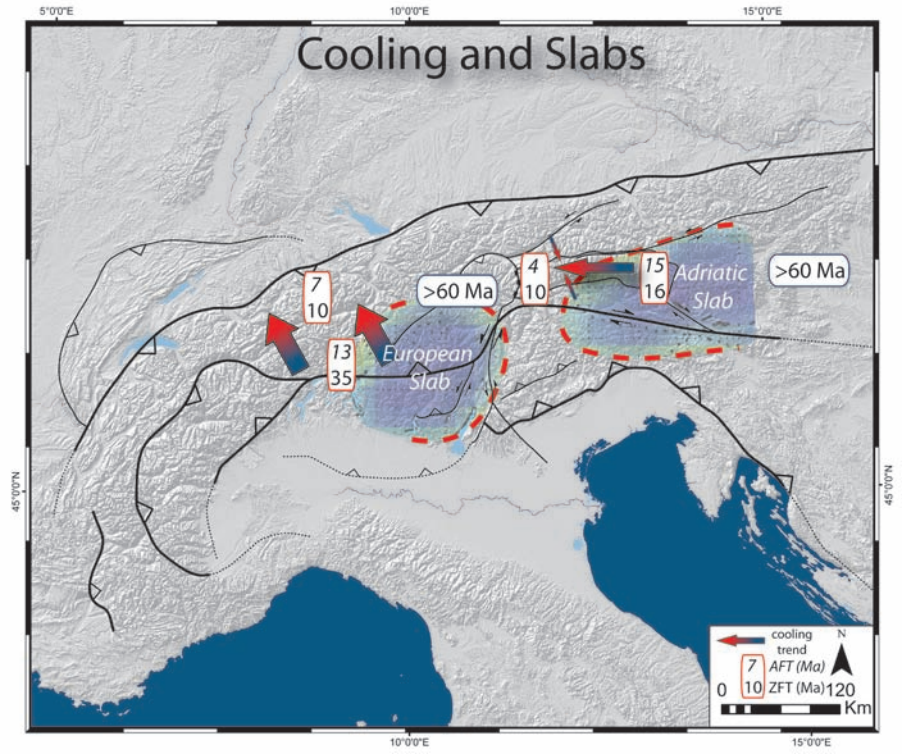

a)

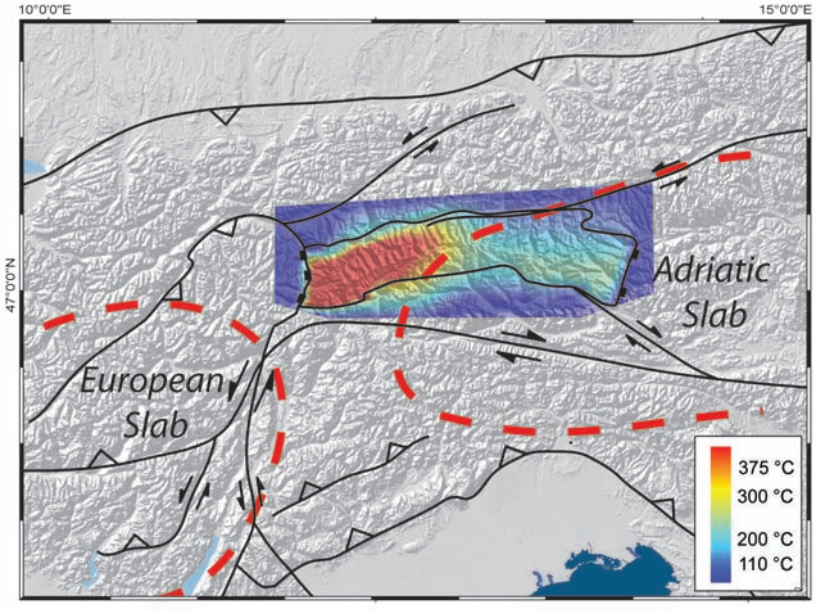

b)

(Figure 5.13)

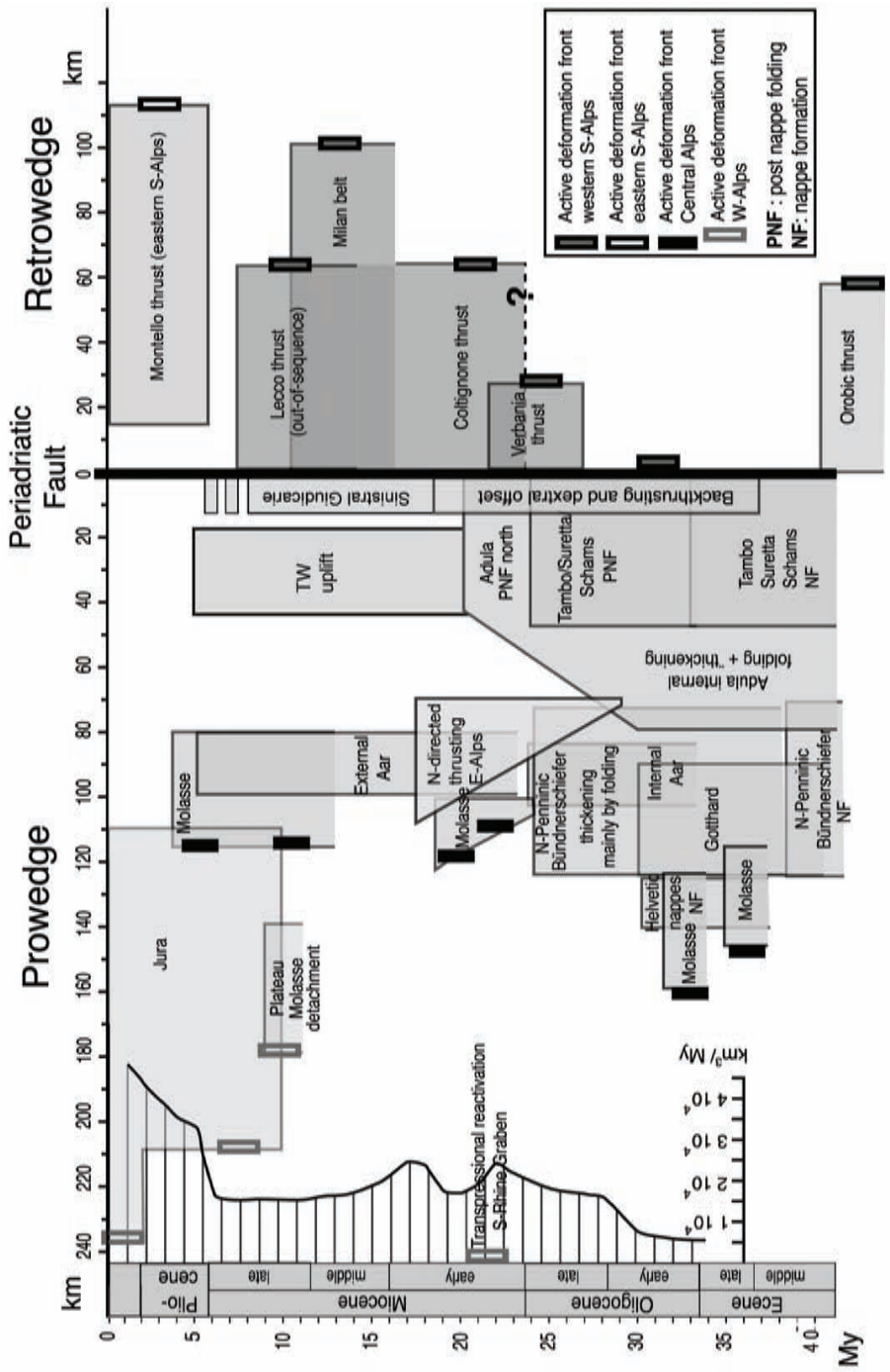

Figure 5.14 Migration of the active Alpine deformation front with respect to the present-day site of the Periadriatic fault. Gray boxes illustrate tectonic phases in time and space. Horizontal bars and associated curve on the left side show the sediment budgets after *Kuhlemann* (2000). Diagram is modified after *Rosenberg and Berger* (2009).

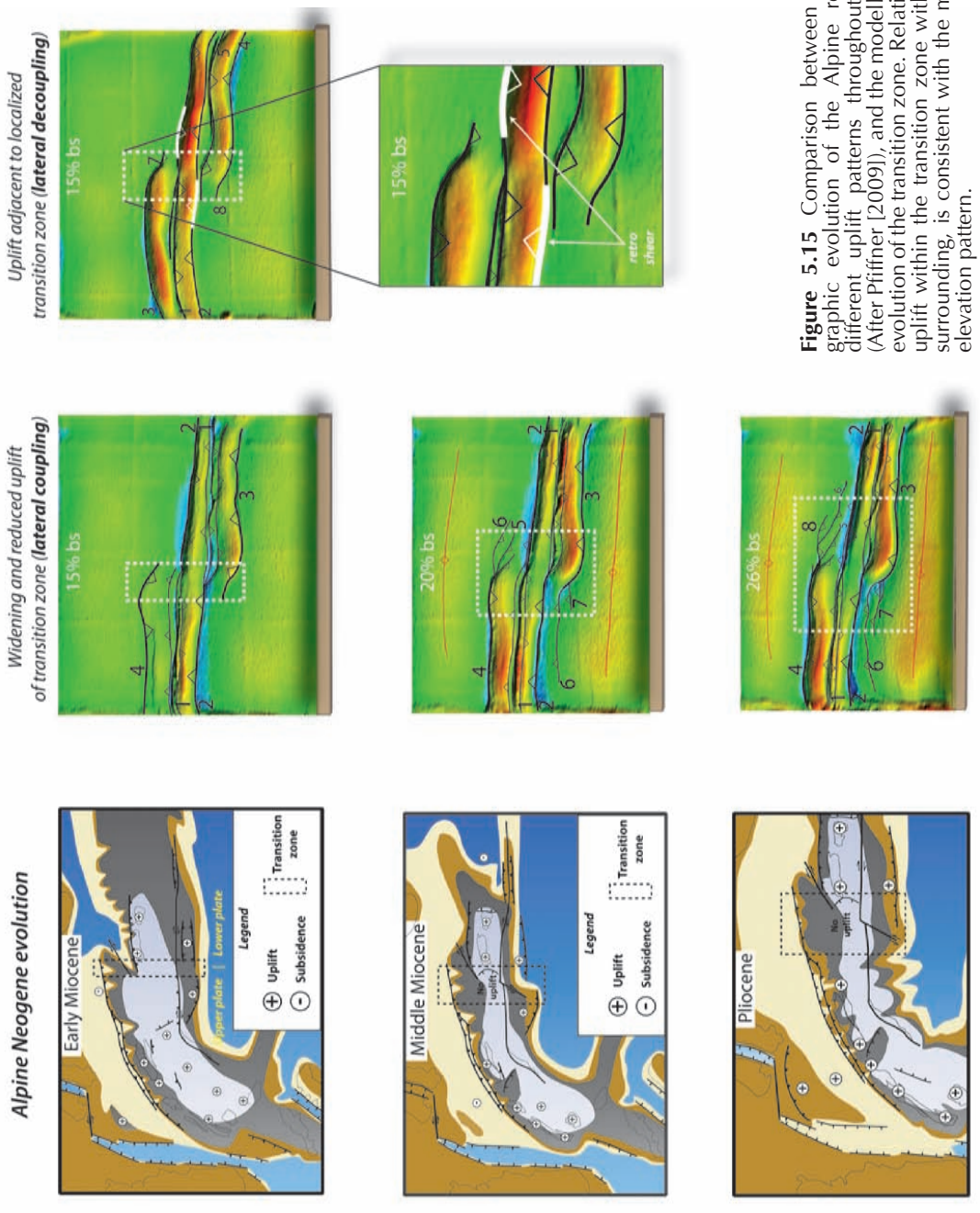

Figure 5.15 Comparison between the paleogeographic evolution of the Alpine region showing different uplift patterns throughout the Miocene (After Pfiffner [2009]), and the modelled topographic evolution of the transition zone. Relative little vertical uplift within the transition zone with respect to its surrounding, is consistent with the modelled lateral elevation pattern.

the eastern part became mountainous not before the Late Miocene (Fig. 5-15). This lateral topographic distinction has been assigned to the process of lateral extrusion.

In the Southern Alps, initiation of shortening and the amount of shortening is poorly constrained owed to lack of Miocene sediments [e.g. *Roeder,* 1992; *Schumacher et al.,* 1996; *Schönborn,* 1999; *Stipp et al.,* 2004; *Castellarin et al.,* 2006]. Most of these authors suggest thrusting is not older than 20-16 Ma based on the overprinting relationships between the Periadriatic line and Giudicarie line. In the western Southern Alps, the Milan belt formed during the Middle-Late Miocene, and was followed by a retreat of the active wedge by temporarily out of sequence thrusting (Fig. 5.14). The estimates on total amount of Neogene shortening in the western Southern Alps range between 30 and 70 km [*Roeder*, 1992; *Schönborn,* 1999; *Castellarin et al.*, 2006]. Thrusting in the western Southern Alps lasted probably until the Messinian [*Schmid et al.*, 1996; *Schönborn,* 1999; *Castellarin and Cantelli,* 2000; *Stipp et al.,* 2004]. However, it has been argued that younger Southern Alpine shortening migrated all the way to the frontal thrust of the Apennines [Piana, 2000; Rosenberg and Berger, 2009]. In either case, the amount of shortening must have been minor owed to Adria's anticlockwise rotation causing a westward reduction in northward plate motion [*Schönborn,* 1999; *Caporali and Martin*, 2000; *Ustaszewski et al.,* 2008].

In the eastern Southern Alps, shortening probably also initiated in the Early Miocene, and was coeval with the sinistral displacement of the PA by the Giudicarie line, and shortening and exhumation of the Tauern window [e.g. *Picotti et al.*, 1995; *Fügenschuh et al.*, 1997; *Schönborn*, 1999; *Laubscher*, 2010]. Apatite fission track ages, which are generally sparse throughout the Southern Alps, document uplift along the Valsugana thrust around 10 Ma [*Zattin et al.*, 2006]. Estimations on the amount of Miocene shortening in the eastern Southern Alps range between 35 km and 50 km [*Schönborn*, 1999; *Castellarin et al.*, 2006]. Note that this amount, although a little bit less, is comparable to the western Southern Alps (see also Rosenberg et al., 2009). In contrast to the western Southern Alps, however, uplift and shortening is still ongoing as indicated by present-day seismicity along the Belluno thrust [*Benedetti et al.*, 2000; *Castellarin and Cantelli*, 2000].

In summary, deformation-style and exhumation differ significantly between the Western- and Central Alps and the Eastern Alps. During the early-mid Miocene, exhumation of the internal massifs in the Western- and Central Alps was coeval with southward thrusting in the Southern Alps, whereas from the Late Miocene onward exhumation of the external massifs was coeval with thrusting in the Jura Mountains. In contrast, in the Eastern Alps rapid exhumation of the Tauern Window was coeval with southward thrusting during almost the entire Miocene.

Erosion and topography

Although not implemented in our models, erosion exerts an important control on the style of deformation of a growing crustal wedge [e.g. *Beaumont et al.*, 2000]. In general, fast erosion rates and the removal of topography localize deformation and the wedge reaches a steady state. Low erosion rates lead to an increase of mass in the orogen, and result in outward growth of the wedge [*Willett et al.*, 2006]. Hence, the evolution of the Alpine wedge cannot be solely explained by tectonic factors, but needs to include

erosional efficiency throughout the Neogene as well. So far, variations of erosional efficiency are inferred from low temperature geochronology and the sediment volumes deposited in the sedimentary basins. [*Kuhlemann et al.*, 2001]. Correlations between changes in the efficiency of erosion, climate change, and the shift of the alpine deformation front throughout the Miocene have been used to emphasise a strong climate control on the growth of the Alpine [e.g. *Willett et al.*, 2006]. However, the role of climate on shaping the Alpine wedge throughout the Neogene has been criticized by *Rosenberg and Berger* [2009], who argued for 1) a misfit between timing of erosion reduction and wedge growth during the mid-Miocene, and 2) ongoing shortening in the Southern Alps during a rapid increase in erosion efficiency during the post-Messinian. According to *Rosenberg and Berger* [2009] these contradictions suggests that erosion was not the controlling factor on wedge growth. Moreover, a similar trend in the sediment budgets of the Western, central and Eastern Alps, should indicate coeval lateral shifts of the exhumation fronts of these parts (Fig. 5.14) [*Rosenberg and Berger*, 2009]. However, as discussed above, remarkable differences in deformation-style and exhumation exist between those regions, suggesting that erosion was not the prime control on the observed lateral variations.

5.6.3 Consistency between model results and Alps

Comparison between the model results and the Alpine orogeny alludes to consider certain Alpine features as the expression of the lateral change in subduction polarity. In this context, the first order modelling results, indicating the correspondence between along-strike variation at depth and along strike-variations at crustal levels, are consistent with the Neogene Alpine evolution comprising along-strike variations between the Central- and Eastern Alps. As such, three-dimensional complexities, comprising wedge geometry and surface topography, can be explained by a lateral change of subduction polarity.

The modelled deep plate geometry, resulting from a lateral change in subduction polarity, is comparable with the interpreted outline of the lower lithosphere below the Alps. The transition zone, defined as the region where adjacent plates interact, is then located between the opposing subducted slabs and extends within the Alps from the western Tauern Window towards the Giudicarie line. This region is characterized by lateral discontinuous subducting slabs marked as a "gap" displayed by tomography [*Lippitsch et al.*, 2003]. Here, the amount of mantle lithosphere subduction dropped significantly and down bending of both lithospheres occurred (Fig. 5.10). Additionally, down bending of both plates below this region appears from the Moho topography (Fig. 5.12). At some distance from the transition zone the upper plate recovered from down bending as inferred from Moho topography and interpretations on the NFP-20 east transect. Furthermore, a significant amount of lower crustal thickening occurred within the modelled transition zone. Hampering of mantle lithosphere subduction was probably the main cause of this thickening similar to experiments described in Chapter 4. Within the Alps, indications for lower crustal thickening below the transition zone do exist, and are primarily based on the thick nappe stack of mainly ductile deformed rocks now exposed in the Tauern Window. Hence, the lower lithospheric strain pattern observed in our models seems to be consistent with the Alpine configuration.

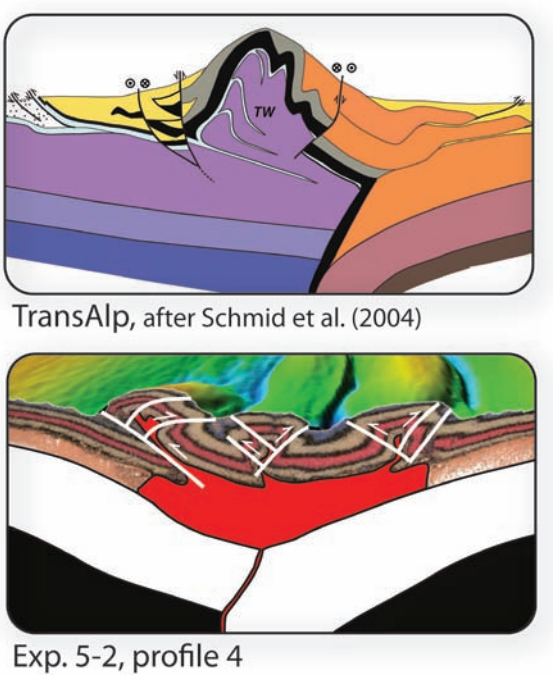

Figure 5.16 Comparison between wedge geometries from TRANSALP interpretation of Schmid et al. (2004) and experiment 5-2.

At upper crustal scale, the modelled crustal wedges grew mainly onto the lower plates and induced along-strike variation by the termination of lower plate thrusts in the transition zone. A similar pattern on wedge growth characterized the Alps since the middle to late Miocene as portrayed by the TransAlp transect (Fig. 5.16). A northward cooling trend together with the formation of the Jura Mountains in the Western- and Central Alps contrasts with uplift in the Tauern Window coeval with southward thrusting in the Eastern Alps [*Rosenberg and Berger*, 2009] In addition, geometric features such as widening of the orogenic wedge as well as its large-scale symmetry are a good analogue for the modelled transition zone. Furthermore, it is worth noticing that prominent crustal features, such as the sinistral Giudicarie fault and the Brenner normal fault, have no modelled equivalents. These structures and in particular the Giudicarie fault have been interpreted to be the surface expression of the subduction flip [*Schmid et al.,* 2004; *Laubscher,* 2010]. A simple explanation for their absence might be related to the fact that no lateral rheology contrast existed in the models, which allowed for the formation of relative small, discrete brittle strike-slip faults. In addition, the lateral shear induced by the subduction zones affecting the entire lithosphere was accommodated within a wide region in where no brittle deformation localized. However, the Giudicarie fault pattern is probably also related to a combination of indentation and eastward extrusion. Analogue models, which mimic this crustal pattern, are presented by *Rosenberg et al.* [2007] and Chapter 6.

The modelled uplift pattern within and around the transition zone has implications for interpretations involving the Alpine exhumation (Fig. 5.15). The modelled topographic lows, which characterize the transition zone, can be compared with regions in the Alps where uplift was minor throughout the Neogene. Such conditions are fulfilled for the Ötztal complex, which is located between the TW and the Central Alps. Here, the bulk of the Austroalpine units underwent cooling below 110 °C already before Neogene times [*Fügenschuh et al.*, 1997; *Hejl*, 1997] (Chapter 2). Since then no major uplift phases affected this region. In this perspective, the Ötztal complex can be considered as part of the transition zone. In our experiments the relative low transition zone was bounded by relative high elevated regions (e.g. exp 5-1). These uplifted regions might be compared with the Miocene uplift affecting mainly the western Tauern window. An important role is then assigned for the Brenner fault, which accommodated relative subsidence in the Ötztal complex and relative uplift in the Tauern window according to the observed cooling pattern (Fig. 5.13) (Chapter 2). In addition, the observed diachronous cooling in the Tauern Window indicating that rocks of the eastern Tauern Window were already cooled to around 230 °C at 20 Ma, suggests that the western Tauern Window represents the uplifted eastern "rim" of the transition zone (Fig. 5.13b).

In summary, the modelling results show relevance with respect to the crustal and lithosphere-scale structure of the Alps and the associated vertical movements. The orogenic wedge in the Western Alps is asymmetric and a relatively large pro-wedge overlays the downgoing European plate. Eastwards, the upper crustal deformation is more symmetrically distributed above both colliding plates, and the orogen widens reaching maximum values along the TransAlp profile. In general terms, lateral variations of the crustal architecture such as symmetry of mountain belts may be indicative for changes in the subduction polarity of the lower lithosphere. Or in other words, a lateral subduction flip at mantle depth promotes primarily complex three-dimensional deformation, and produces along-strike variations throughout the lithosphere.

5.6.4 Another natural analogue: New Zealand

Besides the Alps, the model results may have implications for understanding other collision zones where a continental plate transitions along-strike into another subduction zone. For instance, in the New Zealand region the Pacific-Australia plate boundary has been considered a continuous feature. However, a lateral distinction can be made between three domains accommodating convergence differently. As such, the Southern Island is a region of active continental collision, but is bounded by oceanic plate subduction with opposing polarity. Beneath North Island the oceanic lithosphere of the Pacific plate subducts westward below the Australian plate (Hikurangi zone), whereas south of South Island the Australian plate steeply subducts eastward beneath the Pacific plate (Puysegur) (Fig. 5.17a). The subduction zones are linked by the dextral transpressive Alpine fault that runs along Southern Island and accommodates most of the highly oblique convergence. Note that this fault is a long-lived feature that was previously (20 Ma) active as a strike-slip plate boundary, and can therefore not be considered as an expression of lateral subduction polarity change. Despite the continuous transform fault, the Southern Island is characterized by along-strike variations comprising the orogens width and the amount of uplift [e.g. *Upton et al.*, 2009]. Interpretations on the deep

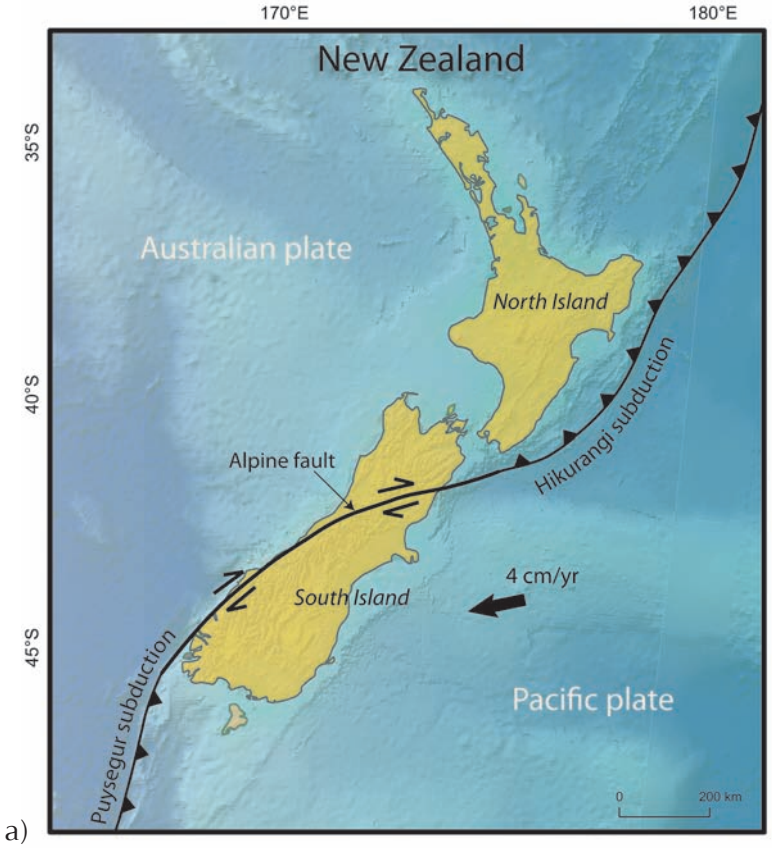

a)

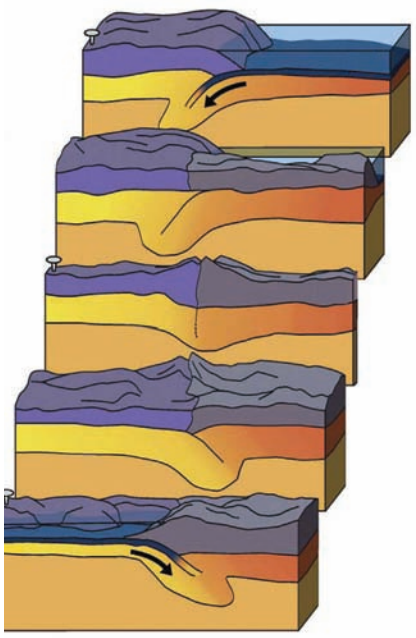

b)

Figure 5.17 a) Map displaying the tectonic setting of New Zealand. Two subduction zones with different polarity trend along strike, and are connected by the transpressive dextral Alpine fault zone. Black arrow indicates direction of relative plate motion. b) Schematic cartoon from Pysklywec et al. [2010] of the lateral change of subduction polarity in New Zealand (not to scale) based on numerical modelling results from the same authors.

structure vary between steep westward underthrusting of Pacific mantle to distributed thickening of a mantle root [*Stern et al.*, 2000]. In either case, tomographic images do indicate along-strike variations where broad roots of thickened lithosphere occur close to the subduction zones [*Kohler and Eberhart-Phillips*, 2002].

Based on 3-D numerical modelling by *Pysklywec et al.* [2010], lateral variations of mantle lithosphere geometry below Southern Island can be well explained by a lateral effect of the adjacent subduction zones (Fig. 5.17b). As such, subduction induced descending of adjacent mantle lithosphere, which implies coupling between the subduction zones and the intervening continental lithosphere. Such explanation is also consistent with our obtained model results where along strike variations are due to the influence of bounding subduction. For instance, descending mantle lithospheres affecting a "regular" (non-subducting) lithosphere" occurred in experiment 5-5 (Fig. 5-8a-b). In this experiment, however, the surface of the intervening domain finally subsided, caused by the interplay of buckling and lateral down warping by the neighbouring continental lithospheres. Intuitively, referring to the New Zealand setting, the lateral interaction induced by subducting oceanic lithosphere would be probably less than that of continental lithosphere. Nevertheless, in both the New Zealand and the Alpine settings, evolution of mantle lithosphere seems susceptible to the larger scale geodynamics around it.

5.7 Conclusions

Analogue lithosphere-scale models, which simulate a lateral polarity change of mantle lithosphere subduction, produce major variations along the orogens strike. As such, an initial sharp boundary between adjacent subduction zones grows out laterally into a wide region where the amount of subduction is reduced, upper plates bend down, lower crust is thickened, crustal wedges are widened, and topography lowered. The degree of lateral interaction correlates with the degree of (de)coupling between the subduction domains. In addition, the experiments stress the dependence of crustal deformation on the behaviour of the underlying viscous layers. Lower crustal shearing and thickening govern upper crustal thrusting and surface topography, respectively. In contrast, thrusting above strong lower crust only happened in the scenario where the entire plate strongly descends, such as down bending of the upper plate along the plate contact.

The modelling results show a first order consistency with along-strike variations of crustal and lithosphere-scale structure throughout the Alps. In particular, the transition from an asymmetric wedge in the Western- and Central Alps towards a wide and symmetric wedge in the Eastern Alps is in line with the gradual change of subduction polarity. Hence, along-strike variations of the crustal architecture, such as symmetry of mountain belts, may be indicative for lateral changes in the subduction polarity.

Chapter **6**

Kinematic analysis of the Passeier- and Jaufen faults: Linking the Giudicarie and Brenner lines?

6.1 Introduction

Orogens often contain a crustal unit which fulfils the role of an indenter and intensively deforms adjacent regions. Typically, indentation has a strong imprint on the crustal strain pattern ranging from local fault kinematics to the entire shape of an orogen [e.g. *Molnar and Tapponnier*, 1975]. Important actors affecting the resulting strain pattern are indenter shape, motion path, upper- or lower-plate position, and rheology contrast between the indenter and the indented plate.

Within the Eastern Alps, the pattern of brittle deformation and young exhumation of highly metamorphosed rocks is attributed by many authors to indentation tectonics [e.g. *Ratschbacher et al.*, 1991; *Rosenberg et al.*, 2007]. In this scenario the advancing Adriatic plate including the Southern Alps is considered as an indenter. The triangular outline of the indenter is the result of three fault segments, which are from west to east the Giudicarie line, Meran-Mauls line, and Pustertal line (Fig. 6.1). Activation of these fault segments was coeval with deformation and uplift in front of the indenter affecting also the Passeier-, Jaufen-, and Brenner faults [*Laubscher*, 1996; *Fügenschuh et al.*, 1997]. These faults are considered to represent a combined fault system due to their synchronic activity [e.g. *Selverstone*, 1988; *Viola et al.*, 2001; *Pomella*, 2010]. Moreover, estimates on the amount of slip along the Passeier line were used by Viola et al., [2001] to balance for slip along the Giudicarie line. In addition, it has been suggested by *Schmid et al.,* (2004) that this roughly N-S-trending fault system might be the surface expression of the observed lateral change in subduction polarity (see also Chapter 5). In this perspective, the Adriatic crust fulfilled the role on an indenter yet being the incoming plate for the last 20 Ma. This situation is comparable to the Asian collision zone, where India is an indenter in lower plate position.

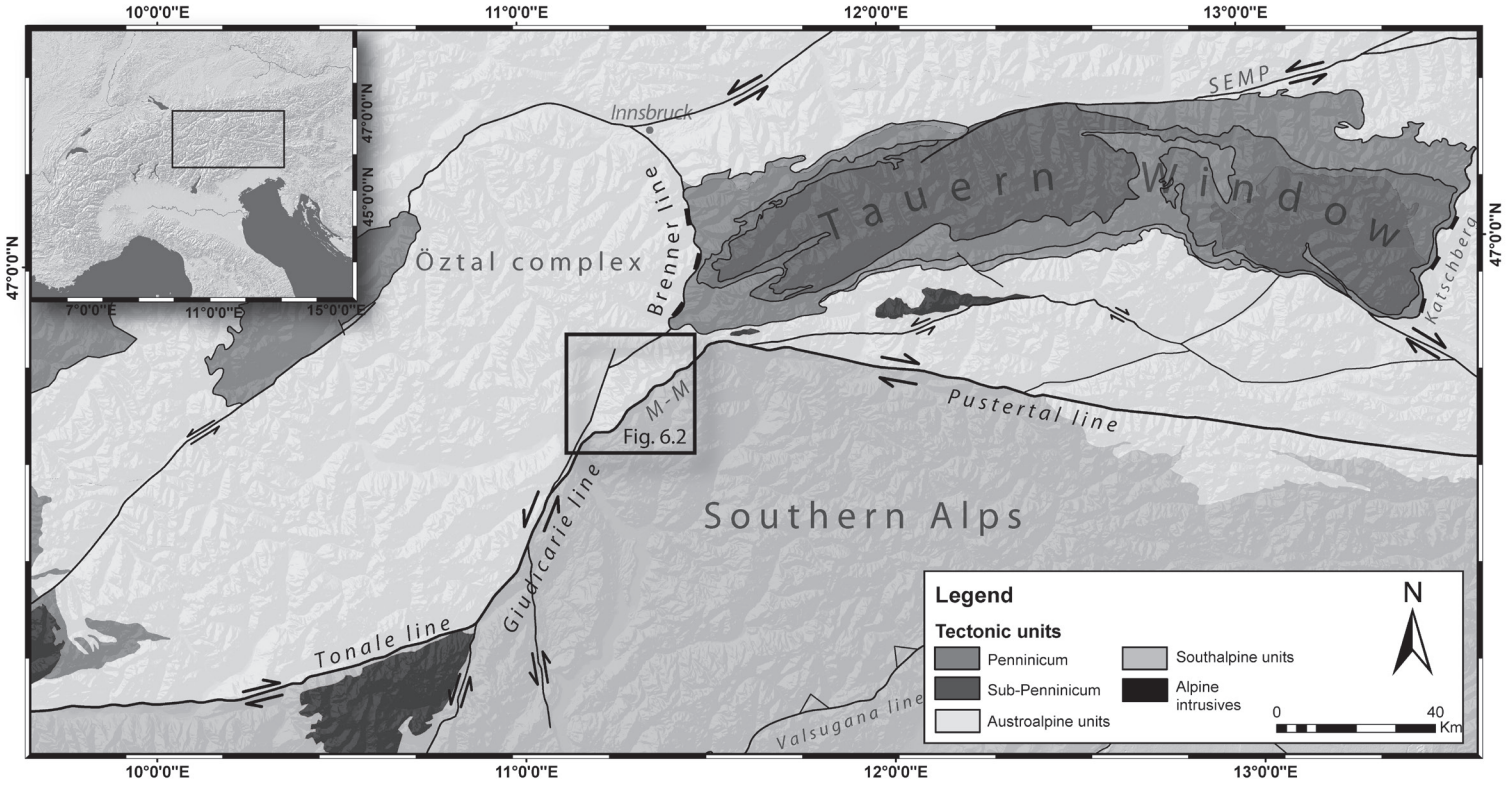

Figure 6.1 Simplified tectonic map of the Central- and Eastern Alps displaying the main tectonic features based on Bigi et al. (1990-92) and Egger et al. (1999). The Jaufen-Passeier region (black square) is situated at the northwest corner of the Southern Alps curvature, and between the Giudicarie- and Brenner lines. M-M: Meran-Mauls line, SEMP: Salzach-Ennstal-Mariazell-Puchberg line.

The interpretation of the complex strain pattern directly north of the indenter (i.e. Jaufen-Passeier faults) as part of a larger fault system remains ambiguous in terms of the mutual relation of the different fault segments, and their kinematic history as well as their link to the deep structure of the mountain belt. In particular, a possible relation of coeval fault activity demands for a more detailed study. The close vicinity of the Passeier- and Jaufen lines to the indenter tip makes us believe that these faults may result from indentation and should therefore not be considered as part of a larger fault system. As such, we have investigated the kinematic compatibility among fault segments, which are oriented at high angle to each other (Passier- and Jaufen faults) in front of the Adriatic indenter as a function of the indenter's shape and motion path. The discussion is based on results of detailed structural field mapping, including fault slip analysis along the Passeier- and Jaufen faults, and crustal-scale analogue modelling. The latter serves to infer the kinematics and timing of fault activity of faults created in front of an already curved indenter through Particle Image Velocimetry (PIV). Implications of the modelling results are discussed in the light of the new and already published field- and geochronological data north of the Giudicarie line.

6.2 Geological setting

6.2.1 The Adriatic Indenter and Giudicarie line

For the scope of this study the Eastern Alps consists of two Alpine mega units: the Southern Alpine Indenter, and the Austroalpine Unit directly north of the indenter. Both units were part of the Adriatic microplate, which collided with the European plate since Eocene times after south directed subduction of the Piemonte-Liguria Ocean [e.g. *Frisch*, 1979; *Schmid et al.*, 2004]. Collision resulted in the formation of an orogenic wedge in where the Austroalpine units were intensively deformed and transported northwards. During this episode, exhumation was localized directly north of the Periadriatic line, meanwhile vertical displacement within the Southern Alps was relatively low. These observations are diagnostic to consider the Southern Alps as an indenter where the bulk plate motion is transferred into intense deformation of the orogens internal part. In addition, several authors emphasized a rheology contrast between a relative strong Adriatic lithosphere and a weak internal orogen. This strength difference is explained among others by heating of mainly the internal part as a consequence of crustal thickening [*Willingshofer and Cloetingh*, 2003], or by crustal composition [*Castellarin et al.*, 2006].

In the eastern Southern Alps, the indenter is outlined by the Giudicarie line in the west, the Meran-Mauls line in the northwest, and the Pustertal line in the north (Fig. 6-1). A remarkable NNE-SSW strike of the Giudicarie fault system defines the border between the western- and eastern Southern Alps. Whether this abrupt change is pre-collisional or represents displacement of an originally straight Periadriatic line during its post-collision stage is still debated. Uncertainty exists in particular on the amount of Miocene fault displacement along the Giudicarie line [*Laubscher*, 1988a; *Picotti et al.*, 1995; *Frisch et al.*, 1998; *Schönborn*, 1999; *Prosser*, 2000; *Viola et al.*, 2001; *Schmid et al.*, 2004; *Stipp et al.*, 2004; *Castellarin et al.*, 2006]. Estimations vary from 15 to 70 km and are primarily based on the following observations: 1) Field evidence, such as fission track ages and kinematic indicators record both sinistral-slip and thrusting along the

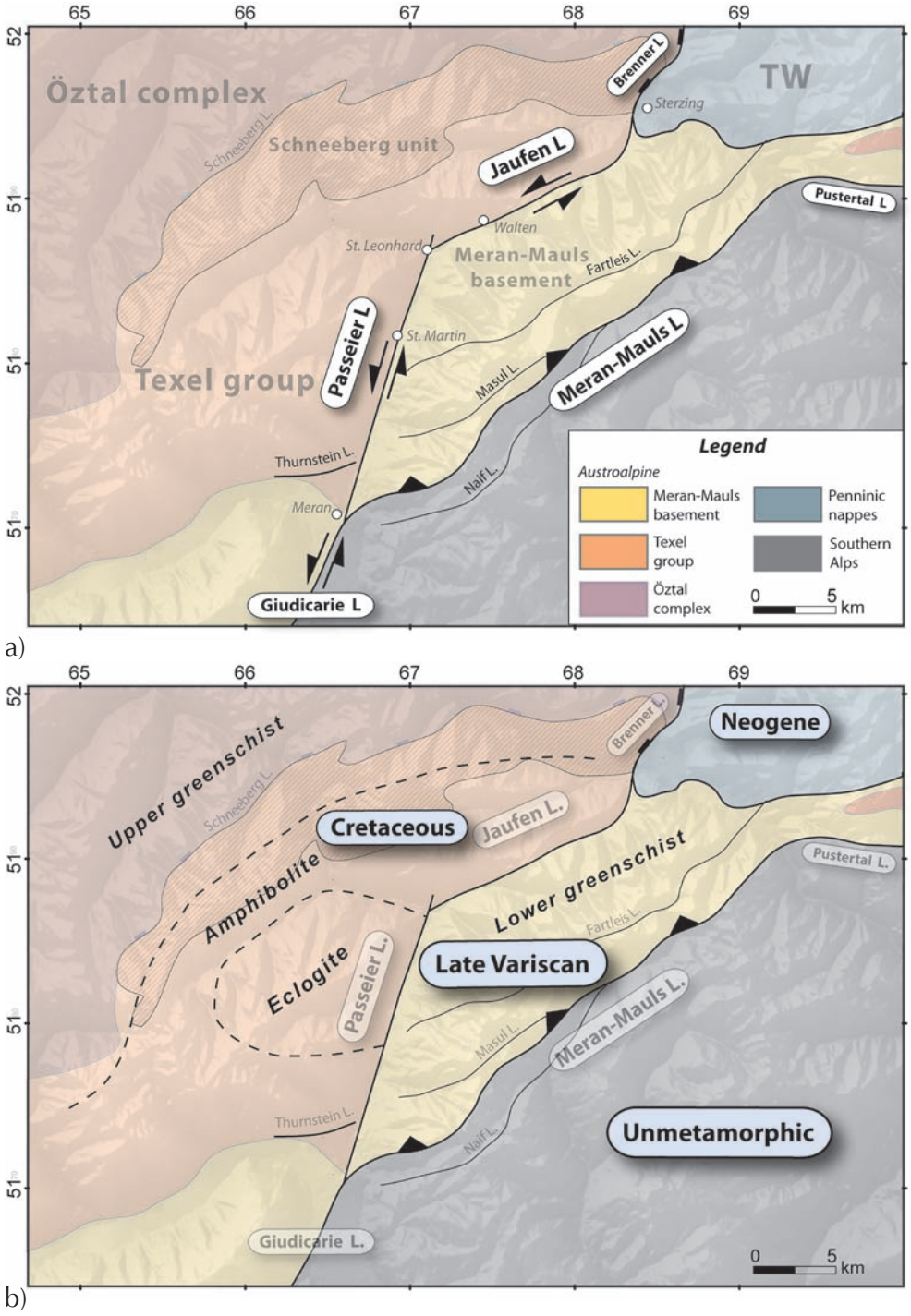

Figure 6.2 a) Overview of the Jaufen-Passeier region. Fault locations and kinematics are based on literature data [e.g. *Selverstone,* 1988; *Fügenschuh et al.,* 1997; *Viola et al.,* 2001]. b) Outline of metamorphic facies and timing of peak temperatures as interpreted by Sölva et al. [2005].

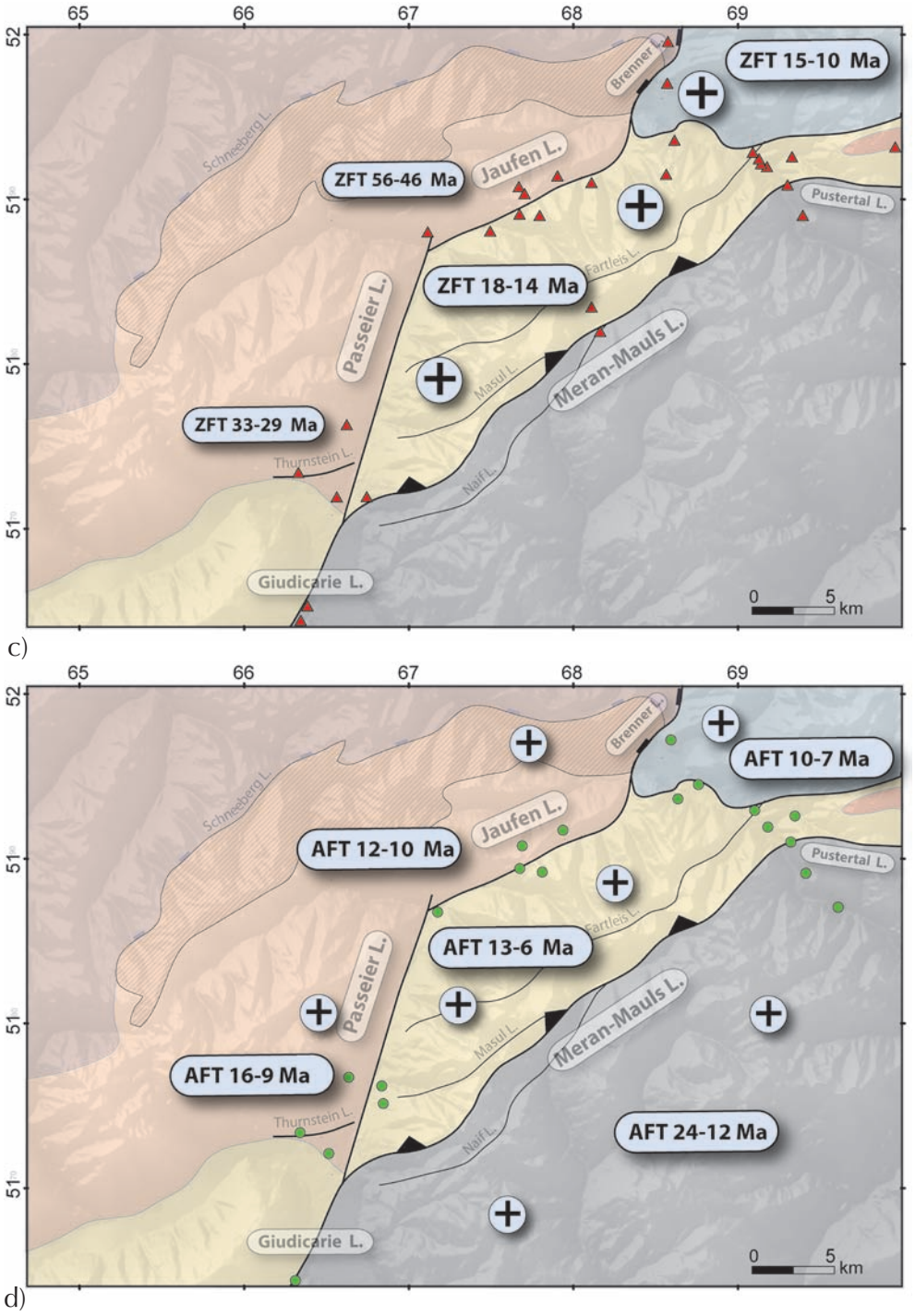

Figure. 6.2c) Distribution of zircon fission track ages (triangles) taken from [*Viola et al.,* 2001; *Pomella,* 2010]. d) Distribution of apatite fission track ages (circles) taken from [*Viola et al.,* 2001; *Pomella,* 2010]. Age ranges refer to particular fault blocks, and + indicates relative uplift.

Giudicarie line and Meran-Mauls line [*Picotti et al.*, 1995; *Prosser*, 2000; *Pomella et al.*, 2010]. 2) Lateral differences on the amount of shortening throughout the Southern Alps. The eastern Southern Alps underwent slightly less Miocene shortening than the western Southern Alps [*Roeder*, 1989; *Castellarin et al.*, 1992; *Zampieri*, 1995]. This implies for the east domain that Miocene shortening had to be partly accommodated elsewhere, like for instance in the Tauern Window where more than 70 km of shortening was accommodated through thrusting and folding [*Laubscher*, 2010]. Especially the Miocene cooling ages indicate high exhumation rates in the Tauern window during this period [see for compilation *Luth and Willingshofer*, 2008].

6.2.2 The Jaufen-Passeier fault region

Directly north of the Meran-indenter-tip, the Austroapline unit is dissected by the NNE-trending Passeier line, which runs towards the village of St. Leonhard (Fig. 6.2). Here, the Passeier line intersects with the NE-trending Jaufen line, which strikes all the way to Sterzing and possibly connects with the Brenner line. Displacements along both the Passeier and Jaufen lines juxtaposed Austroalpine fragments of contrasting metamorphic facies and deformation style. The south-eastern fragment, named Meran-Mauls Basement, contains a strong Variscan metamorphic overprint. The northern and western blocks are part of the Texelgroup and underwent eo-Alpine metamorphism (Fig. 6.2b).

The Jaufen line

Previous mapping and kinematics of the Jaufen line was constrained by the following criteria:

1) ***Metamorphic facies.*** A contrast between amphibolite facies in the north (Texelgroup) and greenschist facies in the south (Meran-Mauls basement) indicates a relative uplift of the northern block (Fig. 6.2a-b) [*Del Moro et al.*, 1982].

2) ***Cooling ages.*** *Del Moro et al.* [1982] and *Spiess* [1995] mapped the Jaufen line according to the distribution of Rb/Sr and K/Ar ages, with Cretaceous ages recorded from the Texelgroup, but Variscan ages from the Meran-Mauls basement. Hence, such an age distribution implies a relative uplift of the northern block. Also geochronological studies from *Viola et al.* [2001] and *Pomella* [2010] indicate displacement along the Jaufen line throughout the Paleogene. In addition, differential exhumation of the different blocks have been portrayed by zircon fission track ages, which cluster north- and south of the shear zone around 55 Ma and 18-14 Ma, respectively *Viola et al.* [2001] (Fig. 6.2c). Note that this implies an inverse relationship compared to the high temperature systems indicating exhumation of the southern block. The apatite fission track ages are more or less equal on both sides of the line ranging from 15-6 Ma, suggesting that no significant vertical displacement occurred along the Jaufen line since that period [*Viola et al.*, 2001] (Fig. 6.2d).

3) ***Kinematic indicators.*** During the Cretaceous, the Jaufen line was formed under compression, but was subsequently reactivated by a phase of extension [*Pomella et al.*, 2010]. According to *Pomella* [2010], the initial thrust-related shear sense, associated with the emplacement of the Öztal nappe onto the Meran-Mauls basement, was completely overprinted by SE-directed normal faulting during late Cretaceous extension. These older

N-dipping foliations with WNW plunging stretching lineations were finally discordantly cut by a more discrete greenschist-mylonite throughout the Tertiary. *Müller et al.* [2001] and *Viola et al.* [2001] studied the Tertiary evolution of the greenschist-mylonites in detail. Both recognized a steeply NW-dipping mylonitic foliation with top-to-the-(north)west sense of shear implying sinistral and northern block down displacement. Deformation conditions estimated by analyzing microstructures were in the order of 300 °C [*Viola et al.*, 2001]. Note that the observed fault kinematics is consistent with the Zircon Fission Track (ZFT)-age distribution implying early-mid Miocene activity. In addition, shearing took place presumably no more than 31.7±3.4 Ma ago as is evident from the U/Pb dating of a deformed dyke [*Müller et al.*, 2001].

The mylonites are overprinted by a semi-ductile to brittle phase, which produced besides discrete steeply dipping fault planes also cataclasites and pseudotachylytes. The latter has been dated with Ar/Ar between 21.0±1.5 and 16.9±0.8 Ma [*Müller et al.*, 2001]. *Viola et al.* [2001] inferred that the direction of shortening during the brittle phase ranged between N and WNW. However, a detailed paleo-stress tensor analyzes confirming this direction has never been published.

Passeier line

Along the Passeier line, a jump in metamorphic facies suggests Neogene upward motion of the western block (Texelgroup). However, so far further evidence from cooling ages or kinematic indicators supporting such fault motion is sparse. Within the Passeier valley, intensive semi ductile- to brittle deformation was observed in a few outcrops. These mostly proto-mylonitic and cataclastic zones were up to a few meters thick consisting of low-cohesion lithoclasts surrounded by fault gouge, and often pseudotachylytes [*Viola et al.*, 2003]. Based on a limited number of fault measurements, *Viola et al.* [2001] assigned to the Passeier line a sinistral transpressive deformation regime associated with a steeply NW-dipping foliation and a gently NNE-plunging stretching lineation. In addition, the 2001 earthquake below the city of Meran confirms the presence of an active fault zone below the valley that slipped, according to focal mechanism solutions in a sinistral strike-slip mode along a steep WNW dipping fault plane [*Caporali et al.*, 2005].

Whether the Passeier- and Jaufen lines belong to a single fault system in terms of synchronous activity and kinematic compatibility is debated. Spiess [1995] considers the Passeier- and Jaufen lines as a single fault system simply based on constant cooling ages within the Meran-Mauls basement. However, examining the fault zones and in particular the fault rocks challenged the idea of a a shared ductile history *Viola et al.* [2001] and *Müller et al.* [2001]. Within the Passeier valley ductile shearing is only expressed by a few local zones of proto-mylonites, whereas the Jaufen line bears mylonites containing a pervasive shearing fabric formed under greenschist facies conditions. On the other hand, brittle faulting must have been coeval during the Miocene as indicated by dated pseudotachylytes along both faults *Müller et al.* [2001]. Consistency of timing and brittle fault kinematics are the main arguments to link the former two faults [*Müller et al.*, 2001; *Viola et al.*, 2001]. Moreover, during this period the faults may have been part of a larger fault system comprising the Giudicarie-, Passeier-, Jaufen-, and possibly the Brenner-line. For reducing speculation, a more detailed study on the kinematics of both the Passeier- and Jaufen line is presented in this chapter. In addition, simple analogue models were

used to better understand the interactions between different fault segments as a result of indentation.

6.3 Field results

To unravel the deformation history of the Jaufen-Passeier region, and in particular the kinematics of the fault zones and their overprinting relations, the orientations of ductile- and brittle fabrics , such as regional- and mylonitic foliations, and stretching lineations as well as fault planes, striations and cataclastic zones have been measured. Subsequently, the data was categorized and analyzed using stereoplots, rose-diagrams, and paleostress tensors.

6.3.1 Ductile fabrics

Orientations of the ductile fabrics are displayed in Figure 6.3. Regional foliations dip between 30° and 60° towards the north- northwest in the Texelgroup unit. The foliation is folded varying from microscopic crenulations to hectometre-scale (Fig. 6.3, plot 5, 6, 9). Within the Meran-Mauls basement the regional foliations dip slightly steeper, 50° to 70° and strike sub-parallel to the Jaufen Valley and the Meran-Mauls fault (Fig. 6.3).

Mylonitic fabrics related to the Jaufen shear zone were found on the northern flank of the Jaufen valley, and between St. Leonhard and the Jaufenpass (Fig. 6.1). Between Jaufenpass and the village of Walten good exposure allow estimating the shear zone width at ±50 meter including a 10 meter transition zone. Here, the regional shallow, NNW-dipping, regional schistosity becomes gradually overprinted by a steep NW dipping mylonitic foliation and a shallow-plunging, dominantly west-trending stretching lineation (Fig. 6.3). The mylonitic foliation consists mainly of muscovite, quartz and chlorite, and bends around brittlely deformed feldspar, which indicates deformation under greenschist facies conditions (Fig. 6.5a). Kinematic indicators such as shear bands and rotated sigma clasts reveal dominantly sinistral top-to-the-west sense of shear (Fig. 6.5a). However, at micro-scale dextral shear indicators are equal in amount suggesting an overall pure shear deformation regime, or postulate the possibility for another deformation phase (Fig. 6.6a).

Within the Passeier valley no mylonites comparable to those of the Jaufen line were found. Further southwards, however, near the castle of Thurnstein, another WSE-ENE striking mylonite zone (>100m) known as the Thurnstein mylonite zone contains a NW dipping foliation and mainly westward plunging stretching lineations developed in orthogneiss. Microscopic shear bands and sigma-clast indicate dominantly sinistral as well as some dextral sense of shear.

6.3.2 Brittle fabrics and paleostress analysis

Brittle deformation is portrayed by the large amount of fault planes and slickensides distributed throughout the entire study area.

In order to determine the orientation of the principal stresses under which the diverse fault population formed, paleostress tensors were calculated covering the major fault

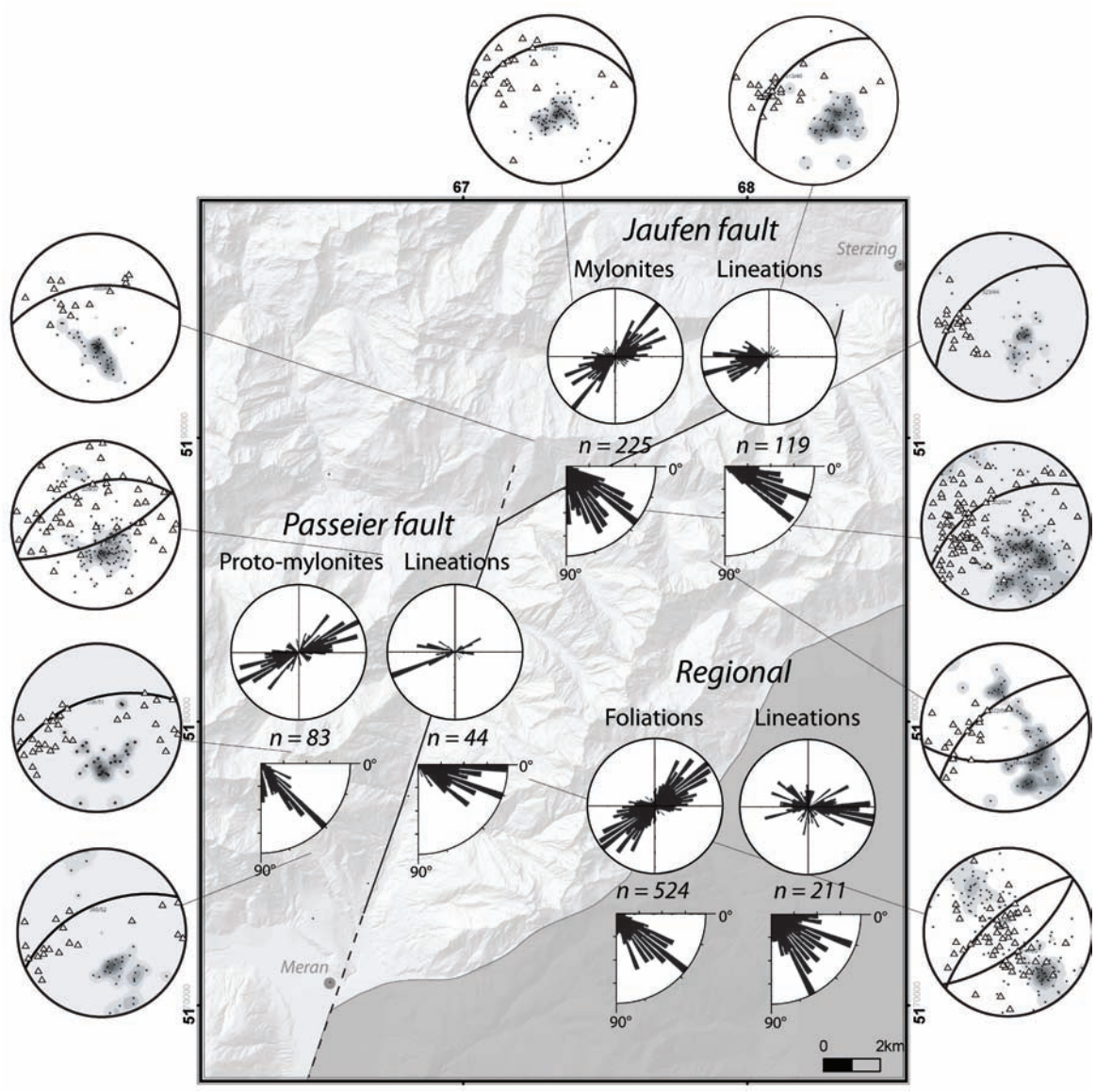

Figure 6.3 Ductile fabric orientations plotted in rose diagrams (inner) and stereoplots (outer). Rose diagrams display strike and dip of mylonitic foliations and stretching lineations along the Jaufen- and Passeier lines. Plotted regional foliations and lineations were collected form both sides of the faults. Gray stereoplots refer to mylonitic fabrics. Stereoplots contain contoured poles (dots) and lineations (triangles). Great circle represents plane average based on contour clusters. Numbers refer to amount of plotted planes/lines.

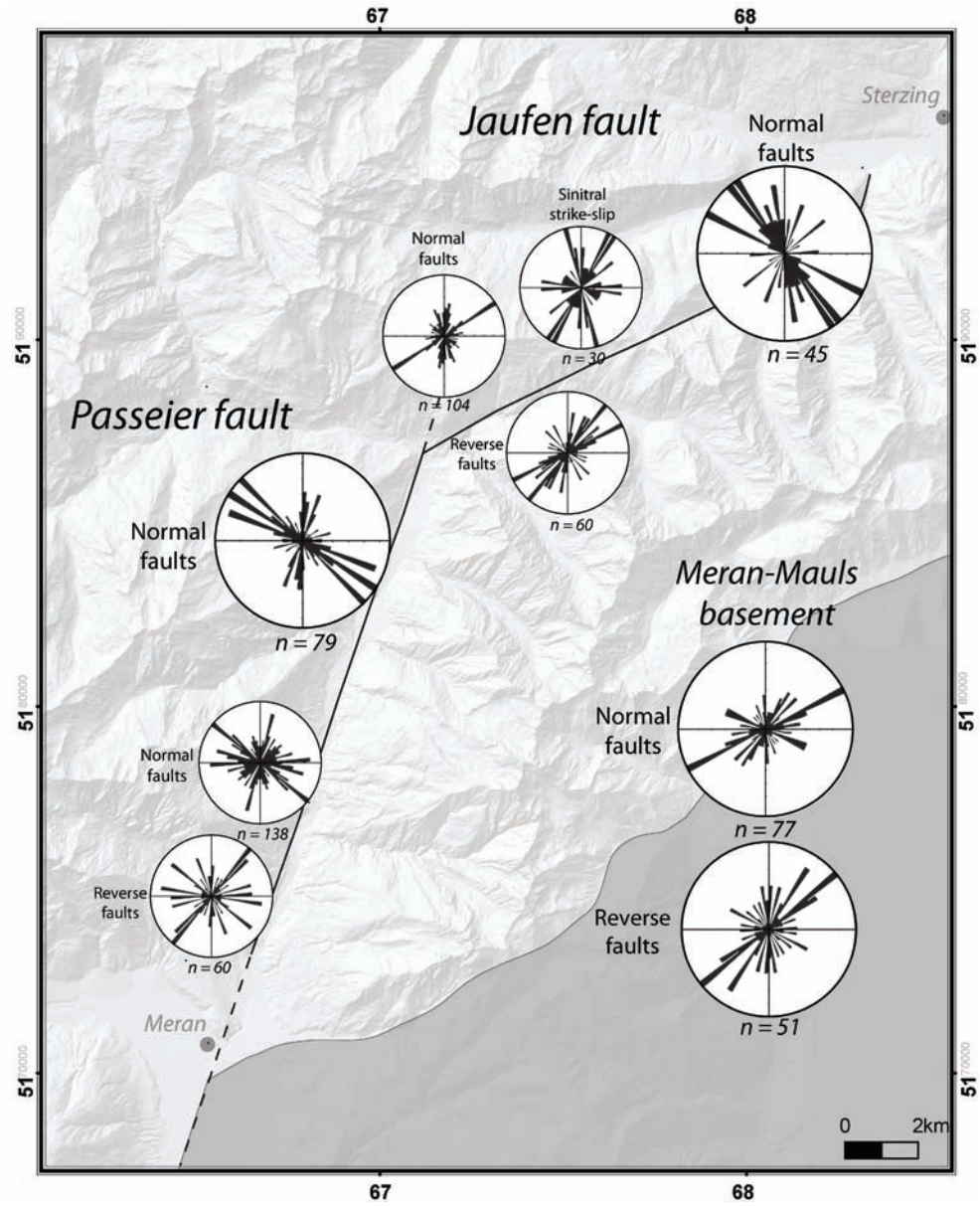

Figure 6.4a Brittle fabrics orientations plotted in rose diagrams and stereoplots for several regions along the Jaufen-Passeier faults and surrounding basement. Plots are categorized according to prevailing kinematics and orientations (see text for further explanation). Numbers refer to the amount of plotted planes/lines.

Figure 6.4b (facing page) Paleostress directions calculated from brittle fault data. Great circles and dots represent fault planes and striations, respectively. Frequency diagrams at the lower left represents deviations between observed and calculated fault-slip angles. Orientations and data quality are summarized in Table 6-1.

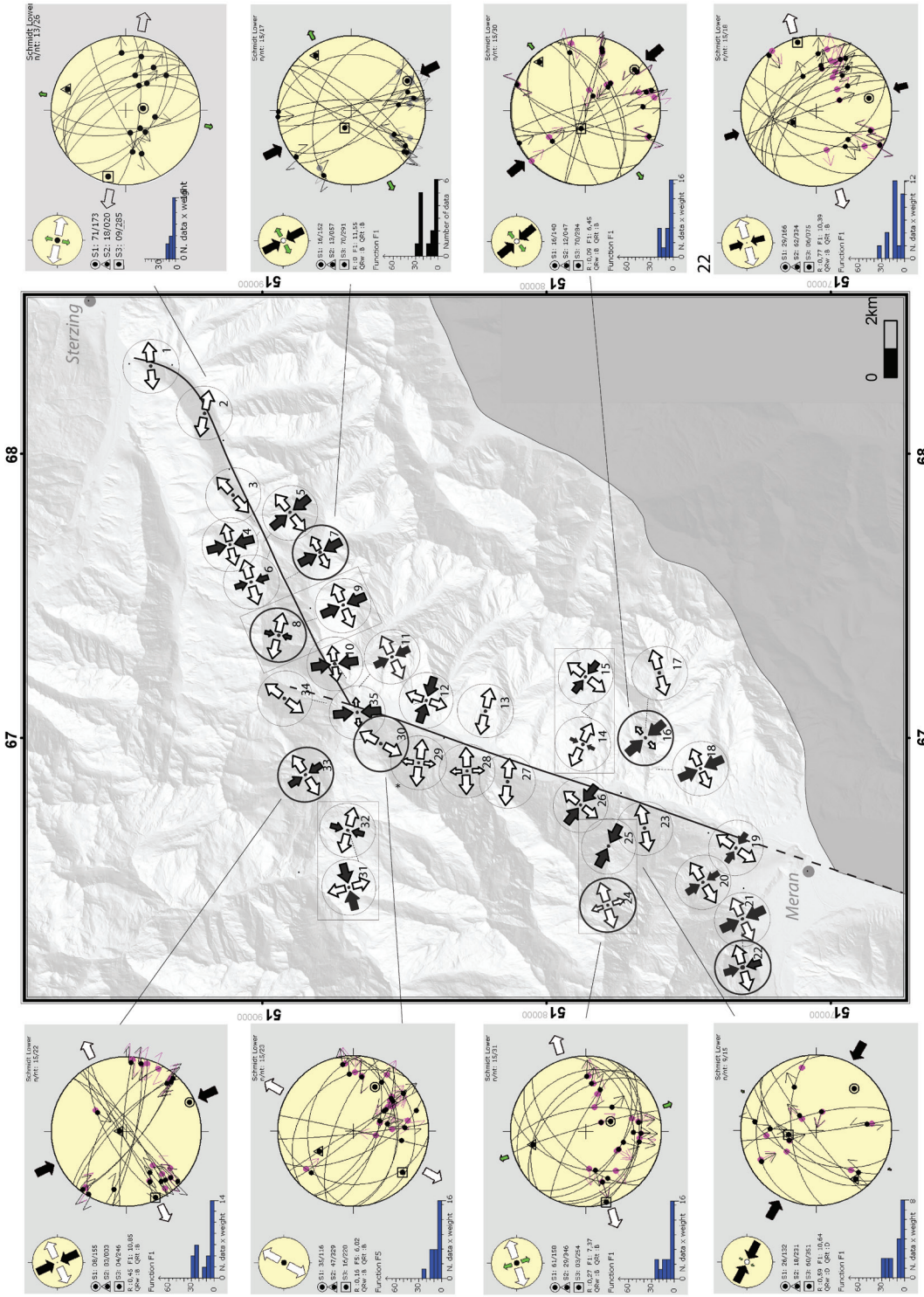

Figure. 6.4b

Cluster	n	n_t	σ_1	σ_2	σ_3	R'	α_w	QRt	regime	Sh_{max}	Sh_{min}
1	9	12	148/66	001/21	265/12	0.71	9.07	D	pure extensional	174	84
2	13	26	173/71	020/18	285/09	0.3	11.79	C	pure extensional	11	101
3	8	13	112/62	326/23	232/14	0.63	10.4	D	pure extensional	138	48
4	10	15	164/22	021/63	260/16	1.8	9.64	C	strike-slip compressional	166	76
5	6	9	323/09	066/55	227/35	1.5	7	D	pure strike-slip	141	51
6	10	21	341/15	190/74	071/08	0.84	9.03	C	extensional strike-slip	163	73
7	15	20	152/16	057/13	291/70	2	11.55	B	strike-slip compressional	152	62
8	15	26	252/78	009/05	102/11	0.63	11.97	B	strike-slip extensional	13	103
9	6	26	335/25	176/64	072/10	1.4	5.42	D	pure strike-slip	157	67
10	8	12	353/28	148/60	257/10	1.77	10.93	D	compressional strike-slip	168	78
11	15	24	331/18	185/71	064/14	1.4	13.03	C	pure strike-slip	154	64
12	6	8	106/28	309/60	201/10	1.73	4.37	D	compressional strike-slip	108	18
13	6	17	162/67	020/18	286/14	0.52	6.63	D	pure extensional	12	102
14	16	44	017/54	221/35	123/11	0.57	10.21	C	pure extensional	30	120
15	11	44	144/28	280/54	042/22	1.47	15.38	D	pure strike-slip	137	47
16	15	30	140/16	047/12	284/70	2.09	6.45	B	stike-slip compressional	140	50
17	9	20	155/41	292/36	039/24	0.26	2.11	D	oblique extensive	147	57
18	8	12	155/23	318/66	062/06	1.68	8.04	D	stike-slip compressional	156	66
19	8	13	117/22	342/61	215/20	1.11	7.92	D	extensional strike-slip	124	34
20	10	18	146/12	021/71	243/14	1.3	8.16	C	pure strike-slip	148	58

Table 6.1 Results of the tensor analysis for each outcrop cluster (see Fig. 6.4b for locations)

Cluster	n	n_t	σ_1	σ_2	σ_3	R'	α_w	QRt	regime	Sh_{max}	Sh_{min}
21	10	15	154/06	034/78	245/11	1.4	4.4	C	pure strike-slip	155	65
22	17	20	166/29	334/62	075/06	1.23	10.39	B	extensional strike-slip	164	74
23	18	52	180/56	338/32	75/10	0.49	9.72	C	pure extensional	169	79
24	15	31	158/61	346/29	254/03	0.27	7.37	B	pure extensional	162	72
25	9	31	132/26	231/18	351/60	2.59	2.6	D	pure compressional	118	28
26	8	10	310/30	151/57	046/09	1.59	7.55	D	pure strike-slip	133	43
27	14	33	050/82	184/05	274/05	0.53	11.95	C	pure extensional	5	95
28	15	18	179/62	352/28	083/03	0.05	8	C	radial extensional	178	88
29	7	11	131/66	032/04	300/24	0.49	4.46	D	radial extensional	6	96
30	15	23	116/35	329/47	220/16	1.84	11.47	B	oblique extensive	119	29
31	8	33	256/14	010/60	159/27	1.8	3.72	D	compressional strike-slip	75	165
32	12	33	010/07	271/50	106/40	1.1	10.1	C	extensional strike-slip	15	105
33	18	28	147/03	004/87	237/01	1.18	8.7	B	extensional strike-slip	147	57
34	17	46	126/43	310/47	218/02	1.6	8.35	C	oblique extensive	127	37
35	7	18	175/20	265/04	004/69	2.26	11.03	D	pure compressional	175	85

Table 6.1 (continued)

zones and tectonic units (Fig. 6-4b and Tab. 6-1). The paleostress analysis was performed using the WinTensor program developed by Delvaux [see also *Delvaux and Sperner*, 2003]. This program is based on the Right Dihedron method [*Angelier and Mechler*, 1977], and allows for Rotational Optimization of the calculated tensor. The tensor quality is described by the Tensor Quality Rank ranging from A (very good) to E (very poor), and depends on the number of used measurements, the average slip deviation angle, the confidence level of the field observation, and the variety of measured orientations. For further elaboration on the calculation methods the reader is referred to *Delveaux and Sperner* [2003]. The results of the stress tensor analysis are shown in Fig. 6.4b and Table 6.1. The horizontal stress directions are plotted in map view as maximum (solid arrows) and minimum (white arrows) components.

Jaufen line

The Jaufen line can be divided into a northern and southern segment based on the amount of brittle structures and the different orientated stress regimes. North of the Jaufen pass, the amount of fault planes is modest compared to the southern segment, and limited to NW-dipping normal faults with often only a few centimetres of oblique-sinistral displacements. In addition, only a few reverse-, strike-slip-faults, and cataclastic shear zones were found (Fig. 6.5b). Paleostress tensors indicate NE-SW to E-W extension along the northern Jaufen segment, close to the Brenner normal fault.

Along the southern segment, fault density is higher and increases towards the Jaufen mylonite zone. Steeply dipping (>65°) sinistral- and dextral strike-slip faults are abundant (Fig. 6-4a). In addition, half of the fault population consists of oblique normal faults, which can be subdivided in steeply dipping NE-SW-striking faults, and N-S-striking west-dipping faults. Fault striations dominantly plunge 40° south to southwest (Fig. 6-4a). Abundantly observed pseudotachylytes, in particular at the Jaufen pass, are often associated with NE-SW-striking reverse faults (e.g. Fig. 6.5c, and Fig. 6.6b). Paleostress tensor calculations along the southern segments resolve a prevailing strike-slip regime with $Sh_{max}=\sigma_1$ trending NNW-SSE and sub-orthogonal to the Jaufen shear zone. Furthermore, near the village of Walten, two good quality tensors (nr. 8 and 9) obtained from a single site suggest an alteration between a pure strike-slip regime and a WNW-ESE-directed extensional strike-slip regime.

Passeier line

Measurements from the Passeier valley include faults and striae from the Texel group unit and the Meran-Mauls basement unit (Fig. 6-2a).

The fault population throughout the Meran-Mauls basement unit is comparable to the southern Jaufen segment: NE-SW striking normal- and reverse faults prevail, and shallow-plunging striae indicate oblique slip. Sinistral or dextral-oblique-slip components are equally abundant among both reverse- and normal fault. In contrast to the Jaufen valley, however, the relative contribution of dip-slip along normal and reverse faults is high (29%). The amount of reverse faults increases southwards towards the city of Meran.

The Texelgroup unit marking the western flank of the Passeier valley is more intensively faulted than the Meran-Mauls basement unit. Normal faults are most abundant and

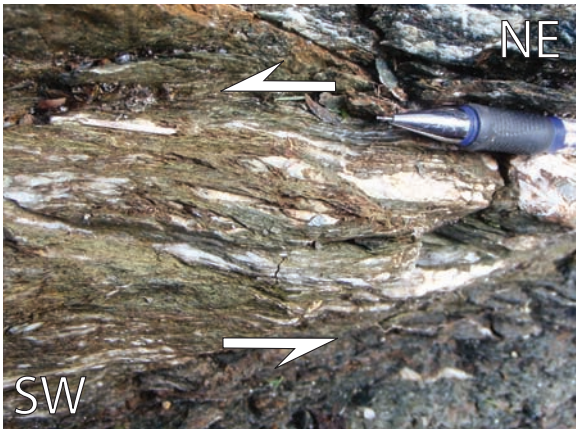

a)

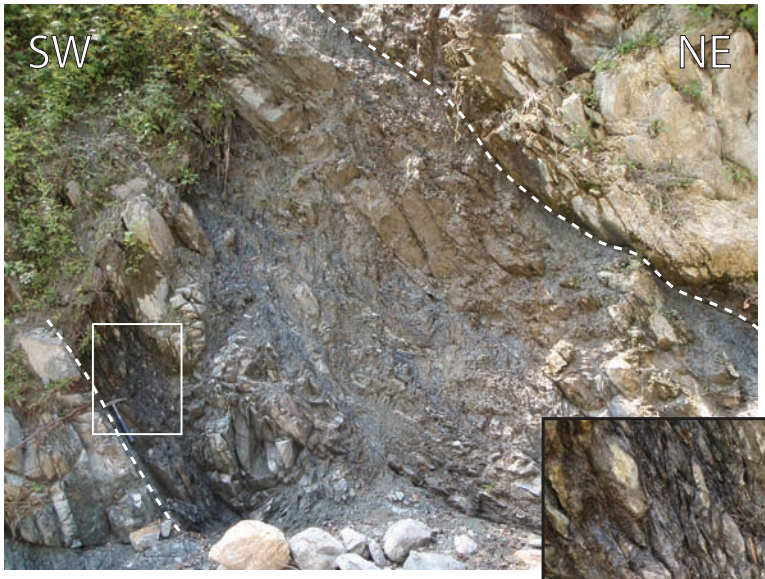

b)

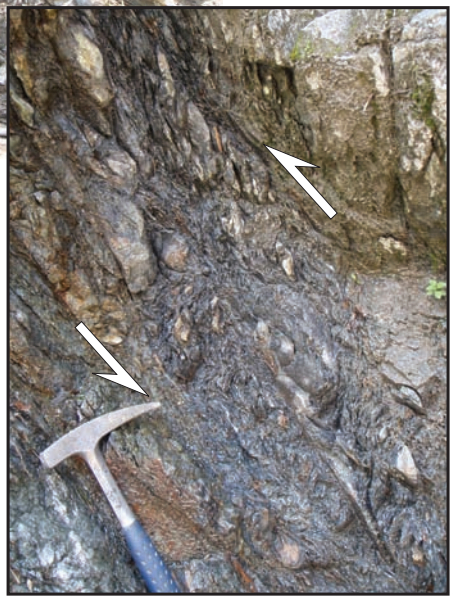

Figure 6.5 a) Sinistral shear affecting quartz-rich greenschist within the Jaufen mylonite zone. Example located directly northeast of St. Leonhard. b) Sinistral shear zone formed under semi-ductile conditions overprinting the Jaufen mylonite zone along its southern segment.

c)

d)

Figure 6.4 (continued) c) Pseudotachylyte associated with southvergent thrusting near the Jaufen pass. d) Southvergent thrusting intersecting a sub-vertical fold limb within the Meran-Mauls Basement.

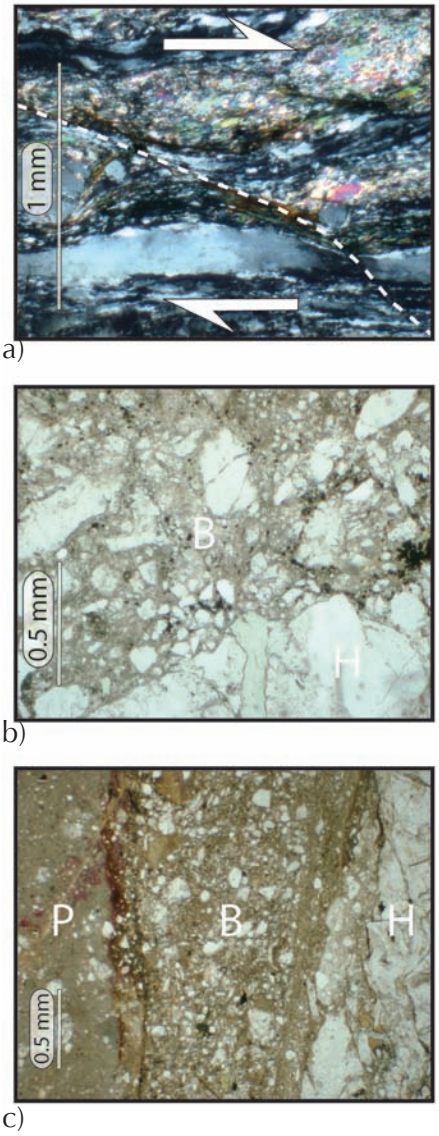

Figure 6.6 Thin-sections. a) Mylonite of the northern Jaufen shear zone (Jaufen valley) consisting of elongated quartz, muscovite, biotite, chlorite and feldspar. C'-type shear band (dashed line) and mica fish texture reveals dextral sense of shear. Image taken with crossed polar light. b) Coherent fault breccia (B) from the Jaufen Pass region. The cataclasized zones consist of angular feldspars and some quartz fragments floating within a very fine, mica rich matrix. Note the sharp transition with the quartz-rich host rock (H). c) Brittle fault rock from the southern Passeier valley showing the sharp transitions from the host rock (H) to breccia (B), to pseudotachylyte (P). Fragments within the breccia and pseudotachylyte consist of quartz and feldspars. The transitions suggest that the pseudotachylyte overprinted the breccia.

can be according to their orientation divided in two subsets: 1) NW-SE-striking dextral transtensional faults, 2) NNE-SSW-striking sinistral transtensional faults. As within the Meran-Mauls basement, NE-SW striking reverse faults become more abundant southward between the villages San Martin and Saltus. Additionally, the regional foliation is locally overprinted by 3 to 5 meter wide, sub-vertical dipping zones of intense cataclastic deformation. These cataclastic zones often parallel the regional foliation (NE-SW), but E-W and N-S-trends are also observed. The zones typically comprise a mixture of semi-ductile and brittle fabrics in where shear bands and lithoclasts (up to 1 m) are intersected by fault gauge and pseudotachylytes (Fig. 6.6c).

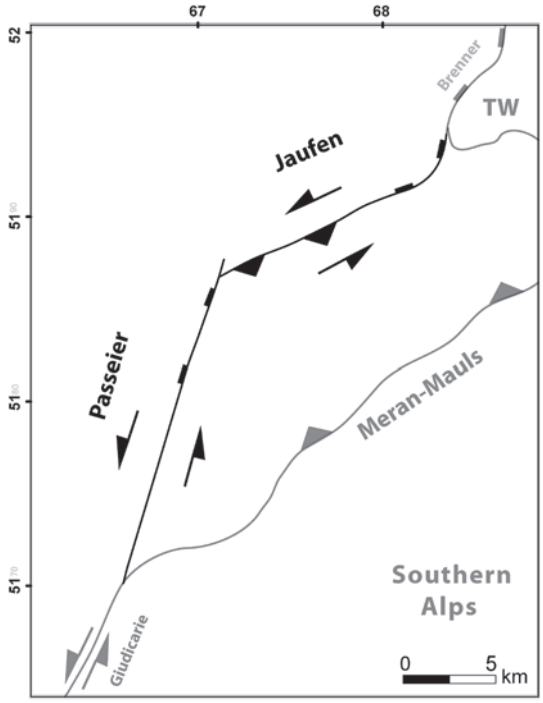

Figure 6.7 Sketch of the Jaufen-Passeier region highlighting spatial variation of brittle fault kinematics based on the calculated paleostress directions. The Jaufen line comprises a northern- and southern segment accommodating extension and compression, respectively. Along the Passeier line, a normal component increases gradually northward.

The paleostress analysis along the Passeier line reveals an extensional stress regime in the north, while southwards the increase of reverse faults along both sides of the fault suggests a transition towards a sinistral strike-slip regime (Fig. 6.4b). However, the presence of a few second phase tensors portraying an extensional stress regime indicates that some extension might occurred in the south as well.

6.3.3 Summary of field results

Kinematic indicators throughout the Jaufen valley derived from steeply dipping mylonites formed under greenschist facies conditions mainly record sinistral transtension. According to ZFT-ages along both sides of the valley, transtension resulted in a relative uplift of the Meran-Mauls basement from the early Miocene onward. The ductile fabrics of the Jaufen line are overprinted by discrete brittle fault planes. The increasing amount of NE-SW-striking faults towards the shear zone as well as the appearance of pseudotachylytes, indicate brittle activation of the Jaufen fault's southern segment. Although most calculated stress tensors reveal a strike-slip regime (Fig. 6.4b), Sh_{max} orthogonal to the fault zone suggests faulting occurred most likely in a transpressional mode (Fig. 6.7). However, assuming that brittle deformation occurred within a temperature window bounded by ZFT and AFT closure temperatures (230-110 °C), the absence of a clear

break in AFT-ages along the fault allows only minor vertical throw (Fig. 6.2d). Vertical displacement associated with brittle faulting along the Jaufen shear zone was therefore probably minor.

Structural data obtained from the Passeier valley implies that deformation was mainly brittle. Along-strike variations comprise normal faulting and sinistral strike-slip along its northern and southern segments, respectively (Fig. 6.7).

6.4 Crustal modelling of the Jaufen– Passeier region

Analogue models were performed to gain insights in the kinematic evolution of fault systems resulting from indentation. These models intend to investigate whether the Passeier- and Jaufen faults can indeed be associated with indentation. And if so, do their orientations and kinematic signature record a specific motion path of the advancing indenter? Or in other words, does the indenter's motion path influence the evolving fault systems in terms of fault orientations and kinematics?

In this particular study, both the outline and motion path of the Adriatic indenter are still under discussion. These experiments therefore primarily serve to investigate indentation during the Alpine post-collisional stage, during which the amount of shortening was only modest, and the indenter outline did not significantly differ from its present shape.

6.4.1 Experimental set-up

The analogue models were constructed such that a rigid indenter, representing the Adriatic plate, was pushed into a pile of quartz sand with Mohr-Coulomb type behaviour (Fig. 6.8). The indenter outlined three differently orientated segments referred to as left, middle, and right segment. These segments are considered analogues for the Giudicarie, Meran-Mauls, and Pustertal faults, respectively. The segment junctions are referred to as indenter tips. The models were scaled such that 1 cm within the model represented 3 km in nature. All experiments were shortened for 10 cm amounting to 30 km in nature.

The experiments were subdivided in two series based on varying the indenter's motion path or its rheology (Fig. 6.8 and Table 6.2). Within the first series, the applied convergence direction was respectively N, NE, and NW deforming a 5 cm thick sand pile. In addition, in experiment 1-D a 20° counter clockwise rotation of the indenter was modelled. A second series of 3 cm thick experiments was carried out to test additional rheological parameters, such as the influence of a thinner sand pile on thrust spacing and shearing in front of the indenter tip (exp. 2-A), and the role of ductile lower crust on wedge geometry (exp. 2-B).

Particle Image Velocimetry

Particle Image Velocimetry (PIV) has been used to monitor horizontal motion throughout the model and helped to identify fault kinematics. The PIV technique is based on comparing photos of the model surface taken at a regular time interval. In order to recognize surface motion we implemented markers by sprinkling the top layer with coffee grains. The open source MatPIV software was then used to perform the calculations in Matlab. Output images include vector fields, magnitude maps, and fault kinematics.

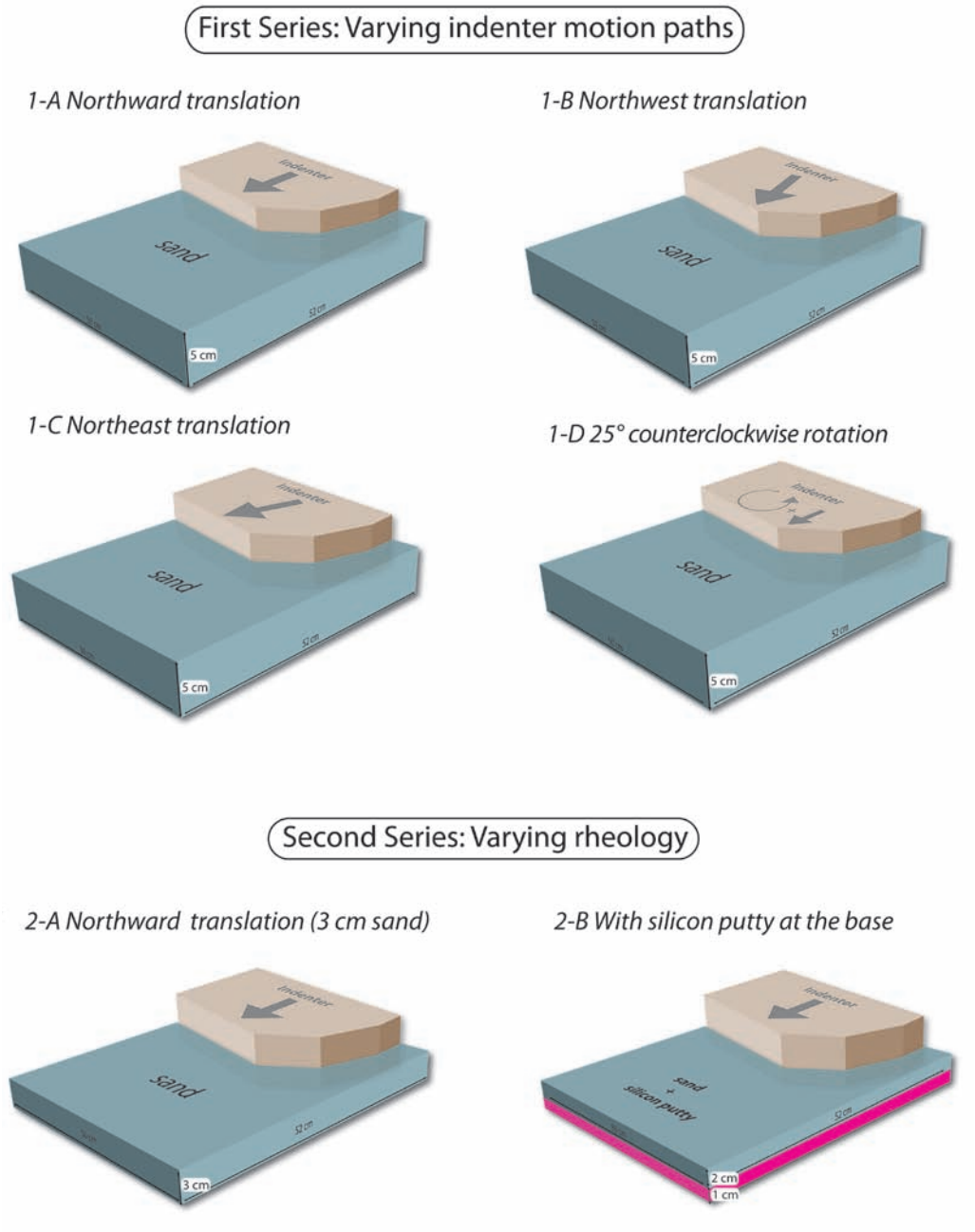

Figure 6.8 Experimental set-up. Gray colour refers to the rigid indenter. Blue and pink layers represent quartz sand and silicone putty (PDMS), respectively.

Experiment	Motion path	Rheology	Total thicknes (cm)	Shortening (cm)
1-A	N-translation	Sand	5	10
1-B	NW-translation	Sand	5	10
1-C	NE-translation	Sand	5	10
1-D	Counterclockwise rotation (25°)	Sand	5	-
2-A	N-translation	Sand	3	10
2-B	N-translation	Sand/Putty	3	10

Table 6.2 Overview on model parameters

Fault kinematics were derived by subtracting adjacent vectors in both the x- and y-direction. For a more detailed overview on the involved mathematics the reader is referred to *Sveen* [2004] and [*Leever et al.*, 2011]. Note that for the final interpretation of the fault kinematics a vertical component could only be deduced from surface topography. For simplicity, within the presented output pictures only a few vectors are shown highlighting the velocity field along the evolving faults (Fig. 6.9 and 6.10).

6.4.2 Modelling results

Series I

Northward translation (Exp. 1-A)
Within the first centimetre of shortening a wedge formed that curved around the indenter. Width and height of the wedge decreased gradually towards the left (Fig. 6.9). Synchronous with wedge formation was the initiation of a NNW-trending strike-slip fault sprouting from the Meran-indenter-tip. This fault type is referred to as "tip fault". With ongoing shortening, the Meran-tip-fault accommodated differential uplift within the wedge as well. After 6 cm Bulk Shortening (BS), the first-tip deactivated as it disconnected from the Meran-tip meanwhile a second Meran-tip-fault formed, which remained active until final shortening (10 cm).

PIV output images revealed a divergent particle flow roughly correlating with the indenter shape. In addition, the westward increasing obliquity of the limbs with respect to the shortening direction led to a magnitude drop. Interpretations on the fault kinematics could be derived from the combination of monitored changes in particle flow and uplift patterns. Within the first centimetre of bulk shortening, the frontal thrust accommodated mainly dip-slip motion. The Meran-tip fault, however, underwent a kinematic lateral

Model set-up
1-A Northward translation
1-B Northwest translation
1-C Northeast translation
1-D 25° CCW-rotation
shortening
4.5 mm
6 mm
7.5 mm
no normal faulting
3 cm
6 cm
10 cm
Rotation

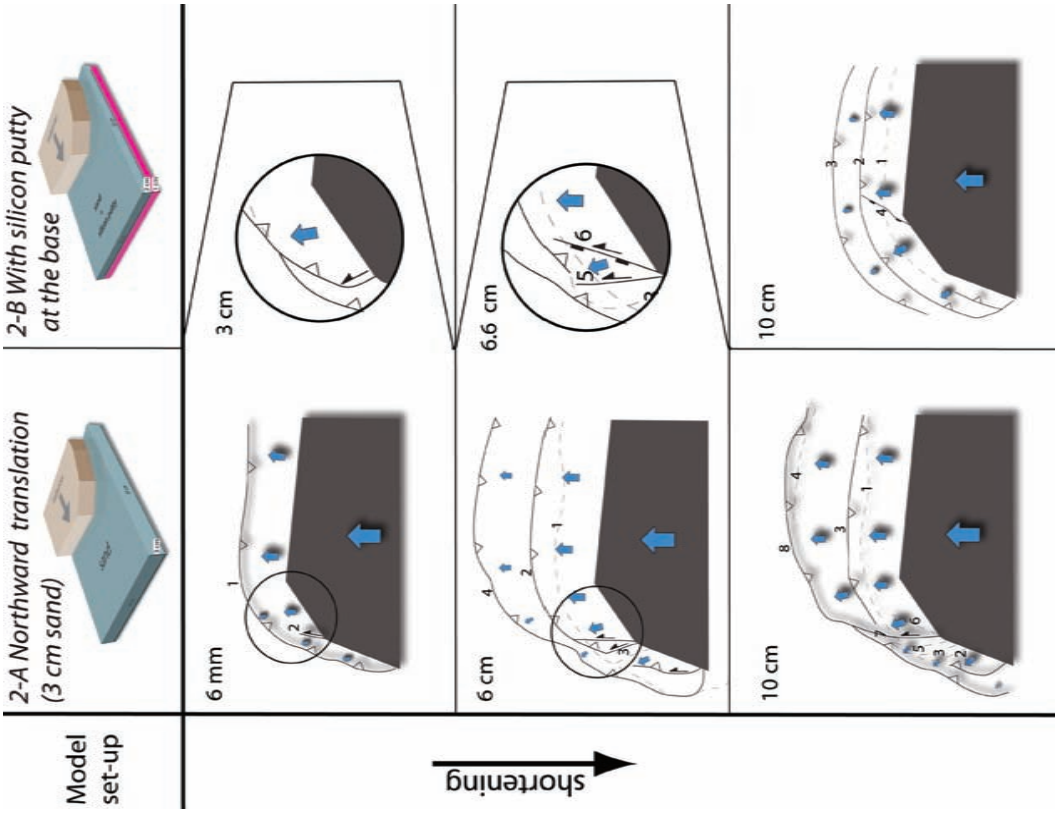

Figure 6.9 (facing page), and Figure 6.10 Experimental results of the first series (varying motion path) and second series (varying rheology), respectively, at different shortening intervals. Indenter (black) induced a horizontal velocity field (blue arrows) as interpreted from Particle Image Velocimetry, which together with the 3D-structure was used to determine fault kinematics (black lines). Vector size corresponds with relative magnitude. Dashed lines represent inactive faults numbered chronologically. Circled windows are zoomed-in regions.

transition from sinistral-transtension to sinistral-transpression (Fig. 6.9). Transtension was more pronounced at some distance from the indenter tip, whereas transpression prevailed close to the indenter tip (6 mm BS, in Fig. 6.9). Finally, from 6 cm BS onward particle flow vectors oriented orthogonal to the indenter segments. As a result of this more divergent particle flow, the kinematics of the second Meran-tip-fault was sinistral transpressive already in its initial stage.

Northwest translation (Exp. 1-B)

Differences in deformation style between north-westward-directed shortening and northward translation were only modest (Fig. 6.9). Outward growth of the crustal wedge proceeded along three in sequence fore-thrusts. Two short-lived Meran-tip faults trended NNW. Note that these faults did not connect to the active fore-thrusts. Lateral topographic gradients associated with the indenter limbs were minor compared to the previous experiment.

PIV images revealed minor lateral variations of vector orientations, NW to NNW, and vector magnitude. Two subsequent Meran-tip-faults were recognized, both accommodated sinistral transpression. Hence, these faults were not affected by an early transtensional phase as observed in the northward translation experiment (Exp. 1-A). More towards the right, vectors turned (sub)orthogonal in front of the right segment as shortening progressed.

Northeast translation (Exp. 1-C)

During northeast translation the lateral extent of the orogenic wedge was limited to the right- and middle indenter segments. No thrusting occurred in front of the left segment. Instead, the fore-thrusts in front of the middle limb curved towards the Meran indenter tip where it accommodated transpression.

From the PIV-images we observed, as in the previous models, a divergent fanning of the vector orientations. Despite the applied northeast translation the bulk vectors within the model space trended NNW- to NW. Short-lived Meran tip-faults trended NNE to NNW and underwent transpression. With ongoing shortening some of these faults connected with the fore-thrust, while others became already inactive before a connection was made (e.g. fault nr. 5, Fig. 6.9). Hence, the Meran indenter tip acted as a junction between active and inactive faults. Finally, the inactive faults slightly rotated meanwhile they slide downwards along the left segment with ongoing shortening.

Rotation (Exp. 1-D)

In this model the indenter was rotated anticlockwise by 25°. A different indenter shape was used in order to finally reproduce the present day indenter geometry. As a result of rotation a wedge formed with constant width along strike (Fig. 6.9). In addition, a series of two curved dextral faults sprouted from the Mauls indenter tip. Remarkably no faults were produced in front of the Meran indenter tip. PIV images are in line with the observed fault pattern and record particle motion paths varying between WSW and ENE. Vector magnitude decreased gradually westward.

Series 2

Northward translation (Exp. 2-A)
Using a thinner sand pile (3cm) resulted in narrower thrust spacing. After 6 cm BS, the wedge propagated outward by the formation of a second frontal thrust. No other features were identified from top-view images.

From PIV-images, however, a NNE-trending Meran-tip fault was recognized, which formed even before 1 cm BS and accommodated mainly strike-slip (Fig. 6.10). This structure was short-lived as deformation propagated towards a NNW-trending feature which finally connected to the major fore-thrust (nr. 3). In total several short-lived Meran-tip faults formed with different orientations varying between NNE and NNW and each accommodated not more than 1 mm slip. Some of these tip-faults were coevally active. At 6.6 cm BS the NNE trending fault (nr. 6) underwent sinistral transtension. Between 6 cm and 10 cm bs several inactive Meran-tip faults relocated in front of the left-segment (Fig. 6.10). The overall vector field diverged slightly more during this later stage of shortening.

The effect of a ductile layer at the base (Exp. 2-B)
The implementation of a ductile layer at the base, as analogue for weak lower crust, has a major impact on the style of thrusting (Fig. 6.10). The final wedge consisted of several fore-thrusts that propagated north- and westward through time. Thrust spacing remained constant along-strike and seemed to hardly influenced by the different indenter limbs.

The PIV-images indicate that in sequence formed fore-thrusts were coevally active. A lateral westwards decrease in horizontal velocities correlated with the different indenter limbs. These relative differences were highest directly in front of the indenter and around the indenter tips, and resulted in sinistral displacement zones. However, discrete brittle tip-fault zones, as observed in the other experiments did not develop.

6.4.3 Summarized model results

All experiments developed a diverging strain pattern mimicking the indenter shape. Even with NE-translation (Exp. 1-C), shortening in front of the middle limb was perpendicular to the limbs (NW-directed) (Fig. 6.9 and 6.10). Within the translation models, N-trending strike-slip faults sprouted from the indenter tips and compensated for lateral variations in strain orientation and magnitude induced by the indenter shape. Formation of these in general short-lived Meran-tip faults did not strongly depend on the indenter's motion path. However, the motion path did influence fault orientation varying between NNE and NW, and also led to lateral and temporal varying fault kinematics in front of the indenter tip. As such, alternation between transpression and transtension along the Meran-tip faults occurred in the N-translation experiments (Exp. 1-A and 2-A). Furthermore, anticlockwise rotation of the indenter resulted in a series of dextral transpressive faults in front of the Mauls indenter tip, but no Meran-tip fault formed. The same counts for the model with a ductile layer at the base, where strain was too dispersed to develop discrete faults.

6.5 Discussion

Passeier-type faults formed in front of the indenter tip within most experiments, indicating an allowed variance of 40° of the indenter's translation direction. Solely the formation of the Passeier fault seems therefore inadequate to unequivocally constrain the movement path of the Adriatic plate. However, the direction of indentation left a strong imprint on fault kinematics. As such, modelling northward translation induced initially sinistral-transtension along a N-S trending tip-fault, which with ongoing shortening then changed to sinistral-transpression (Fig. 6.9). Such strain dynamics is consistent with calculated paleostress tensors where transtension and transpression dominate along the Passeier's northern and southern segment, respectively. On the other hand, modelled NW- or NE-indentation resulted directly in sinistral transpression along the tip-fault, and did not reproduce the observed extension along the Passeier line. Therefore, based on the consistency between modelled northward indentation resulting in sinistral-transtension and sinistral-transpression along a tip fault, and the measured fault kinematics along the Passeier line, we suggest a northward progression of the Adriatic indenter was most likely throughout the Miocene.

By means of the above interpretation, the Passeier line can be considered as a relative short-lived fault accommodating minor displacement with respect to the amount of total indentation. In fact, the varying amount of shortening between the different indenter limbs is accommodated by a series of parallel faults, which one by one became inactive as the indenter advanced northwards. The presence of such parallel faults is indeed argued for in field studies from *Viola at al.* [2004] and *Sölva et al.* [2005]. Consequently, the amount of sinistral slip along the Passeier line is by no means an indicator for the amount of indentation, and hence the amount of sinistral slip along the Giudicarie line. Viola et al. [2001] proposed a 15 km sinistral offset along the Passeier line based on a pre-existing connection between the Jaufen- and Thurnstein lines northwest of Meran. Despite weak evidence of such a correlation solely based on similar strike and mylonitization, the amount of displacement along this fault is according to our models no measure for the amount of Late Miocene sinistral slip along the Giudicarie line, and hence neither its role in modifying the Periadriatic line.

Furthermore, linking the Passeier fault kinematics with the rotation of Adria is unlikely, since no comparable structure formed in such a model set-up. However, ductile fabrics along the Jaufen line with dextral sense of shear may relate to rotation, but care is needed since *Müller et al.,* [2001] assigned dextral shear as being related to pre-Miocene strike-slip along the Periadriatic line. Also the role of a preceding phase of ductile deformation affecting the Passeier line is unlikely, since the indenter geometry did not induce discrete north trending fault zones in front of the indenter tip.

6.5.1 Indentation and associated strain partitioning

The use of a rigid indenter block in combination with sand as a deforming material led to a high rheology contrast. In fact, this rheology contrast is highly overestimated with respect to the natural analogue. Kinematic implications of a high rheology contrast have been studied by e.g. *Robl and Stüwe* [2005]. Based on their viscous sheet models, they infer a minimum rheology contrast of 1:10 between the internal Alps and a triangular shaped indenter. A lower strength contrast would not have preserved a triangular

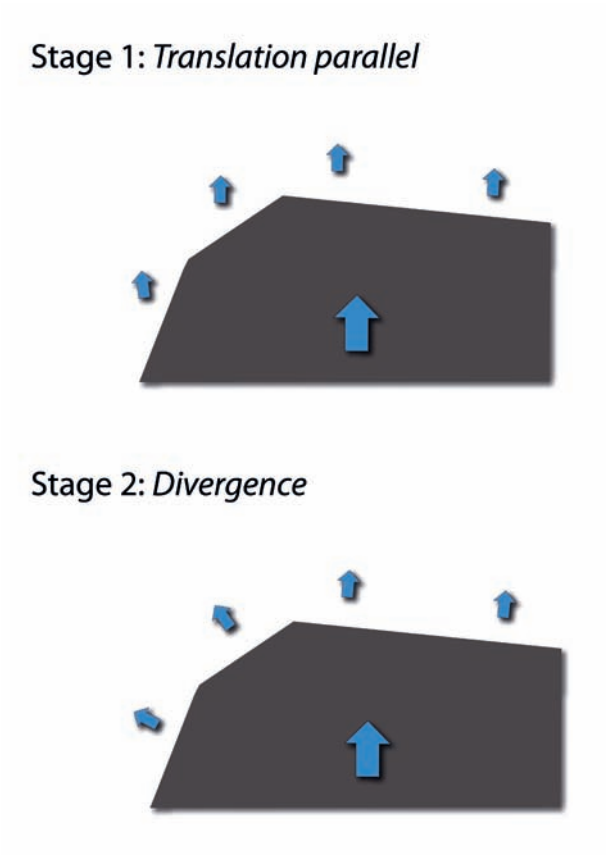

Figure 6.11 Schematic cartoon suggesting two follow-up stages based on an alternating horizontal velocity field (blue arrows). During initial shortening the velocity field is strongly governed by the direction of indentation (stage 1), whereas with ongoing shortening the velocity field changes according to the indenter shape (stage 2). See text for further explanation.

shape throughout Miocene convergence. Moreover, researchers like *Ratschbacher et al.,* [1991] and *Robl and Stüwe* [2005] argue that the indenters rigidity and shape are a prerequisite for lateral extrusion of the orogen towards the Pannonian basin.

The high rheology contrast induced changes of the velocity field observed in front of the indenter. As such, within the first centimetre of shortening vectors trend (sub) parallel to the direction of indentation, while with progressive shortening the vectors become more orthogonal to the indenter boundary. Suggestively, with ongoing shortening strain becomes increasingly partitioned into components parallel- and orthogonal to the indenter (Fig. 6.11). The strain partitioning affected deformation along the Meran-tip fault, expressed by changes from sinistral transtensive towards sinistral transpressive in Exp. 1-A and 2-A (Fig. 6.9). As a result of partitioning, deformation relates less to the direction of indentation since the vectors tend to arrange orthogonal to the indenter segments in all experiments. A divergent strain pattern is supported by field observations of dip-slip in front of the indenter. In particular, along the Meran-Mauls fault a ductile horizontal stretching lineation has been overprinted by dip-slip stretching lineations indicating top-to-the-SE thrusting [*Pomella*, 2010]. Based on fission track data thrusting was synchronous with 17 Ma deformation along the Passeier line [*Müller et al.*, 2001; *Pomella*, 2010]. I therefore presume that the interference of strain induced by both faults

affected not only the deformation within the Mauls basement unit, but probably also influenced fault kinematics along the southern segment of the Passeier line, and in particular near the Meran indenter-tip. As such, considering the Passeier line simply as a Riedel shear branching of the Giudicarie line as modelled by *Viola et al.,* [2004] is to my opinion too simplistic. Hence, the role of the indenter shape is regarded as increasingly important on the induced strain pattern, whereas the imprint of indentation direction is actually minor.

6.5.2 Link between the Giudicarie, Passeier, Jaufen and Brenner lines

With the recognition of the Giudicarie and the Brenner lines, a link in terms of large scale kinematics between the two have been proposed [e.g. *Laubscher*, 1973; *Behrmann*, 1988; *Selverstone*, 1988; *Fügenschuh et al.*, 1997]. In this view, the Giudicarie line is not solely considered as a bend of the Periadriatic line curving towards the north east into the Pustertal segment [e.g. *Bigi et al.*, 1990-92], but propagated northwards through the Austroalpine units into the Brenner line. Important roles are then assigned to the Passeier- and Jaufen lines as they connect the Giudicarie- and Brenner lines and separate domains of Alpine metamorphism from no metamorphic domains. As such, the Passeier line is a northward prolongation of the northern Giudicarie line, accommodating mainly sinistal strike-slip [e.g. *Viola et al.*, 2001], whereas the Jaufen line additionally accommodated a normal component most likely in response to normal faulting along the Brenner line [e.g. *Selverstone*, 1988]. Coeval faulting is also supported by Miocene cooling ages sampled along the entire fault system [e.g. *Fügenschuh et al.*, 1997; *Viola et al.*, 2001; *Pomella*, 2010]. However, insights on the fault kinematics along the Passeier- and Jaufen lines were up to now a missing link in those regional interpretations.

Although the interpretations of our field data are largely in agreement with the above presumed kinematics along the Passeier- and Jaufen lines, the faults are not necessarily linked. For example, the Jaufen line reveals a polyphase deformation as was already recognized by [e.g. *Fügenschuh et al.*, 1997; *Müller et al.*, 2001; *Viola et al.*, 2001] and thus strain indicators are various, among which only the sinistral transtension is considered as being consistent with Brenner fault kinematics. In addition, the (sub) vertical dipping Jaufen shear zone is geometrically difficult to connect with the shallow dipping Brenner mylonites. Note also that the total thickness of mylonites along the Jaufen line is far less than those of the Brenner line, tens versus hundreds of meters respectively [*Fügenschuh*, 1995; *Müller et al.*, 2001]. Furthermore, explaining brittle (re)activation along the Jaufen line in a regional context is twofold. Along the Jaufens northern segment the appearance of tensional tensors suggests a linkage with the Brenner normal fault during the late Miocene. While along the southern segment, dominant strike-slip and compression are more likely a direct result of indentation. Further southward, the Jaufen-Passeier junction is characterized by the absence of mylonites within the Passeier valley implying a cut-off of the Jaufen line rather than a continuation into the Passeier valley. A disconnection between both brittle faults is also supported by the crustal analogue model results, which indicate that the Passeier sprouted from the Meran-indenter tip, and should therfore not be treated as a prolongation, nor a Riedel-shear, splaying from the Giudicarie line as suggested by *Viola et al.,* [2001]. This implies that the Passeier- and Jaufen lines should be considered as separate faults during their brittle stage, and not as a single fault system as for instance suggested by *Spiess* [1995].

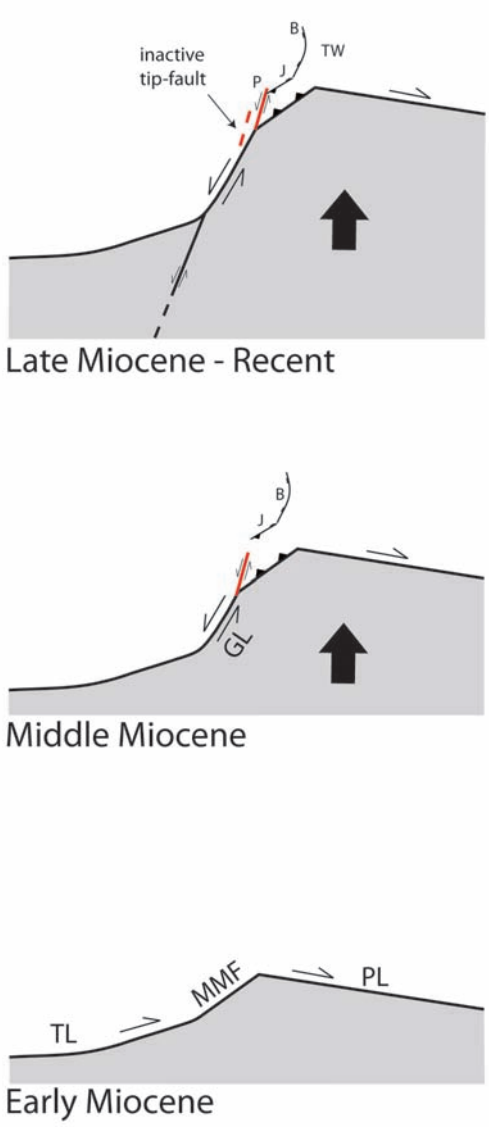

Figure 6.12 Evolution sketch of indentation from Miocene to recent times. During the early-Miocene the outline of the present day indenter was formed and dextral slip along the Periadriatic line became no longer possible. During mid-Miocene times, northward indentation was accommodated by mainly sinistral-slip along the Giudicarie line and primarily thrusting along the Meran-Mauls line (see also *Pomella* [2010]). In front of the Meran indenter-tip deformation in the Austroalpine units was partly accommodated by "short-lived" tip-faults (red), reactivation of the Jaufen line, and uplift of the Meran-Mauls Basement. From late-Miocene onward, the Passeier line formed as a "new" "short-lived" tip-fault and intersected the Jaufen line, which since then accommodated minor thrusting along its southern segment, while extension along its northern segment could considered transitional towards the Brenner line. TL: Tonale Line, MMF: Meran-Mauls Fault, PL: Pustertal Line, GL: Giudicarie Line, J: Jaufen Line, P: Passeier Line, B: Brenner Line, TW: Tauern Window.

The combined field- and modelling studies emphasize that the Jaufen- and Passeier lines both result from indentation. However, the various deformation imprints along and between both faults devaluate its entity as a single fault system (Fig. 6.12). As such, Miocene deformation along the Giudicarie- and Jaufen lines was probably strongly affected by inherited weaknesses dating back to Triassic rifting in the Southern Alps, and extension overprinting mid-Cretaceous stacking of Austroalpine units, respectively [e.g. *Bertotti et al.*, 1993; *Pomella*, 2010]. On the other hand, the complex kinematics along the Passeier line can be fully explained by indenter geometry. Consequently, the amount of slip along the Passeier line cannot be directly balanced with its neighbouring faults.

In short, considering the Giudicarie and Brenner faults as a single lithosphere-scale fault system is too simplistic. Although coeval activity and large-scale kinematics suggest a single fault system, displacements along the different faults were governed by local induced strain fields. As such, from the early Miocene onwards, the Giudicarie fault might have directly accommodated lateral displacement, induced by fragmentation of the Adriatic indenter underlain by the lateral change in subduction polarity as suggested by *Schmid et al.* [2004] and *Ustaszewski* [2008]. However, during the mid- to late Miocene, formation of the Passeier line was probably not a prime response to along-strike reconfigurations at mantle depths, but resulted from the distinct shape of the Adriatic crustal indenter.

6.6 Conclusions

Integration of field data and crustal modelling showed that the Passeier fault is kinematically compatible with northward indentation of an indenter with present day geometry.

The field study resolved for sinistral transtension along the Jaufen line, implying uplift of the Meran-Mauls basement unit, and a brittle overprint indicating transtension and transpression along its northern and southern segments, respectively. The Passeier line contains only a brittle imprint, which varies along-strike from normal faulting in the north to sinistral strike-slip in the south.

Interpretations of the analogue modelling results suggest that the Passeier line most likely resulted from indenter curvature by sprouting from the “Meran” indenter-tip, and is probably a short-lived feature accommodating only minor displacement. The associated fault kinematics along such a tip-fault strongly depends on the outline of the Adriatic indenter, and less on the motion path. The observed fault kinematics along the Passeier line, however, is most consistent with northward advancing of the Adriatic indenter during Miocene times.

In a regional perspective, the Passeier line should not be treated as a feature connecting the much larger Giudicarie- and Brenner fault zones, but can simply be considered the expression of crustal indenter curvature.

Chapter 7

Synthesis

The modelling- and field results presented in this thesis aimed to improve our understanding on the interplay between mantle-lithosphere subduction and crustal deformation. In particular, the crustal and topographic expressions of a lateral change in subduction polarity of the mantle lithosphere have been investigated, and discussed in the context of the Alps.

To these aims, we studied 1) the exhumation history of the post-collisional stage throughout the Eastern Alps by means of a compilation of cooling ages, 2) the crustal response on mantle lithosphere subduction by conducting lithosphere-scale analogue experiments, 3) the lithospheric response on a lateral change in subduction polarity within analogue experiments, 4) the fault kinematics along the Jaufen- and Passeier lines, and 5) crustal deformation in front of the Adriatic indenter by applying crustal-scale analogue experiments.

The results of the lithosphere-scale analogue experiments revealed how the interaction between the deep- and shallow lithosphere depends on important parameters, such as plate boundary geometry; rheology of the plate boundary, lower crust and mantle lithosphere; and subduction polarity. Varying these parameters has strong implications for the degree of (plate) decoupling, which in turn influences the deformational response of the lithosphere. In this perspective, the diversity of orogenic wedges and surface topography resulting from continental collision can be explained. Within the Alps, the along-strike differences of wedge build-up as well as the exhumation history between the Western/Central Alps, and the Eastern Alps are then at least partly considered reflections of lateral variations at mantle depth, of which most outstanding, a lateral change of subduction polarity.

7.1 Exhumation history of the Eastern Alps

The compilation of geochronological data presented in Chapter 2 documents the post-collisional cooling history of the Eastern Alps. A series of cooling maps, based on different isotope systems, portray that early Miocene cooling was mainly restricted to two thermal domes within the Tauern Window (TW). Observed cooling trends reveal both updoming and fault controlled cooling (e.g. Brenner line), and suggest a strong interplay between E-W extension and N-S orientated shortening during exhumation of the TW. In contrast, cooling towards near surface conditions was more spatially distributed throughout the middle- to late Miocene affecting also the surrounding Austroalpine units. The lateral cooling trends as well as the transition from localized towards more distributed cooling can be best explained by increased coupling between the European and Adriatic plates. In combination with the here presented modelling results, the significant differences in exhumation between the TW and the adjacent Ötztal complex divided by the Brenner line might be a reflection of the lateral polarity change at mantle depths.

7.2 Crust-mantle decoupling and crustal wedge formation

The importance of the plate boundary on the structural and topographic evolution of continental collision zones was stressed in Chapter 3. It turned out that the geometry of the plate contact together with the abundance and distribution of lubricants along the plate contact control the amount of mantle lithosphere subduction and the corresponding surface deformation. Favorable conditions for subduction of the mantle lithosphere include an inclined weak plate interface in combination with crust-mantle decoupling. Mantle subduction is coeval with localized crustal deformation and results in the formation of an orogenic wedge. Final hampering of subduction caused by thinning or consumption of lubricants, and/or crust-mantle coupling results in the distribution of crustal deformation toward the plate interiors. This defined “coupled stage” is characterized by buckling and thickening of both the upper- and lower plates, and vertical motions affecting the crustal wedge and foreland basins.

Ongoing subduction and localization of crustal deformation can be assured for if plate- and crust-mantle decoupling is maintained. In the experiments presented in Chapter 4, a high degree of crust-mantle decoupling was achieved by weaken the lower crust. Varying the rheological stratification of the lithosphere has, however, strong implications on the construction of the orogenic wedge. If a crustal detachment level is present, the wedge typically widens onto the lower plate. In contrast, if the extent of weak lower crust is restricted to the plate boundary region the wedge will remain narrow. Furthermore, the experiments carried out for this thesis highlight the dependence of crustal deformation on the underlying viscous layers. As such, upper crustal thrusting and surface topography are largely determined by deformation and thickening of the lower crust.

A summary on the wedge geometries described in this thesis is given in Figure 7.1. The various wedges are placed in a context including the amount of mantle subduction and the degree of plate and crust-mantle decoupling. The resulting picture emphasizes that plate boundary geometry and the rheological stratification of the lithosphere directly govern the amount of subduction of the mantle lithosphere as well as the build-up of orogenic wedges.

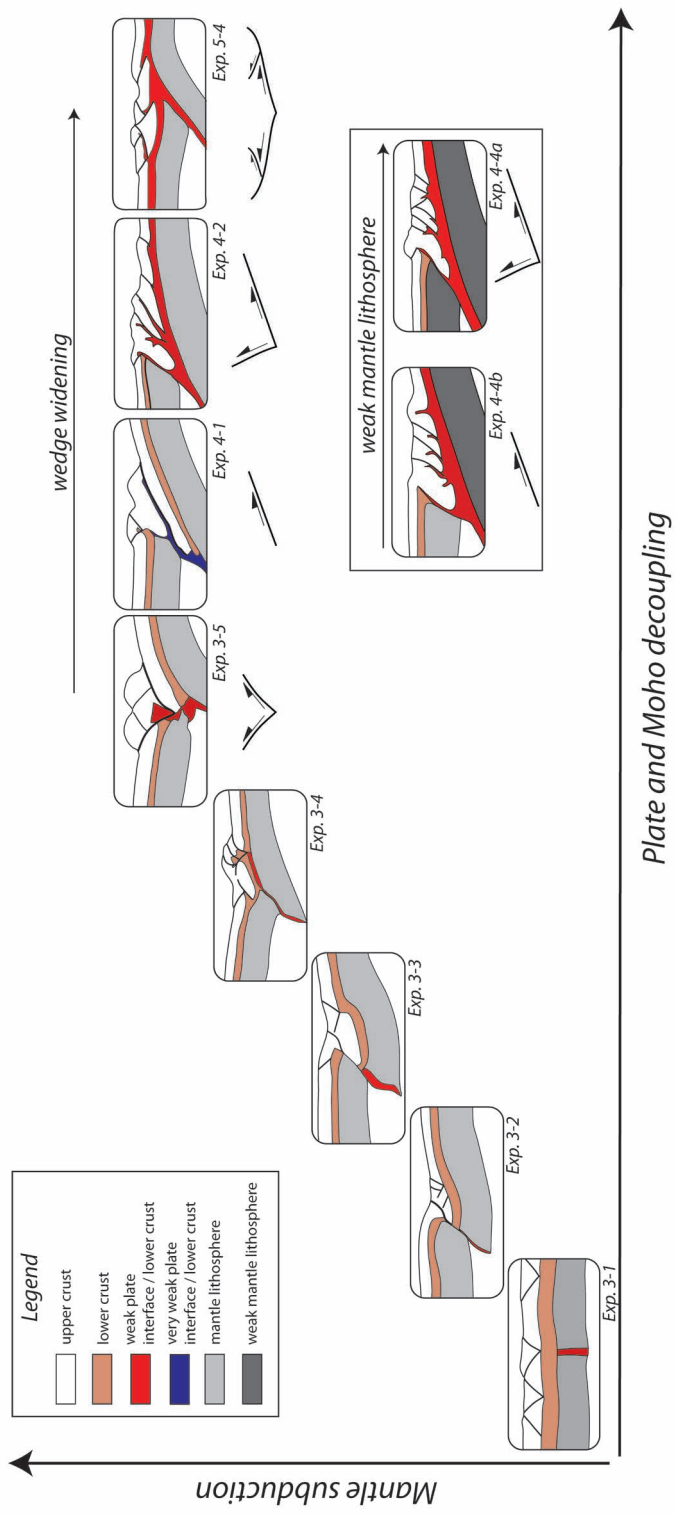

Figure 7.1 Overview on wedge geometries in relation to the amount of mantle subduction and the degree of plate- and Moho decoupling.

7.3 Implications of a changing subduction polarity on crustal architecture and vertical motions

The geometry of a crustal wedge can be drastically modified by a lateral change in subduction polarity (see Chapter 5). At mantle depth, interaction between adjacent domains of opposing subduction polarity results in a transition zone in where the amount of mantle lithosphere subduction is reduced and the upper plates are dragged down. The crust responses by thickening of the lower crust, widening of the wedge onto the lower and upper plates, and lowering of surface topography. The width of the transition zone depends directly on the amount of shortening and the degree of lateral coupling between the adjacent subduction domains. If the domains are only weakly coupled the width of the transition zone remains modest. Subduction below the transition zone is hardly hampered, and upper plate down bending and thrusting is limited. The surface expression is characterized by relative low vertical uplift within the transition zone, but by relative high topography owed to retro-shearing directly adjacent to the transition zone. In contrast, strong coupling between the adjacent subduction domains results in a wide transition zone. This transition zone is characterized by strong down bending of the upper plates, a modest amount of subduction of the lower plates, and lower crustal thickening. The upper crust responds in this broad region by thrusting onto the upper plate, and relative little vertical uplift.

7.4 Kinematic analysis of the Jaufen/Passeier lines

A detailed field study along the Jaufen and Passeier lines revealed that these faults are not representing a single fault system. The Jaufen mylonites record sinistral transtension and are brittely overprinted by transtension and transpression along its northern and southern segments, respectively. The Passeier line underwent only brittle deformation with a distinction between normal faulting in the north and dominantly sinistral strike-slip in the south.

Crustal modelling also implies that the faults do not share the same kinematic history. As such, the Passeier line originated from northward indentation by sprouting from the “Meran” indenter-tip, and is a short-lived feature, accommodating only minor displacement. Consequently, the Passeier line should not be considered as a lithosphere cutting fault connecting the Giudicarie- and Brenner fault zones, but as the expression of indenter curvature.

In this context, northward indentation of the Adriatic upper crust may still be underlain by northward subduction of Adriatic mantle lithosphere. However, there is no reason to treat the Giudicaire-Brenner fault system as a single fault system that relates to the lateral change in subduction polarity.

7.5 Implications on the tectonic evolution of the Alps

Based on the above model several along-strike variations within the Alps can be explained in the context of the observed change of subduction polarity.

The transition from an asymmetric wedge in the Western- and Central Alps towards a wide and symmetric wedge in the Eastern Alps corresponds with the lateral change of

subduction polarity. From the mid- to late Miocene onwards, large scale deformation and exhumation patterns differ significantly between the Western- and Central Alps and the Eastern Alps. During the early-mid Miocene, exhumation of the internal massifs in the Western- and Central Alps was coeval with southward thrusting in the Southern Alps, whereas from the late Miocene onward exhumation of the external massifs was coeval with thrusting in the Jura Mountains. In contrast, in the Eastern Alps rapid exhumation of the Tauern Window was coeval with southward thrusting during almost the entire Miocene. The along-strike asymmetry of Alpine wedge growth is comparable with the asymmetry observed in our experiments. The modelled crustal wedges grew mainly onto the lower plates and induced along-strike variations by the termination of lower plate thrusts within the transition zone. In addition, the transition zone was characterized by widening of the orogenic wedge, large-scale symmetry, and little vertical uplift, which is a good analogue for the Öztal region directly west of the Tauern Window.

Tele-seismic tomography revealed that the Adriatic mantle lithosphere subducted below the European plate, and partly below the Eastern Alps. In contrast, the crustal part of the Adriatic plate behaved as a rigid indenter. This controversy implies decoupling between the crust and mantle lithosphere, which allows Adria to be an indenter at crustal levels, but to be the subducting plate at mantle depth. Decoupling between the plate's deep and shallow parts must then have occurred from the Miocene onwards. During this episode, deformation at crustal levels within the Eastern Alps is characterized by sinistral slip along the Giudicarie fault zone, and localized rapid cooling within the Tauern Window (Chapter 2). Both are considered as an expression of the interplay between the northward advancing Adriatic indenter on one hand, and Eastward extrusion on the other hand. Additionally, we associate deformation along the Jaufen line and in particular the Passeier line, with indentation at crustal levels (Chapter 6).

To relate distinct crustal structures directly to the subduction polarity change at depth is complicated. Interference exists between the surface imprint related to crustal indentation and the crustal response related to subduction of the mantle lithosphere. Nevertheless, based on our analogue modelling results we address the following features as directly resulting from crustal indentation: 1) high amount of Miocene uplift in the Tauern Window, 2) faulting and uplift of the Passeier- and Jaufen region, 3) sinistral-transpression along the Giudicarie fault zone, and 4) normal shearing along the Brenner line. Although eastward extrusion probably contributed significantly to normal faulting along the Brenner line, fault initiation might have been associated with indentation. Pronounced surface features which probably reflect subduction of the Adriatic mantle-lithosphere are: 1) southward thrusting within the eastern Southern Alps, 2) diachronous cooling in the Tauern Window, with in particular rapid uplift of its western dome, and 3) a relative low amount of vertical uplift in the Ötztal complex.

7.6 Outlook

The presented modelling results successfully integrated continental mantle subduction with crustal mountain building. To build further upon these findings I suggest that the experimental set-ups can be extended by 1) Varying the rheology of the upper crust, by for instance using different sand types, 2) Implementation of decoupling levels at different depth within the crust, representing i.e. anhydrite layers, and 3) Decreasing

the bulk shortening rate and/or increasing the slab-pull force. Another challenge would be to obtain a more realistic strength contrast between compositional layers. To do this, one can implement more layers with a relative low strength contrast between them, or even control the layers strength by varying temperature within the model. Furthermore, applying erosion to the model surface would probably give interesting results as it would affect wedge formation, strain localization, and may induce an isostatic response as well.

During this study, a first attempt was made to visualize the interior of an analogue experiment by using a Computer Tomographer (CT-scanner). This technique would have greatly improved the accuracy of visualizing lateral variations of deformation without the need to destroy the experiment by cutting. Within the pilot experiments, with set-ups conform Chapter 5, the lateral changing subducting slab was recognized on CT-scans. Unfortunately, detailed visualization of crustal deformation was not possible, presumably owed to the low-density contrasts of the used materials. Hence, analogue modelling is further challenged by a search for materials producing higher contrasts when transmitting X-rays, and which are also properly scaled.

Finally, improving analogue modelling techniques should coincide with a better understanding of the natural analogue. This implies ongoing geological- and geophysical field studies to constrain boundary conditions, but more important, to confirm model predictions. Such integration between field- and modelling studies has so far greatly extended our knowledge on the behaviour of the lithosphere. For example, insights on the thermal- and rheological state of the lithosphere depend on combining great computational power with large global data sets. However, we should also realize that processing large data sets often coincides with an increased model uncertainty. Therefore, simple experiments, confined by only a few physical parameters, are needed.

References

Abers, G.A., 2005. Seismic low-velocity layer at the top of subducting slabs: observations, predictions, and systematics. Physics of The Earth and Planetary Interiors, 149(1-2): 7-29.

Ampferer, O., 1906. Über das Bewegungsbild von Faltengebirgen Jb. Geol. Reichsanst. Wien., 77: 539-622.

Angelier, J. and Mechler, P., 1977. Sur une méthode graphique de recherche des contraintes principales également utilisable en tectonique et en séismologie: la méthode des dièdres droits. Bulletin de la Société géologique de France.

Barth, S., Oberli, F. and Meier, M., 1989. U-Th-Pb systematics of morphologically chracterised zircon and allanite: a high-resolution isotopic study of the Alpine Rensen Pluton (northern Italy). Earth and Planetary Science Letters, 95(3-4): 235-254.

Beaumont, C., Fullsack, P. and Hamilton, J., 1994. Styles of crustal deformation in compressional orogens caused by subduction of the underlying lithosphere. Tectonophysics, 232(1-4): 119-132.

Beaumont, C., Ellis, S., Hamilton, J. and Fullsack, P., 1996. Mechanical model for subduction-collision tectonics of Alpine-type compressional orogens. Geology, 24(8): 675-678.

Beaumont, C., Munoz, J.A., Hamilton, J. and Fullsack, P., 2000. Factors controlling the Alpine evolution of the central Pyrenees inferred from a comparison of observations and geodynamical models. J. Geophys. Res., 105.

Behrmann, J.H., 1988. Crustal-scale extension in a convergent orogen: the Sterzing-Steinach mylonite zone in the Eastern Alps. Geodinamica acta, 2(2): 63-73.

Benedetti, L., Tapponnier, P., King, G.C.P., Meyer, B. and Manighetti, I., 2000. Growth folding and active thrusting in the Montello region, Veneto, northern Italy. Journal of Geophysical Research, 105(B1): 739-766.

Bertotti, G., Picotti, V., Bernoulli, D. and Castellarin, A., 1993. From rifting to drifting: tectonic evolution of the South-Alpine upper crust from the Triassic to the Early Cretaceous. Sedimentary Geology, 86(1-2): 53-76.

Bigi, G., Castellarin, A., Coli, M., Del Piaz, G., Sartori, R., Scandone, P., Vai, G., Cosentino, D. and Parotto, M., 1990-92. Structural Model of Italy, scale 1:500000 sheet 1-3. Consiglio Nazionale delle Ricerche, Progetto Finalizzato Geodinamica, SELCA Firenze.

Bird, P., 1979. Continental delamination and the Colorado Plateau. J. Geophys. Res., 84: 7561-7571.

Borsi, S., Del Moro, A., Sassi, F. and Zirpoli, G., 1978b. On the age of the periadriatic Rensen massif (Eastern Alps). Neues Jahrbuch fur Geologie und Palaontologie 5: 267-272.

Bousquet, R., Oberhansli, R., Goffe, B., Wiederkehr, M., Koller, F., Schmid, S.M., Schuster, R., Engi, M., Berger, A. and Martinotti, G., 2008. Metamorphism of metasediments at the scale of an orogen: a key to the Tertiary geodynamic evolution of the Alps. Geological Society London Special Publications, 298(1): 393.

Brückl, E., Behm, M., Decker, K., Grad, M., Guterch, A., Keller, G.R. and Thybo, H., 2010. Crustal structure and active tectonics in the Eastern Alps. Tectonics, 29(2): TC2011.

Brun, J.-P., Sokoutis, D. and van den Driessche, J., 1994. Analogue modelling of detachment fault systems and core complexes. Geology, 22(4): 319-322.

Brun, J.-P., 2002. Deformation of the continental lithosphere: insights from brittle-ductile mod-

els. In: S. De Meer, M.R. Drury, J.H.P. de Bresser and G.M. Pennock (Editors), Deformation Mechanisms, Rheology and Tectonics: Current Status and Future Perspectives. The Geological society of London, Special Publications, pp. 355-370.

Burov, E. and Toussaint, G., 2007. Surface processes and tectonics: Forcing of continental subduction and deep processes. Global and Planetary Change, 58(1-4): 141-164.

Burov, E. and Yamato, P., 2008. Continental plate collision, P-T-t-z conditions and unstable vs. stable plate dynamics: Insights from thermo-mechanical modelling. Lithos, 103(1-2): 178-204.

Burov, E.B. and Watts, A.B., 2006. The long-term strength of continental lithosphere:"jelly sandwich" or "crème brûlée"? GSA Today, 16(1): 4-10.

Caporali, A. and Martin, S., 2000. First results from GPS measurements on present day alpine kinematics. Journal of Geodynamics, 30(1-2): 275-283.

Caporali, A., Braitenberg, C. and Massironi, M., 2005. Geodetic and Hydrological Aspects of the Merano Earthquake of July 17, 2001. J. of Geodynamics, 39: 317-336.

Castellarin, A., Cantelli, L., Fesce, J., Mercier, V., Picotti, G., Pini, G., Prosser, G. and Selli, L., 1992. Alpine compressional tectonics in the Southern Alps. Relationships with the N-S Apennines. Annales Tectonicae, 6: 62-94.

Castellarin, A. and Cantelli, L., 2000. Neo-Alpine evolution of the Southern Eastern Alps. Journal of Geodynamics, 30(1-2): 251-274.

Castellarin, A., Nicolich, R., Fantoni, R., Cantelli, L., Sella, M. and Selli, L., 2006. Structure of the lithosphere beneath the Eastern Alps (southern sector of the TRANSALP transect). Tectonophysics, 414(1-4): 259-282.

Chemenda, A.I., Mattauer, M. and Bokun, A.N., 1996. Continental subduction and a mechanism for exhumation of high-pressure metamorphic rocks: new modelling and field data from Oman. Earth Planet. Sci. Lett., 143: 173-182.

Chemenda, A.I., Yang, R.K., Stephan, J.F., Konstantinovskaya, E.A. and Ivanov, G.M., 2001. New results from physical modelling of arc-continent collision in Taiwan: evolutionary model. Tectonophysics, 333(1-2): 159-178.

Choukroune, P., 1989. The ECORS Pyrenean deep seismic profile reflection data and the overall structure of an orogenic belt. Tectonics, 8(1): 23-39.

Cliff, R., Droop, G. and Rex, D., 1985. Alpine metamorphism in south-east Tauern Window, Austria, 2. Rates of heating, cooling and uplift. Journal of Metamorphic Geology, 3: 403-415.

Cloetingh, S., Wortel, M. and Vlaar, N., 1982. Evolution of passive continental margins and initiation of subduction zones. Nature, 297(5862): 139-142.

Cloetingh, S., Burov, E., Beekman, F., Andeweg, B., Andriessen, P.A.M., Garcia-Castellanos, D., de Vicente, G. and Vegas, R., 2002. Lithospheric folding in Iberia. Tectonics, 21(5): 1-26.

Costa, C.H., Murillo, M.V., Sagripanti, G.L. and Gardini, C.E., 2001. Quaternary intraplate deformation in the southeastern Sierras Pampeanas, Argentina. Journal of Seismology, 5(3): 399-409.

Davy, P. and Cobbold, P.R., 1991. Experiments on shortening of a 4-layer model of the continental lithosphere. Tectonophysics, 188: 1-25.

De Franco, R., Govers, R. and Wortel, R., 2007. Numerical comparison of different convergent plate contacts: subduction channel and subduction fault. Geophysical Journal International, 171(1): 435-450.

De Franco, R., Govers, R. and Wortel, R., 2008a. Dynamics of continental collision: influence of the plate contact. Geophys. J. Int. , 174: 1101-1120.

De Franco, R., Govers, R. and Wortel, R., 2008b. Nature of the plate contact and subduction zones diversity. Earth and Planetary Science Letters, 271(1-4): 245-253.

Del Moro, A., Puxeddu, M., Radicatie de Brozolo, F. and Villa, I., 1982. Rb-Sr and K-Ar ages on minerals at temperatures of 300-400 °C from deep wells in de Larderello geothermal field (Italy). Contributions to Mineralogy and Petrology, 81: 340-349.

Delvaux, D. and Sperner, B., 2003. New aspects of tectonic stress inversion with reference to the

TENSOR program. Geological Society London Special Publications, 212(1): 75.
Dengo, C.A. and Covey, M.C., 1993. Structure of the Eastern Cordillera of Colombia; implications for trap styles and regional tectonics. AAPG Bulletin, 77(8): 1315-1337.
Dèzes, P. and Ziegler, P., 2005. Map of the European Moho. EUCOR-URGENT: available at http://compl.geol.uni-bas.ch/downloads/Mohonet/euro-moho13.pdf.
Droop, G., 1985. Alpine Metamorphism in the south-east Tauern Window, Austria. Schweizerische Mineralogische und Petrographische Mitteilungen, 61: 237-273.
Dunkl, I. and Demeny, A., 1997. Exhumation of the Rechnitz window at the border of the Eastern Alps and the Pannonian Basin during Neogene extension. Tectonophysics, 272: 197-211.
Dunkl, I., Frisch, W. and Grundmann, G., 2003. Zircon fission track thermochronology of the southeastern part of the Tauern Window and the adjacent Austroalpine margin, Eastern Alps. Eclogae Geologicae Helvetiae, 96: 209-217.
Dunkl, I., Kuhlemann, J., Reinecker, J. and Frisch, W., 2005. Cenozoic relief evolution of the Eastern Alps – constraints from apatite fission track age-provenance of Neogene intramontane sediments. Austrian Journal of Earth Sciences, 98.
Egger, H., Krenmayer, H., Mandl, G., Matura, A., Nowotny, A., Pascher, G., Pestal, G., Pistotnik, J., Rockenschaub, M. and Schnabel, W., 1999. Geologische Űbersichtskarte der Republik Österreich 1:1500000. Geologische Bundesanstalt.
Ellis, S., 1996. Forces drivingcontinental collision: reconciling indentation and mantle subduction tectonics. Geology, 24: 699-702.
Escher, A., Masson, H. and Steck, A., 1988. Coupes géologiques des Alpes occidentales suisses, 2. Mem. Geol. Lausanne.
Faccenda, M., Burlini, L., Gerya, T.V. and Mainprice, D., 2008a. Fault-induced seismic anisotropy by hydration in subducting oceanic plates. Nature, 455(7216): 1097-1100.
Faccenda, M., Gerya, T.V. and Chakraborty, S., 2008b. Styles of post-subduction collisional orogeny: Influence of convergence velocity, crustal rheology and radiogenic heat production. Lithos, 103(1-2): 257-287.
Faccenda, M., Minelli, G. and Gerya, T.V., 2009. Coupled and decoupled regimes of continental collision: Numerical modeling. Earth and Planetary Science Letters, 278: 337--349.
Faure, M., Lin, W., Schärer, U., Shu, L., Sun, Y. and Arnaud, N., 2003. Continental subduction and exhumation of UHP rocks. Structural and geochronological insights from the Dabieshan (East China). Lithos, 70(3-4): 213-241.
Foster, D. and John, B. (Editors), 1999. Quantifying tectonic exhumation in an extensional orogen with thermochronology: examples fromthe southern Basin and Range Province. Exhumation processes: normal faulting, ductile flow and erosion, 154. Geological Society, London, Special Publications, 343-364 pp.
Frank, W. (Editor), 1987. Evolution of the Austroalpine elements in the Cretaceous. Geodynamics of the Eastern Alps. Deuticke, Vienna, 379-406 pp.
Frisch, W., 1979. Tectonic progradation and plate tectonic evolution of the Alps. Tectonophysics, 60(3-4): 121-139.
Frisch, W., Kuhlemann, J., Dunkl, I. and Brügel, A., 1998. Palinspastic reconstruction and topographic evolution of the Eastern Alps during late Tertiary tectonic extrusion. Tectonophysics, 297: 1-15.
Frisch, W., Dunkl, I. and Kuhlemann, J., 2000. Post-collisional orogen-parallel large-scale extension in the Eastern Alps. Tectonophysics, 327: 239-265.
Fritz, H., Tenczer, V., Hauzenberger, C., Wallbrecher, E. and Muhongo, S., 2009. Hot granulite nappes--Tectonic styles and thermal evolution of the Proterozoic granulite belts in East Africa. Tectonophysics, 477(3-4): 160-173.
Froitzheim, N., Schmid, S.M. and Conti, P., 1994. Repeated change from crustal shortening to orogen-parallel extension in the Austroalpine units of Graubünden. Eclogae Geologicae Helvetiae, 87(2): 559-612.
Fügenschuh, B., 1995. Thermal and kinematic history of the Brenner area (Eastern Alps, Tyrol),

ETH, Zürich, 226 pp.
Fügenschuh, B., Seward, D. and Mancktelow, N., 1997. Exhumation in a convergent orogen: the western Tauern window. Terra Nova, 9: 213-217.
Fügenschuh, B., Mancktelow, N. and Seward, D., 2000. Cretaceous to Neogene cooling and exhumation history of the Oetztal-Stubai basement complex, Eastern Alps: A structural and fission track study. Tectonics, 19: 905-918.
Fügenschuh, B. and Schmid, S.M., 2003. Late stages of deformation and exhumation of an orogen constrained by fission-track data: a case study in the Western Alps. Geological Society of America Bulletin, 115(11): 1425.
Funiciello, F., Faccenna, C. and Giardini, D., 2004. Role of lateral mantle flow in the evolution of subduction systems: insights from laboratory experiments. Geophysical Journal International, 157(3): 1393-1406.
Gallagher, K., Brown, R. and Johnson, C., 1998. Fission track analysis and its application to geological problems. Annu. Rev. Earth Planet. Sci., 26: 519-572.
Genser, J. and Neubauer, F., 1989. Low angle normal faults at the eastern margin of the Tauern Window (Eastern Alps). Mitteilungen der Österreichischen Mineralogischen Gesellschaft 81: 233-243.
Genser, J., van Wees, J., Cloetingh, S. and Neubauer, F., 1996. Eastern Alpine tectono-metamorphic evolution; constraints from two-dimensional P-T-t modeling. Tectonics, 15(3): 584-604.
Genser, J., Cloetingh, S. and Neubauer, F., 2007. Late orogenic rebound and oblique Alpine convergence: New constraints from subsidence analysis of the Austrian Molasse basin. Global and Planetary Change, 58(1-4): 214-223.
Gerya, T.V. and Stockhert, B., 2002. Exhumation rates of high pressure metamorphic rocks in subduction channels: The effect of Rheology. Geophys. Res. Lett., 29.
Gerya, T.V., Connolly, J.A.D. and Yuen, D.A., 2008. Why is terrestrial subduction one-sided? Geology, 36(1): 43-46.
Giamboni, M., Ustaszewski, K., Schmid, S.M., Schumacher, M.E. and Wetzel, A., 2004. Plio-Pleistocene transpressional reactivation of Paleozoic and Paleogene structures in the Rhine-Bresse transform zone (northern Switzerland and eastern France). International Journal of Earth Sciences, 93(2): 207-223.
Glasmacher, U., Tremblay, A. and Clauer, N., 2003. K–Ar dating constraints on the tectonothermal evolution of the external Humber zone, southern Quebec Appalachians. Canadian Journal of Geosciences, 40: 285-300.
Glotzbach, C., Reinecker, J., Danišík, M., Rahn, M., Frisch, W. and Spiegel, C., 2010. Thermal history of the central Gotthard and Aar massifs, European Alps: Evidence for steady state, long-term exhumation. Journal of Geophysical Research, 115(F3): F03017.
Govers, R. and Wortel, M.J.R., 2005. Lithosphere tearing at STEP faults: response to edges of subduction zones. Earth and planetary science letters, 236(1-2): 505-523.
Grundmann, G. and Morteani, G., 1985. The young uplift and thermal history of the central Eastern Alps (Austria/Italy), evidence from apatite fission track ages. Geologisch Jahrbuch, 128(197-216).
Hall, C.E., Gurnis, M., Sdrolias, M., Lavier, L.L. and Müller, R.D., 2003. Catastrophic initiation of subduction following forced convergence across fracture zones. Earth and Planetary Science Letters, 212(1-2): 15-30.
Hames, W. and Bowring, S., 1994. An emperical evaluation of the argon difussion geometry in muscovite. Earth and Planetary Science Letters, 124: 161-167.
Handy, M.R., Babist, J., Wagner, R., Rosenberg, C. and Konrad, M., 2005. Decoupling and its relation to strain partitioning in continental lithosphere: insight from the Periadriatic fault system (European Alps). Geological Society, London, Special Publications, 243(1): 249-276.
Hassani, R. and Jongmans, D., 1997. Study of plate deformation and stress in subduction processes using two-dimensional numerical models. Journal of Geophysical research 102(B8): 951-965.

Hejl, E., 1997. "Cold Spots"during the Cenocoic ecolution of the Eastern Alps: thermochronological interpretation of apatite fission-track data. Tectonophysics, 272: 159-174.
Hoinkes, G., Koller, F., Rantitsch, G., Dachs, E., Hock, V., Neubauer, F. and Schuster, R., 1999. Alpine metamorphism of the Eastern Alps. Schweizerische Mineralogische und Petrographische Mitteilungen, 79: 155-181.
Holland, T., 1979. High water activities in the generation of high pressure kyanite eclogites of the Tauern Window. Journal of Geology, 87: 127.
Hurford, A.J., 1986. Cooling and uplift patterns in the Lepontine Alps South Central Switzerland and an age of vertical movement on the Insubric fault line. Contributions to mineralogy and petrology, 92(4): 413-427.
Inger, S. and Cliff, R., 1994. Timing of metamorphism in the Tauern Window, Eastern Alps; Rb-Sr ages and fabric formation. Journal of Metamorphic Geology, 12(5): 695-707.
Janak, M., Froitzheim, N., Vrabec, M., Krogh Ravna, E.J. and Hoog, J.C.M., 2006. Ultrahigh pressure metamorphism and exhumation of garnet peridotite in Pohorje, Eastern Alps. Journal of Metamorphic Geology, 24(1): 19-31.
Jarvis, G.T. and Lowman, J.P., 2005. Sinking slabs below fossil subduction zones. Physics of The Earth and Planetary Interiors, 152(1-2): 103-115.
Karner, G.D. and Watts, A.B., 1983. Gravity Anomalies and Flexure of the Lithosphere at Mountain Ranges. J. Geophys. Res., 88.
Kissling, E., Schmid, S.M., Lippitsch, R., Ansorge, J. and Fugenschuh, B., 2006. Lithosphere structure and tectonic evolution of the Alpine arc: new evidence from high-resolution teleseismic tomography. Geological Society London Memoirs, 32(1): 129.
Kito, T., Thomas, C., Rietbrock, A., Garnero, E., Nippress, S. and Heath, A., 2008. Seismic evidence for a sharp lithospheric base persisting to the lowermost mantle beneath the Caribbean. Geophysical Journal International, 174(3): 1019-1028.
Kohler, M.D. and Eberhart-Phillips, D., 2002. Three-dimensional lithospheric structure below the New Zealand Southern Alps. Journal of Geophysical Research, 107(B10): 2225.
Koller, F., 1985. Petrologie und Geochemie der Ophiolite des Penninikums am Alpenostrand Jahrbuch Geologische Bundesanstalt, 128: 83-150.
Krabbendam, M. and Dewey, J.F., 1998. Exhumation of UHP rocks by transtension in the Western Gneiss Region, Scandinavian Caledonides. Geological Society, London, Special Publications, 135(1): 159-181.
Krenn, K., Fritz, H., Biermeier, C. and Scholger, R., 2003. The Oligocene Rensen Pluton (Eastern Alps, South Tyrol): magma emplacment and structures during plate convergence. Mitteilungen der Österreichischen Mineralogischen Gesellschaft, 94: 9-26.
Kuhlemann, J., Frisch, W., Dunkl, I. and Szekely, B., 2001. Quantifying tectonic versus erosive denudation by the sediment budget: the Miocene core complexes of the Alps. Tectonophysics, 339(1-2): 1-23.
Kuhlemann, J., 2007. Paleogeographic and paleotopographic evolution of the Swiss and Eastern Alps since the Oligocene. Global and Planetary Change, 58(1-4): 224-236.
Kurz, W., Neubauer, F., Genser, J. and Dachs, E., 1998. Alpine geodynamic evolution of passive and active continental margin sequences in the Tauern Window (Eastern Alps, Austria, Italy): a review. Geologische Rundschau, 87: 225-242.
Lamb, S., 2006. Shear stresses on megathrusts: Implications for mountain building behind subduction zones. J. Geophys. Res., 111.
Lambert, S., 1970. A Potassium-Argon Study of the Margin of the Tauernfenster at Dollach, Austria. Eclogae Geologicae Helvetiae, 63/1: 197-205.
Lammerer, B. and Weger, M., 1998. Footwall uplift in an orogenic wedge: the Tauern Window in the Eastern Alps of Europe. Tectonophysics, 285: 213-230.
Laubscher, H., 1988a. Material balance in Alpine orogeny. Geological Society of America Bulletin, 100(9): 1313-1328.
Laubscher, H., 1996. Shallow and deep rotations in the Miocene Alps. Tectonics, 15.

Laubscher, H., 2010. Jura, Alps and the boundary of the Adria subplate. Tectonophysics, In Press, Corrected Proof.

Laubscher, H.P., 1973. Alpen und Plattentektonik. Das Problem der Bewegungsdiffusion an kompressiven Plattengrenzen. Zeitschrift der Deutschen Gesellschaft für Geowissenschaften ZDGG, 124: 295-308.

Laubscher, H.P., 1977. The Tectonics of Subduction in the Alpine System. Mem. Soc. geol. ital., 13: 275-283.

Laubscher, H.P., 1988b. Décollement in the Alpine system: an overview. International Journal of Earth Sciences, 77(1): 1-9.

Leever, K.A., Gabrielsen, R.H., Sokoutis, D. and Willingshofer, E., 2011. The effect of convergence angle on the kinematic evolution of strain partitioning in transpressional brittle wedges: Insight from analogue modeling and high-resolution digital image analysis,. Tectonics, doi:10.1029/2010TC002823.

Linzer, H.-G., Decker, K., Peresson, H., Dell'Mour, R. and Frisch, W., 2002. Balancing lateral orogenic float of the Eastern Alps. Tectonophysics, 354(3-4): 211-237.

Lippitsch, R., Kissling, E. and Ansorge, J., 2003. Upper mantle structure beneath the Alpine orogen from high-resolution teleseismic tomography. Journal of Geophysical research 108: 1-15.

Lister, G. and Davis, G., 1989. The origin of metamorphic core complexes and detachment faults formed during Tertiary continental extension in the northern Colorado River region, U.S.A. Journal of Structural Geology, 11: 65-95.

Liu, Y., Genser, J., Handler, R., Friedl, G. and Neubauer, F., 2001. $^{40}Ar/^{39}Ar$ muscovite ages from the Penninic-Austroalpine plate boundary, Eastern Alps. Tectonics, 20: 526-547.

Lu, C.Y. and Malavieille, J., 1994. Oblique convergence, indentation and rotation tectonics in the Taiwan Mountain Belt: Insights from experimental modelling. Earth and planetary science letters, 121(3): 477-494.

Luth, S.W. and Willingshofer, E., 2008. Mapping of the post-collisional cooling history of the Eastern Alps. Swiss Journal of Geosciences, 101: 207-223.

Madritsch, H., Schmid, S.M. and Fabbri, O., 2008. Interactions between thin-and thick-skinned tectonics at the northwestern front of the Jura fold-and-thrust belt (eastern France). Tectonics, 27(5).

Madritsch, H., Fabbri, O., Hagedorn, E.M., Preusser, F., Schmid, S.M. and Ziegler, P.A., 2009. Feedback between erosion and active deformation: geomorphic constraints from the frontal Jura fold-and-thrust belt (eastern France). International Journal of Earth Sciences: 1-20.

Mancktelow, N., Stokli, D., Balz, G., Müller, W., Fügenschuh, B., Viola, G., Seward, D. and Villa, I., 2001. The DAV and Periadriatic fault systems in the eastern Alps south of the Tauern window. International Journal of Earth Sciences, 90: 593-622.

Mancktelow, N.S., 1995. Nonlithostatic pressure during sediment subduction and the development and exhumation of high pressure metamorphic rocks. J. Geophys. Res., 100(B1): 571-583.

Martinod, J. and Davy, P., 1994. Periodic instabilities during compression of the lithosphere 2. Analogue experiments. J. Geophys. Res., 99(B6): 12057-12069.

Molnar, P. and Tapponnier, P., 1975. Cenozoic Tectonics of Asia: Effects of a Continental Collision. Science, 189(4201): 419-426.

Most, P., 2003. Late Alpine cooling histories of tectonic blocks along the central part of the TRANSALP-traverse (Inntal-Gadertal): Constraints from geochronology. Ph.D. Thesis, Tübinger Geowissenschaftliche Arbeiten Reihe A 67, 97 pp.

Müller, W., Prosser, G., Mancktelow, N.S., Villa, I.M., Kelley, S.P., Viola, G. and Oberli, F., 2001. Geochronological constraints on the evolution of the Periadriatic fault system (Alps). Int. J. Earth Sci., 90: 623-653.

Muñoz, J.A., 1992. Evolution of a continental collision belt: ECORS-Pyrenees crustal balanced cross-section. In: K.R. McClay (Editor), Thrust tectonics. Chapman & Hall, pp. 235-246.

Naylor, M. and Sinclair, H.D., 2008. Pro- vs. retro-foreland basins. Basin Research, 20(3): 285-

303.
Neubauer, F., Genser, J. and Handler, R., 2000. The Eastern Alps: result of a two-stage collision process. Mitteilungen der Österreichischen Mineralogischen Gesellschaft, 92: 117-134.
Oberhänsli, R. and Goffé, B., 2004. Metamorphic structure of the Alps. Mitteilungen der Österreichischen Mineralogischen Gesellschaft(149): 115-199.
Oberhauser, R., 1995. Zur Kenntnis der Tektonik und der Paläogeographie des Ostalpenraumes zur Kreide-, Paleozän- und Eozänzeit. Jahrbuch der geologischen bundesanstalt, 138: 369-432.
Pawley, A.R., 1994. The pressure and temperature stability limits of lawsonite: implications for H2O recycling in subduction zones. Contributions to Mineralogy and Petrology, 118(1): 99-108.
Pfiffner, O.A., Lehner, P., Heitzmann, P., Mueller, S. and Steck, A. (Editors), 1997b. Deep structure of the Swiss Alps: Results from NRP 20. Birkhäuser Verlag, Basel-Boston-Berlin, 380 pp.
Pfiffner, O.A., Ellis, S. and Beaumont, C., 2000. Collision tectonics in the Swiss Alps: Insight from geodynamic modeling. Tectonics, 19(6): 1065-1094.
Pfiffner, O.A., 2009. Geologie der Alpen. Haupt Berne, Stuttgart, 360 pp.
Philip, H., Cisternas, A., Gvishiani, A. and Gorshkov, A., 1989. The Caucasus: an actual example of the initial stages of continental collision. Tectonophysics, 161(1-2): 1-21.
Piana, F., 2000. Structural Setting of Western Monferrato (Alps-Apennines Junction Zone, NW Italy). Tectonics, 19(5): 943-960.
Picotti, V., Prosser, G. and Castellarin, A., 1995. Structures and kinematics of the Giudicarie±Val Trompia fold and thrust belt (Central Southern Alps, northern Italy). Mem Sci Geol, 47: 95-109.
Plan, L., Grasemann, B., Spötl, C., Decker, K., Boch, R. and Kramers, J., 2010. Neotectonic extrusion of the Eastern Alps: Constraints from U/Th dating of tectonically damaged speleothems. Geology, 38(6): 483.
Pomella, H., 2010. The Cenozoic evolution of the Giudicarie fault system (Eastern/Southern Alps, northern Italy). A geochronolgical, structural and paleomagnetic study, University of Innsbruck, Innsbruck, 150 pp.
Pomella, H., Klötzli, U., Scholger, R., Stipp, M. and Fügenschuh, B., 2010. The Northern Giudicarie and the Meran-Mauls fault (Alps, Northern Italy) in the light of new paleomagnetic and geochronological data from boudinaged Eo-/Oligocene tonalites. International Journal of Earth Sciences: 1-24.
Prosser, G., 2000. The development of the North Giudicarie fault zone (Insubric line, Northern Italy). Journal of Geodynamics, 30(1-2): 229-250.
Pysklywec, R.N., Ellis, S.M. and Gorman, A.R., 2010. Three-dimensional mantle lithosphere deformation at collisional plate boundaries: A subduction scissor across the South Island of New Zealand. Earth and planetary science letters, 289(3-4): 334-346.
Raith, M., Raase, P., Kreuzer, P. and Müller, P. (Editors), 1978. The age of the Alpidic metamorphism in the Western Tauern Window, Austrian Alps, accordign to radiometric dating Alps, Apennines, Hellenides, 38. Inter-Union Commission on Geodynamics, 140-148 pp.
Ranalli, G. and Murphy, D.C., 1987. Rheological stratification of the lithosphere. Tectonophysics, 132(4): 281-295.
Ranalli, G., 1995. Rheology of the earth, second edition. Chapman & Hall, 413 pp.
Ranalli, G., 1997. Rheology of the lithosphere in space and time. In: J.P. Burg and M. Ford (Editors), Orogeny through time. Geol. Soc. Spec. Pub., pp. 19-37.
Ranalli, G., 2000. Rheology of the crust and its role in tectonic reactivation. J. Geodyn., 30: 3-15.
Ratschbacher, L., Frisch, W., Linzer, H. and Merle, O., 1991. Lateral extrusion in the eastern Alps, part2: structural analysis. Tectonics, 10: 257-271.
Regard, V., Faccenna, C., Martinod, J., Bellier, O. and Thomas, J.-C., 2003. From subduction to collision: Control of deep processes on the evolution of convergent plate boundary. J. Geophys. Res., 108.

Regenauer-Lieb, K., Yuen, D.A. and Branlund, J., 2001. The Initiation of Subduction: Criticality by Addition of Water? Science, 294(5542): 578-580.

Reinecker, J., Danišík, M., Schmid, C., Glotzbach, C., Rahn, M., Frisch, W. and Spiegel, C., 2008. Tectonic control on the late stage exhumation of the Aar Massif (Switzerland): Constraints from apatite fission track and (U-Th)/He data. Tectonics, 27(6).

Robl, J. and Stüwe, K., 2005. Continental collision with finite indenter strength: 2. European Eastern Alps. Tectonics, 24(4).

Roeder, D., 1989. South-Alpine thrusting and trans-Alpine convergence. Geological Society London Special Publications, 45(1): 211.

Roeder, D., 1992. Thrusting and wedge growth, Southern Alps of Lombardia (Italy). Tectonophysics, 207(1-2): 199-243.

Rosenberg, C.L., Berger, A. and Schmid, S.M., 1995. Observations from the floor of a granitoid pluton: Inferences on the driving force of final emplacement. Geology, 23(5): 443.

Rosenberg, C.L., Brun, J.P., Cagnard, F. and Gapais, D., 2007. Oblique indentation in the Eastern Alps: Insights from laboratory experiments. Tectonics, 26(2).

Rosenberg, C.L. and Berger, A., 2009. On the causes and modes of exhumation and lateral growth of the Alps. Tectonics, 28(6).

Roure, F., Choukroune, P., Berastegui, X., Munoz, J.A., Villien, A., Matheron, P., Bareyt, M., Seguret, M., Camara, P. and Deramond, J., 1989. ECORS deep seismic data and balance cross sections: Geometric constraints on the evolution of the Pyrenees. Tectonics, 8(1): 41-50.

Roure, F., 2008. Foreland and Hinterland basins: what controls their evolution? Swiss Journal of Geosciences, 101(0): 5-29.

Ruppel, C. and McNutt, M., 1990. Regional compensation of the Greater Caucasus mountains based on an analysis of Bouguer gravity data. Earth and Planetary Science Letters, 98(3-4): 360-379.

Sachsenhofer, R., 2001. Syn- and post-collisional heat flow in the Cenozoic Eastern Alps. international Journal of Earth Sciences, 90: 579-592.

Saintot, A. and Angelier, J., 2002. Tectonic paleostress fields and structural evolution of the NW-Caucasus fold-and-thrust belt from Late Cretaceous to Quaternary. Tectonophysics, 357(1-4): 1-31.

Schlunegger, F. and Willett, S., 1999. Spatial and temporal variations in exhumation of the central Swiss Alps and implications for exhumation mechanisms. Geological Society, London, Special Publications, 154(1): 157-179.

Schmid, S.M., Pfiffner, O.A., Froitzheim, N., Schönborn, G. and Kissling, E., 1996. Geophysical-geological transect and tectonic evolution of the Swiss-Italian Alps. Tectonics, 15(5): 1036-1064.

Schmid, S.M., Pfiffner, O.A., Schönborn, G., Froitzheim, N. and Kissling, E. (Editors), 1997. Integrated cross section and tectonic evolution of the Alps along the eastern traverse. Deep structure of the Swiss Alps: Results of NRP20. Birkhauser Verlag, Basel, 289–304 pp.

Schmid, S.M. and Kissling, E., 2000. The arc of the western Alps in the light of geophysical data on deep crustal structure. Tectonics, 19: 62-85.

Schmid, S.M., Fügenschuh, B. and Lippitsch, R., 2003. The Western Alps-Eastern Alps transition: tectonics and deep structure. Spec. Vol. Mem. Sci. Geol., 54: 257-260.

Schmid, S.M., Fügenschuh, B., Kissling, E. and Schuster, R., 2004. Tectonic map and overall architecture of the Alpine orogen. Swiss journal of geosciences, 97(1): 93-117.

Schönborn, G., 1999. Balancing cross sections with kinematic constraints: The Dolomites (northern Italy). Tectonics, 18(3): 527-545.

Schumacher, M.E., Schönborn, G., Bernoulli, D. and Laubscher, H.P., 1996. Rifting and collision in the Southern Alps. Deep structure of the Swiss Alps: Birkhäuser, Results of the National Research Program, 20: 186–204.

Schuster, R., Koller, F., Hoeck, V., Hoinkes, G. and Bousquet, R., 2004. Explanatory notes to the map: Metamorphic structure of the Alps-Metamorphic evolution of the Eastern Alps. Mitt.

Österr. Miner. Ges, 149: 175-199.
Selverstone, J. and Spear, F., 1985. Metamorphic P-T paths from pelititc schists and greenstones from the south-west Tauern Window, Eastern Alps. Journal of Metamorphic Geology, 3: 439-465.
Selverstone, J., 1988. Evidence for east-west crustal extension in the eastern Alps: implications for the unroofing history of the Tauern Window. Tectonics, 7: 87-105.
Shemenda, A.I. and Grocholsky, A.L., 1992. Physical modelling of lithosphere subduction in collision zones. Tectonophysics, 216(3-4): 273-290.
Smit, J., Burg, J.P., Dolati, A. and Sokoutis, D., 2010. Effects of mass waste events on thrust wedges: Analogue experiments and application to the Makran accretionary wedge. Tectonics, 29(3).
Sobouti, F. and Arkani-Hamed, J., 2002. Thermo-mechanical modeling of subduction of continental lithosphere. Physics of The Earth and Planetary Interiors, 131(3-4): 185-203.
Sokoutis, D., Burg, J.-P., Bonini, M., Corti, G. and Cloetingh, S., 2005. Lithospheric-scale structures from the perspective of analogue continental collision. Tectonophysics, 406(1-2): 1-15.
Sölva, H., Grasemann, B., Thöni, M., Thiede, R. and Habler, G., 2005. The Schneeberg Normal Fault Zone: normal faulting associated with Cretaceous SE-directed extrusion in the Eastern Alps (Italy/Austria). Tectonophysics, 401(3-4): 143-166.
Souriau, A., Chevrot, S. and Olivera, C., 2008. A new tomographic image of the Pyrenean lithosphere from teleseismic data. Tectonophysics, 460(1-4): 206-214.
Spiess, R., 1995. The Passeier-Jaufen Line: a tectonic boundary between Variscan and eo-Alpine Meran-Mauls basement. Schweiz. Mineral. Petrogr. Mitt, 75: 413-425.
Stauder, W., 1973. Mechanism and spatial distribution of Chilean earthquakes with relation to subduction of the oceanic plate. J. geophys. Res, 78(23): 5033-5061.
Staufenberg, H., 1987. Apatite fission-track evidence for postmetamorphic uplift and cooling history of the Eastern Tauern window and the surrounding Austroalpine (Central Eastern Alps, Austria). Geologisch Jahrbuch, 130: 571-586.
Steenken, A., Siegesmund, S., Heinrichs, T. and Fugenschuh, B., 2002. Cooling and exhumation of the Rieserferner Pluton (Eastern Alps, Italy/Austria). International Journal of Earth Sciences, 91: 799-817.
Stern, T., Molnar, P., Okaya, D. and Eberhart-Phillips, D., 2000. Teleseismic P wave delays and modes of shortening the mantle lithosphere beneath South Island. New Zealand, J. Geophys. Res, 105(21): 615–21.
Stipp, M., Fügenschuh, B., Gromet, L.P., Stünitz, H. and Schmid, S.M., 2004. Contemporaneous plutonism and strike-slip faulting: A case study from the Tonale fault zone north of the Adamello pluton (Italian Alps). Tectonics, 23(3).
Stöckhert, B., Brix, M., Kleinschrodt, R., Hurford, A. and Wirth, R., 1999. Thermochronometry and microstructures of quartz-a comparison with experimental flow laws and predictions on the temperature of the brittle-plastic transition. Journal of Structural Geology, 21: 351-369.
Sveen, J.K., 2004. An introduction to MatPIV v. 1.6. 1. Mechanics and Applied Mathematics, 2.
Tagawa, M., Nakakuki, T., Kameyama, M. and Tajima, F., 2007. The Role of History-Dependent Rheology in Plate Boundary Lubrication for Generating One-Sided Subduction Pure and Applied Geopysics, 164(5): 879-907.
Thöni, M., 1999. A review of geochronological data from the Eastern Alps. Schweizerische Mineralogische und Petrographische Mitteilungen, 79: 209-230.
Tichelaar, B.W. and Ruff, L.J., 1993. Depth of seismic coulpling along subduction zones Journal of Geophysical Research-Solid Earth, 98(B2): 2017-2037.
Toth, J. and Gurnis, M., 1998. Dynamics of subduction initiation at preexisting fault zones. Journal of geophysical research 103(B8): 18053-18067.
Toussaint, G., Burov, E. and Avouac, J.P., 2004a. Tectonic evolution of a continental collision zone: A thermomechanical numerical model. Tectonics, 23.
Toussaint, G., Burov, E. and Jolivet, L., 2004b. Continental plate collision: Unstable vs. stable

slab dynamics. geology, 32(1): 33-36.
TRANSALP Working Group, 2002. First deep seismic reflection images of the Eastern Alps reveal giant crustal wedges and transcrustal ramps. Geophys. Res. Lett., 29: 10.1029/2002GL014911.
Tsuru, T., Park, J.-O., Miura, S., Kodaira, S., Kido, Y. and Hayashi, T., 2002. Along-arc structural variation of the plate boundary at the Japan Trench margin: Implication of interplate coupling. J. Geophys. Res., 107.
Upton, P., Koons, P.O., Craw, D., Henderson, C.M. and Enlow, R., 2009. Along-strike differences in the Southern Alps of New Zealand: Consequences of inherited variation in rheology. Tectonics, 28(2).
Ustaszewski, K., Schmid, S.M., Fügenschuh, B., Tischler, M., Kissling, E. and Spakman, W., 2008. A map-view restoration of the Alpine-Carpathian-Dinaridic system for the Early Miocene. Swiss Journal of Geosciences, 101: 273-294.
Valasek, P. and Mueller, S. (Editors), 1997. A 3D crusatl model of the Swiss Alps based on integrated interpretation of seismic refraction and NRP 20 seismic reflection data. Deep structure of the Swiss Alps: Results of NRP20, 305–325 pp.
Viola, G., Mancktelow, N. and Seward, D., 2001. Late Oligocene-Neogene evolution of Europe-Adria collision: new structural and geochronological evidence from the Giudicarie fault system (Italian Eastern Alps). Tectonics, 20: 999-1020.
Viola, G., Mancktelow, N.S., Seward, D., Meier, A. and Martin, S., 2003. The Pejo fault system: An example of multiple tectonic activity in the Italian Eastern Alps. Bulletin of the Geological Society of America, 115(5): 515-532.
Viola, G., Odonne, F. and Mancktelow, N.S., 2004. Analogue modelling of reverse fault reactivation in strike–slip and transpressive regimes: application to the Giudicarie fault system, Italian Eastern Alps. Journal of Structural Geology, 26(3): 401-418.
von Blanckenburg, F., Villa, I., Baur, H., Morteani, G. and Steiger, R., 1989. Time calibration of a PT-path from the Western Tauern window, Eastern Alps: the problem of closure temperatures. Contributions to Mineralogy and Petrology.
von Blanckenburg, F. and Davies, J., 1995. Slab breakoff: A model for syncollisional magmatism and tectonics in the Alps. Tectonics, 14(120-131).
Weijermars, R. and Schmeling, H., 1986. Scaling of Newtonian and non-Newtonian fluid dynamics without inertia for quantitative modelling of rock flow due to gravity (including the concept of rheological similarity). Phys. Earth.Planet. Inter., 43: 316-330.
Willett, S., Beaumont, C. and Fullsack, P., 1993. Mechanical model for the tectonics of doubly-vergent compressional orogens. Geology, 21: 371-374.
Willett, S.D., Schlunegger, F. and Picotti, V., 2006. Messinian climate change and erosional destruction of the central European Alps. Geology, 34(8): 613.
Willingshofer, E. and Cloetingh, S., 2003. Present-day lithospheric strength of the Eastern Alps and its relationship to neotectonics. Tectonics, 22(6): 1075.
Willingshofer, E., Sokoutis, D. and Burg, J.-P., 2005. Lithospheric-scale analogue modelling of collision zones with a pre-existing weak zone. Geological Society, London, Special Publications, 243(1): 277-294.
Willingshofer, E. and Sokoutis, D., 2009. Decoupling along plate boundaries: Key variable controlling the mode of deformation and the geometry of collision mountain belts. Geology, 37(1): 39-42.
Windley, B.F. and Tarney, J., 1986. The structural evolution of the lower crust of orogenic belts, present and past. Geological Society, London, Special Publications, 24(1): 221-230.
Wölfler, A., 2008. Tectonothermal evolution of the southeastern Tauern Window and the adjacent austroalpine basement of the Kreuzeck Massif: Evidence from combined fission track and (U-Th)/He analysis. Ph.D. Thesis, Tübingen, 80 pp.
Yamato, P., Agard, P., Burov, E., Le Pourhiet, L., Jolivet, L. and Tiberi, C., 2007. Burial and exhumation in a subduction wedge: Mutual constraints from thermomechanical modeling and natural PTt data (Schistes Lustrés, western Alps). Journal of Geophysical Research, 112(B7):

B07410.
Yin, A. (Editor), 2004. Gneiss domes and gneiss dome systems. Gneiss domes and orogeny Special paper 380. Geological Society of America, 1-14 pp.
Zampieri, D., 1995. Tertiary extension in the southern Trento Platform, Southern Alps, Italy. Tectonics, 14.
Zattin, M., Cuman, A., Fantoni, R., Martin, S., Scotti, P. and Stefani, C., 2006. From Middle-Jurassic heating to Neogen cooling: The thermochronological evolution of the Southern Alps. Tectonophysics, 414: 191-202.
Ziegler, P.A., Bertotti, G. and Cloetingh, S.A.P.L., 2002. Dynamic processes controlling foreland development. The role of mechanical (de)coupling of orogenic wedges and forelands. EGU Stephan Mueller Special Publication Series, 1: 17-56.
Zimmermann, R., Hammerschmidt, K. and Franz, G., 1994. Eocene high pressure metamorphism in the Penninic units of the Tauern window (Eastern Alps): Evidence from ^{40}Ar-^{39}Ar dating and petrological investigations. Contributions to Mineralogy and Petrology, 117: 175-186.